1 of 3

AD A
105895

tate Water Survey Division

METEOROLOGY SECTION
AT THE
UNIVERSITY OF ILLINOIS

AD A105895

THE BEHAVIOR OF SURFACE WIND AND THERMODYNAMIC FIELDS IN THE PRESENCE OF DEEP CONVECTION

Henry J. Cooper
Michael Garstang

Department of Environmental Sciences
University of Virginia
Charlottesville, Virginia 22903

10 10 19

REPORT DOCUMENTATION PAGE		READ INSTRUCTIONS BEFORE COMPLETING FORM
1. REPORT NUMBER 16816.2-GS	2. GOVT ACCESSION NO. AD-A105 895	3. RECIPIENT'S CATALOG NUMBER
4. TITLE (and Subtitle) The Behavior of Surface Wind and Thermodynamic Fields in the Presence of Deep Convection.		5. TYPE OF REPORT & PERIOD COVERED Technical
		6. PERFORMING ORG. REPORT NUMBER
7. AUTHOR(s) Henry J. Cooper Michael Garstang		8. CONTRACT OR GRANT NUMBER(s) DAAG29 80 K 0053
9. PERFORMING ORGANIZATION NAME AND ADDRESS University of Virginia Charlottesville, VA 22903		10. PROGRAM ELEMENT, PROJECT, TASK AREA & WORK UNIT NUMBERS
11. CONTROLLING OFFICE NAME AND ADDRESS U. S. Army Research Office Post Office Box 12211 Research Triangle Park, NC 27709		12. REPORT DATE May 81
		13. NUMBER OF PAGES 240
14. MONITORING AGENCY NAME & ADDRESS(if different from Controlling Office)		15. SECURITY CLASS. (of this report) Unclassified
		15a. DECLASSIFICATION/DOWNGRADING SCHEDULE

16. DISTRIBUTION STATEMENT (of this Report)

Approved for public release; distribution unlimited.

17. DISTRIBUTION STATEMENT (of the abstract entered in Block 20, if different from Report)

NA

18. SUPPLEMENTARY NOTES

The view, opinions, and/or findings contained in this report are those of the author(s) and should not be construed as an official Department of the Army position, policy, or decision, unless so designated by other documentation.

19. KEY WORDS (Continue on reverse side if necessary and identify by block number)

20. ABSTRACT (Continue on reverse side if necessary and identify by block number)

Surface wind measurements, taken in 1973 and 1975 in fine-mesh networks in Florida and in Illinois in 1979, are used to calculate surface divergence on the convective scale. The behavior of convective scale convergence fields is shown to be similar in Florida and Illinois. Analysis of profiles of network divergence and subsequent rainfall rates shows the value of such measurements in short-term forecasting of convective rainfall.

DD FORM 1473 EDITION OF 1 NOV 65 IS OBSOLETE

BLANK PAGE

THE BEHAVIOR OF SURFACE WIND AND THERMODYNAMIC

FIELDS IN THE PRESENCE OF DEEP CONVECTION

Henry J. Cooper

Michael Garstang

Department of Environmental Sciences

University of Virginia

Charlottesville, Virginia   22903

May 1981

THE BEHAVIOR OF SURFACE WIND AND THERMODYNAMIC FIELDS IN THE PRESENCE OF DEEP CONVECTION

Henry J. Cooper and Michael Garstang

ABSTRACT

Surface wind measurements taken in 1973 and 1975 in fine-mesh networks in Florida and in Illinois in 1979 are used to calculate surface divergence on the convective scale. The behavior of convective scale convergence fields is shown to be similar in Florida and Illinois. Analysis of profiles of network divergence and subsequent rainfall rates shows the value of such measurements in short-term forecasting of convective rainfall.

Comparison of the convective-scale mass transports in Florida, with the Florida peninsular scale forcing reveals a relationship between the two. After the initiation of a convective scale feedback mechanism by the peninsular scale forcing, downdraft induced convergence maintains and intensifies the convective-scale activity long after the peninsular scale forcing has passed its peak. A feedback mechanism between the larger and convective scale is thus established. The decline in the efficiency of the convective scale feedback mechanism is related to the rate of change in the peninsular scale forcing.

The evolution of the convective activity from a condition of weak convection to a condition of deep convection is shown to depend upon the amount of moisture mixed up into the lower cloud layer by the shallower convection.

A composite Florida storm is used to show that the diurnal convective process is a very efficient mechanism in the vertical mixing of water vapor, and a relatively inefficient mechanism in production of rainfall.

ACKNOWLEDGMENT

TABLE OF CONTENTS

Table of Contents (cont.)

LIST OF FIGURES

Page

List of Figures (cont.)

List of Figures (cont.)

List of Figures (cont.)

List of Figures (cont.)

List of Figures (cont.)

List of Figures (cont.)

List of Figures (cont.)

LIST OF TABLES

CHAPTER 1

INTRODUCTION AND OBJECTIVES

A. THE IMPORTANCE OF CUMULUS CONVECTION

The importance of the role of cumulus convection in the global
energy cycle is well appreciated (Riehl and Malkus, 1958; Malkus, 1963;
Simpson, 1973). This basic role is described by Riehl and Malkus as an
inability of the slow ascent of the large scale meridional circulations
to fulfill the energy balance between the lower and upper troposphere
or between low and high latitudes of the globe, for the given sources
and sinks. Riehl and Simpson (1979) and Augstein et al. (1980) provide
further observational evidence of the crucial role played by deep convec-
tion in the global energy balance.

Yanai (1975) describes deep convection as being a major source of
available potential energy (APE), formed in the upper troposphere by
release of latent heat of condensation of organized convection, which
in turn is a source of energy which drives tropical waves. He views the
convection as being organized by the moisture inflow into a region due
to large scale processes. This view is modified by those of Simpson
(1979) and Garstang (1980), who consider the process to be more of an
interactive one between larger and smaller scales, and between the cloud
and subcloud layers.

B. PREVIOUS RESEARCH

Research into cumulus convection and its role in the global
atmospheric processes has taken two main forms. The first form has been

in modeling of individual cumulus, of single cell storms and squall
lines. The second form has involved attempts to determine the inter-
actions of the convection with the mesoscale environment through
various parameterization schemes, mixed layer models and mesoscale sea
breeze models.

1. Cumulus Models: Theoretical

Interest in modeling cumulus convection heightened with the
introduction of the concept of entrainment by Stommel (1947) and
continued with the bubble models of the fifties, which are typified
in Levine (1959), Malkus and Witt (1959) and Ludlam and Scorer (1956).
These one-dimensional models evolved into more complicated treatments
such as that of Simpson and Wiggert (1969) and have since been developed
into fully three-dimensional models such as that of Schlesinger (1975).
Cotton (1975) gives an excellent review of the cloud physics aspects
of these models, and Lilly (1979) provides a review of the dynamics of
the various models of thunderstorms and squall lines.

2. Cumulus Models: Empirical

Parallel to the development of these theoretical models, there
have been a number of observational studies, notably the observational
work carried out by the Woods Hole Oceanographic Institution (Malkus,
1952, 1954, 1956, 1960) and by the work at Imperial College (Scorer and
Ludlam, 1953). The role of vertical shear in the horizontal wind on
cumulus (Malkus, 1949) and the forcing of a heated surface (Malkus and
Stern, 1953; Malkus, 1955; Charnock et al., 1956) in the generation and
maintenance of convective clouds was examined.

that possible through the actions of isolated short-lived single cell storms. The importance of relationships between severity of squalls, prolongation of lifetime, and propagation has long been recognized (Newton, 1968). Although these relationships are not yet fully understood, a linkage to the presence of higher momentum air aloft has been postulated.

3. The Role of Downdrafts

Houze (1977) and Leary (1979) describe the structure of a tropical squall line system and cloud cluster which passed over the GATE array, and which propagated by means of lifting provided by convective scale downdrafts on the leading edge of the system. Purdom (1979) in an analysis of high resolution satellite data concludes that "convective scale interaction is of primary importance in determining the evolution of deep convection. This interaction manifests itself as the merger and intersection of convection-produced outflow boundaries with other convective areas, lines and boundaries." Satellite photographs show visible evidence of the process in some detail. Brandli and Orndorff (1976) display a visual satellite image of the interaction of three storms and their outflows. Black (1979) offers pictures taken during the Apollo-Soyuz test project (ASTP) which clearly show the outflow from a thunderstorm complex and the subsequent growth of TCUs along the gust front convergence zones.

Because of the role of outflows in the propagation of storms, in the triggering of new growth, and the injection of low energy air into the boundary layer, many studies have been made of the nature of gust fronts and outflows, both with a view towards better understanding of their relationship to convection as a whole, and with the intention of providing better short-term forecasts.

The Thunderstorm Project (Byers and Braham, 1949) provided the first major experimental study of these storms, and, until the meso-scale networks laid out in south Florida during the FACE experiments of the seventies and the SESAME experiments in Oklahoma in the same decade, was the only such intensive study of thunderstorms in that region. Their model of a thunderstorm, derived from data collected in Ohio as well as in Florida, remains the basic empirical view of thunderstorm behavior today. Using aircraft data, surface wind and thermodynamic data, upper air balloon data and radar data, they were able to document the various features of the thunderstorm. They determined the three-stage life cycle of growth, maturity and decay, and were able to quantify the dimensions of the convective cells which drive the storms.

In a synopsis of convective cloud dynamics Newton (1968) outlined the flow in and around steady state propagating storms, in a manner similar to the flows described by Fujita (1955) and Browning and Ludlam (1962). As mentioned in the Thunderstorm report by Byers and Braham and as depicted in the early observational models mentioned above, one of the features of these storms is the process by which they propagate and interact with one another. Byers and Braham state explicitly (p. 78) that the vast majority of new convective cells occur within close proximity of existing ones, and postulate that the process of propagation and regeneration is a result of energy-rich air being lifted to condensation by outflows from mature cells. This particular feature of thunderstorm behavior is extremely important, since it prolongs the convective activity by releasing latent instability in previously unaffected regions, and at the same time enhances the effect that the convective activity will have on the larger scale environment beyond

In a study similar to that of Charba (1974), Goff (1976) examines the general outflow characteristics of storms using an instrumented 461 m tower in Oklahoma. As well as displaying thermodynamic time-height cross-sections of, and describing the circulation within the outflow, he notes that "outflow gust fronts may be observed up to 45 minutes before measurable precipitation commences...." Fankhauser and Mohr (1979) show a strong correlation between the emergence of new cells in a Colorado storm and the boundary layer convergence associated with the leading edge of the storm outflow some 10-20 km ahead of the maximum region of reflectivity. Ulanski and Garstang (1978) found that significant convergence appeared in the FACE 1973 network on the average 30-40 minutes before the onset of rain, and on occasion on the order of an hour in advance of the first rainfall. The relationship between the mesoscale convergence and convection is investigated .y Matsumoto (1967), Chen and Orville (1980) and Ogura and Chen (1977). All find a positive correlation between low-level convergence and the intensity and initiation of convection.

It is evident, then, that storms often are initiated and propagate via a process involving lifting of surface air by outflows, to a condition where new convective cells will develop. Attempts have been made to this process in terms of a hydraulic jump (Tepper, 1950); Moncrieff and Miller (1976) explain the speed of propagation in terms of what they call CAPE (Convective Available Potential Energy) which is essentially a modified cloud work function. Charba (1974), finds the dynamics and structure of the outflow from an Oklahoma storm to be similar to that of a laboratory-produced density current. Raymond (1975) explains the propagation speed of the outflows in terms of a convectively forced internal gravity wave packet.

All of the previous experimental work has suffered from the lack
of sufficiently detailed observations and their analysis. It has been
difficult to isolate cause and effect without adequate temporal and
spatial definition of the cloud. The time continuity and detail near
the surface, of the observations available from FACE 73, FACE 75 and the
1979 VIN experiment, which include data from over 100 storms, will be
drawn upon in this study to address in particular, the response of the
lower atmosphere to convective outflow near the surface.

4. Scale Interaction: Theoretical

Attempts to link the mass and energy transports on the convective
scale to the mesoscale and larger scales have been made. Pielke (1974)
constructed a primitive-equation 3-D seabreeze model and demonstrated
the relationship between mesoscale convergence and the synoptic scale
forcing. He found that "the differential heating between land and water
over south Florida is the primary determinant of the magnitude of the
convergence...," highlighting the connection between the transfer
functions, both in the vertical and the horizontal, of intense convec-
tion.

Various parameterization schemes have been developed in an attempt
to model the interaction between the convective scale and the meso-synop-
tic scale. These schemes fall into two categories, the convective
adjustment type and the direct parameterization type. The convective
adjustment type essentially account for the effects of cumulus on the
larger scales by adjusting unstable profiles to neutral states using
various schemes. These schemes do not demonstrate great detail of the
processes (Cho, 1975).

The more direct parameterization schemes of Arakawa and Schubert (1974), Yanai et al. (1973), Ogura and Cho (1973), Kuo (1974) and Anthes (1977) all treat the effects of cumulus as eddies on the large scale flow in various ways, and use diagnosed values for cloud base mass fluxes and energy fluxes. Johnson (1976) developed a model which shows that the large scale budgets of parameterization models will be severely affected by cumulus downdrafts, and that "...the neglect of cumulus downdrafts and their associated rainfall evaporation leads to the diagnosis of excessively large populations of shallow cumulus....(and)... excessive warming and drying in the lower troposphere."

5. Scale Interaction: Empirical

The findings of Pielke (1974) have been supported by observational studies made by Frank (1967) and Gerrish (1971). Both of these studies emphasize the dominance of the seabreeze zones in the initiation of convection over south Florida, and show the progression of lines of convection inland in response to the larger-scale flow. Frank (1967) and Burpee (1979), using rawinsonde stations which formed polygons over various peninsular scale regions, found the time of peak surface convergence to be 1300 EST (1400 EDT). The time of peak convergence on the peninsular scale over Florida appears to be persistent during the summer months and over different areas of the state.

Numerous other attempts have been made to describe the interaction between the convective scale and the mesoscale. Zipser (1969, 1977) using data from the Line Islands Experiment (LIE), showed the drastic effects of tropical squall lines on the larger scale thermodynamics. Betts (1976) used a two layer model to demonstrate convective activity which appeared "to strip off the subcloud layer (to ascend in

updrafts) and replace it by an equal amount of air from a layer from just above cloud base." Miller (1977) examined soundings from the same data set used by Betts and found a system similar to that described by Zipser, i.e., convective scale precipitation downdrafts and mesoscale dynamically driven downdrafts acting to alter the tropospheric thermo-dynamic profile. Both Betts' and Miller's work correlates well with the density current ideas discussed previously.

The land-sea breeze circulation over the peninsula of Florida and the almost daily occurrence of deep convection there provides one of the most outstanding experimental environments in which to study the inter-action between the large (peninsular scale) forcing and convective scale activity.

The large sample of 101 storms observed in FACE 73 and FACE 75 will be drawn upon in this study to describe the transformations taking place in a convectively active atmosphere.

An important contribution of the large scale models which ade-quately include convective processes would be the specification of the total heat and energy transfers accomplished by the atmospheric systems. An alternate approach is to examine the transports of the individual clouds or cloud complexes and from this calculation deduce the total transport. In this study, the latter approach is taken. Sufficient observational data exist to allow the calculation of mass transports of cloud systems which are defined in the low level velocity fields. The efficiency in terms of rainfall yielded to water supplied to the storm can be examined as well as the relationship between storm size and efficiency.

C. OBJECTIVES

    The extensive research in convection described above provides the
background to pursue five questions which can be answered in part by this
study:

    1) What is the relationship between the large scale forcing
        such as the peninsular scale forcing in Florida, and the
        convective scale forcing?

    2) How is convection, convective growth and propagation
        related to the outflow from previously existing storms?

Both 1 and 2 relate to cause and effect. The observations drawn upon in
this work provide some insight into the way in which convection is
initiated.

    3) What is the efficiency in terms of rainfall yielded to
        moisture ingested by a storm?

    4) What changes are effected by a storm on the environment
        and what are the implications of these changes?

    5) Can knowledge of the relationship between outflows and
        convective growth, and organization in the low level
        velocity fields be used to predict convective activity?

CHAPTER 2

DESCRIPTION OF THE DATA SET

A. THE 1973 FACE DATA SET

The 1973 FACE data set has been described by Ulanski and

Garstang (1978), and in more detail in NOAA Technical Memorandum

ERL WMPO-12 (1974). The network contained 229 fence-post rain

gauges which were read and emptied daily. The network covered an

area of 639 km^2 and was operated from 16 June to 14 August 1973. In

addition, there were 22 C-set recording anemometers which also

recorded rainfall on a minute by minute basis. Soundings were taken

as required by the concurrent cloud seeding program, for use in deter-

mining seedability criteria.

The National Hurricane Center's WSR-57 radar was operated in

conjunction with the program, and data from these observations were

made available on microfilm. Of the 90 days when the network was

operational, surface wind data were available on tape for 49 days.

The location of the network in 1973 is shown in Figure 1, and

a detailed picture of the rain gauge and anemometer layout is contained

in Figure 2.

B. THE 1975 FACE DATA SET

The 1975 FACE (Florida Area Cumulus Experiment) provided another

excellent data set for the same region in southern Florida, although the

surface wind network in 1975 was rearranged onto a more geometrically

regular grid, which was larger in area and in the number of wind sets

Figure 1. Location of the FACE 73 networks.
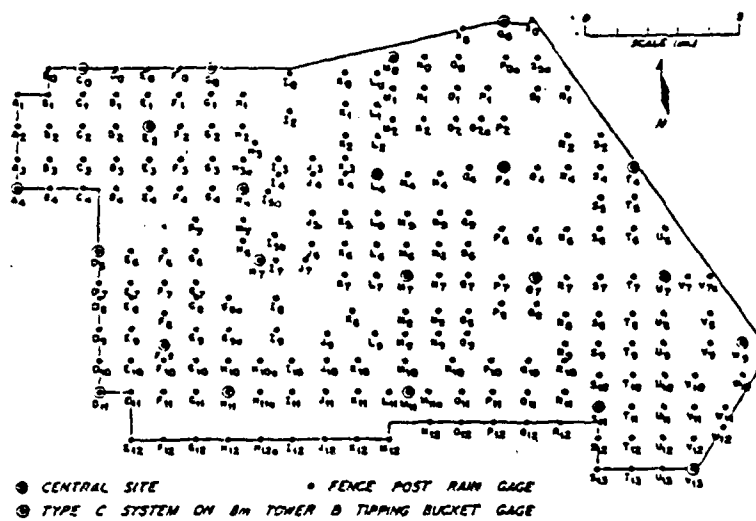
Figure 2. FACE 73 rain gauge and wind set arrays.

and recording rain gauges used than the network of 1973. A map of the network and the surrounding region for FACE 1975 is displayed in Figure 3a.

The network consisted of two nested networks, one of rain gauges and one of anemometers. The tipping bucket rain gauge network was operated in conjunction with the anemometer network, as layed out in Figure 3b, during July and August 1975.

The 50 rain gauges covered 171 statute mi^2 (441 km^2) and were laid out on a 2-statute mile grid. The wind recorders were laid out so as to cover the area occupied by the recording rain gauges, the region inside the dashed line in Figure 3b occupying 231 statute mi^2 (595 km^2), an area comparable to that covered by the entire network in 1973.

The total area covered by anemometers during 1975 was larger than that covered by the network in 1973, consisting of 46 stations over 720 statute mi^2 (1865 km^2) with one station every 4 statute miles. The types of stations and their locations are indicated in Figure 3b.

Radar observations were taken using the Miami WSR-57 10 cm radar as in 1973, and rawinsonde soundings were taken from the Field Observing Site (F.O.S.) at 1500, 1800 and 2100 GMT whenever possible. (A detailed description of the net is found in NOAA Technical Memorandum ERL-WMPO-28, 1976.)

C. THE 1979 VIN (VIRGINIA, ILLINOIS, NOAA) PROJECT DATA

The 1979 VIN data set is unique, in that it consists of 288 recording rain gauges (see Figure 4) coupled into a geometrically regular wind network of 49 wind sets. Of the 49 wind recorders used, 27 of them were provided by the PAM (Portable Automated Mesonetwork) system operated by the National Center for Atmospheric Research (NCAR).
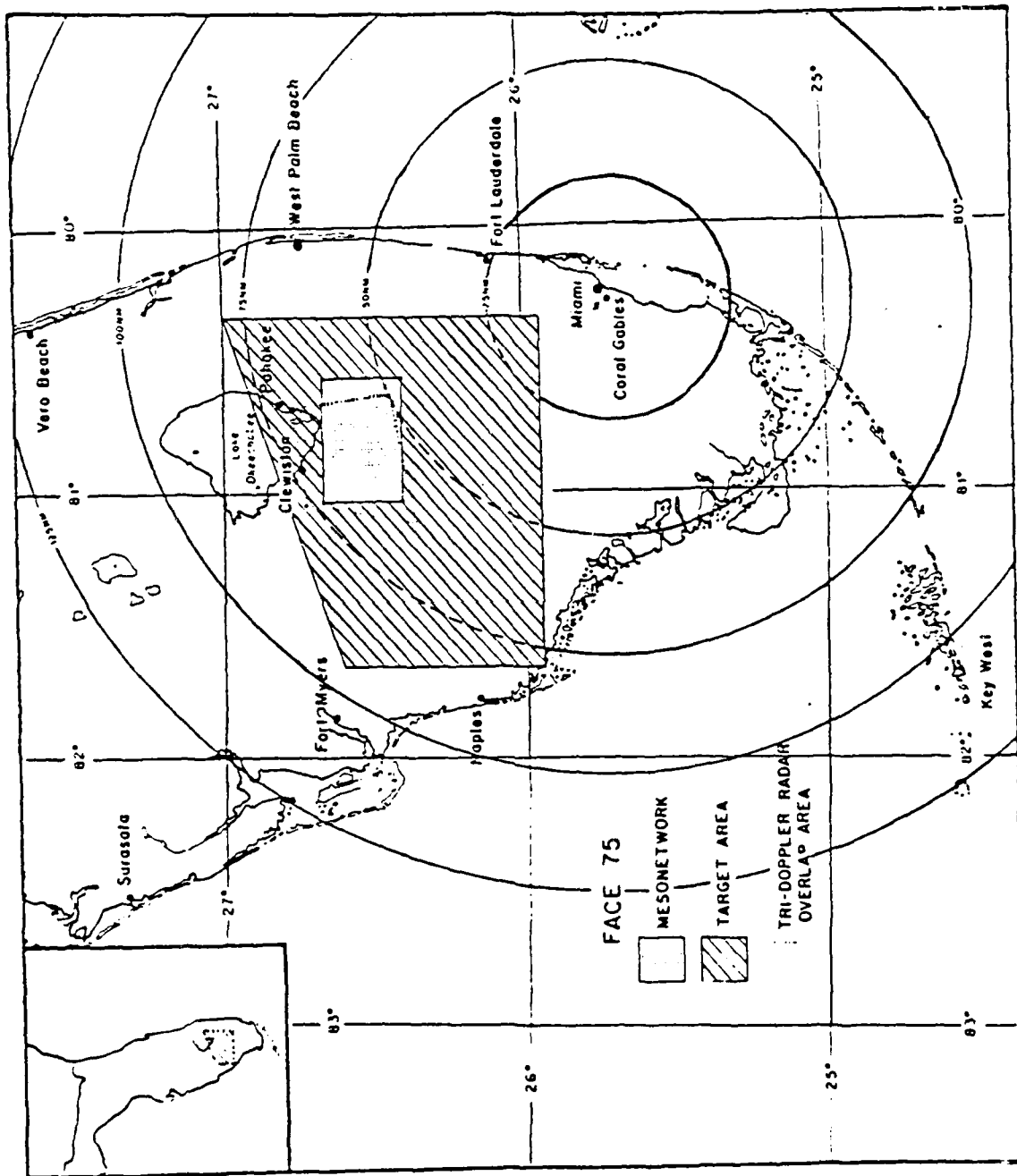
Figure 6d. Location of the FACE 75 networks.

Figure 5b. FACE 75 rain gauge and wind set arrays.

The rest of the sets were standard analogue wind sets, with the exception of some experimental digital recording anemometers being field tested by the University of Virginia (see Figure 5). The recording rain gauges were laid out as shown in Figure 4 on a 3 statute mile grid spacing, while the anemometers as a whole were laid out on a 4x4 statute mile grid spacing, with the PAM stations spaced 8 statute miles apart in the East-West plane, and 4 statute miles apart in the North-South plane. The PAM stations alternated with analogue wind sets, as shown in Figure 5.

The rain gauge network and the wind set network provided analogue rain and surface wind data every 5 minutes. The height of all anemometers was 4 m from ground level.

The PAM system collected and recorded a variety of surface meteorological data at each station including rainfall, wind direction and speed, dry bulb temperature, wet bulb temperature and surface pressure. Each station averaged these collected data over a 60 second period, and then transmitted the information, by radio, to a central site for analysis. The data were then stored on disk and on tape at the central site, and a NOVA 840 computer was programmed to compute and display on a Tektronix CRT terminal the surface wind divergence field, the area averaged divergence fields computed over any desired period of time from one minute to 24 hours. A list of other meteorological variables available for display in real time at the central site is in Table 1. A detailed description of the PAM system can be found in Brock and Govind (1977).

Rawinsondes and pibals were taken each operational day, and the CHILL radar provided local radar coverage during the project.
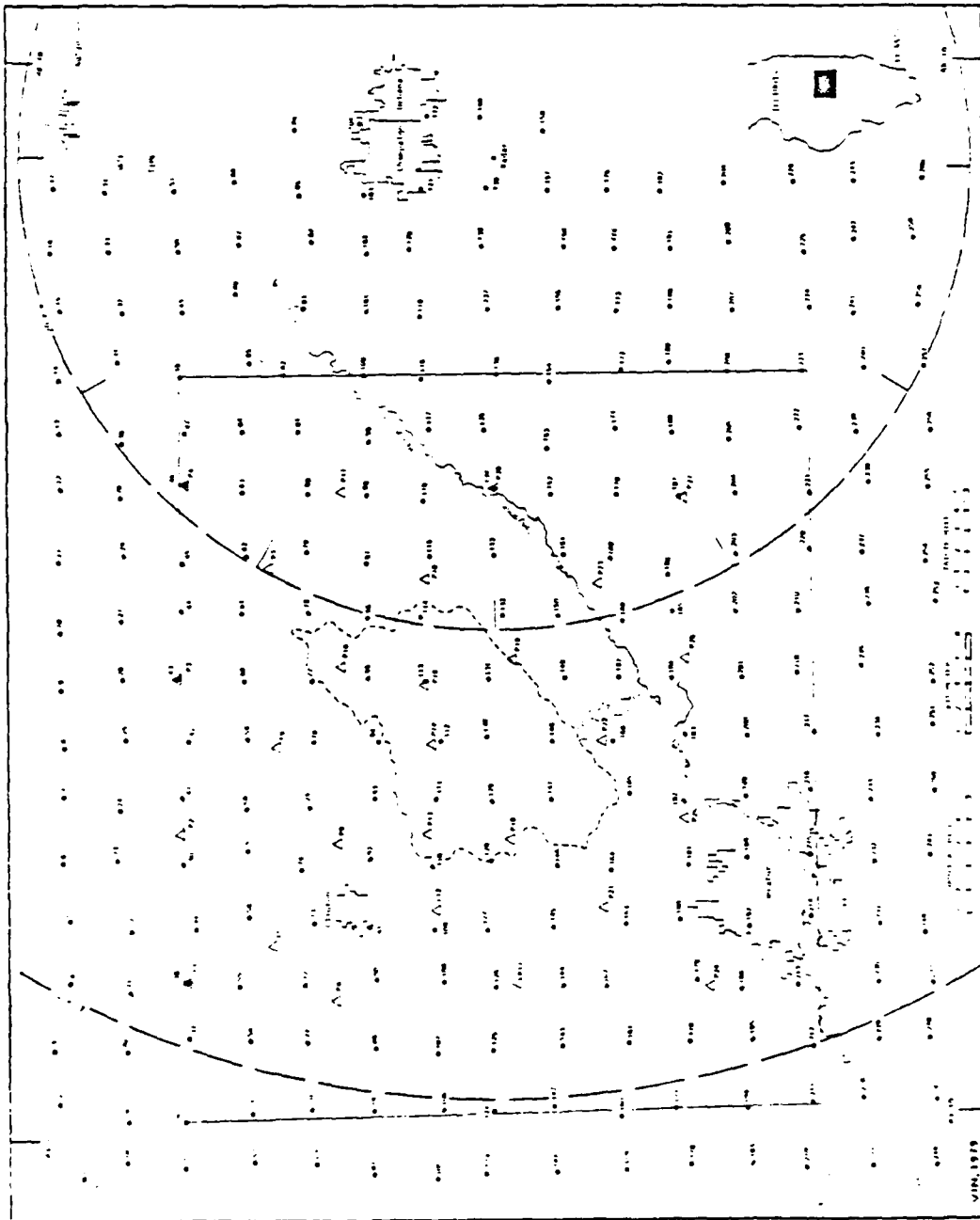
Figure 4. VIN intense rain gauge array.
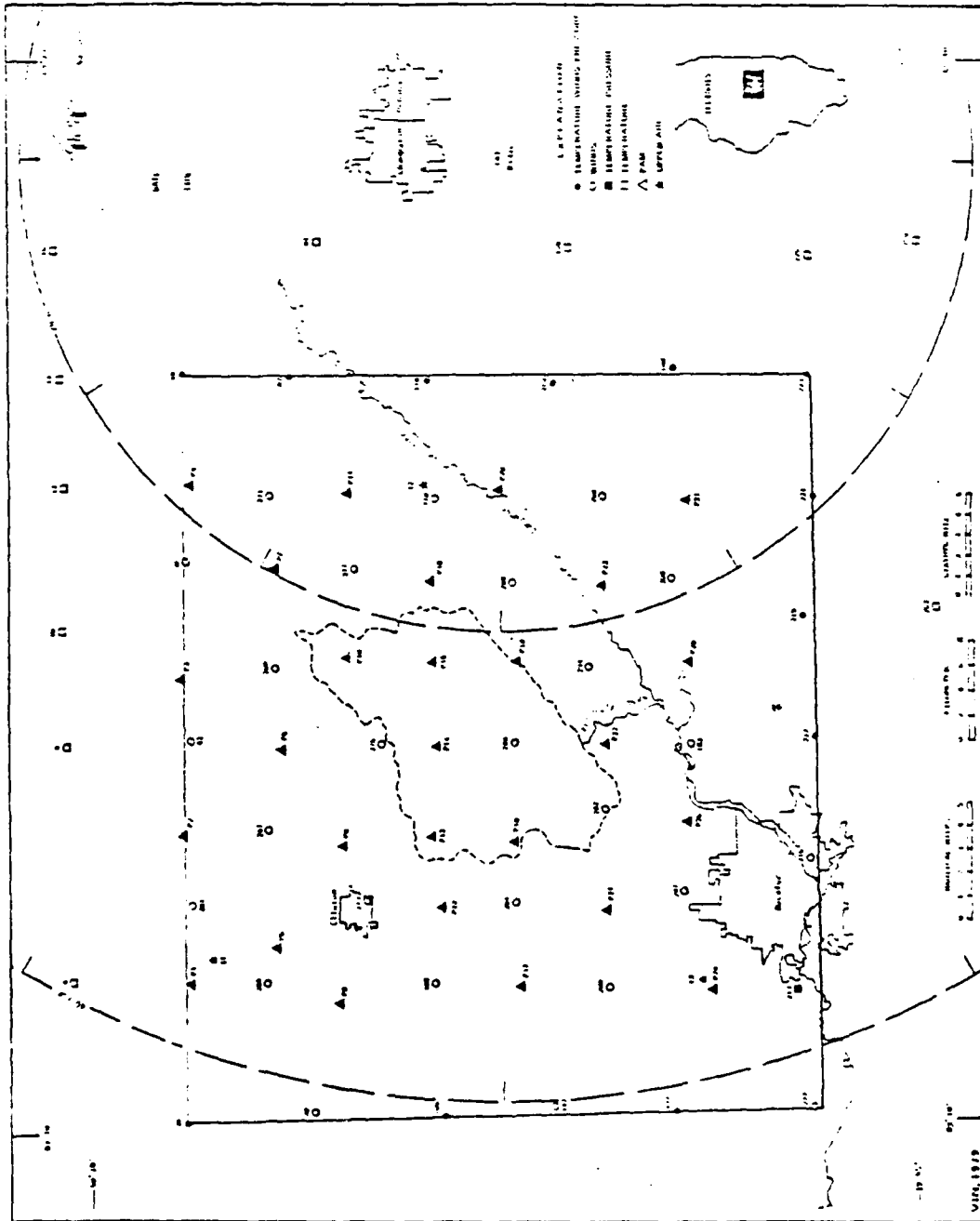
Figure 5. VIN PAM and analogue set array.

Table 1. Displayed data type definitions
(PAM System) 1979.

Number	Name	Units	Class
12	Dry bulb	°C	Meteorological
13	Wet bulb	°C	Meteorological
14	Rainfall	mm	Meteorological
15	Wind run	m/sec	Meteorological
16	Wind speed	m/sec	Meteorological
17	Wind direction	degrees	Meteorological
18	Pressure	mb	Meteorological
19	Dew point	°C	Derived
20	Potential Temperature	°K	Derived
21	Equivalent Potential Temperature	°K	Derived
22	Mixing Ratio	g/kg	Derived
23	Relative Humidity	%	Derived

D. DATA REDUCTION

The available data from 1973 FACE had already been digitized and put on tape, for 5-minute intervals, for periods of time surrounding the occurrence of storms over the 1973 network. The 1975 data were digitized and put onto tape through a joint effort of personnel at the University of Virginia and at NOAA/NHEML, Miami.

The 1975 data were taken off wind rolls in five minute averages. These data were digitized for each day during the months of July and August 1975, from 0800 EDT until 2000 EDT, and put onto magnetic tape.

Combined with the 49 days of data available from 1973, the total FACE data set available gives access to data on tape from 101 storms in southern Florida.

The PAM data from the VIN 1979 experiment were digitized and recorded on tape in the field, and were made available by the NCAR archiving facility.

E. DATA ANALYSIS

In order to perform a consistent analysis of data from field surface wind stations, it is necessary to develop an interpolation scheme which will allow accurate estimates of wind variables to be made on a regularly spaced grid. This is especially true of networks similar in layout to the 1973 FACE network, which, compared to the relatively regular layouts of the FACE 75 and VIN 79 networks, is non-uniform. In addition, in estimating divergence at a given point, one must be able to provide an estimate of the value of divergence at that point in the case when a nearby station breaks down. The interpolation of the data provides a consistent, regular estimate of wind variables at fixed points in space for intercomparison between different time periods. A description of the interpolation scheme used is contained in the Appendix.

For each 5-minute period of analysis, a check was run by calculating the divergence fields from a fixed velocity potential[1] simultaneously with calculations of divergence fields from the real data. In this way, badly distorted fields, which occur due to station break-downs, were detected and removed from the analysis.

---

[1]See Appendix A.

CHAPTER 3

THE PROFILES OF DIVERGENCE TAKEN OVER THE
ENTIRE NETWORK

The 1973 wind data that were on tape were in blocks of time
centered around the occurrence of showers in the network. Detailed
5-minute divergence and vorticity fields were calculated for each
period of available data, using the interpolation scheme described in
the Appendix.

The purpose of the analysis was to relate the horizontal velocity
divergence at the level of the anemometers (8 m) to subsequent rainfall
inside the network.

The divergence of velocity in the network was calculated in two
ways. First, the normal component of velocity relative to the sides
of the interpolation grid was integrated around the perimeter of the
interpolation grid. Second, the value of divergence at the center of
each grid square was found, and the average value of the divergence of
all grid squares was determined. In all tests run comparing the methods,
there was close agreement between the values of divergence calculated
using the first method (the "inflow") and those calculated using the
second method (the area averaged divergence), providing a check on the
internal consistency of the interpolation scheme. The area averaged
divergence calculations are used in this study. Using the area averaged
divergence calculations has two major advantages. It allows separations
and comparison of divergence over various regions within the network, in
terms of their contribution to the total network divergence, and it
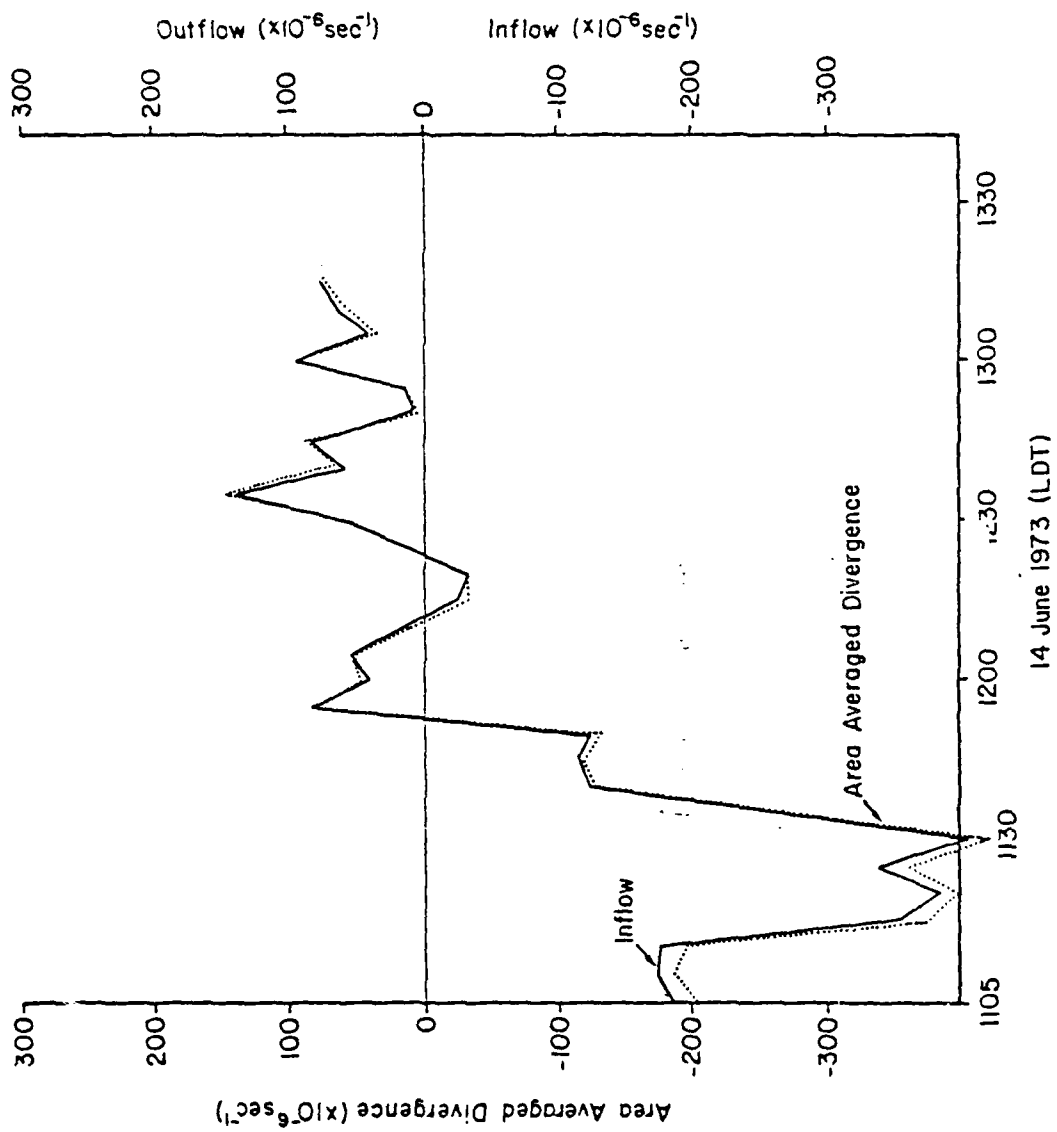
Figure 6a. Comparison of area-averaged divergence to inflow.

makes use of stations interior to the perimeter of the network. Figure 6a gives an example of the excellent agreement between the two types of calculations.

Two basic types of signal in the area averaged divergence fields were found, and typical examples of each kind are given in Figures 6b and 6c.

In Figure 6b the values of area averaged divergence, area averaged vorticity, net mass transport (to be defined later) and the total network recorded rainfall are plotted against time. Graphs of the same variables, for a different day, are plotted in Figure 6c. The type of signal in the surface area averaged divergence field shown in Figure 6c is typical of days when little or no rain fell, and no large storms came close to the wind instrument network. In contrast to Figure 6c, Figure 6b exhibits a strong sinusoidal signal in the area averaged divergence fields. This type of signal is usually associated with storms which deposit large amounts of rain in the network. The signal in the surface area averaged vorticity field exhibited no consistent behavior.

Similar analyses were carried out using data from 1975 FACE for 56 days in July and August for that year, and the same types of signal were found; that is, strong sinusoidal signals on heavy rain days and noisy signals on light rain days.

It is of interest to estimate the possibility of short term forecasting of local convective storms and the severe weather associated with them using the total network area-averaged divergence in the wind fields as a tool. Recall that the area-averaged divergence can be duplicated using a perimeter of stations many fewer in number than required to calculate the convective cell scale divergences within the
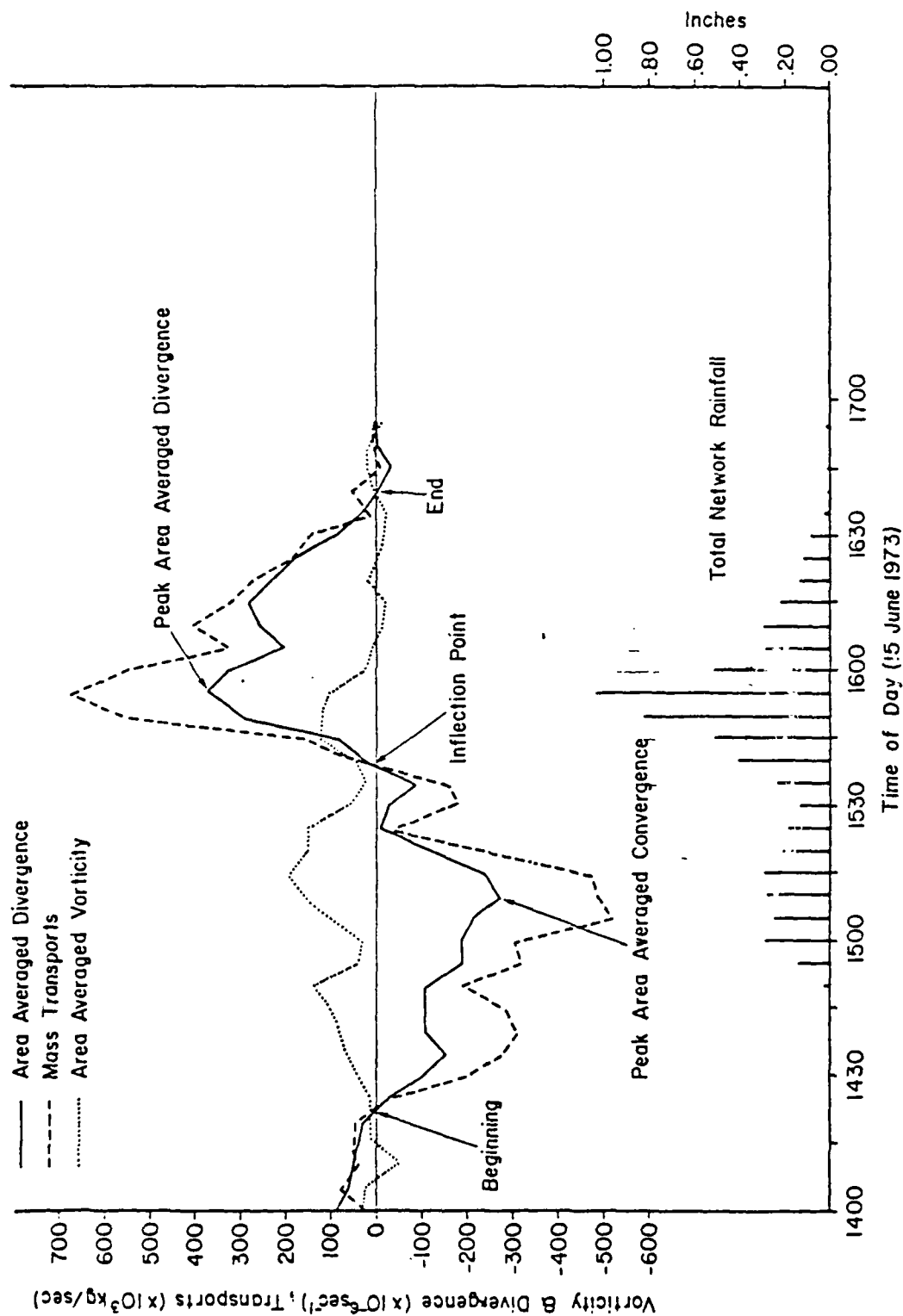
Figure 6. Definition of the stages of a storm, moderate-heavy shower.
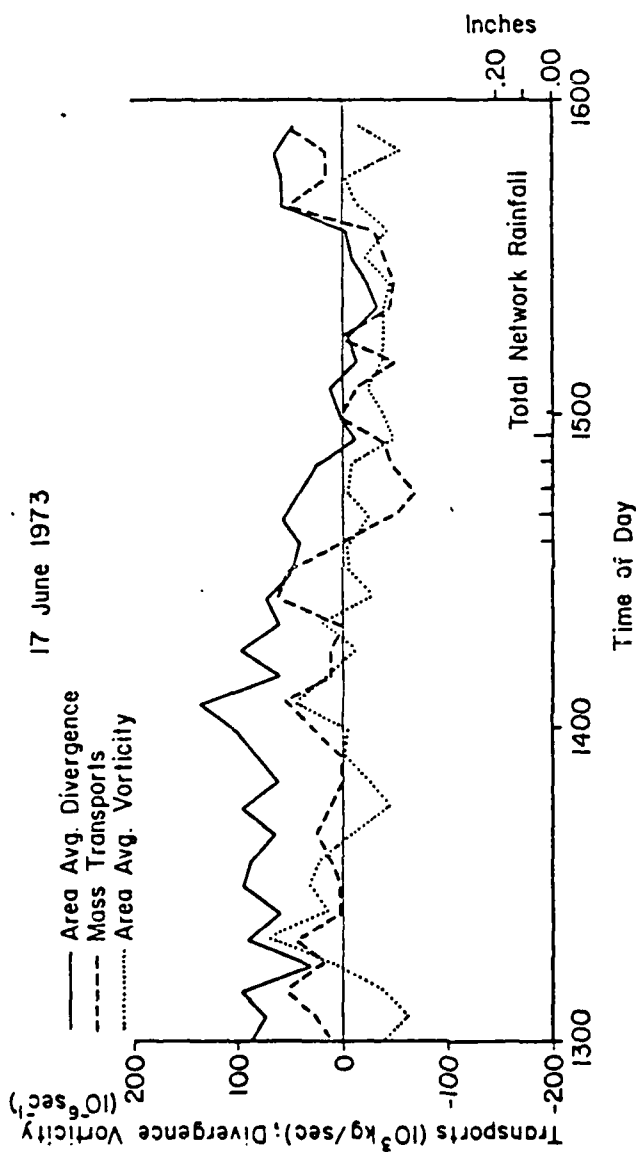
Figure 6c. Profiles in divergence on light or no-rain days.

interior of the network.

To demonstrate the relationship between the type of signal illustrated in Figure 6b and storm intensity, storms from 1973 were classified according to their 5-minute maximum point rainfall intensity, as shown in Table 2. The categories chosen in maximum point rainfall were arbitrarily set at ranges of 0.10 of an inch per five minutes. Of a total of 101 storms in 1973-75, 23% were classified as light, 24% were classified as moderate, and 53% were classified as heavy.

The standard observing values for precipitation intensity are found in the manual of surface observations (WBAN-10), and are as follows:

Light	Trace $\rightarrow$ 0.01 in 6 minutes
Moderate	0.1 $\rightarrow$ 0.03 in 6 minutes
Heavy	0.03 in 6 minutes

These values were considered to be unrealistic for the treatment of intense tropical thunderstorms being measured on a 5-minute basis. The maximum recorded 5-minute rainfall intensity during 1973 was 0.55 inches on 16 June. It was therefore arbitrarily decided to classify the storms relative to this value, as shown in Table 2.

To test the validity of separating the storms in the way described, the total storm rainfall as calculated by EML was used to compare the means of the total rainfall of the three different categories. The total and average rainfall is presented in units of 10^7 kg. Using a t-test, it was found that the difference in the means were significant at the 99.9% level except in the case of Light vs Moderate, which was significant at the 99% level.

Table 2. Total rainfall amounts, 1973 and 1975.

FACE		1973		1975
Intensity	#	x 10^7 kg	#	x 10^7 kg
Light	8	503.16	14	561.55
Average	8	62.90	14	40.11
Moderate	9	3278.68	14	3094.59
Average	9	364.30	14	221.04
Heavy	30	19899.29	24	15437.13
Average	30	663.31	24	643.21

The signal in the area averaged divergence fields was then examined for each day, and classified as being of the S-type (similar to the profile shown in Figure 6b) or as an N-type (noisy, similar to the profile shown in Figure 6c). For each day, the peak area averaged convergence (negative divergence) prior to the maximum point rainfall intensity was noted. The peak area averaged divergence (positive divergence) after the maximum five minute rainfall intensity was also noted. On days of the N-type (noisy) the peak divergences (most positive and most negative for that day) were noted.

The types of signal in the area averaged divergence fields and their associated rainfall intensities are listed in Tables 3-10. The units of the network peak area averaged divergences are 10^{-6} sec^{-1}.

It is found that for the light rain days, 17.4% of the signals were of the S type, while 82.6% of them were N types. For the moderate rain days, 58.4% of the signals were S types and 41.6% were N types. In the heavy rain day cases, 90.7% were S type signals with only 9.3%

Table 3. FACE 1973 5-minute maximum point rainfall (inches).

0 - 0.10		0.11 - 0.20		0.21 - 0.30		0.31 - 0.40		> 0.41	
Day	Amount	Day	Amount	Day	Amount	Day	Amount	Day	Amount
6/17	0.01	6/24	0.19	6/20	0.29	6/14	0.34	6/19	0.42
7/10	0.02	6/25	0.16	6/21	0.21	6/18	0.34	6/26	0.45
7/11	0.02	6/27	0.12	7/08	0.28	6/22	0.40	7/01	0.43
7/18	0.09	7/07	0.20	7/17	0.25	6/23	0.38	7/02	0.43
7/20	0.07	7/09	0.15	7/19	0.25	6/28	0.40	7/10	0.42
7/21	0.09	7/13	0.11	7/29	0.25	6/29	0.34	7/14	0.46
7/24	0.02	7/21	0.14	7/31	0.28	7/06	0.40	6/15	0.55
7/25	0.06	7/26	0.18			7/12	0.31	6/16	0.55
7/30	0.07	7/30	0.14			7/15	0.35		
		8/02	0.19			7/16	0.36		
						7/27	0.32		
						7/28	0.37		
						8/01	0.33		
						8/03	0.35		
						8/04	0.32		

←—LIGHT——— * ———MODERATE——— * ———HEAVY———→

Table 4. 1973 light rain days.

		(x 10^{-6} sec^{-1})	
Date	Type of Signal	Peak Convergence	Peak Divergence
June 17	N	0	+55
July 10	N	-30	+25
July 11	N	-75	+50
July 18	S	-100	+150
July 20	S	-100	+130
July 21	N	0	+125
July 24	N	-45	+75
July 25	S	-160	+125
July 30	N	-10	+40
9 days	3S, 6N	AVG = -57.7	AVG = +86.1
		S_x = -55.01	S_x = 46.49

Table 5. 1973 moderate rain days.

		(x 10^{-6} sec^{-1})	
Date	Type of Signal	Peak Convergence	Peak Divergence
June 24	S	-200	+320
June 25	S	-125	+175
June 27	N	-330	Missing
July 7	S	-160	+230
July 9	S	-235	+150
July 13	S	-75	+175
July 21	N	0	+100
July 26	N	-160	+60
July 30	N	-125	0
August 2	N	-175	0
10 days	5S, 5N	AVG = -158.5	AVG = +134.4
		S_x = -89.20	S_x = 106.05

Table 6. 1973 heavy rain days.

Date	Type of Signal	Peak Convergence	Peak Divergence
		$(\times 10^{-6} \text{ sec}^{-1})$	
June 14	N	-215	+75
June 15	S	-230	+320
June 16	S	-405	+310
June 18	S	-255	Missing
June 19	S	-315	+240
June 20	S	-185	Missing
June 21	N	-40	+125
June 22	S	-125	+270
June 23	S	-115	+310
June 26	S	-250	+320
June 28	S	-80	+95
June 29	S	-190	+110
July 1	S	-180	+190
July 2	S	-225	+410
July 6	S	-50	+535
July 8	N	-50	+130
July 10	S	-140	+390
July 12	S	-130	+500
July 14	S	-140	+250
July 15	S	-225	+240
July 16	S	-210	+285
July 17	S	-275	+325
July 19	S	-110	+175
July 27	S	-185	+170
July 28	S	-190	+400
July 29	S	-85	+330
July 31	S	-220	+160
August 1	S	-190	+210
August 3	S	-320	+160
August 4	S	-180	+375
30 days	27S, 3N	AVG = -184.0	AVG = +265.0
		$S_x = -84.79$	$S_x = 120.12$

Table 7. FACE 1975 5-minute maximum point rainfall (inches).

0 - 0.10		0.11 - 0.20		0.21 - 0.30		0.31 - 0.40		> 0.41	
Day	Amount	Day	Amount	Day	Amount	Day	Amount	Day	Amount
7/05	0.01	7/06	0.13	7/18	0.24	7/04	0.33	7/01	0.42
7/07	0.01	7/10	0.12	7/22	0.23	7/16	0.31	8/20	0.41
7/08	0.01	7/21	0.11	8/06	0.23	7/17	0.31		
7/15	0.06	8/25	0.12	8/08	0.21	8/03	0.31		
8/01	0.01	7/02	0.20	8/14	0.25	8/29	0.31		
8/04	0.01	7/09	0.17	8/16	0.24	7/14	0.35		
8/09	0.03	7/11	0.19	8/21	0.22	7/26	0.36		
8/10	0.00	7/12	0.19	8/30	0.24	8/15	0.38		
8/11	0.04	7/19	0.18	7/03	0.29	8/19	0.38		
8/23	0.05	7/20	0.18	8/07	0.27	7/24	0.36		
8/24	0.00	7/23	0.18	8/18	0.28				
8/22	0.08	8/02	0.20	8/17	0.27				
8/26	0.09	8/13	0.15						
8/27	0.08	8/28	0.14						

←——LIGHT————— * ———MODERATE——— * ————HEAVY————→

(1975: Late storms occurred on 7/13, 7/25, 7/27 and 8/12 after 2000 EDT.)

Table 8. 1975 light rain days.

$(\times 10^{-6} \text{ sec}^{-1})$

Date	Type of Signal	Peak Convergence	Peak Divergence
July 5	N	-100	+130
July 7	S	-110	+90
July 8	N	-100	+40
July 15	N	-40	+110
August 1	N	-100	+70
August 4	N	-160	+40
August 9	N	-20	+90
August 10	N	-60	+80
August 11	N	-140	+30
August 23	N	-240	+10
August 24	N	-190	0
August 22	N	-280	+110
August 26	N	-200	0
August 27	N	-240	0
14 days	1S, 13N	AVG = -143.5	AVG = +55.0
		$S_x = -79.70$	$S_x = 45.65$

Table 9. 1975 moderate rain days.

$(\times 10^{-6} \text{ sec}^{-1})$

Date	Type of Signal	Peak Convergence	Peak Divergence
July 2	S	-390	+190
July 6	S	-220	+200
July 9	S	-300	+280
July 10	N	-200	+50
July 11	N	-188	+100
July 12	S	-130	+170
July 19	N	-230	+150
July 20	S	-190	+380
July 21	S	-260	+180
July 23	N	-210	0
August 2	S	-140	+210
August 13	S	-170	+150
August 25	N	-250	0
August 28	S	-200	+80
14 days	9S, 5N	AVG = -219.8	AVG = +152.8
		$S_x = -66.64$	$S_x = 104.18$

Table 10. 1975 heavy rain days.

$(\times 10^{-6} \text{ sec}^{-1})$

Date	Type of Signal	Peak Convergence	Peak Divergence
July 1	S	-230	+230
July 3	S	-150	+190
July 4	S	-210	+180
July 14	S	-200	+290
July 16	N	-240	+50
July 17	S	-180	+220
July 18	S	-220	+100
July 22	S	-230	+250
July 24	S	-170	+400
July 26	S	-200	+300
August 3	S	-300	+380
August 6	S	-300	+140
August 7	S	-240	+370
August 8	S	-130	+380
August 14	S	-220	+370
August 15	S	-330	+260
August 16	S	-140	+280
August 17	S	-170	+180
August 18	S	-200	+180
August 19	S	-400	+330
August 20	S	-260	+380
August 21	N	-280	+50
August 29	S	-180	+170
August 30	S	-220	+130
24 days	22S, 2N	AVG = -225.0	AVG = +242.1
		$S_x = -63.18$	$S_x = 107.74$

Note: 7/13, 7/25, 7/27 and 8/12 had storms ending after 2000 EDT, and were omitted.

showing noisy area-averaged divergence profiles. Of 101 storms studied in 1973 and 1975, 67 showed a convergence-divergence sequence similar to that in Figure 6b while 34 did not show such behavior. As noted above, almost all of the heavy showers displayed the S type of signal, and the storms classified as heavy made up 53.5% of all the storms studied. The results are summarized in Table 11.

Table 11. Profiles of area-averaged divergence.

Total Number of Storms	Number of S Type	Number of N Type	Intensity
1973 9	3	6	Light
1975 14	1	13	
23 (22.8% of storms)	4	19 (2.5% of total rain)	
1973 10	5	5	Moderate
1975 14	9	5	
24 (23.8% of storms)	14	10 (14.9% of total rain)	
1973 30	27	3	Heavy
1975 24	22	2	
54 (53.5% of storms)	49	5 (82.6% of total rain)	
TOTALS 101	67	34	

Tables 3-10 illustrate the possibilities and difficulties of using the area-averaged divergence of velocity over an area in short-term forecasting. While, on the average, there is consistency in the strength of the maximum area-averaged convergence and the intensity of following rainfall, the variation is great.

The frequency distributions of area-averaged convergence peaks and area-averaged divergence peaks are illustrated in Figures 7a and 7b. Figure 7a suggests that if we wish to distinguish between storms in the light and moderate-heavy categories, we adopt as an empirical criterion

a threshold area-averaged convergence of $\sim$ -150 x 10^{-6} sec^{-1}.

Referring to Tables 3-10, we find that with this criterion, 7 moderate to heavy storms are selected when light showers occurred, and no moderate to heavy showers would have been selected in the other 16 light rain day cases. Of the moderate to heavy showers, 19 of a total of 78 are not distinguishable as being so, and would have been classified as light. This empirical criterion distinguishes between light and moderate-heavy showers in 74% of the total cases in the 1973-75 data set, being correct on 69% of the light shower days, 75% of the moderate shower days and 74% of the heavy shower days.

The relationship between peak area-averaged divergence and intensity of storms is illustrated in Figure 7b, and shows the clear connection between peak network divergence and intensity of rain. Comparison of the frequency distribution of peak area-averaged divergence on light shower days with that on heavy shower days show them to be almost "mirror images" of one another, with a mode of peak area-averaged divergence on light shower days of $\leq$ +50 x 10^{-6} sec^{-1}, while the mode on heavy shower days is > +300 x 10^{-6} sec^{-1}. The moderate shower days frequency distribution lies between the two extremes in form. The t-test significances are noted in each figure.

To use this information in application to short-term forecasting and to improve on that application we need a better understanding of the nature of the causes of the sinusoidal divergence patterns in the surface wind fields. This is investigated in the following manner.

We have seen that on days when heavy showers occurred over the network, the surface area-averaged divergence goes through a sequence of convergence followed by divergence. The moderate and heavy showers
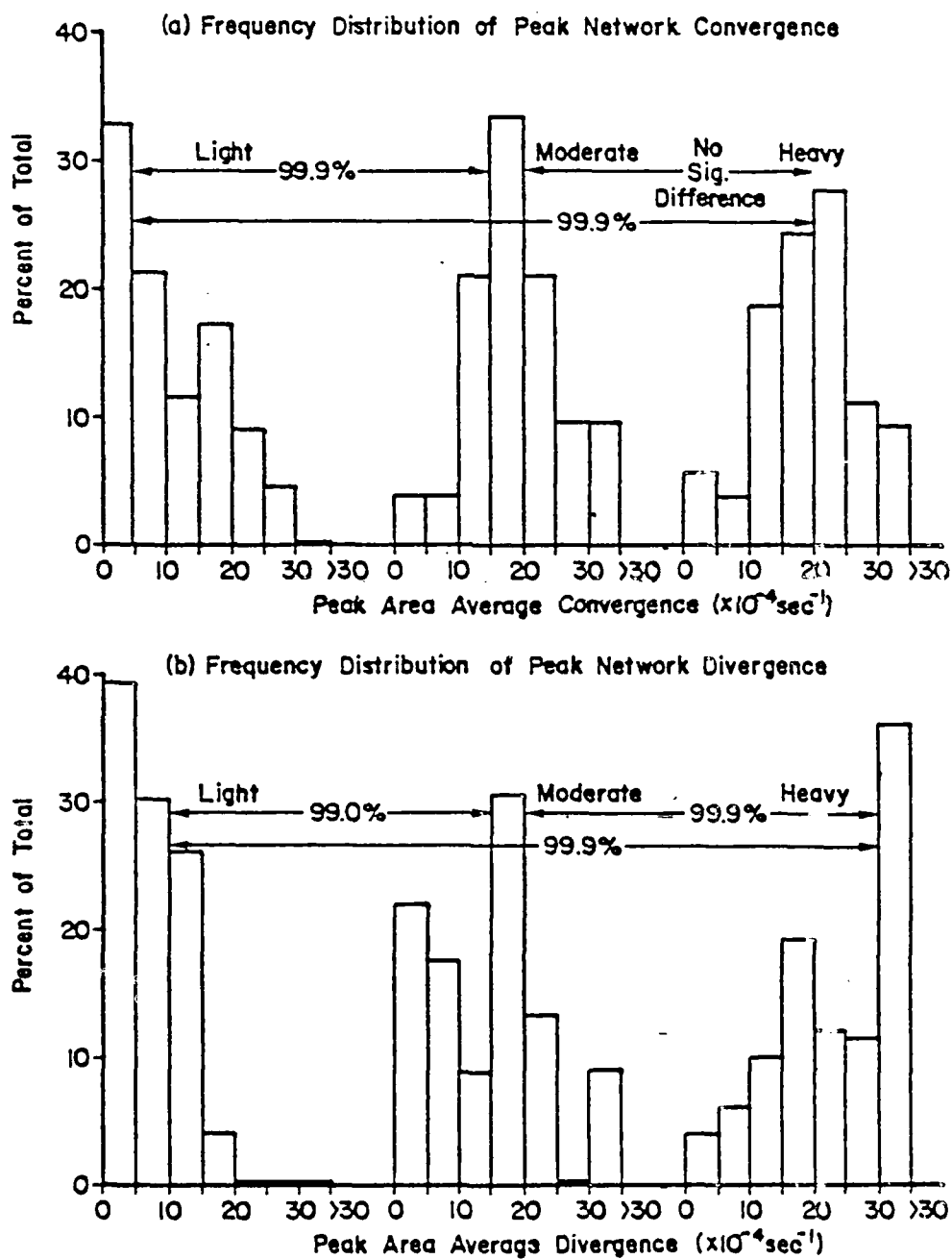
Figure 7a. Frequency distribution of peak network convergence.
Figure 7b. Frequency distribution of peak network divergence.

associated with this type of signal make up 77.2% of all the storms
which occurred, and account for 98% of the total recorded rainfall
which fell during the two experiments.

Using data from all days in 1973 when these sinusoidal signals
were present, a radar echo composite was constructed using data from
the Miami WSR-57 10 cm radar.

The positions and intensities of centers of highest reflectivity
of radar echoes within a radius of 50 n mi ($\approx$ 85 km) of the geometric
center of the wind network were plotted. Five composite maps were
generated, each corresponding in time to one of the five points
indicated on the graph of area-averaged divergence plotted in Figure
94b; that is, at the time of the beginning of persistent area-averaged
convergence over the network, at the time of peak area-averaged conver-
gence (negative divergence), at the inflection point, at the time of
peak area-averaged divergence (positive divergence), and at the time
of cessation of persistent area-averaged divergence. The value of such
plots is that the interaction between the divergence in the network
and storms outside the interpolation grid, but close enough to affect
the anemometers, can be shown. Figures 8 through 13 show the relation-
ship between these fields and surrounding radar echoes for 35 days in
1973. These composites are made as described above, and as such, are
representative of different times of day, and different regimes in the
low-level flow. The effect of the composites is to provide a time
series of the echo coverage throughout the storm cycle. The figures
should be viewed sequentially. The solid dots are echoes representing
rain rates of less than 0.5 inches per hour, while the open circles
represent rain rates $\geq$ 0.5 inches per hour. The range circles are

Cell Positions 1973 (Beginning)

50 n.mi.
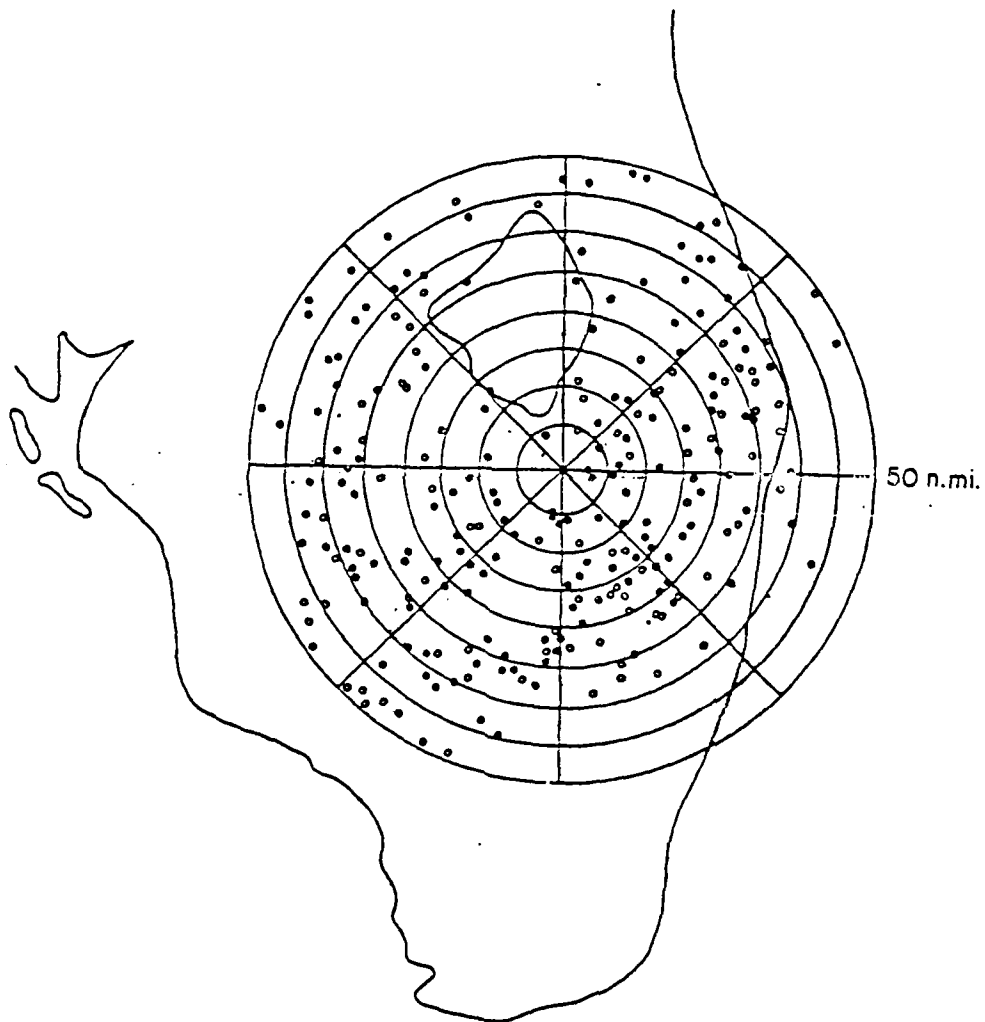
Figure 8. Radar echo composite 1973; beginning of storm cycle.

Cell Positions 1973 (Peak Convergence)

50 n.mi.
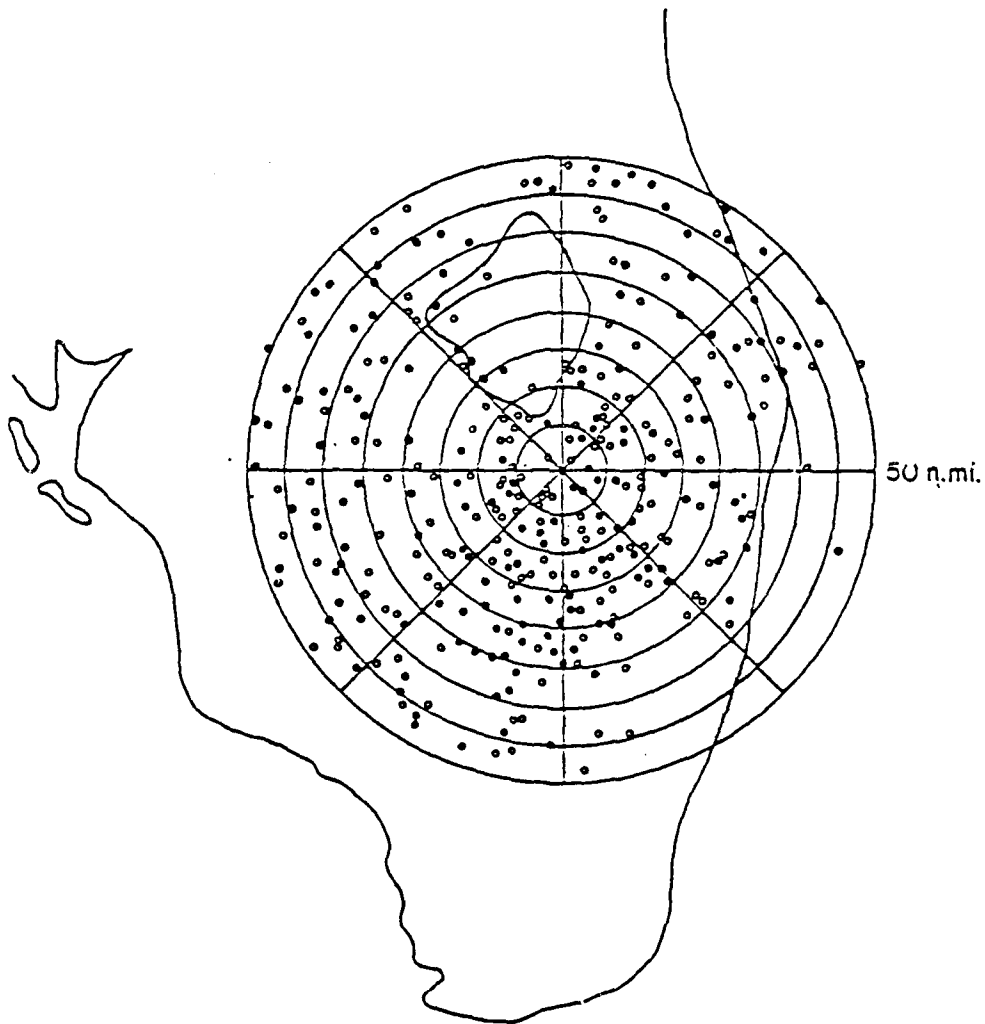
Figure 9. Radar echo composite 1973; peak convergence.

Cell Positions 1973 (Inflection Point)
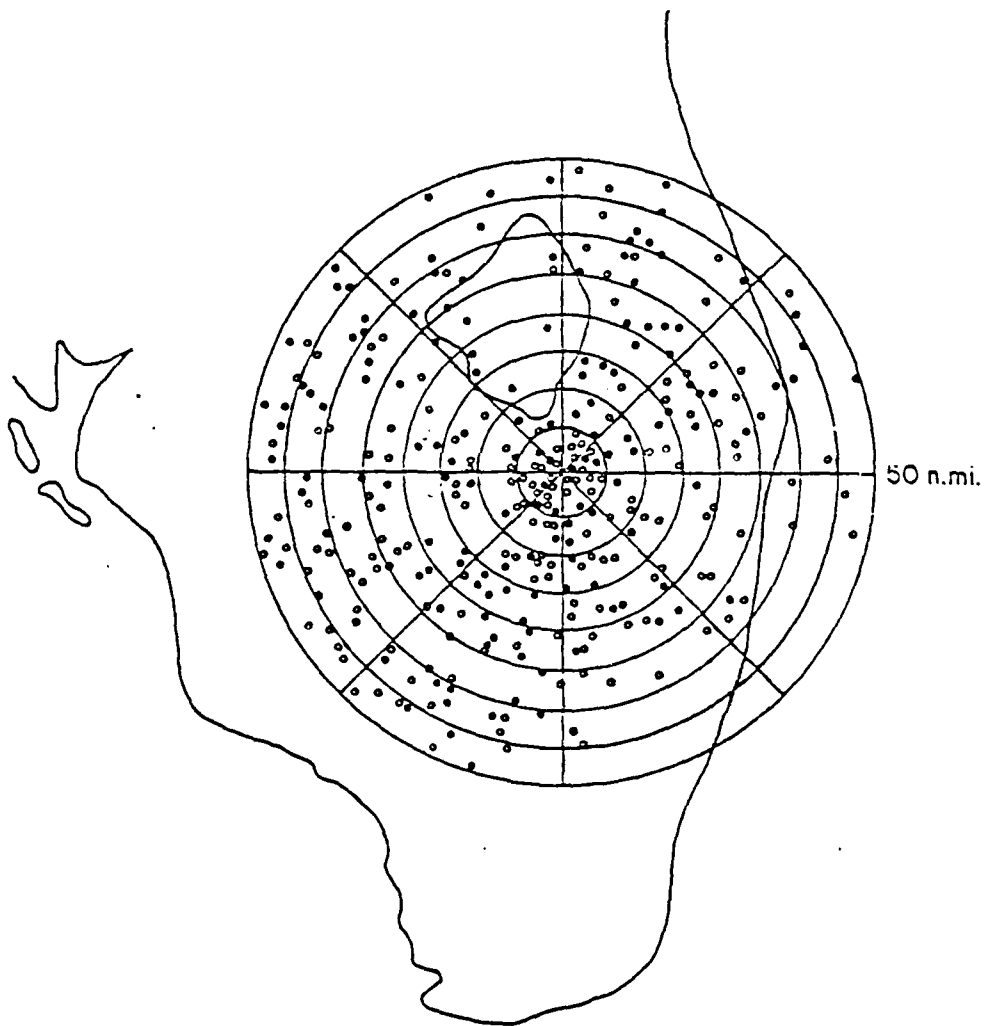
Figure 10. Radar echo composite 1973; inflection point.

Cell Positions 1973 (Peak Divergence)
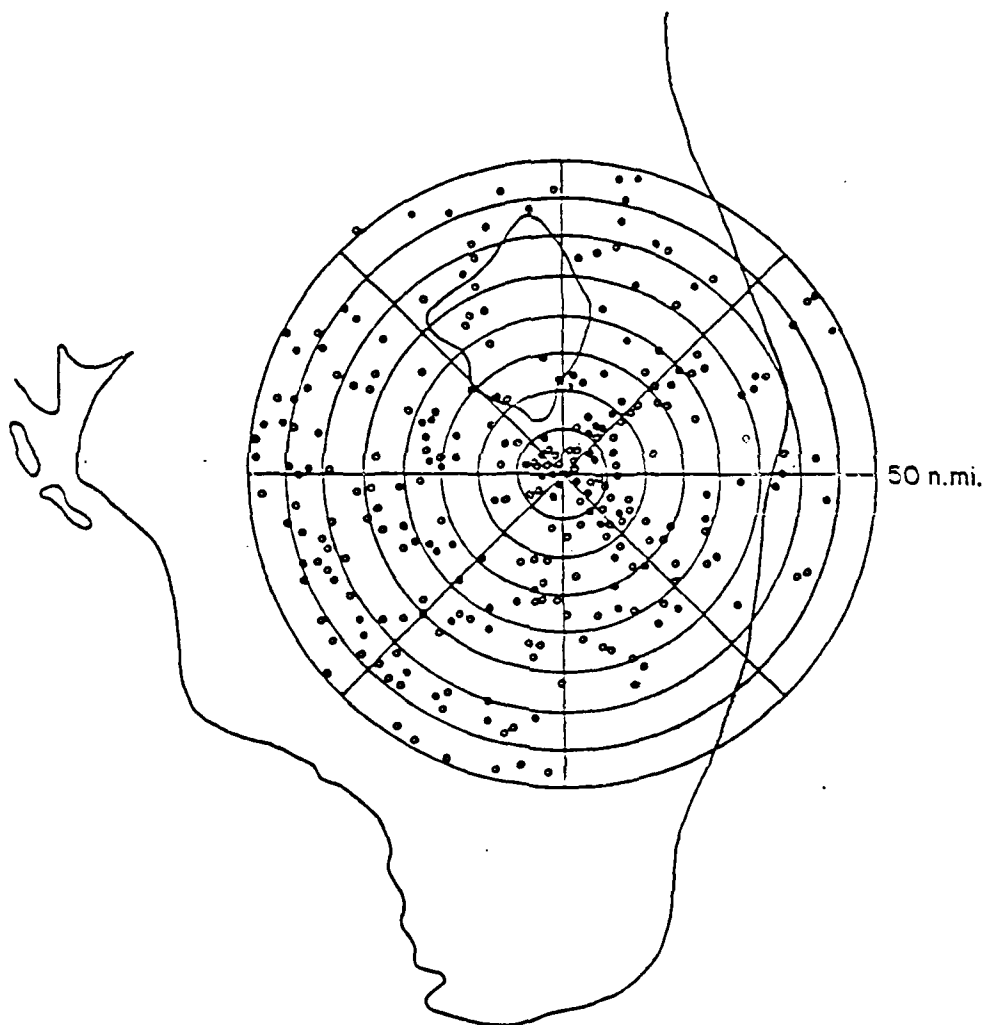
Figure 11. Radar echo composite 1973; peak divergence.

Cell Positions 1973 (End)
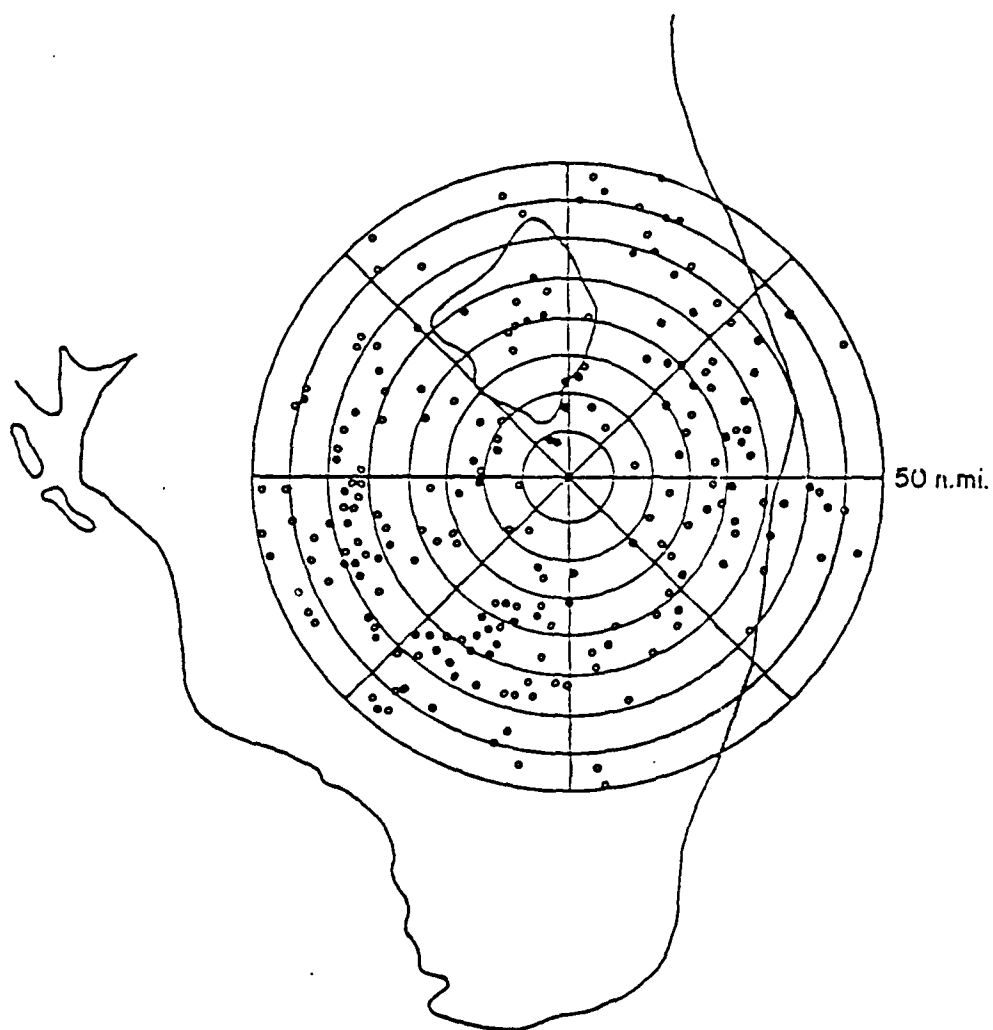
Figure 12. Radar echo composite 1973; end of storm cycle.

centered on the 1973 FACE anemometer network, and are spaced 6.25 n mi
($\sim$ 10.5 km) apart. The shaded area in the region SE-S of the network
center represents the region most affected by ground clutter. The inner
circle of 6.25 n mi covers approximately 70% of the interpolation grid,
and the second circle (12.5 n mi, $\sim$ 22 km) contains a region greater than
the area of the interpolation grid. In considering Figures 8-13, the
center circle may be considered as being the interpolation grid, while
the region enclosed by the 6.25 n mi and 12.50 n mi range markers may
be considered to be a band immediately outside the grid. The coastline
of southern Florida and that of Lake Okeechobee, just north of the net-
work, are outlined.

The area enclosed by a radius of 6.25 n mi around the center of
the network will be referred to as region 1, the area enclosed between
the first range marker at 6.25 n mi and the next will be called range 2,
and so on, out to region 8 at the 50 n mi marker.

Figure 8 shows the distribution of surrounding echoes at the
beginning of persistent area average convergence in the network. There
are 4 weak and 1 strong echoes over the network, but most of the intense
echoes lie northeast and south of the center of the anemometer array, in
regions 2 and 3.

At the time of peak network convergence (Figure 9), region 2 con-
tains a larger percentage of echoes than it did before, many of higher
reflectivity, while fewer echoes than are in region 2 are over the net-
work, and on its edges. Figure 10 shows the shower activity at the point
of inflection in the surface area averaged divergence profiles, and shows
the largest number of echoes over the network thus far, (32 total; 9
weak and 21 strong).

The radar fields during the time of peak divergence are depicted in Figure 11. Again, echoes crowd over the network, although by now the number has diminished slightly there (total of 27; 11 weak and 16 strong). Finally, at the end of the convergence-divergence cycle, as seen in Figure 12, there are no intense echoes over the network, and few in the immediate vicinity of the network.

These composites help to explain, in aggregate, what the sinusoidal signals in the surface area-averaged divergence fields mean.

These figures present evidence that the intense convergence peak which generally precedes the peak rainfall is convergence which is forced by outflow from the downdraft of a storm which is on the edge of the network, or some distance from it. As the storm either moves (or propagates) into the network, an equilibrium point in the area-averaged divergence fields is reached, generally when the storm's downdraft is over the network, the outflow from that downdraft causing enough convergence in the network to balance the divergence due to the downdraft, with the result that the area-averaged divergence over the entire network goes to zero.

As the storm moves out of the net, the rain-forced downdraft dominates the network, and the peak area-averaged divergence is reached; if the storm dissipates over the network, the same effect is observed. After the peak divergence, the sequence of convergence, rain, divergence is concluded. This view is supported by inspection of individual cases, some of which will be presented in the next section as case study examples.

Figures 13-15 show various frequency distributions of intense radar echoes taken from Figures 8-12. The intense echoes were used

Raw No. of Cells 1973
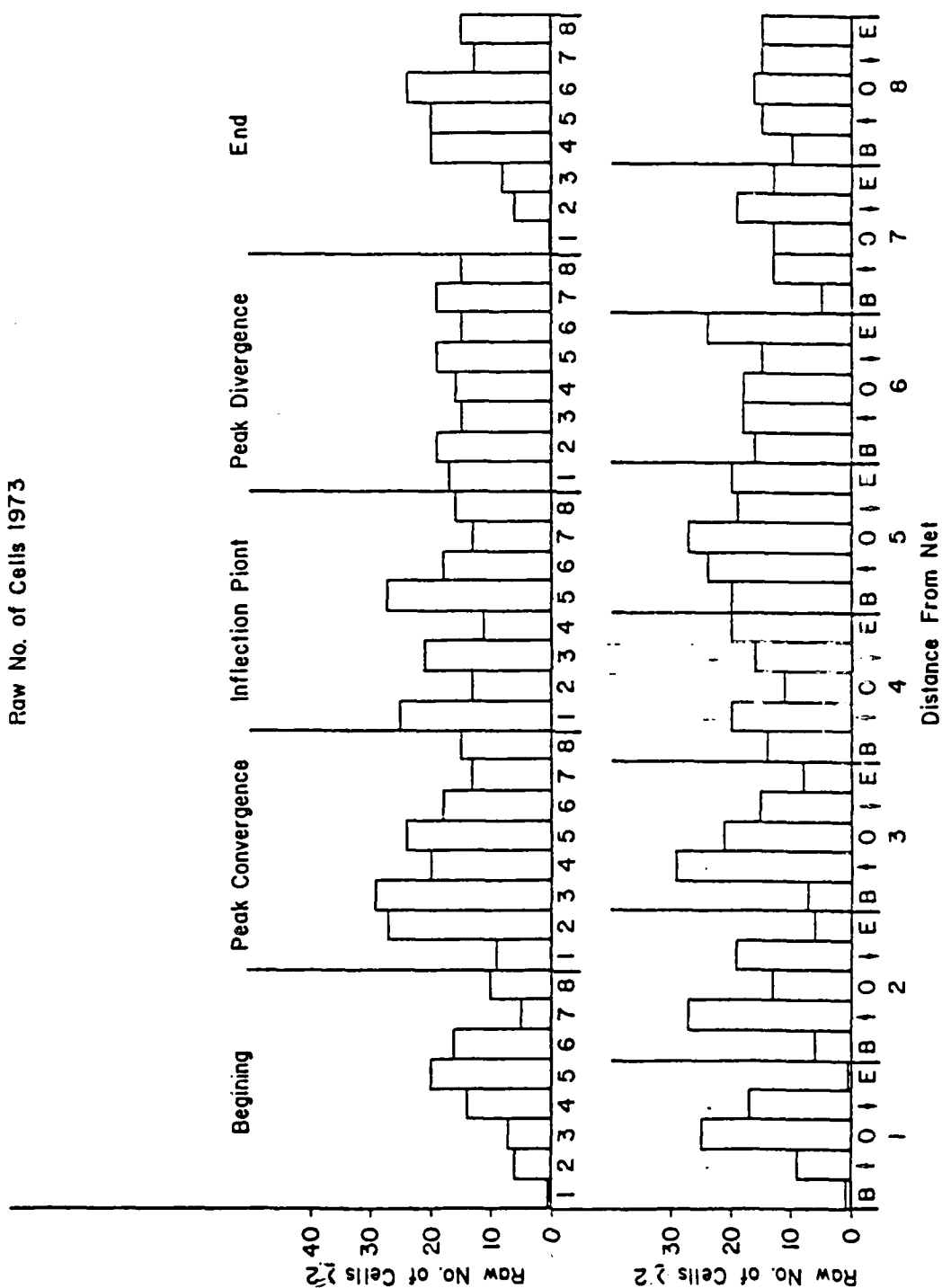
Figure 15a. Radar echoes in network region classified by storm stage.
Figure 15b. Radar echoes in network region classified by distance from net.
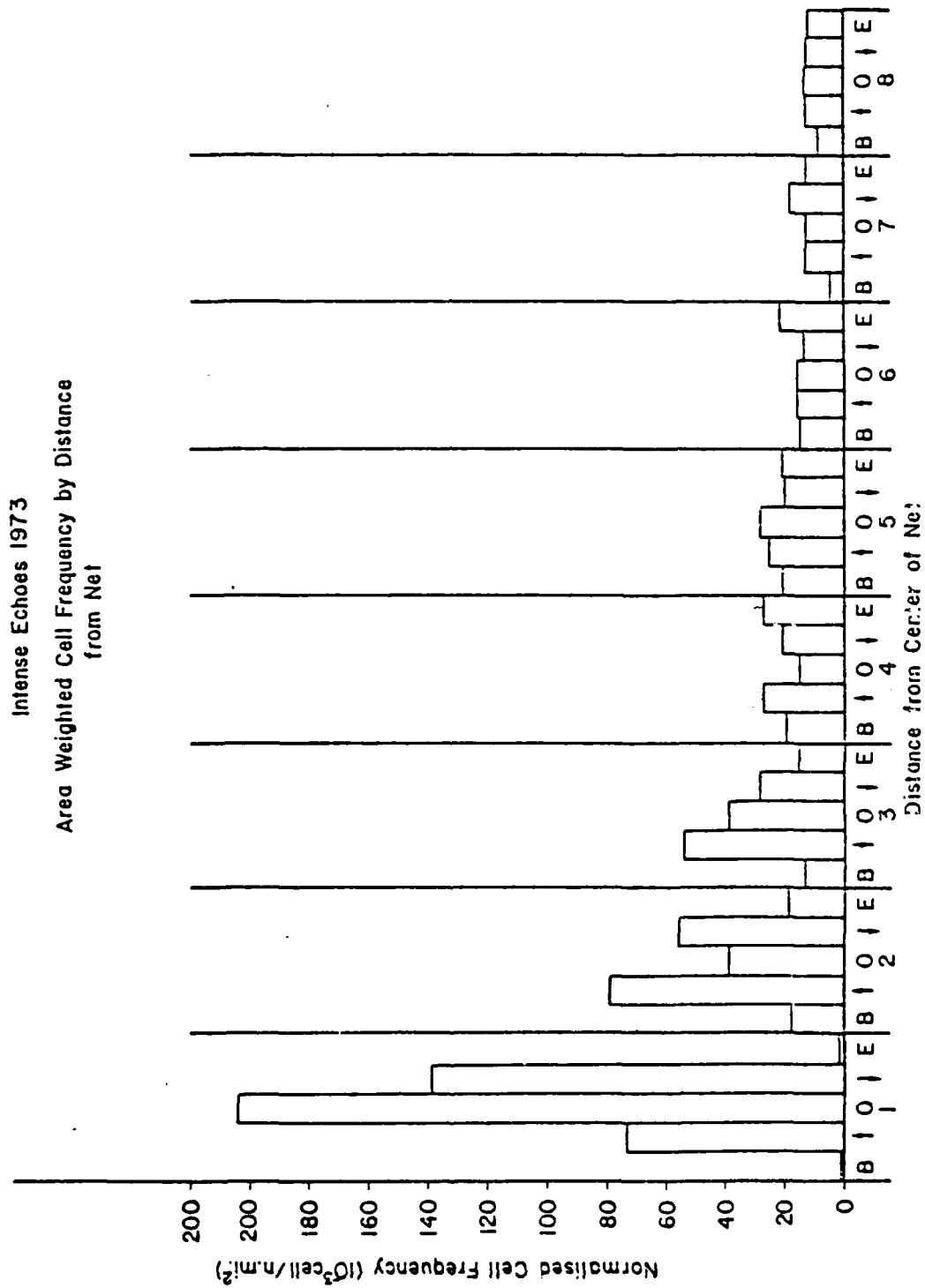
Figure 14. Same as Figure 13b, except echoes are area-weighted.
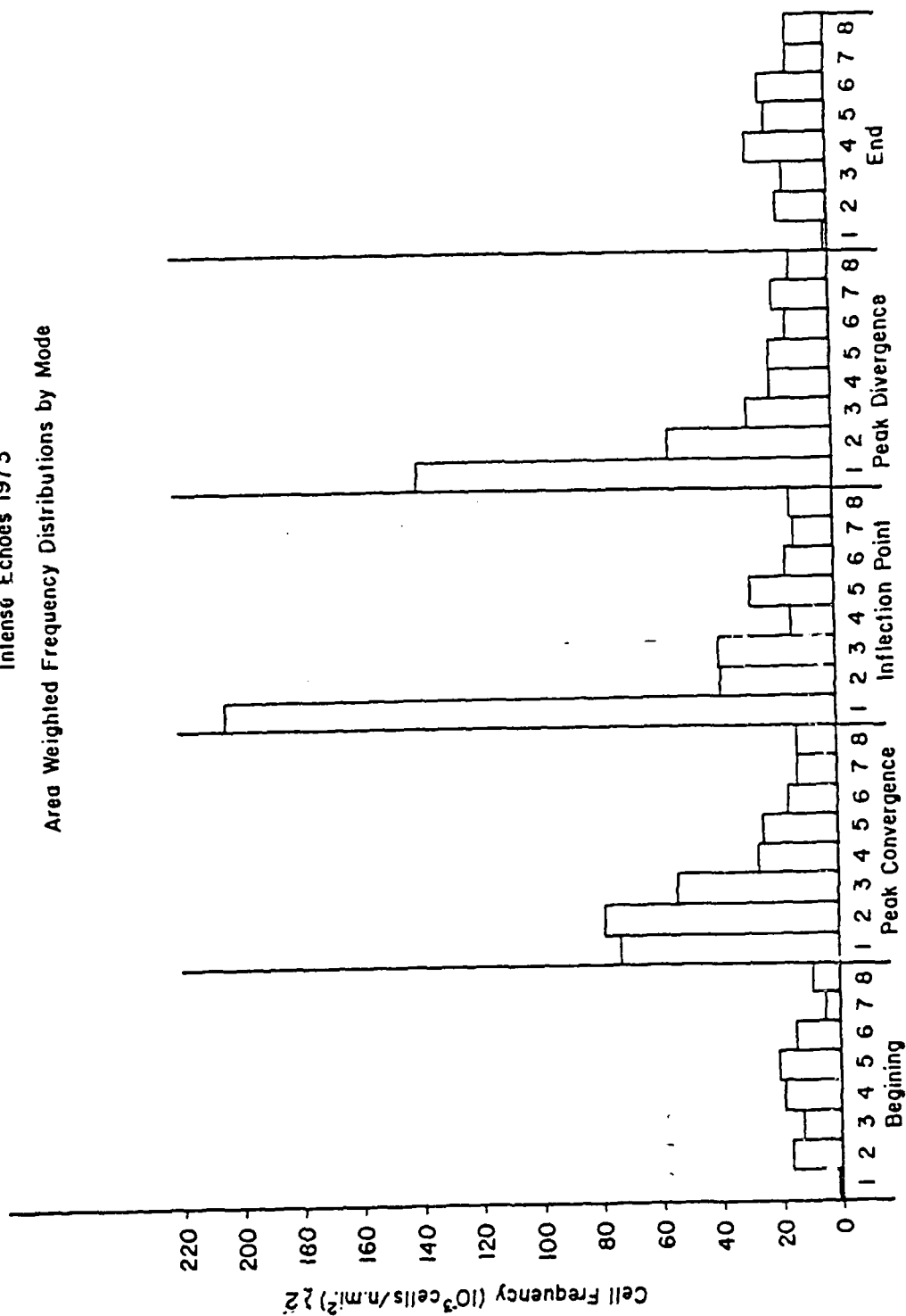
Figure 15. Same as Figure 13a, except echoes are area-weighted.

because their locality can be pinpointed with more confidence than that of the less intense echoes.

Figure 13a shows, in terms of raw numbers, the concentrations of cells in regions 1, 2, 3, 4, 5, 6, 7 and 8 going out from the center of the network to 50 n mi, each region being 6.25 n mi in width, as in Figures 8-12. The distribution of the number of cells in each region is plotted for each stage of the area-averaged divergence field cycle of beginning, peak convergence, inflection point, peak divergence, and end. We see that the mode in the number of echoes in each region varies with the stage in the convergence-divergence cycle of the network. In the beginning stage, the mode in raw number of echoes is in the regions 4, 5 and 6. By the time of peak convergence, the mode has shifted towards the network to regions 2 and 3. At the inflection point, the distribution is tri-modal, with peaks in number of echoes in regions 1 (over the net), 3 and 5. During the peak divergence period, the raw number of echoes differs little with distance from the network, but by the end of the peak divergence stage, the mode of raw number of echoes has moved back out again to region 6, and shows a distribution close to the net similar to that of the undisturbed period at the beginning of the cycle.

Figure 13b shows the same "number of cells" distribution of intense echoes, but in this case, the distribution is organized by the stage of the convergence cycle that the network area-averaged divergence field is going through. The symbols at the bottom of the page refer to those stages. B means the beginning of persistent convergence in the area-averaged divergence in the net, an arrow pointing upwards means the peak convergence stage in the net, a zero signifies the inflection point

in the area-averaged divergence in the net, an arrow pointing downwards
symbolizes the peak divergence mode of the area-averaged divergence
fields in the net and the letter E indicates the end of the cycle. The
numbers beneath these symbols refer to the bands surrounding the net
and start with region 1 (over the network) and end with region 8 (50 n
mi from the center of the network).

Notice that the mode of raw numbers of echoes for the region over
the network (region 1) occurs during the inflection point on the area-
averaged divergence curves, while the regions 2, 3 and 4 (from 6.25 -
25.0 n mi from the center of the network) have modes during the period
of peak convergence over the network. Region 2 also has a mode in raw
numbers of echoes during the divergence mode over the network.

Figures 14 and 15 are the same as Figures 13a and 13b, except
that the echoes are normalized by area. Since region 8, for example,
covers an area some three and a half times the area of region 1 at the
center of the network, this must be done to display the relative behavior
of the various regions during the cycles in the divergence fields in the
network.

Figures 14 and 15, the area weighted cell frequency diagrams,
dramatically display the behavior of regions around the network during
the convergence cycles. The symbols at the bottom of Figure 14 are the
same as those in Figure 13b. Figure 14 shows more clearly the process
described previously than the raw number frequency diagrams of Figures
13a and 13b. There is a prominent mode in the area weighted echo fre-
quency distribution over the network (region 1) during the inflection
stage in the area-averaged fields. More prominent now, there is the
bimodal frequency distribution in the area weighted echo frequencies in

the region just outside the network (region 2), during the peak convergence mode and during the peak divergence mode in the network. Region 3 shows a mode in area weighted frequency during the peak convergence mode over the network. Beyond region 3 (i.e., greater than about 15 n mi, which is $\sim$ 25 km) the area weighted frequency of echoes shows no discernible pattern. This fact is emphasized in Figure 15, which is similar to Figure 13a, except that the variables are the area weighted echo frequencies. This suggests a "range of effect" of cumulonimbus downdrafts in Florida of about 20-25 km, which agrees well with Riehl's (1979) observation that the scale size of convective activity is on the order of 20 km, and with the observations of Goff (1976) as well as those of Fankhauser and Mohr (1979). Figures 8-15 suggest strongly that during the peak convergence stage of the area-averaged divergence field cycle, echoes outside the network produce the peak convergences observed inside the network. As the storms dissipate in or move out of region 1, a second mode in echo frequency appears in region 2, due to convergence caused by outflows from the network, or by storms moving into that region. They also suggest that storms can either initiate new convection in their immediate proximity, or can initiate, through surface convergence formed by outflows from parent storms, new convection at considerable distances (as much as 20 km) from the parent storm. These views are arrived at from individual inspection of 49 different days in 1973, of which the statistical representations of Figures 31-38 are a summation, and support observations by Houze (1977), Leary (1979), Brandli and Orndorff (1976), Purdom (1979), Black (1979), Fankhauser and Mohr (1979) as well as Byers and Braham (1949).

The problem of short term forecasting of heavy showers using the area-averaged fields is therefore a sampling problem, and the foregoing discussion explains why, on few occasions we see weak convergence in the area-averaged divergence fields prior to heavy rainfall. The reasons for such anomalous behavior is that the area-averaged divergence profile is a function of the strength of the storm as it approaches the network, the stage of maturity the storm is in when it first begins to affect the network, the angle at which the outflow from the storms crosses the network, and the portion of the network affected by the outflow. In the case of 8 July 1973, for example, the storm passed over the northwestern corner of the network depositing large amounts of rain there, but affecting only a small region of the anemometer network, so that the area-averaged divergence fields did not show the usual cycle in the area-averaged divergence fields which are associated with severe storms.

In the cases when heavy storms pass right over the network, the peak convergence in the cycle of area-averaged divergence generally occurs on the order of 30-40 minutes before the peak network rainfall.

There is ample evidence that a clear signal in the surface divergence fields precedes heavy showers (by an average of about 30-40 minutes). This signal is distorted when the field sampled is limited.

In the following chapter, the behavior of the surface divergence fields interior to the network (i.e., convective cell scale) will be examined, and specific case studies will be presented.

CHAPTER 4

EXAMPLES OF THE DIVERGENCE FIELDS INTERIOR
TO THE NETWORK

A. THE RELATIONSHIP BETWEEN THE NETWORK AREA-AVERAGED DIVERGENCE AND
MASS TRANSPORTS

The mass transports through 8 meters are calculated by taking

the density of air, ρ, to be 1 kg/m^3, and averaging the divergence for

a given interpolation grid square to 8 meters in the z-plane. The

vertical mass transport through 8 meters for a given square, i, is then

given by M_i, where

$$M_i = -\rho \int_0^8 \vec{\nabla}_H \cdot \vec{v} \; dz \approx \frac{-\rho}{2} (\vec{\nabla} \cdot \vec{v}) \times 8 \text{ m} \quad .$$

Here $(\vec{\nabla} \cdot \vec{v})_i$ is the divergence over grid i. Then the upward mass trans-

ports for a given 5-minute period are defined as

$$M_\uparrow = - \left\{ \sum_{i=1} \frac{[\rho \; \nabla_H \cdot \vec{v})_i \times 8 \text{ m}]}{2} \right\} \Delta x \Delta y$$

where Δx, Δy are the areal dimensions of the interpolation grid squares,

and N is the number of grid squares which have values of convergence

less than -400 x 10^{-6} sec^{-1}.

The downward mass transports are calculated similarly, using grid

squares with divergences greater than +400 x 10^{-6} sec^{-1}. The net trans-

port is the sum of the upward and downward transports. An example of

such a calculation is contained in Figure 16. This figure shows the

various types of calculations made. The area-averaged divergence is

calculated by simply adding up the divergence (both positive and nega-

tive) over every grid square in the interpolation grid, and dividing
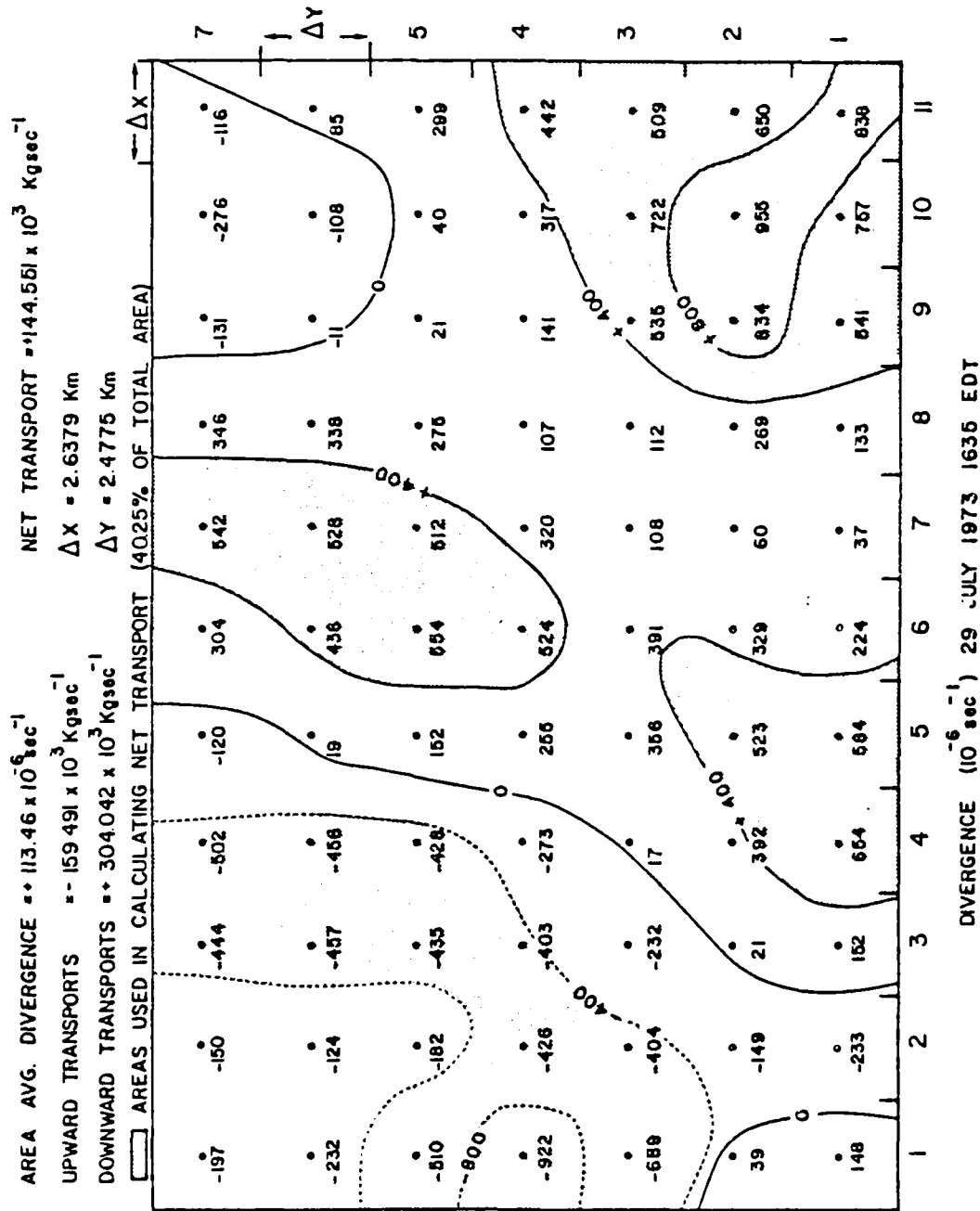
Figure 16. Calculation of mass transports, and area-averaged divergence.

by the total number of grid squares (77). As shown in Figure 6a, there is excellent agreement between the area-averaged divergence and the "inflow" calculations, as discussed in Chapter 3.

The upward transports in the example of Figure 16 are -159.491 x 10^3 kg sec^{-1}, and cover 12 grid squares or $\sim$ 15.58% of the area of the entire interpolation grid. The downward transports in the same figure cover 19 grid squares or $\sim$ 24.67% of the entire interpolation grid, and have the value +304.042 x 10^3 kg sec^{-1}. Thus the net transport for this day and time is +144.551 x 10^3 kg sec^{-1} downward, into the surface layer.

The transports due to convergence $\leq$ -400 x 10^{-6} sec^{-1} and divergence > +400 x 10^{-6} sec^{-1} are also called "convective" transports since values of divergence and convergence of this magnitude and greater are normally associated with the presence, over the network, of deep convection. In the case in Figure 16, the convective transports (up and down) cover a total of 40.25% of the area of the entire interpolation grid.

The convective transports were calculated for every day for which data were available in 1973 and 1975. It was found that if the net convective transport was calculated for every 5-minute period, the profile of the net convective transports, when plotted against time, had the same shape as the profile of the area-averaged divergence. An example of this can be seen in Figure 6b. This was true on all of 49 days during 1973 for which the comparison was made.

Figures 17a and b show a composite of the areas covered by the convective mass transports (as defined) prior to the onset of rain. (The example given in Figure 16 is from a period when rain was falling
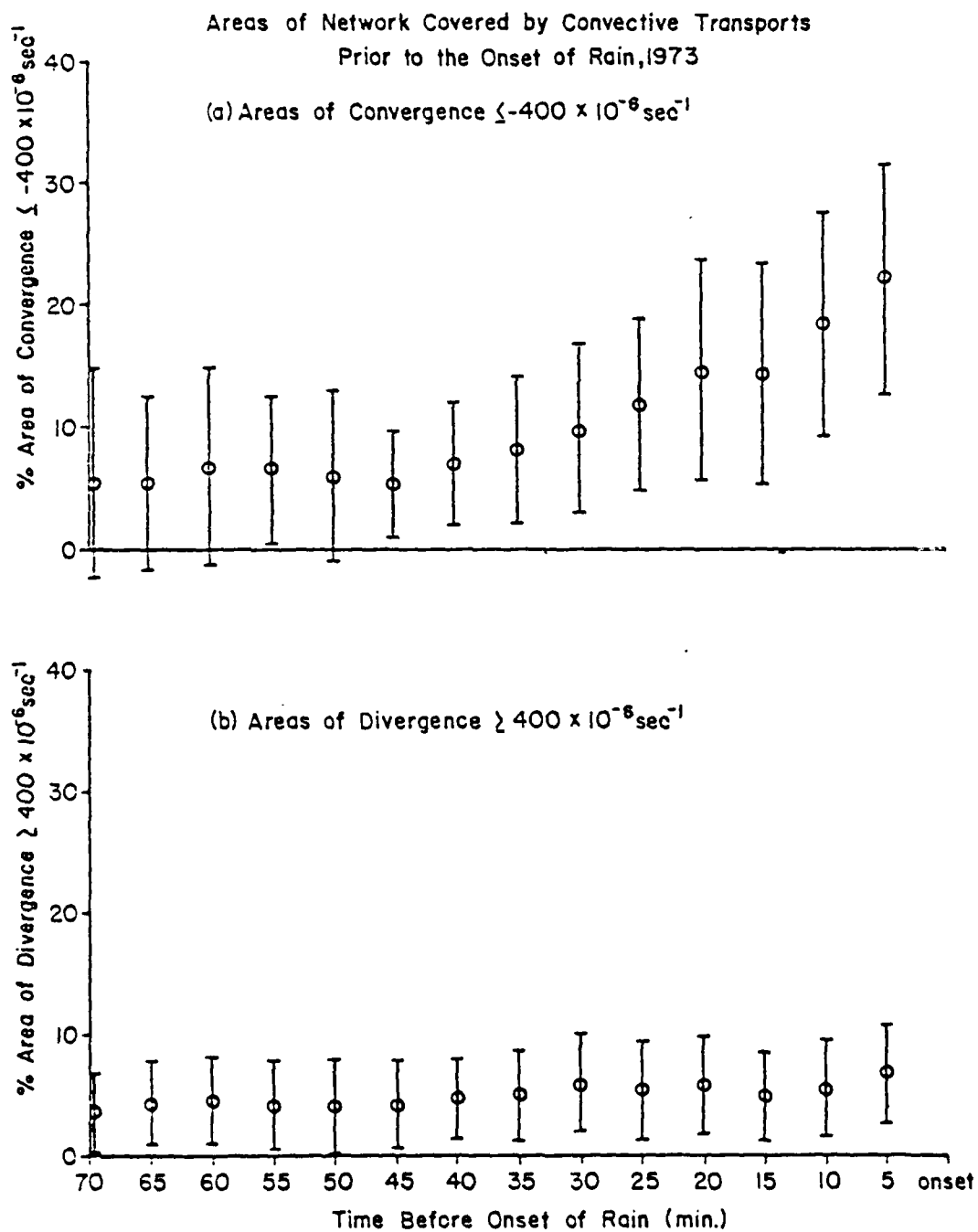
Figure 17a. Area of network covered by upward transports prior to the onset of rain, 1973.
Figure 17b. Areas of network covered by downward transports prior to onset of rain, 1973.

into the net). Figure 17a shows the composite area covered by convergence $\leq$ -400 x 10^{-6} sec^{-1} (upward convective transports), while Figure 17b shows the composited areas covered by divergence $\geq$ +400 x 10^{-6} sec^{-1} (downward convective transports).

There are four main points to be made from this graph:

1) In the mean, there is an increase in the percent of the area of the interpolation grid which is covered by the upward convective transports as the time of onset of rain is approached. This implies that, in the mean, there is an increase in upward convective transports, as defined, through 8 m during this period of time. This increase in upward transports starts around 35-40 minutes before onset.

2) The standard deviation about each of the points on the graph is very large, demonstrating the difficulty in selecting a critical value of mass transport for the onset of rain on a real-time basis.

3) The areas covered by divergences > +400 x 10^{-6} sec^{-1} (down convective transports) show little change prior to the onset of rain, suggesting that the down convective transports may become large only in the presence of downdrafts associated with rainfall, and reflect the presence of non-precipitating cumulus aloft.

4) Convergent regions cover only a small proportion of the total area of the interpolation grid, ranging from 5% of that area (25.6 km^2) 70 minutes before onset of rain, to 22% of the total area (112.7 km^2) at 5 minutes prior to onset of rainfall. The areas covered by regions associated with downward convective transports remain around 4-5% of the interpolation grid throughout the entire period of time. The regions of convective transports are thus clearly identifiable.

The areas of the network covered by divergence $\geq$ |+400| x 10^{-6} sec^{-1} is, generally, less than 50% of the total area of the interpolation grid. Only when storms are situated over the network in a mature or dissipating stage, do these areas cover greater than 50% of the total interpolation grid. This can be seen in the specific examples which follows.

B. CASE STUDIES

The case studies which follow were chosen from data available from days during FACE 75 on which digitized radar plots from the Miami WSR-57 10 cm radar were available. There are three case studies in all, which serve as specific demonstrations of the ideas discussed in Chapter 3.

We have seen in Chapter 3, that the strong, sinusoidal signal in the area-averaged divergence fields is associated with heavy rainfall over the network. Also, the statistical approach of Chapter 3 demonstrated that the signal in the area-averaged fields was often a precursor to the propagation of a storm into the network, or the initiation of new growth there due to outflow from a storm just outside the network.

Simpson et al. (1980a) have shown that the amount of rainfall over the Florida peninsula is related to radar echo merging, the storms associated with merged echoes producing much more rain than those associated with unmerged echoes. Simpson (1980b) postulates that one of the mechanisms by which echo merging occurs is through the initiation of, or aid given to, new growth by convergence regions forced at the surface by outflows from other storms.

Holle et al. (1977) using radar and surface data from the FACE 1975 data set, showed the process of merging in some detail, linking visual observations to radar echoes and convergence within the network, in a detailed case study of August 19, 1975.

The four case studies presented here support these findings, and, when coupled with the observations analyzed in Chapter 3, leave little doubt as to the importance of an outflow-convergence feedback mechanism in the continued production and prolongation of deep convection over the

south Florida peninsula.

These case studies illustrate the interaction between storm out-
flows and show in detail the makeup of the characteristic signals of
heavy showers in the area-averaged divergence fields discussed in Chap-
ter 3. The importance of the effects of strong downdrafts in the
initiation and continuation of convective activity is displayed, and the
importance of strong regions of convergence caused by outflow from
mature and decaying storms in propagation, radar echo merging and pro-
longation of the lifetime of storm systems is shown.

Each case study is illustrated with a number of diagrams. In
each case, the first diagram consists of a time series plot of the area-
averaged divergence taken over the entire interpolation grid, and the
15-minute total network recorded rainfall. The two other curves on the
first diagram in each case study are plots of the upward convective
transports and the downward convective transports.

Subsequent diagrams will include, for each case study, sketches
of concurrent radar echoes, 15-minute total rainfall and the interior
divergence fields. In making up these diagrams, no attempt was made
to adjust the three types of fields (radar, rain, divergence) relative
to one another, in order to allow for vertical shear in the horizontal
wind, or time lags between downdrafts and rainfall. Only the 20, 30
and 40 dBz level radar returns are plotted. In interpreting these dia-
grams it must be realized that the radar plots are digitized 5-minute
averages, while the rain and divergence fields are 15-minute observa-
tions.

For each case the fields will be displayed at the five times
during the lifetime of a storm over the network, i.e., onset, peak
convergence, inflection point, peak divergence and the end of the cycle

as defined in Figure 6b. Fields during intermediate periods will be
shown, when they allow better understanding of the processes being
illustrated.

The small circles represent rain gauges which have recorded
rain in the previous 15 minutes, the filled in circles represent rain-
fall $\geq$ 0.30 inch in the previous 15 minutes and the open circles repre-
sent rainfall rates of < 0.30 inches in the previous fifteen minutes.
The dotted lines are isolines of divergence drawn in intervals of ± 400
x 10^{-6} sec^{-1} up to 1600 x 10^{-6} sec^{-1}. Higher values are plotted when
the diagram does not become cluttered. The shaded regions are regions
of divergence, and the unshaded regions are areas of convergence (nega-
tive divergence). The dashed lines are the lines of zero divergence.
Units of divergence and convergence plotted on the diagrams are 10^{-6}
sec^{-1}. The solid lines are the outlines of radar echo return intensity
up to 40 dBz. A legend is provided at the beginning of the sequence of
diagrams for each case study.

1. The Storm of 3 August 1975

Figure 18 shows the profiles of area-averaged divergence, upward
convective transports, downward convective transports and 15-minute
total network rainfall. The typical sinusoidal signal of a moderate to
heavy storm is clear, with the peak network area-averaged convergence
occurring between 1530-1545 EDT, followed by the peak 15-minute rainfall
intensity at 1700 EDT. The rainfall maximum precedes the peak network
area-averaged divergence by 15 minutes. The greatest 15-minute upward
transport occurs at 1515-1530 EDT while the greatest downward transports
occur at 1645-1700 EDT, simultaneous to the peak 15-minute total rain-
fall. Notice that the difference between the upward transports and the
downward transports will follow the same shape of the area-averaged
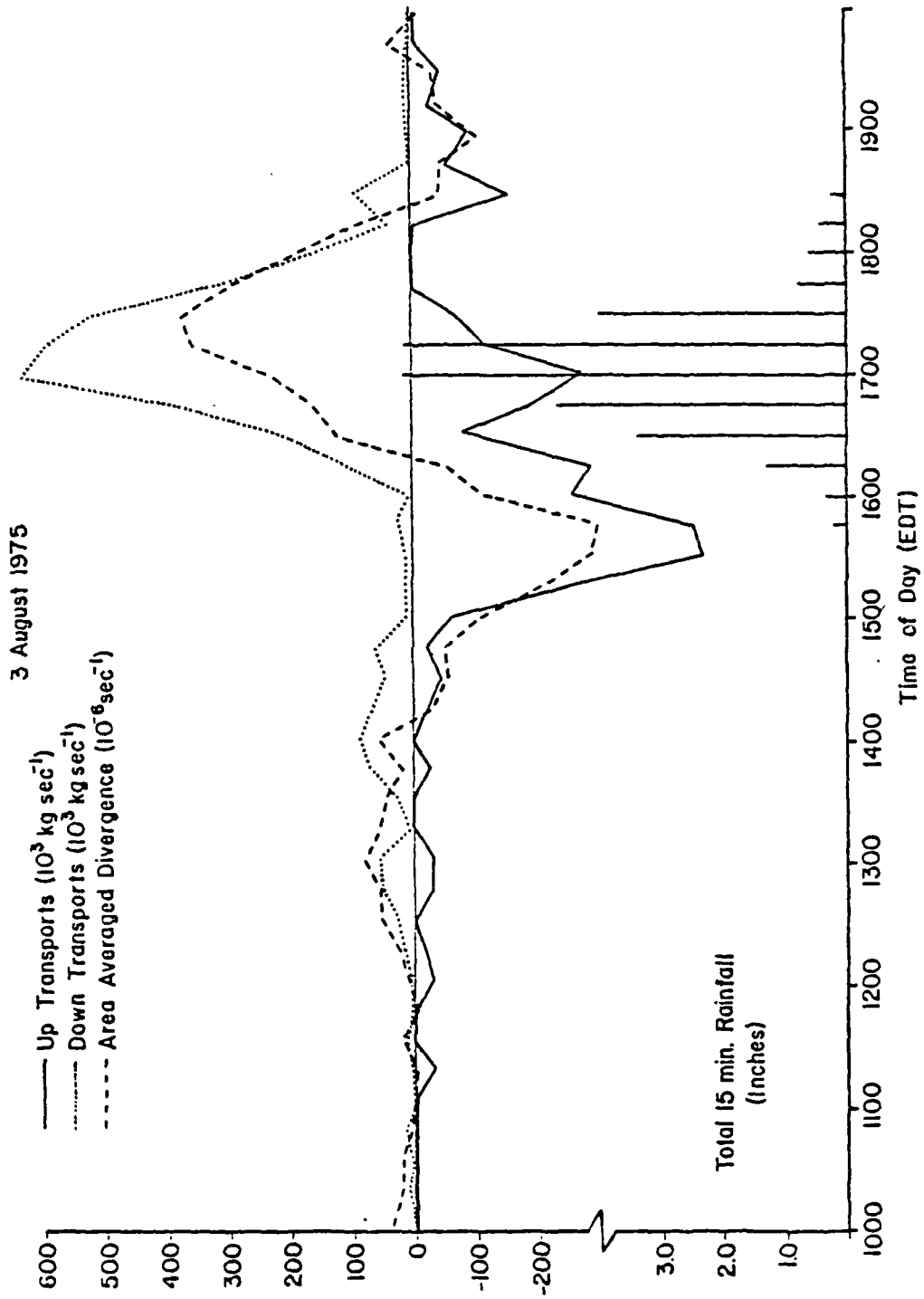
Figure 18. Daily profiles, 3 August 1975.

magnitudes stronger than -1200 x 10^{-6} sec^{-1} there. The center of the
main echo still is roughly 23 km from the center of the strong conver-
gence region.

Fifteen minutes after the peak in the area-averaged convergence
(Figure 22), a strong echo appears directly over the strong convergence
region in the center of the net. Light rain starts to fall near the
center of the network, while the main echo still lies just north of the
network.

By 1610, the echo which appeared over the center of the net has
merged with the northern echo (Figure 23). Moderate-heavy rainfall has
fallen over a region of strong divergence in the center of the network
in the fifteen minutes prior to 1630, and lighter rain has fallen in
the northern part of the net (Figure 24). Figure 24 illustrates the
fields during the point of inflection in the area-averaged divergence
field.

The fields during the peak network divergence in the area-
averaged divergence fields are shown in Figure 25. The complex to the
north of the network has split into western and northern parts, the
western part moving southward west of the network, the northern part
receding northwards, leaving a region of heavy rainfall and divergence
in the northeastern part of the rain gauge network.

By 1830 EDT (Figure 26), the large systems have dissipated,
except the western part, which has deposited light rain over the western
edges of the network, causing a region of divergence to develop there,
and responding weak areas of convergence. Rain stops in the network by
1830.

divergence taken over the entire interpolation grid, even though they occupy less than 50% of the area of the interpolation grid in the initial stages of the storm.

The detailed behavior of the surface divergence over the network during the storm is seen in Figures 19-26. The profiles shown in Figure 18 are typical of days with heavy rainfall over the network, as demonstrated in Chapter 3. The outflow from a large storm north of the network is shown to interact with, and most likely trigger the rapid intensification of another storm cell over the center of the network and its subsequent merger with the main echo.

This type of action-reaction process between outflows from storms is depicted for all the days analyzed in 1973 by the radar composites of Chapter 3. This example is a typical and specific case from 1975, of the processes represented in those radar composites.

Figure 19 shows the fields at 1430, shortly after the beginning of persistent area-averaged convergence. These are regions of weak divergence and convergence in the western part of the grid; with two intense echoes about 30-40 km north and south of the center of the net. Between 1430 and 1530, there is a dramatic increase in upward transports, reaching a peak at 1530 (Figure 20), by which time the large intense echo has moved southwards to a position just north of the network. Figure 20 shows the center of the main echo to be about 23 km from the responding center of strong convergence in the northern portion of the interpolation grid. Light (< 0.30 inches/15 min) rainfall has fallen at one station on the extreme northern rim of the network. Smaller echoes surround the network.

By 1545 (time of peak area-averaged convergence, Figure 21), a large region of convergence dominates the center of the network, with

LEGEND

— — — —   Lines of zero divergence
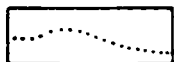
Isolines of convergence, every -400
x 10^{-6} sec^{-1}, up to -1600 x 10^{-6} sec^{-1}

Isolines of divergence, every +400
x 10^{-6} sec^{-1}, up to -1600 x 10^{-6} sec^{-1}

○   Light rainfall (< 0.30 inch in 15 min)

●   Heavy rainfall ($\geq$ 0.30 inch in 15 min)

Radar echo, isolines of reflectivity
at 20, 30 and 40 dBz

```
0        10          20
    5            15
```
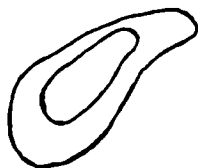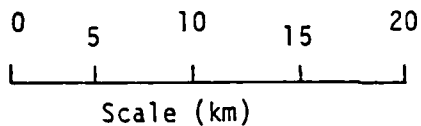
Scale (km)

1430 EDT 3 Aug. 1975 Beginning No Rain

Figure 19. The interior network fields at 1430 EDT, 3 August 1975. The beginning of persistent area-averaged convergence. There are regions of divergence and convergence in the western part of the grid, with two intense echoes about 25 and 40 km north and south of the center of the grid, respectively.
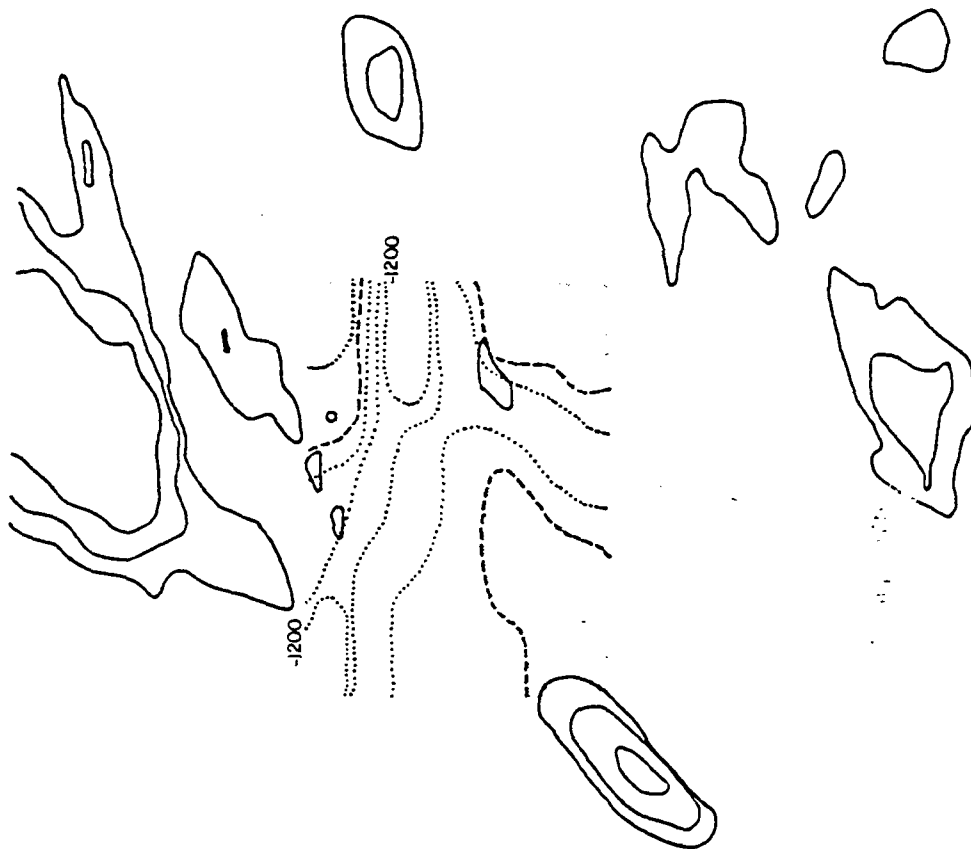
1530 EDT 3 Aug. 1973

Figure 20. The interior network fields at 1530 EDT, 3 August 1973. The maximum in upwind concentration exceeds pts. The echo to the north has moved southwards in the previous hour. Light rain in the north side is present.
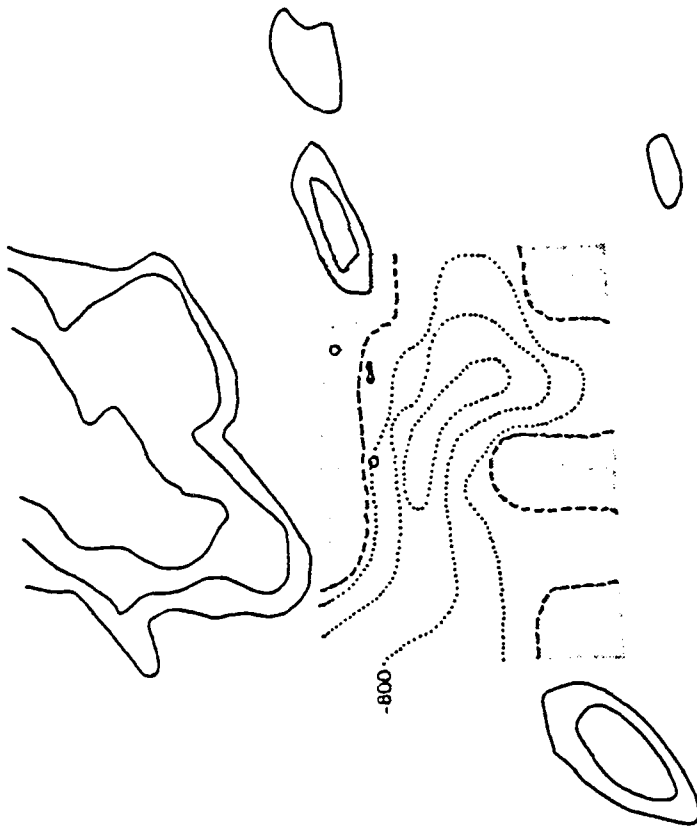
1545 EDT 5 Aug. 1975 Peak Convergence

Figure 21. The interior network fields at 1545 EDT, 5 August 1975. Peak network area-averaged convergence. A large region of convergence covers the center of the network.
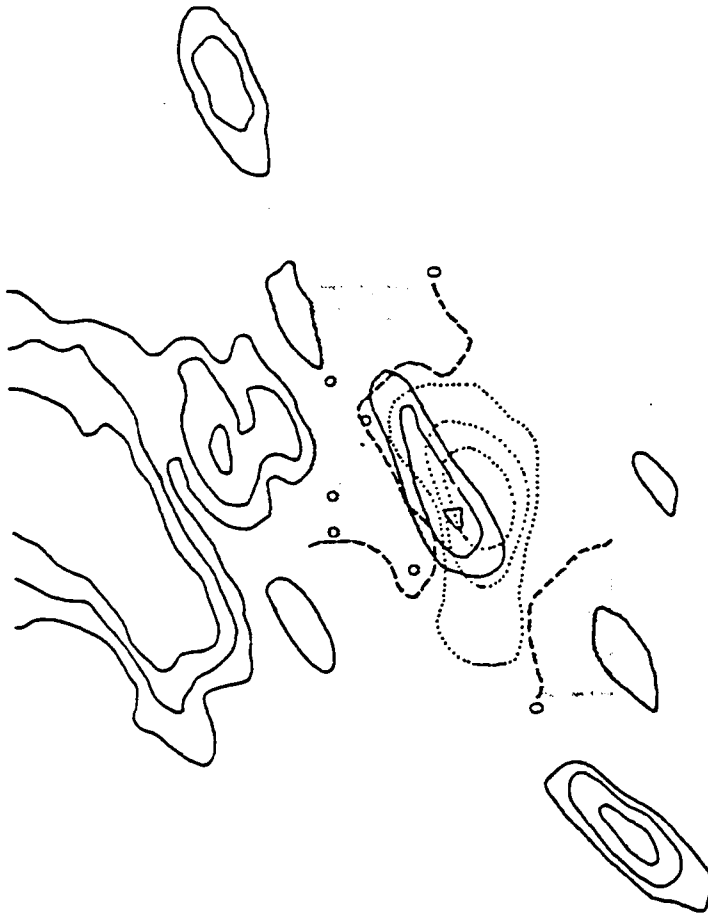
1600 EDT 3 Aug. 1975

Figure 22. The interior network fields at 1600 EDT, 3 August 1975. Fifteen minutes after the peak in area-averaged convergence. A strong echo appears directly over the area of maximum convergence. Light rain starts to fall over the center of the network. The main echo still lies north of the network.
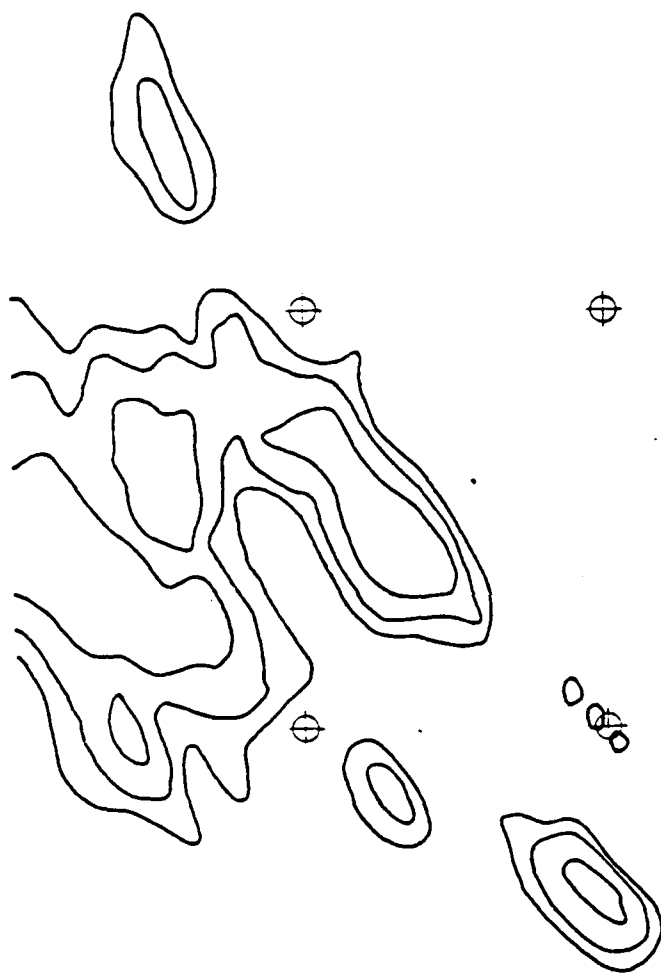
1610 EDT 3 Aug. 1975

Figure 38. The interior network fields at 1610 EDT, 3 August 1975. Merger has taken place between the newly generated cells and the main echoes to the north.
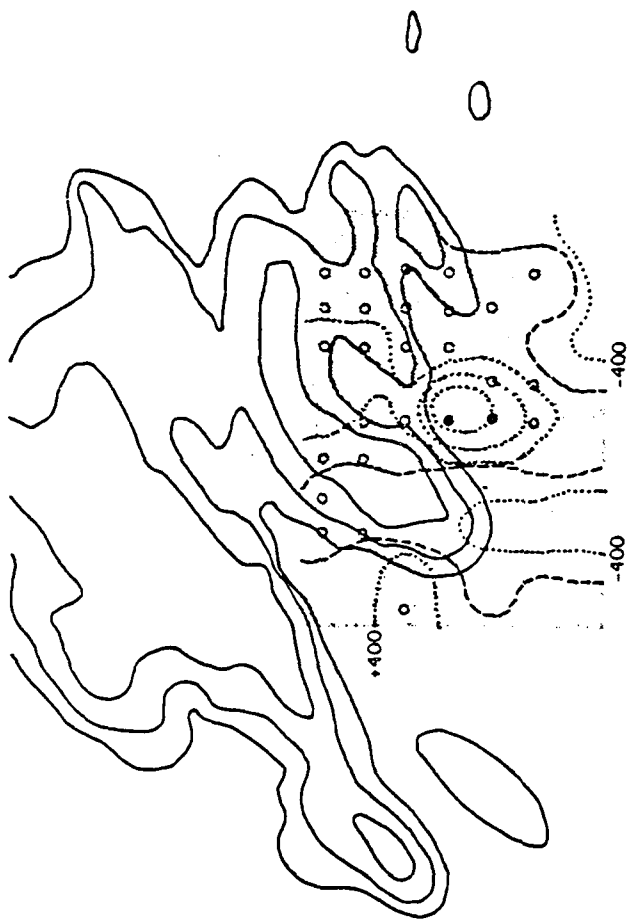
1630 EDT 3 Aug. 1975 Inflection Point

Figure 54. The interior network fields at 1630 EDT, 3 August 1975. Inflection point in the area-averaged discharge fields. Heavy rain falls over the center of the network, producing strong discharges there.

1730 EDT 3 Aug. 1975 Peak Network Divergence

Figure 26. The interior network fields at 1730 EDT, 3 August 1975. Peak in the network area-averaged divergence field. Heavy rain and accompanying strong divergence in the northern part of the grid is in relatively light divergence.
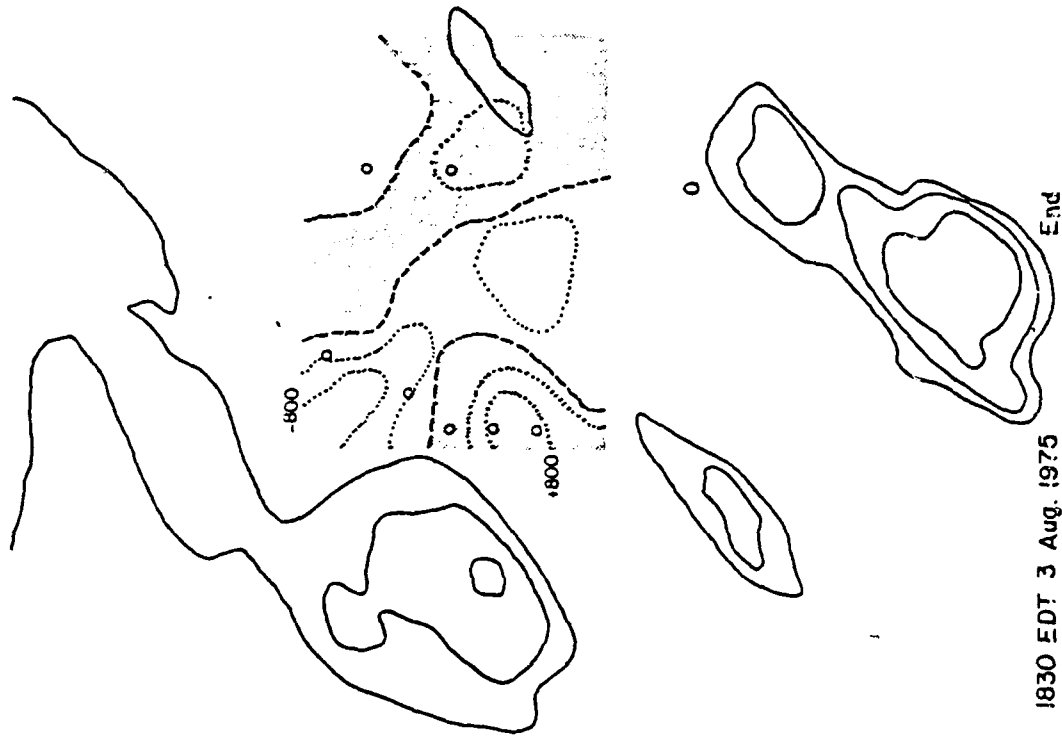
1830 EDT 3 Aug. 1975

Figure 26. The interior network fields at 1830 EDT, 3 August 1975. The end of the cycle. Most of the rain falls along the western edge. No rain fell in the network after 1830 EDT.

2. The Storm of 20 August 1975

This case study differs from the previous one in that two smaller showers occur in the rain gauge network prior to the main shower, which begins to deposit rain in the network at 1715 EDT.

This case illustrates the interaction between smaller storms earlier in the day, and illuminates some of the mechanisms behind radar echo merging. The complicated series of interactions between the smaller storms is shown, and the effects of the propagation of a large system into the network is illustrated. Again, especially in the case of the main shower (1715-1930 EDT), this is a specific and typical example of the ideas represented by the radar echo composites of Chapter 3.

The overall description of the behavior of the surface divergence fields on this day is contained in Figure 27.

The first significant upward transport in the network (Figure 28) occurs at 1145 EDT (45 minutes prior to the first detection of rain in the northern part of the network at 1230 EDT).

There is an echo about 20 km due north of the only significant convergent region in the network, and a large line of echoes orientated N-S about 25-30 km E-SE.

By 1200 (Figure 29) the convergence zones are orientated N-S, and a small echo has appeared over the convergent region in the northern part of the network. The small echo increases in size and intensity by 1215 (Figure 30), and there is a line forming N-S across the network. The large line of echoes to the east of the net remains about 30 km away. Heavy rain falls at one station in the northernmost part of the network by 1230, with a large (-400×10^{-6} sec^{-1}) region of convergence over the center of the network. The line 30 km east of the network is now starting to break up, while the N-S line over the network has intensified

(Figure 31). The heavy rain from the shower in the northern part of the network forces a divergence region there by 1245 (Figure 32), which, together with another rain-forced divergence region in the southern part of the network, intensifies the convergence area over the center of the network. By 1300 (Figure 33) the two main echoes over the network have merged, and a new echo has formed over a convergent region in the northwestern corner. As the rain from the merged echo becomes heavy (Figure 34), the subsequent downdraft strengthens the convergence beneath the new echo on the northwestern edge of the net. By 1330 (Figure 35) the divergence regions associated with the heavy rain in the western part of the network has become strong, and the convergent region over the center of the net at 1315 has intensified. It is assumed that there is another intense convergent region just outside the western edge of the grid, since by 1345, the small echo in that region at 1315 has intensified, while the other echo has moved further towards the strong convergence zone in the center (Figure 36). A similar situation persists through 1400 (Figure 37). The general convergent regions over the center of the network persist after the dissipation of the echo there through 1430 (Figures 38 and 39) and starts to intensify in the southern part of the network as the larger echoes north and northwest of the net dissipate, at 1445 (Figure 40). By 1500, (Figure 41) a new, small, internal echo appears over this convergent zone, and deposits light rain into a divergent region in the southwestern part of the grid by 1530 (Figure 42). This small echo continues to produce light rain in the western part of the network, and to generate very light responding regions of convergence in the central part of the net (Figures 43 and 44). The echo persists, roughly in the

same place until around 1605 (Figure 45), producing rain in the north-
west corner by 1615, and in response, the region of convergence over
the south central part of the net intensifies (Figure 46). There has
been an echo growing south-southeast of the network since 1545, which
now (1615) starts to rapidly intensify, and moves within 20 km of the
southern edge of the network by 1645 (Figure 47). The convergent region
present in the center of the network remains. Small echoes form over
the strong convergent zone oriented N-S over the center of the network
by 1700 (Figure 48), intensifying there and producing an echo by 1715
(Figure 49), which is time of the peak network convergence. Light rain
(maximum 0.15"/15 min) falls NW of the new echo, between 1700 and 1715.
By 1730 (Figure 50) the two radar echo returns over the southern part
of the network between 1700 and 1715 have merged over the main conver-
gent region, and heavy rain has fallen into the center of the network.
Convergence zones form on the east and west flanks of the strong diver-
gence region at the center and new echoes grow over convergence regions
north of the main echo. At 1745 (Figure 51), the main echo has spread
out on both flanks, and has merged with the echoes to the north. Heavy
rain covers the center of the grid with its corresponding strong diver-
gent zone. Convergence areas flank the downdraft region. The inflec-
tion point in the overall divergence profile occurs at this time. The
main storm enters its decaying stage and by 1830 has reached the point
of peak network divergence (Figure 52). No rain falls after 1930 (Figure
53).
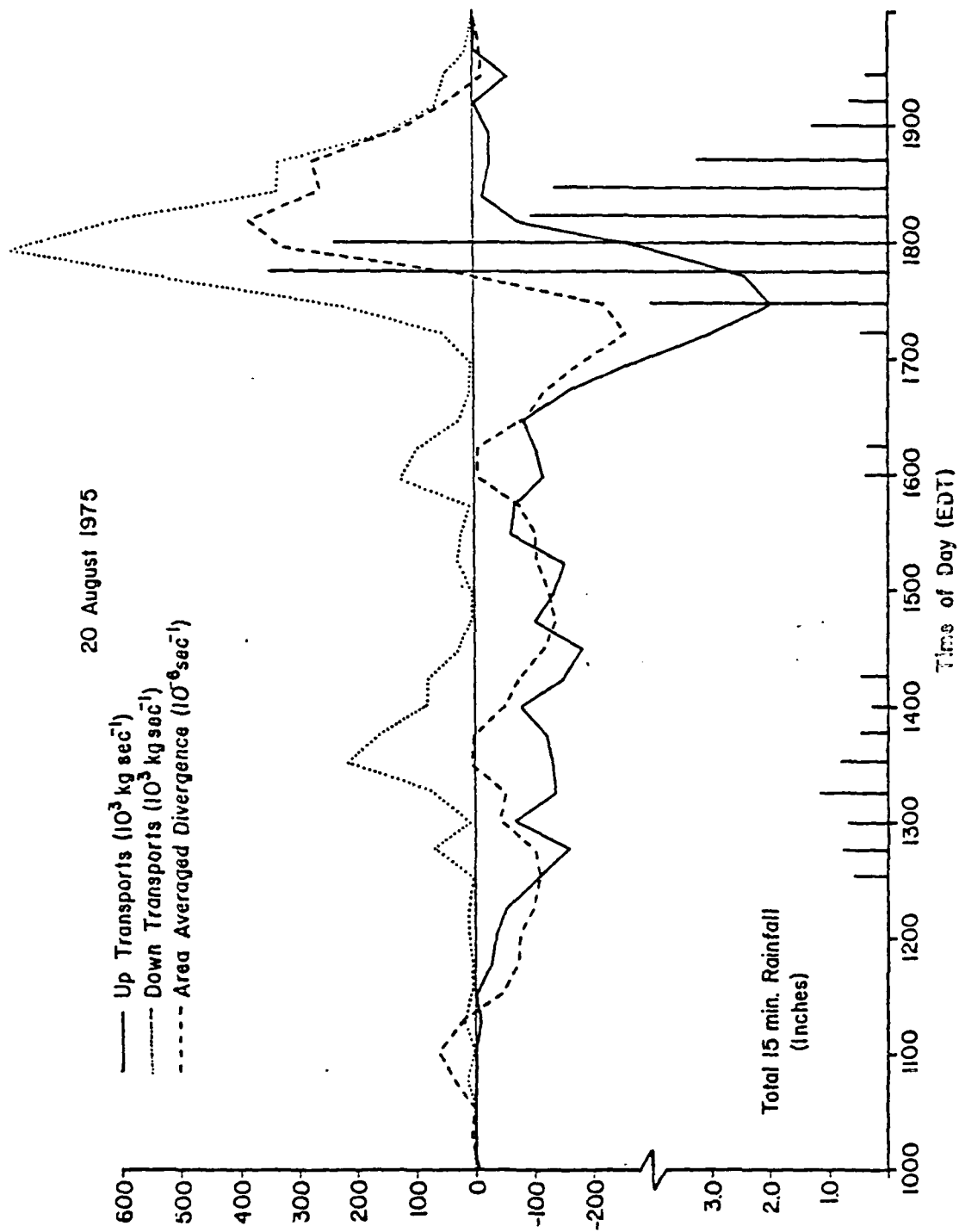
Figure 27. Daily profiles, 20 August 1975.

1975 20 Aug. 1145 EDT

Figure 23. The interior network fields at 1145, 20 August 1975. First significant convergence of the day. There is an echo north of the convergence area, and a strong line orientated N-S off to the NE of the network.
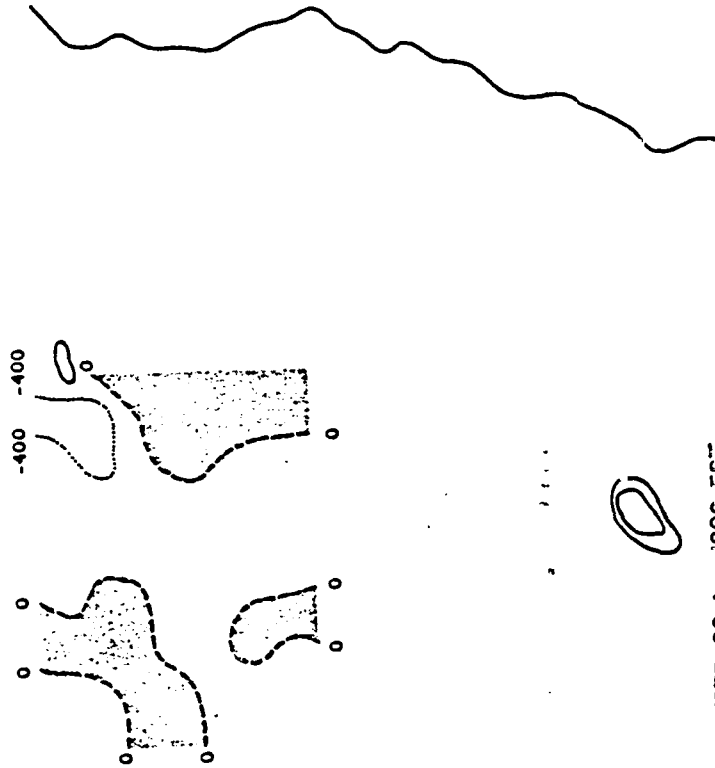
Figure 29. *The interior network fields at 1200 EDT, 20 August 1975. The convergence zones are beginning to take on a N-S orientation. A small echo appears over the only significant convergence at the surface.*

1215 EDT 20 AUG 1975

Figure 20. The interior network fields at 1215 EDT, 30 August 1975. The strong line flanking the eastern side of the network has extended northwards and moved closer to the network. The small cells has grown to a considerable size. The N-S orientation in the surface fields persists, and echoes line up above it.

1975 20 Aug. 1230 EDT

Figure 31. The interior network fields at 1230 EDT, 20 August 1975. A N-S line of echoes has formed over the network. The large line to the east is dissipating. Heavy rain falls in the northern portion of the network, destroying the N-S orientation of the convergence zone there.

1975 20 Aug. 1245 EDT
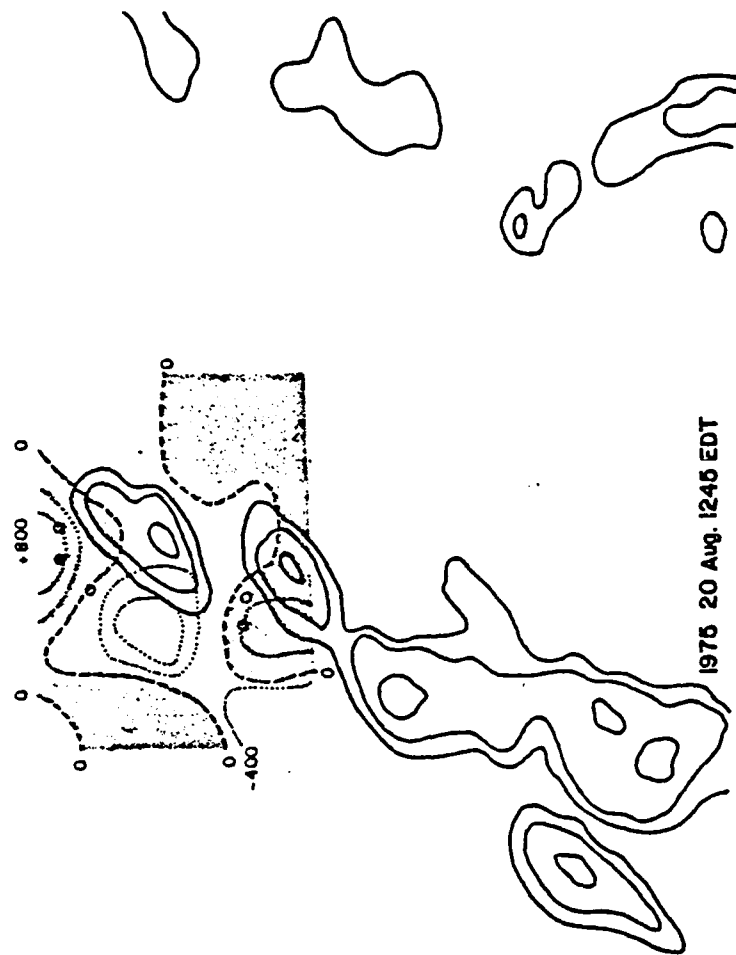
Figure 32. The interior network fields at 1245 EDT, 20 August 1975. Heavy rain falls in the northern section of the grid, producing strong divergence, which intensifies the convergent region just us of the center of the net. The line east of the net has broken up.
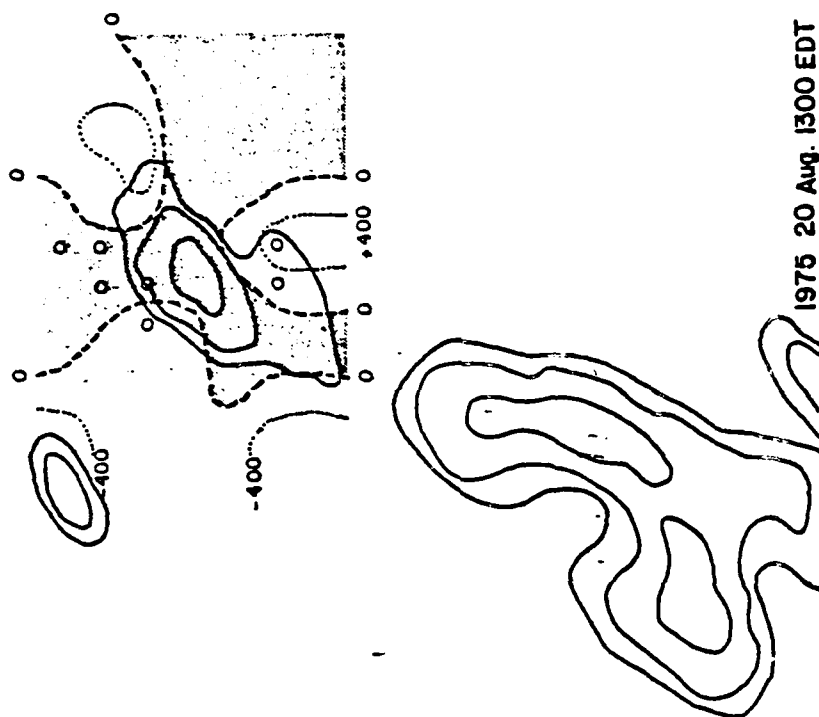
1975 20 Aug. 1300 EDT

Figure 33. The interior network fields at 1300 EDT, 20 August 1975. Radar echo merger occurs over the previous convergent regions, producing a single echo over the center of the network. Beneath the echo, the wind fields at the surface are becoming slightly divergent. Light rain falls. A new echo forms over a convergent region in the NW corner. The main storm now has a NNE-WSW orientation, with convergence on its flanks.

1975 20 Aug. 1315 EDT (Radar from 1305)

RADAR MISSING, PLOTTED FROM 1305
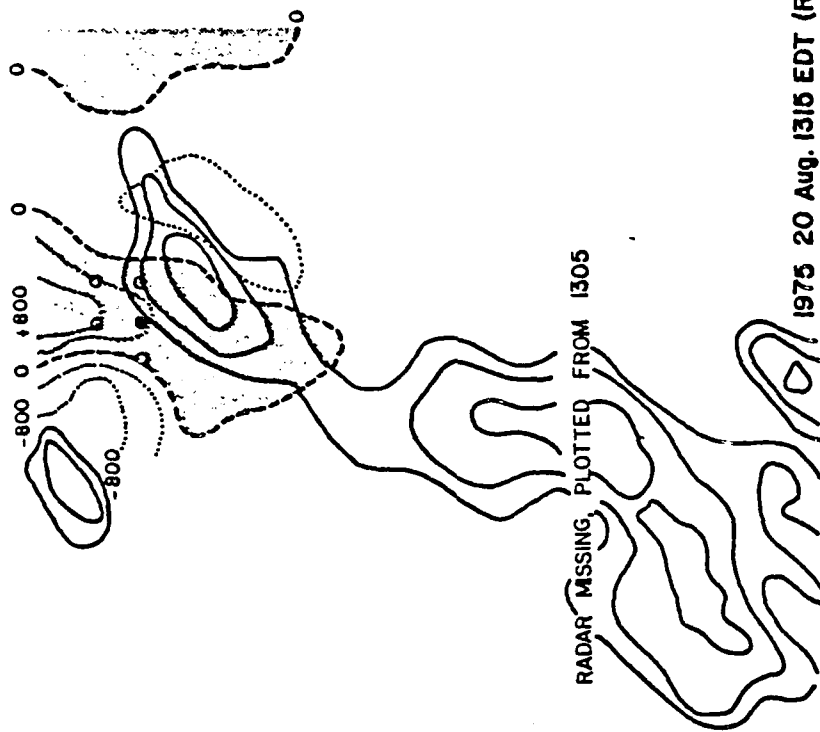
Figure 54. The interior network fields at 1315 EDT, 20 August 1975. Heavy rain has fallen into the north-central part of the network, with strong divergence there. This intensifies the convergence beneath the new echo.
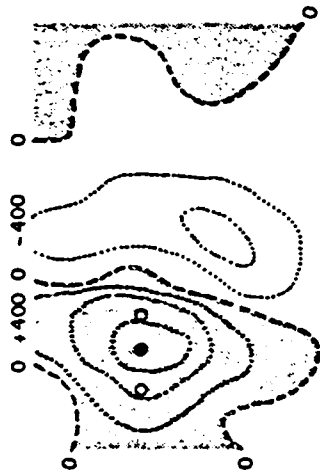
1975 20 Aug. 1330 EDT Radar Missing

Figure 35. The interior network fields at 1330 EDT, 20 August 1975. No radar available. Heavy rain falls in the western portion of the network, producing an intense downdraft, which evidently produces a convergent region N-S down the center of the network, and, it is assumed, outside the network's western edge.

1975 20 Aug. 1346 EDT

Figure 36. The interior network fields at 1345 EDT, 20 August 1975. Two main echoes are now present. One lies west of the network, the other over the convergence region down the center. Light rain falls into both the strong divergent region and into the weaker convergent region.
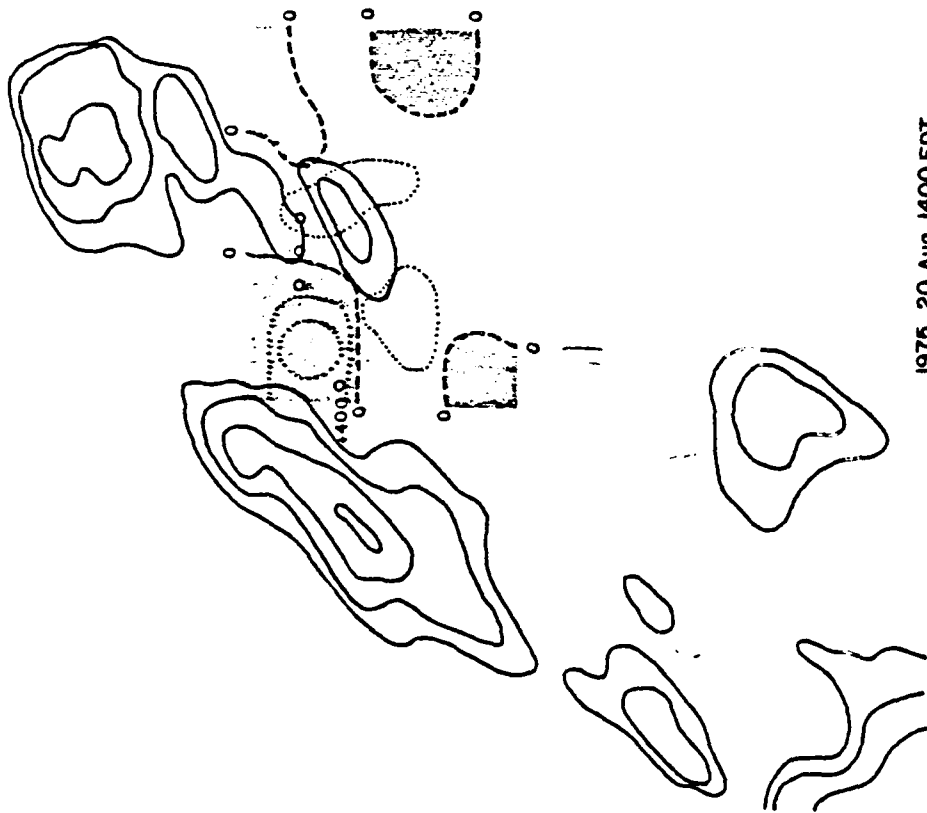
1975 20 Aug. 1400 EDT

Figure 37. The interior network fields at 1400 EDT, 20 August 1975. The situation is similar to that in Figure 36, except that the regions of convergence and divergence have become weaker, and the storm over the center appears to be weakening also.
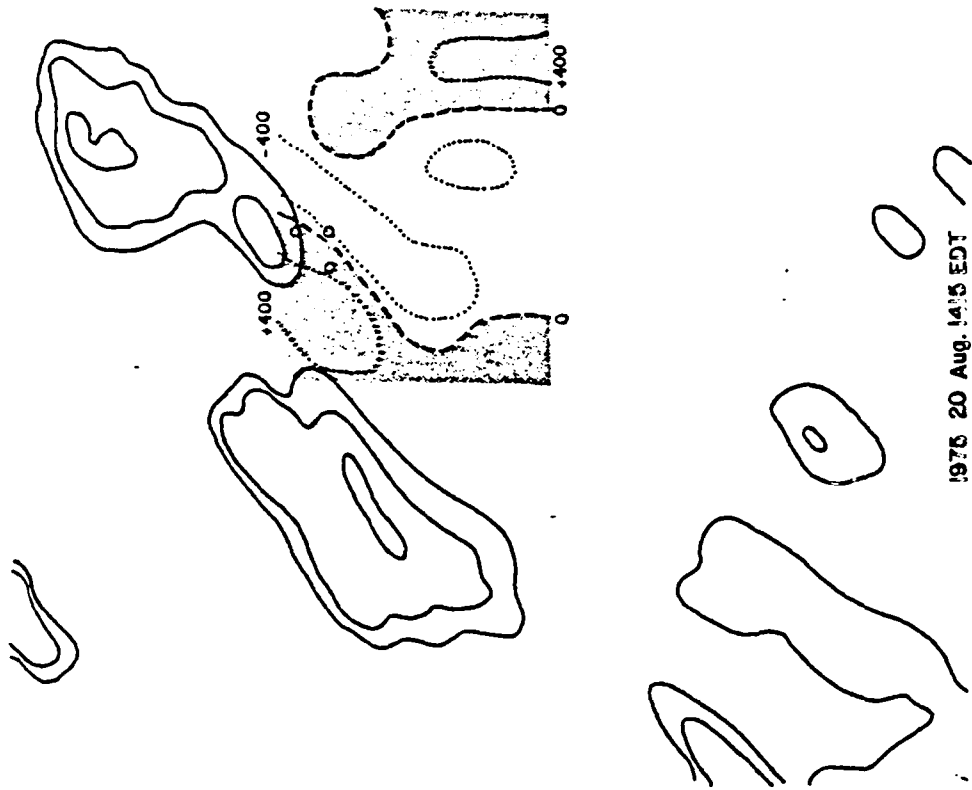
Figure 38. The interior network fields at 1415 EDT, 20 August 1975. The entire system is weakening, with rainfall in the northern network. Regions of light convergence persist over the central part of the network.
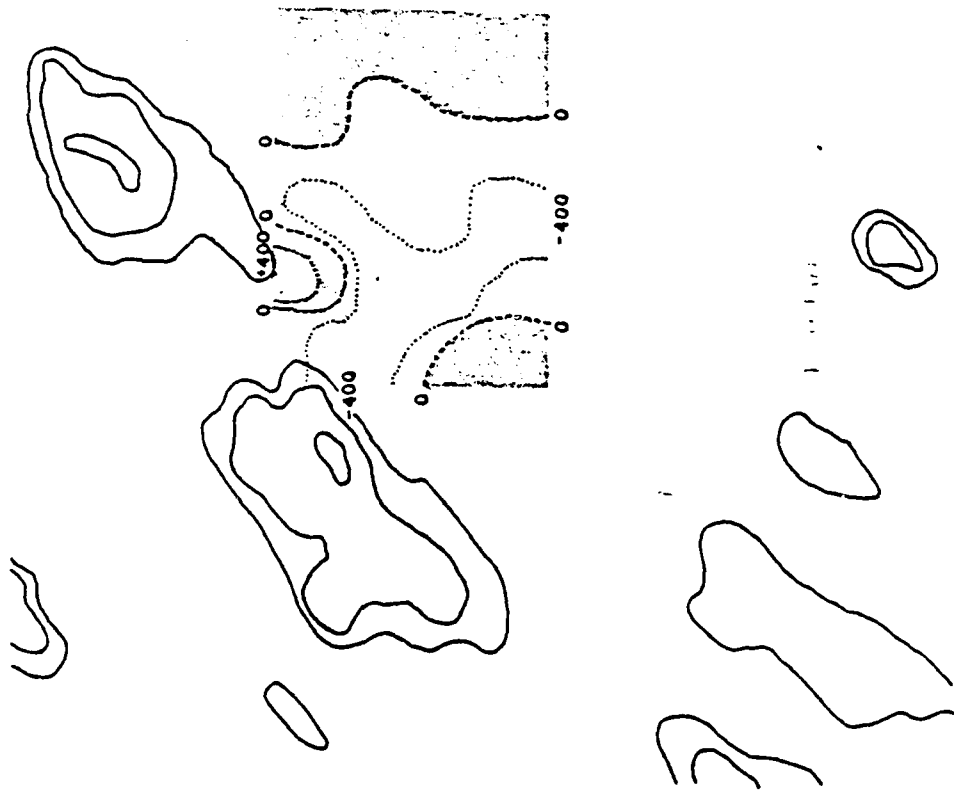
1430 EDT 20 Aug. 1975

Figure 39. The interior network fields at 1430 EDT, 20 August 1975. The convergence zone down the center persists.

1845 EDT 20 Aug. 1975

0   -400   -400   0

Figure 1. The interhour network field at 1845 EDT, 20 August 1975. As the echoes just north of the network indicate, the region of convergence in the south central part of the network is just to the northwest.
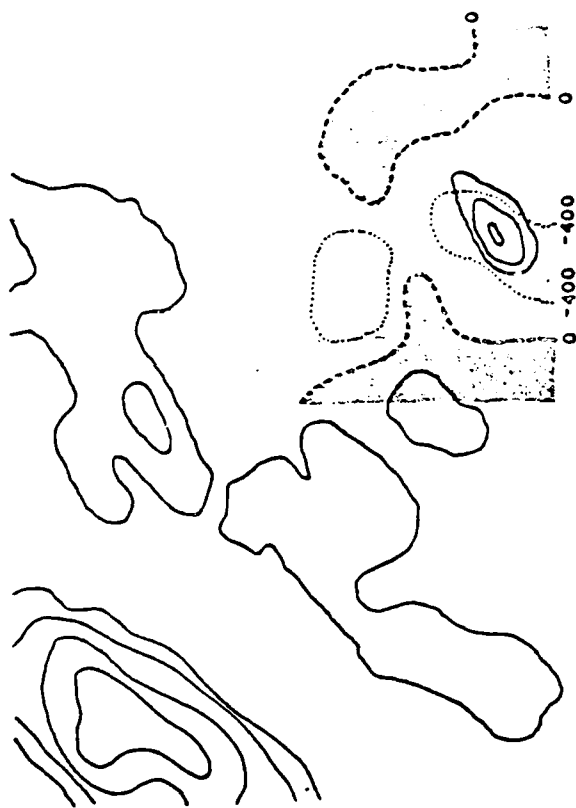
'500 EDT 20 Aug. 1975

Figure 41. The interior network fields at 1500 EDT, 20 August 1975. A new echo appears over the previously strong convergent region.
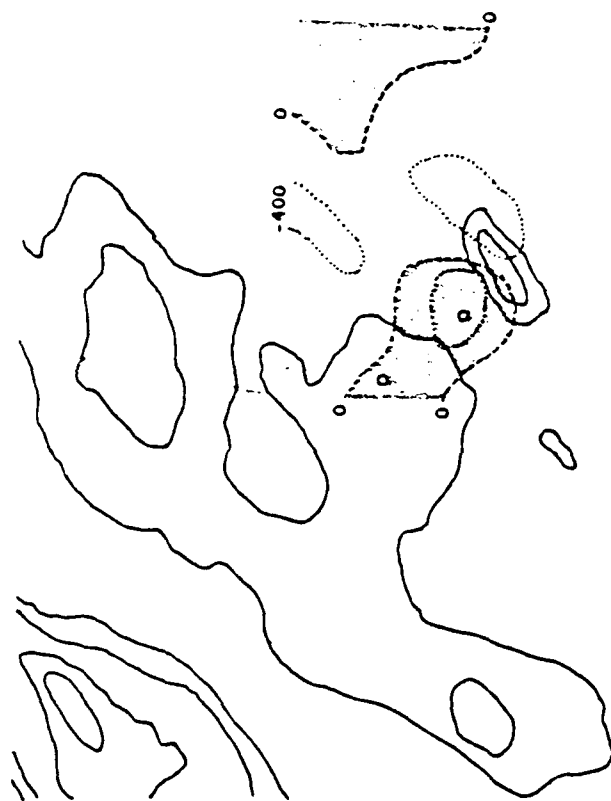
Radar 1515, Divergence 1530 EDT 20 Aug. 1975

Figure 42. The interior network fields at 1515 EDT, 20 August 1975. Light rain falls from the area around the new echo. Widespread rain is present W-NW of the network.

1530 EST 20 Aug. 1976

Figure 46. The interior network fields at 1530 EDT, 20 August 1976. The situation is similar to that in Figure 43. Outflows from the weak, large system west of the network maintain the convergence into the center of the network.
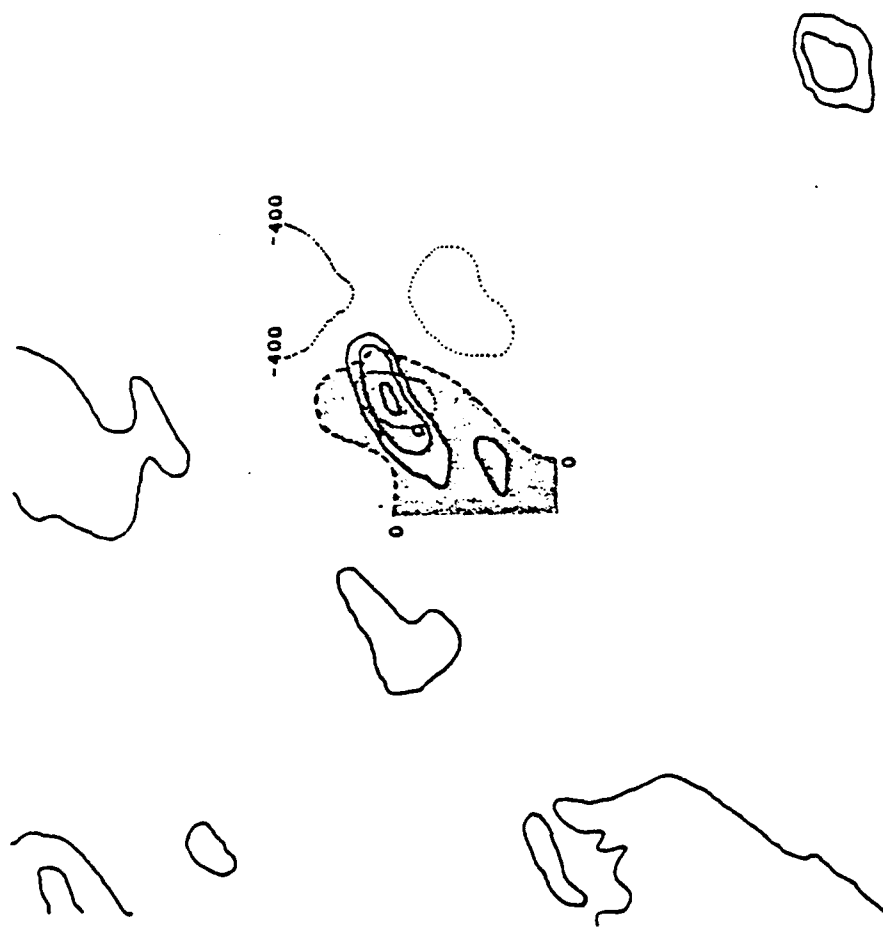
1545 EDT 20 Aug. 1975

Figure 44. The interior network fields at 1545 EDT, 20 August 1975. As the larger, dissipating system to the west dissipates, the convergence down the center is maintained by downdrafts into a region of rainfall in the western half of the net.
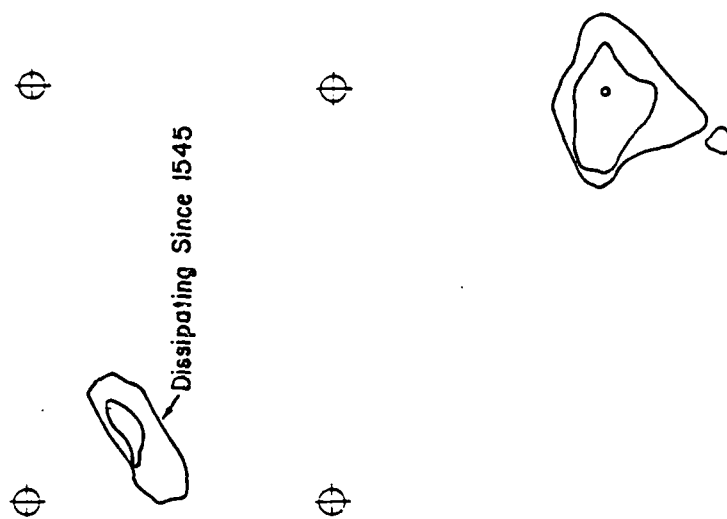
1605 EDT 20 Aug. 1975

Figure 45. The interior network fields at 1605 EDT, 20 August 1975. The small echo in the western net continues to dissipate there through 1605. A new, intense echo has grown outside the network southeast of the center of the net, and is moving northwards towards the grid.
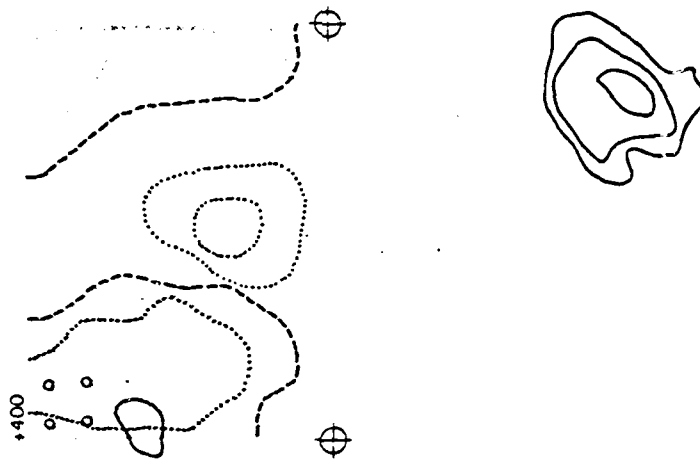
1615 EDT 20 Aug. 1975 Beginning

Figure 46. The interior network fields at 1615 EDT, 20 August 1975. As the echo in the west dissipates in light showers, the convergence down the center intensifies again. The echo to the south is strengthening.
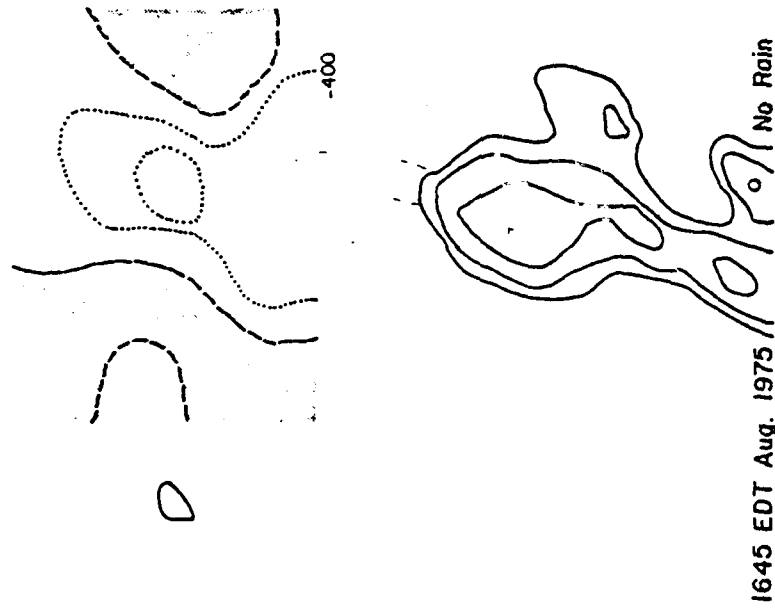
1645 EDT Aug. 1975 No Rain

Figure 47. The interior network fields at 1645 EDT, 20 August 1975. The convergence over the center is now strong and well organized in a N-S orientation. The echo to the south has grown and moved closer to the network.
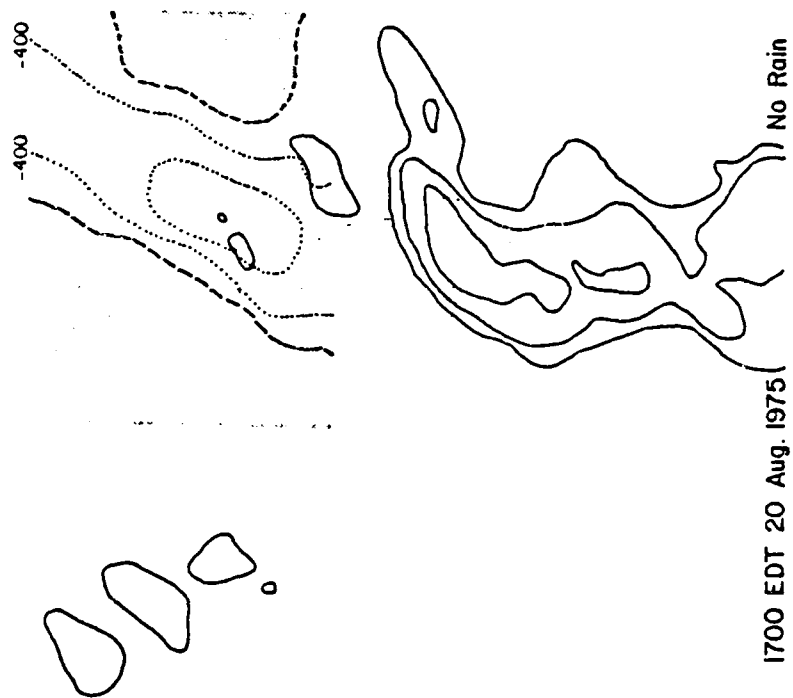
Figure 48. The interior network fields at 1700 EDT, 20 August 1975. Small echoes begin to form in the convergent regions north of the large shower to the south.

1715 EDT 20 Aug. 1975

Peak Network Convergence
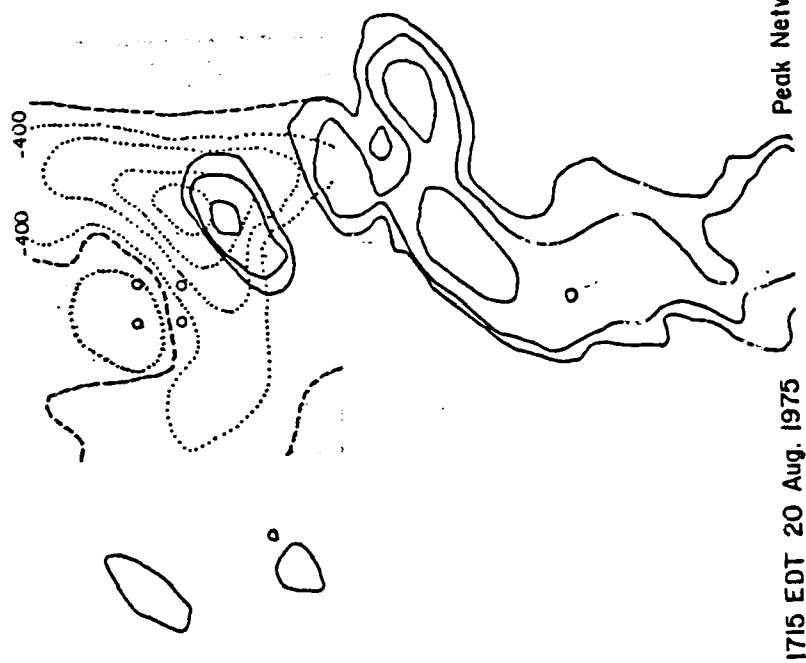
Figure 49. The interior network fields at 1715 EDT, 20 August 1975. The convergent region has become intense, with an echo forming directly over it. The edge of the southern edge of the grid. This is the period of peak network convergence.
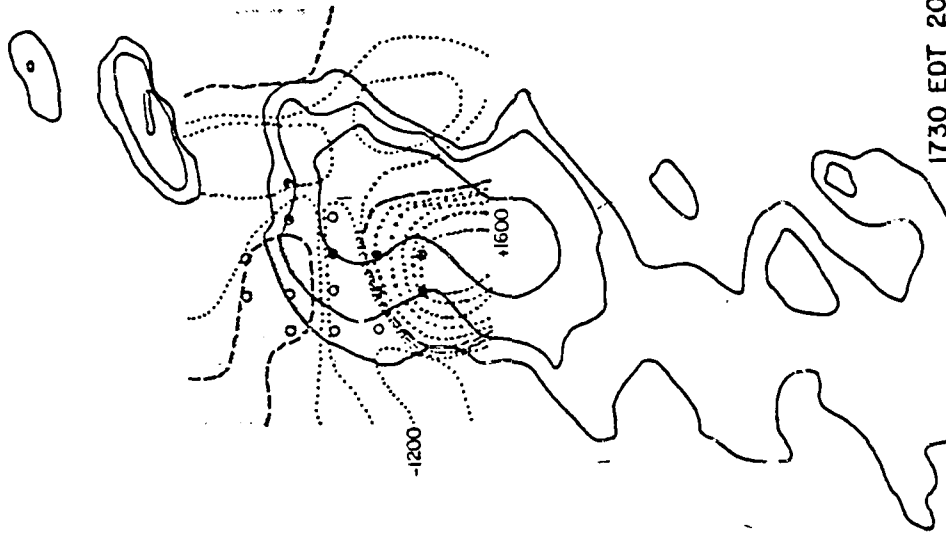
1730 EDT 20 Aug. 1975

Figure 50. The interior network fields at 1730 EDT, 20 August 1975. The echoes in the southern half of the net in Figure 49 have merged, and produce heavy rain over the center of the network. New echoes form over convergent regions north of the main storm. Strong convergence regions form on the east and west flanks of the main echo.
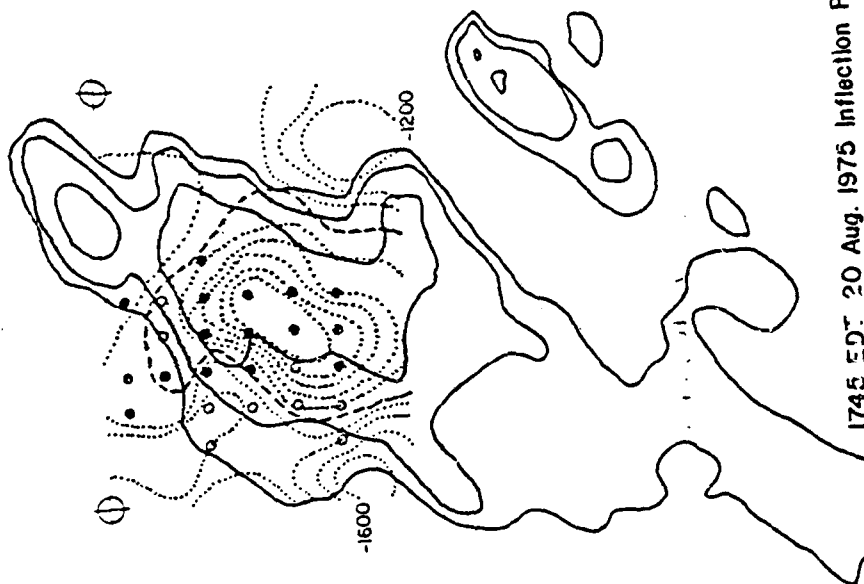
1745 EDT 20 Aug. 1975 Inflection Point

Figure 51. The interior network fields at 1745 EDT, 20 August 1975. The inflection point in the area-averaged divergence profile. Heavy rain has fallen over the center of the network. The echoes to the north of the main echo at 1730 have merged with the main echo. There is strong convergence on the east and west flanks of the storm, and the storm is beginning to spread in both directions.
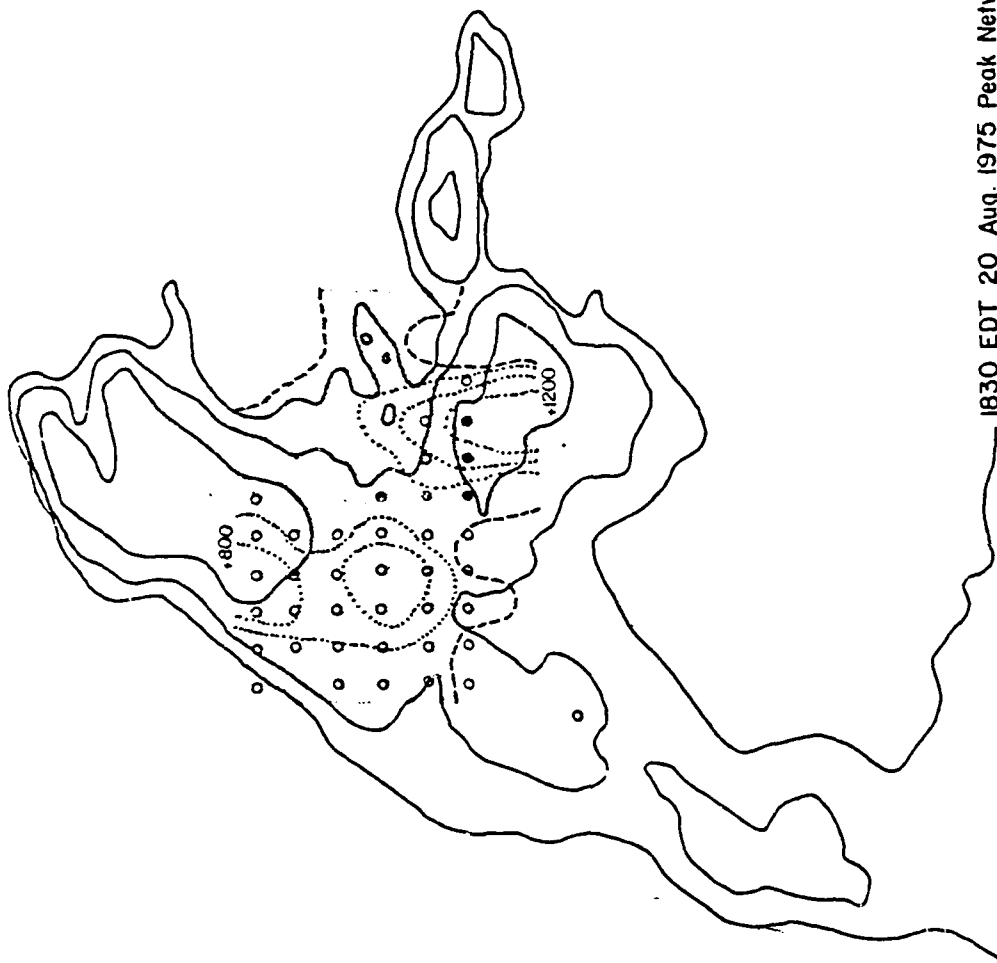
———— 1830 EDT 20 Aug. 1975 Peak Network Divergence .

Figure 52. *The interior network fields at 1830 EDT, 20 August 1975. Peak network divergence. The storm has spread east and west, and to the north. The most intense rain falls into the strongest divergence region in the southeast. (There are no rain gauges in the bottom quarter of the interpolation grid.) New cells continue to grow on the eastern flank, outside the network.*
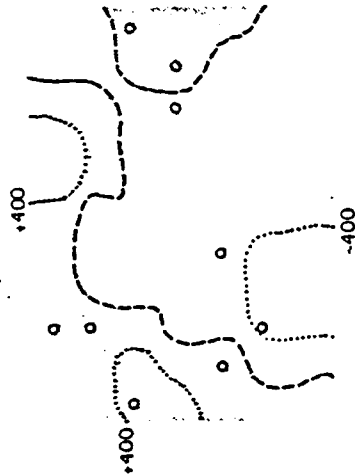
1930 EDT 20 Aug. 1975 End (No Radar Avlbl.)

Figure 53. The interior network fields at 1930 EDT, 20 August 1975. (No radar available.) The storm has dissipated. No rain falls in the network after 1930 EDT.

3. The Storm of 6 August 1975

This storm is different from the previous two in that it was classified as an S-type day although there is weakness in the peak area-averaged divergence. The graph of area-averaged divergence is contained in Figure 54, and shows that there is only a weak response in divergence to the strong convergent peak at 1445. However, when the situation is viewed from the point of view of the mass transports, the reasons for the distortion in the area-averaged divergence fields become clear. Figure 54 contains the daily network profiles for this case. There is a strong down mass transport response at 1545, but at the same time, there is a strong upward mass transport in a different part of the network, which cancels it out. As a result, the area-averaged divergence at 1545 EDT is close to zero.

At the beginning of onset of persistent convergence, we have the familiar picture. An echo is located some 18 km north of the northeastern corner of the grid (Figure 55). By 1415 (Figure 56), it has grown and moved to within 12 km of the northern edge of the interpolation grid, causing a region of strong convergence to develop there. At the time of greatest upward mass transport (Figure 57), an intense echo lies off the northwestern corner, the most intense return being 13 km from the center of an intense region of convergence in the northwestern portion of the network, and light rain has fallen in the NW section. By 1515, (Figure 58) heavy rain is falling in the northwest and western parts of the grid, and smaller echoes are forming along the western edge, over convergence caused by the outflow. At the time of the greatest downward mass transports, (Figures 59 and 60), a well organized, intense divergence-convergence pair in the surface conver-

gence field has formed, with a strong region of convergence persisting over the center of the network. By 1645, (Figure 61), the echo has moved over this convergent region, but the main downdraft region remains in the southwestern corner, and does not cover a large enough area of the interpolation grid to show strong divergence in the network area-averaged field.

By 1715 (Figure 62) the main downdraft is on the southern edge, and again, its effect on the network divergence field is not great.

Between 1745-1800 (Figures 63 and 64), the storm has essentially dissipated outside the network.
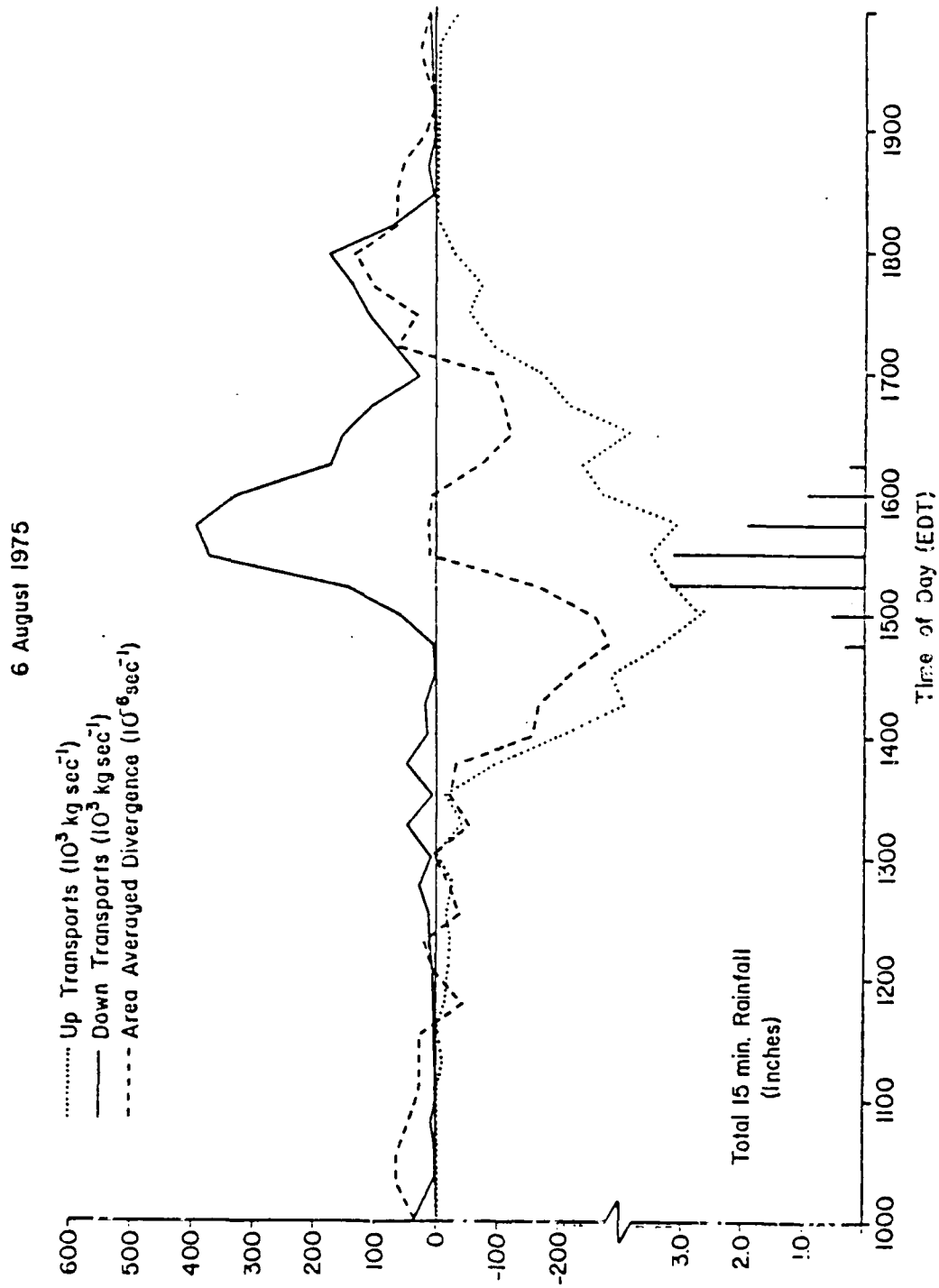
Figure 54. Daily profiles, 6 August 1975.

LEGEND
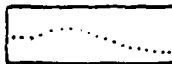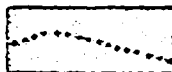
– – – – –	Lines of zero divergence
	Isolines of convergence, every -400 $\times 10^{-6}$ sec^{-1}, up to -1600 $\times 10^{-6}$ sec^{-1}
	Isolines of divergence, every +400 $\times 10^{-6}$ sec^{-1}, up to -1600 $\times 10^{-6}$ sec^{-1}
O	Light rainfall (< 0.30 inch in 15 min)
●	Heavy rainfall ($\geq$ 0.30 inch in 15 min)
	Radar echo, isolines of reflectivity at 20, 30 and 40 dBz
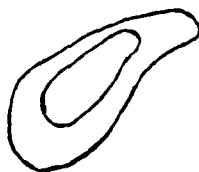
0   5   10   15   20

Scale (km)
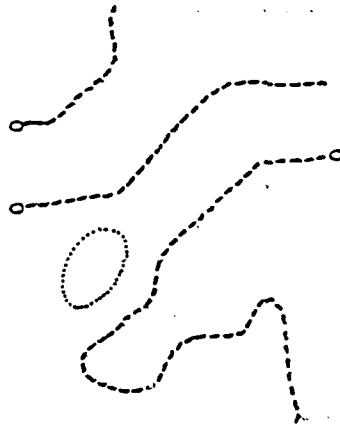
1330 EDT 6 Aug. 1975 Begining

Figure 55. Interior network fields at 1330 EDT, 6 August 1975 at the time of start of predicted area-averaged convergence.
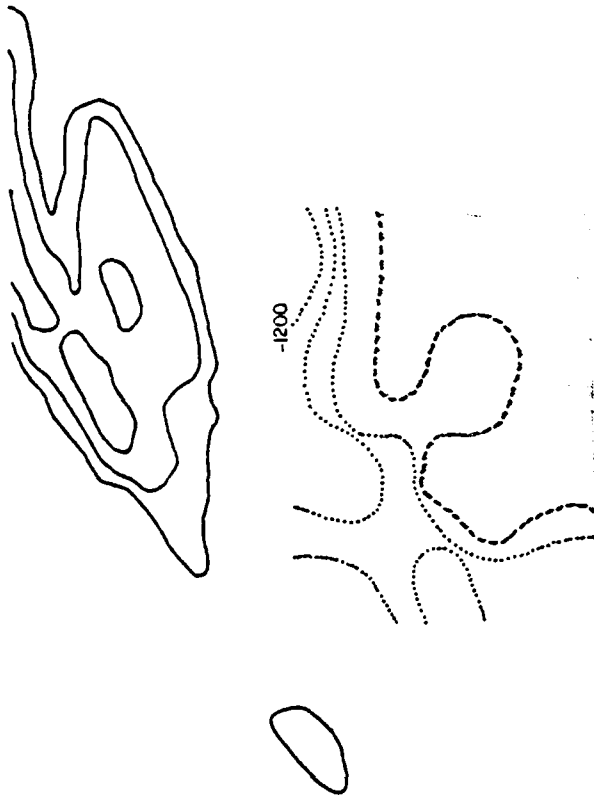
1415 EDT 6 Aug. 1975 No Rain

Figure 56. Interior network fields at 1415 EDT, 6 August 1975. The echo to the north has intensified and moved southwards, to a position just north of the network. Strong convergence occurs in response in the northern and western parts of the grid.
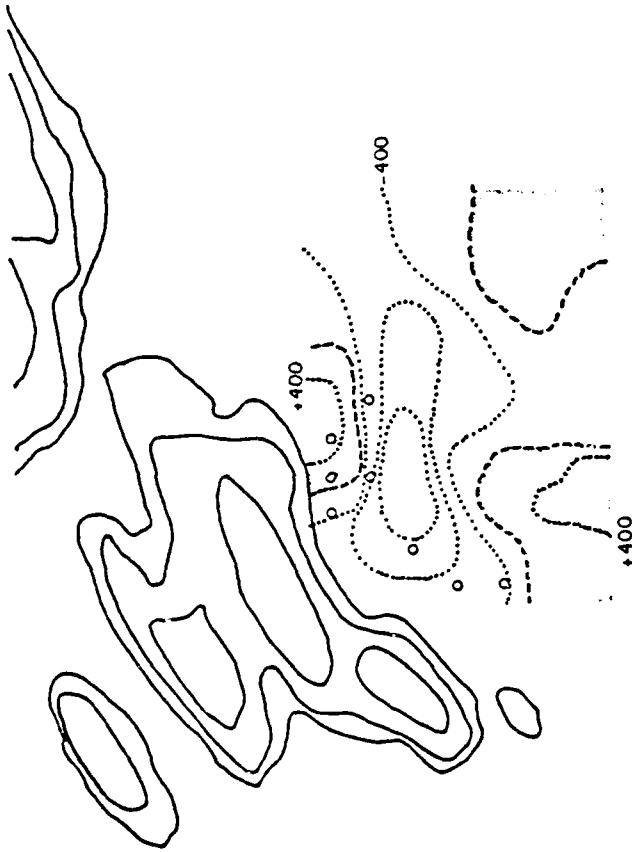
1500 EDT 6 Aug. 1975 Peak Upflux

Figure 57. Interior network fields at 1500 EDT, 6 August 1975. The fields at the time of peak network convergence. A strong region of convergence and light rain occurs in the northwestern sector, with a large echo situated just outside the network.
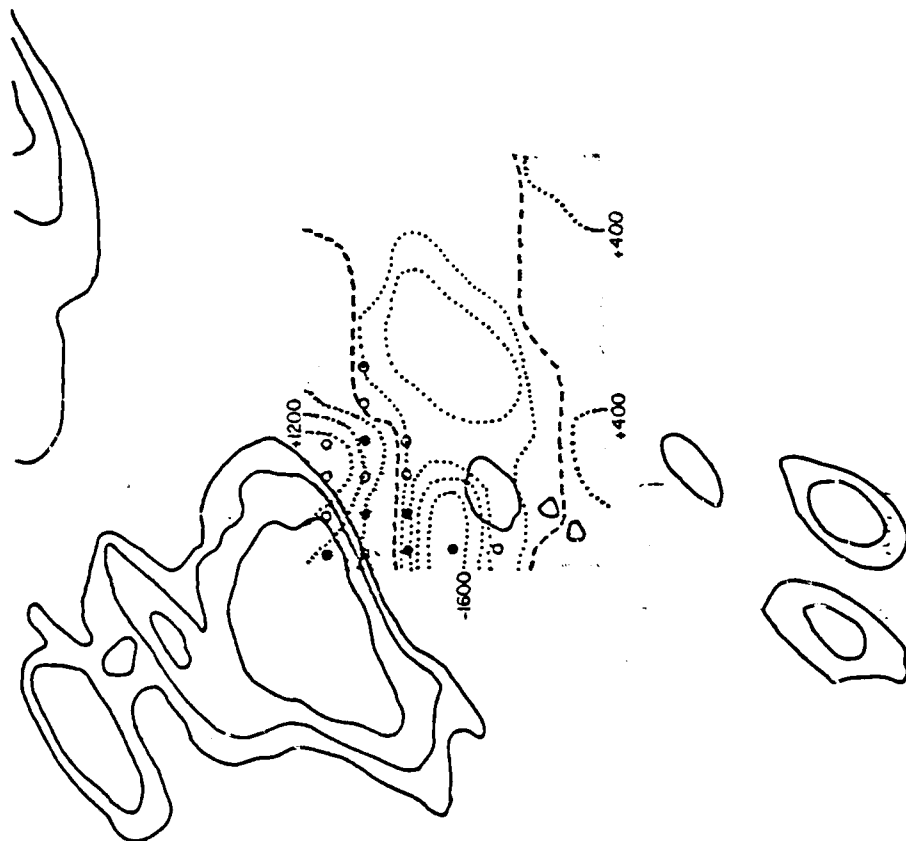
1515 6 Aug. '975

Figure 58. Interior network fields at 1515 EDT, 6 August 1975. Heavy rain, with its accompanying divergence, is in the northwest corner. New echoes form over the most intense region of convergence on the western edge of the grid.
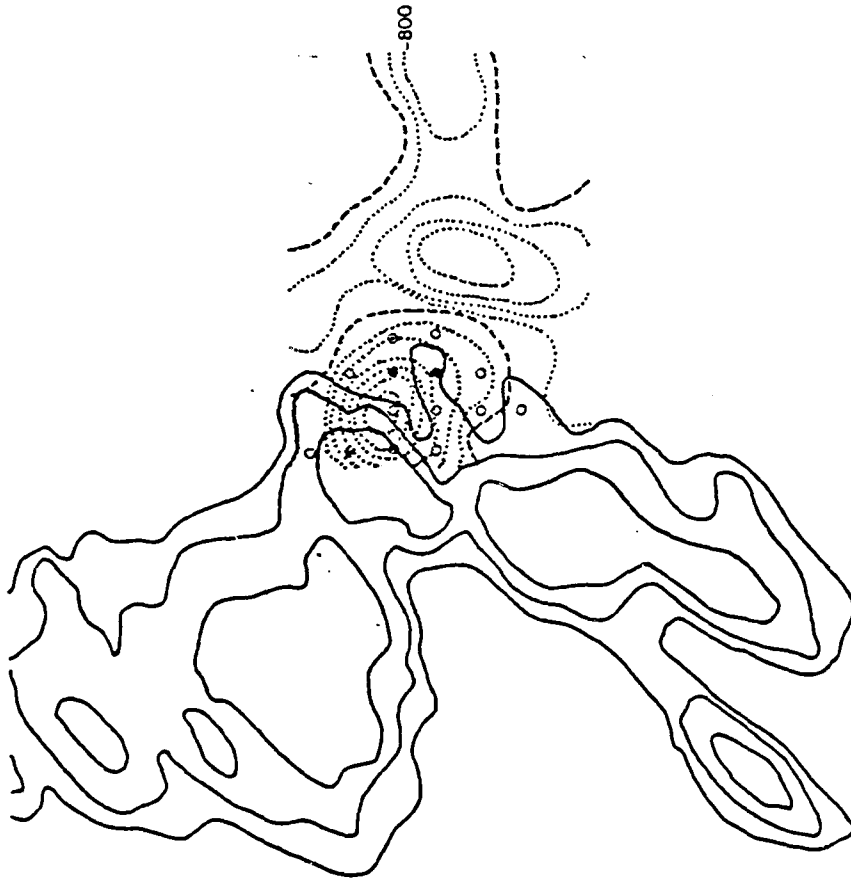
1545 EDT 6 Aug. 1975 Peak Downflux

Figure 4. Interior radar fields at 1545 EDT, 6 August 1975. The time of peak mass is diagrams is rich and strong downdrafts from the newly merged cell outside the radar in edge of ... Strong downdraft persists over the center of the network.

1600 EDT 6 Aug. 1975

Figure 39. *Interior network fields at 1600 EDT, 6 August 1975. The storm remains outside the network edge, with rainfall and divergence there; strong convergence caused by the outflow remains over the south-central grid. Although the divergence is strong, so is the convergence, so that the area-averaged divergence remains close to zero (see Figure 54).*
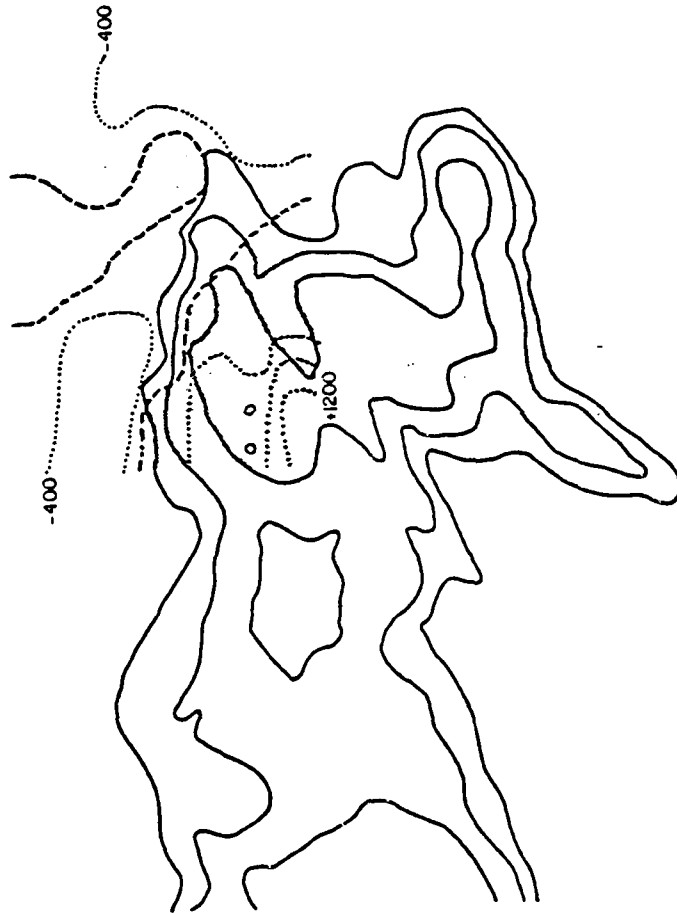
1645 EDT: 6 Aug. 1975

Figure 61. *Interior network fields at 1645 EDT, 6 August 1975. The echo has spread over the previously persistent region of convergence in the south-central part of the grid, but the rainfall is slackening off, and main divergence region is probably south of the grid.*
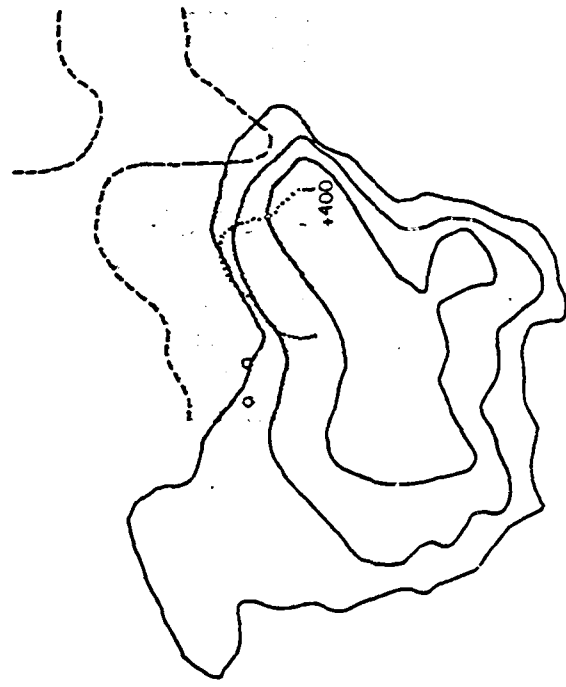
1715 EDT 6 Aug. 1975

Figure 62. Interior network fields at 1715 EDT, 6 August 1975. The storm continues to dissipate outside the southern edge of the network.
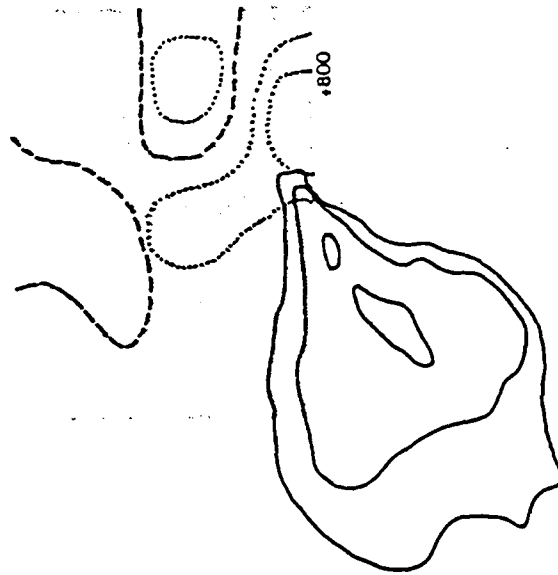
1745 EDT 6 Aug. 1975

Figure 63. Interior network fields at 1745 EDT, 6 August 1975. The echo continues to dissipate south of the network; the divergence region on the edge causes the peak network area-averaged divergence to occur at this time, with no competing convergence to offset it.
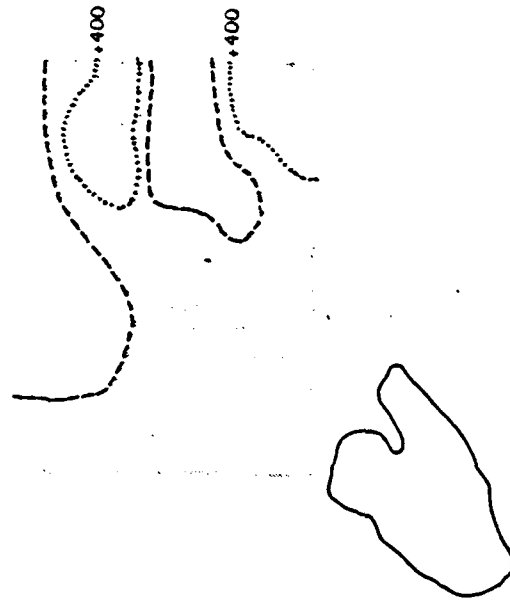
1800 EDT 6 Aug. 1975 No Rain

Figure 64. Interior network fields at 1800 EDT, 6 August 1975. The storm has dissipated outside the network.

The previous case studies illustrate in some detail:

a) The 2-dimensional structure of the divergence fields which makeup the network area-averaged divergence profiles, and which were examined statistically in Chapter 3.

b) The crucial importance of the feedback mechanism on the cumulus-cell scale in the interaction between rain-driven downdrafts and consequent convergent regions.

c) The relationship between divergent regions, convergent regions and rainfall.

The pattern of strong convergence in the network due to outflow from another storm, followed by the initiation of a new cell over, or the propagation of a storm into, the network, is the most common sequence found.

These case studies are examples of the complicated feedback relationship between convective cells and their updrafts and downdrafts. Once initiated, the lifetime of convective activity locally can be extended to a considerable period of time with the help of convergence in the lower levels caused by downdraft outflow.

For all of the cases examined, the outflow from storms is the source of almost all intense convergence seen at the surface. The probability of a storm growing to maturity directly over the center of the network is small, and a storm growing over the edge of the grid would probably not be as easily detected in the surface divergence fields. However, the case study of 20 August shows an echo forming over the only region of significant convergence in the northeastern part of the net- work, the convergent region preceding the echo by 15 minutes.

The initiation stages of storms are difficult to isolate for two major reasons.

1) The thermals which initiate the growth of the storms occur on an areal scale much smaller than the spacing between the anemometers and hence may be difficult to detect.

2) The values of convergence associated with such initiation
    processes would likely be relatively low in magnitude, and
    as such, may be indistinguishable from convergences caused
    by eddies in the wind field related to the presence of
    cumulus aloft which do not produce rain or radar echo returns.

Without knowledge of the state of the visible cloud cover, it is

extremely difficult to specifically relate surface convergence to the

initial stages of storm growth. However, by considering the mean con-

vective transports throughout the months of July and August, great

insight can be obtained into the entire cycle of diurnal convective

activity over the Florida peninsula. This will be done in the follow-

ing chapter.

CHAPTER 5

THE DIURNAL EVOLUTION OF CONVECTON

A. THE FREQUENCY DISTRIBUTIONS

The statistical relationship between the positions of radar echoes and the profiles in the area-averaged divergence fields, and between those fields and intensity of rainfall was considered in Chapter 3. This information, together with individual examination of over a hundred storms in 1973 and 1975 (of which the case studies in Chapter 4 are specific examples), leaves no doubt as to the importance of the outflow-convergence feedback mechanism in the diurnal evolution of deep convection. In this chapter, the statistical description of that evolution and its decay is presented.

The data available in 1975 allowed calculation of area-averaged divergence and interior convective mass transports for each day of July and August for that year. The calculations were made from 1000 EDT until 2000 EDT on each day. Fifteen minute total network recorded rainfall was also available for these two months.

The resulting frequency diagrams for the occurrence of various magnitudes of convergence and divergence are contained in Figures 65 and 66. Figure 65 also displays the frequency of occurrence, between 1000 EDT and 2000 EDT, of the fifteen minute total network rainfall rates which were; (a) greater than 0.1 inch, (b) greater than 1.0 inch and (c) greater than 2.0 inches. The center graph in Figure 65 is the mean network scale area-averaged divergence for the period July-August 1975, taken over the entire interpolation grid. Figure 66 contains graphs of
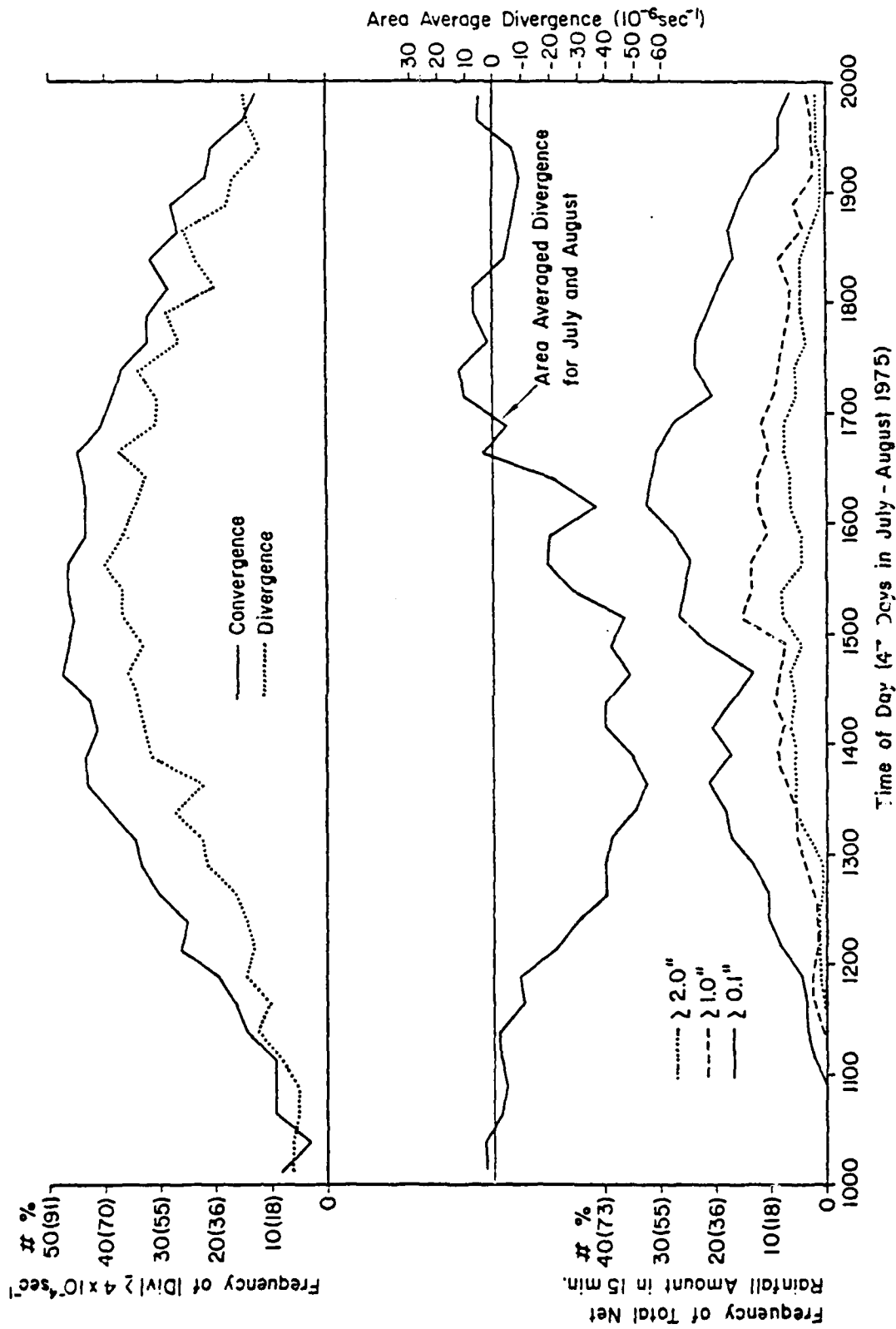
Figure 65. Frequencies of occurrence of convergences and divergences stronger than ± 400 x 10⁻⁶ sec⁻¹; the network area-averaged divergence and the frequencies of occurrence of rainfall rates ≥ 0.1", ≥ 1.0", and ≥ 2.0" in 1975.
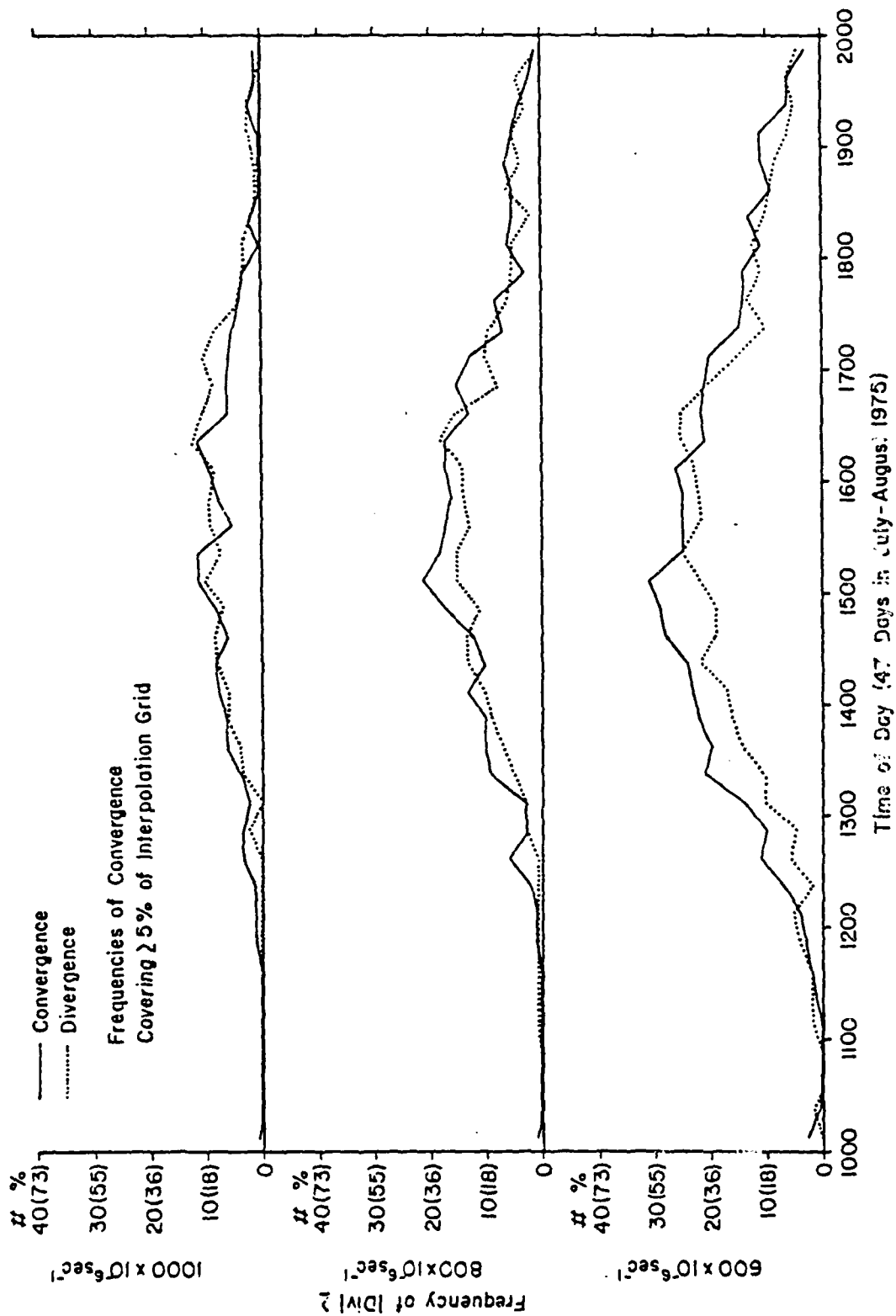
Figure 66. Frequencies of occurrence of convergences and divergences stronger than ± 600 x 10⁻⁶ sec⁻¹, ± 800 x 10⁻⁶ sec⁻¹ and ± 10⁻³ sec⁻¹, 1975.

similar frequency distributions for the occurrence of divergences and convergences whose magnitude exceeded $\pm$ |600| x 10^{-6} sec^{-1}.

We see from Figure 65, that there is a maximum of frequency of rainfall rates $\geq$ 0.01 inch between 1600 and 1615 EDT, while frequency distribution of the heavier rainfall rates varies little from around 1500 EDT until around 1700 EDT. The mean network scale area-averaged divergence for July and August is most convergent (negatively divergent) around 1330-1345 EDT, and becomes nearly zero around 1700 EDT. The magnitude of the peak convergence is -56 x 10^{-6} sec^{-1}. This peak in convergence occurs some 90 minutes before the peak in the $\geq$ 1.0 inch rainfall maximum frequency at 1500-1515 EDT, and a full two and one half hours before the peak in the $\geq$ 0.1 inch maximum frequency. As will be seen later, the peak convergence in the mean area-averaged divergence profile is also in phase with the maximum net convective transports.

Considering the convergence-divergence frequency diagrams of Figures 65 and 66, it is seen that the frequency distributions are smooth in form and show an obvious pattern of diurnal growth and decay. The frequency diagrams for convergences with values $\leq$ -400 x 10^{-6} sec^{-1} and divergences $\geq$ +400 x 10^{-6} sec^{-1} (i.e., the convergences and divergences which go to make up the calculations of the "convective" trans-ports) are virtually symmetric in form about 1500 EDT. The maximum frequency of the divergences and convergences interior to the network of all magnitudes occur later in the day than does the peak convergence in the network scale area-averaged divergence profile. There is a peak in the frequency of convergence (negative divergences) which have magnitudes $\leq$ -400 x 10^{-6} sec^{-1} around 1430 EDT, with the peak in the same category of divergence ($\geq$ +400 x 10^{-6} sec^{-1}) occurring about an hour later at 1530 EDT.

If Figures 65 and 66 are considered simultaneously it is seen that the frequency distributions of the values of convergence and divergence $\geq |+600| \times 10^{-6} \text{ sec}^{-1}$ are skewed towards the later afternoon than are the frequency distributions for convergences and divergences of magnitude $\geq |+400| \times 10^{-6} \text{ sec}^{-1}$. For example, the convergence (negative divergences) of value $\leq -400 \times 10^{-6} \text{ sec}^{-1}$ reach half their maximum frequency by 1200 EDT, while convergences of value $\leq -600 \times 10^{-6} \text{ sec}^{-1}$ reach half of their maximum frequency by 1315 EDT, and the convergences of value $\leq -800 \times 10^{-6} \text{ sec}^{-1}$ and $\leq -1000 \times 10^{-6} \text{ sec}^{-1}$ do not attain half of their maximum frequencies until around 1400 EDT. The divergence (positive divergence) frequencies allow the same pattern, but lag the convergence frequencies by about an hour.

Figures 65 and 66 show, therefore, that;

1) The mean network scale divergence has a maximum convergence (negative divergence) at 1330 EDT, which precedes the maximum frequency of heavy rainfall by 90 minutes, and the maximum frequency of total rainfall by 2.5 hours.

2) The convective activity, as represented by the diurnal profile of frequency of occurrence of divergences $> +400 \times 10^{-6} \text{ sec}^{-1}$ and convergences $< -400 \times 10^{-6} \text{ sec}^{-1}$, goes through a smooth diurnal cycle, with the peak in frequency, and hence convective activity, occurring around 1500 EDT.

3) The intensity of convective activity increases gradually with time of day, the more intense values of convergence and divergence having their maximum frequencies later in the day than the weaker values of divergence and convergence.

B. THE CONVECTIVE MASS TRANSPORTS AND THE NETWORK SCALE DIVERGENCE

Figure 67 shows the average convective mass transports in comparison with the average 15-minute rainfall, and the mean network scale area-averaged divergence for the rainy days during the months of July and August 1975. Plotted with the mean area-averaged divergence is a graph of the net convective transports (i.e., the difference between up
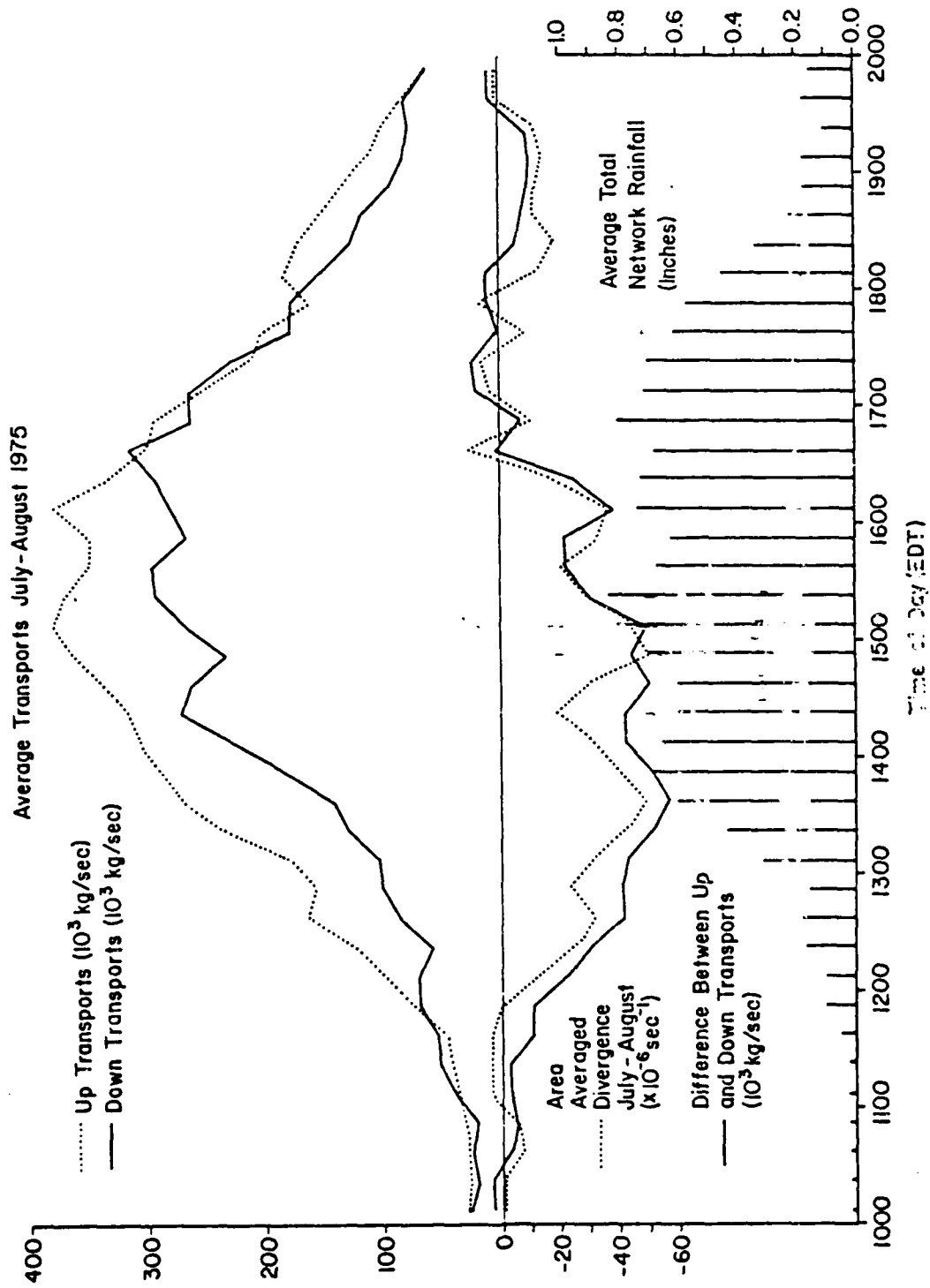
Figure 67. The upward and downward convective mass transports as compared to rainfall rates and area-averaged divergence.

and down convective transports), in units of 10^3 kg/sec. The relation-
ship between the area-averaged divergence on the scale of the interpola-
tion grid (718 km^2) and the net convective transports is clear. On
this scale, the area-averaged divergence, and hence the inflow taken
about the interpolation grid, is directly related to the difference
between the amount of mass being transported upwards through the level
of the anemometers and the amount of mass being brought down through
that level by smaller scale convective activity.

The convective transports between 1000 EDT and 1200 EDT, are
essentially in balance, and small in magnitude (Figure 67). At 1200
EDT, there is a dramatic increase in the upward transports, which
continues until a peak in these upward transports is reached around
1500-1615. After that, the amount of mass transported upwards through
the level of the anemometers declines until 1945-2000, at which time
their magnitude has returned to the same level as it was at noon.
Comparison with the center graph of Figure 65 shows the maximum upward
transport lagging the network peak convergence (negative divergence)
by 90 minutes.

The downward mass transports follow a similar pattern as the
upward mass transport but, like their respective frequency distributions,
lag the upward mass transports by 45 minutes to an hour, until around
1700, when the excess of upward transport drops off rapidly.

Figure 67 shows the onset of strong convective activity around
noon, followed by the production of strong downdrafts 45 minutes to an
hour later. The sharpest rate of increase in rainfall during the entire
day occurs between 1300 and 1400, as a result of the initiation of the
strong upward transports during the previous hour. This sharp increase

in rainfall is followed by the greatest <u>rate of increase</u> in downward transports during the entire day, between 1330 and 1430. The rainfall rate and the magnitudes of upward and downward transports remain more or less steady between 1430 and 1615, at which time the upward transports rapidly diminish, followed by the downward transports and the rainfall.

C. THE CONVECTIVE MASS TRANSPORTS AND THE PENINSULAR SCALE DIVERGENCE

From Figure 67, it is seen that there is a definite relationship between the convective transports and the network scale area-averaged divergence. On the scale of the network, the action-reaction process between the smaller convective cell scale and the network scale is almost instantaneous.

The network scale divergence may be compared to the Florida peninsular scale divergence as calculated by Frank (1967) and Burpee (1979). Frank and Burpee both found a minimum in the surface peninsular scale divergence of about -30×10^{-6} sec^{-1} around 1400 EDT, for the months of July and August.

Figure 68 shows the relationship between the peninsular scale divergence, as calculated by Frank, and the network scale divergence calculated from the 1975 FACE surface wind data. <u>The peninsular scale and network scale divergences are of the same order of magnitude, and both reach their most convergent (negative) values at approximately the same time.</u> The network scale divergence does approach zero more rapidly than the peninsular scale divergence does, the latter remaining convergent (negative) until after 2000 EDT.

The upward convective transports in Figure 67 are considered to be made up of four components;
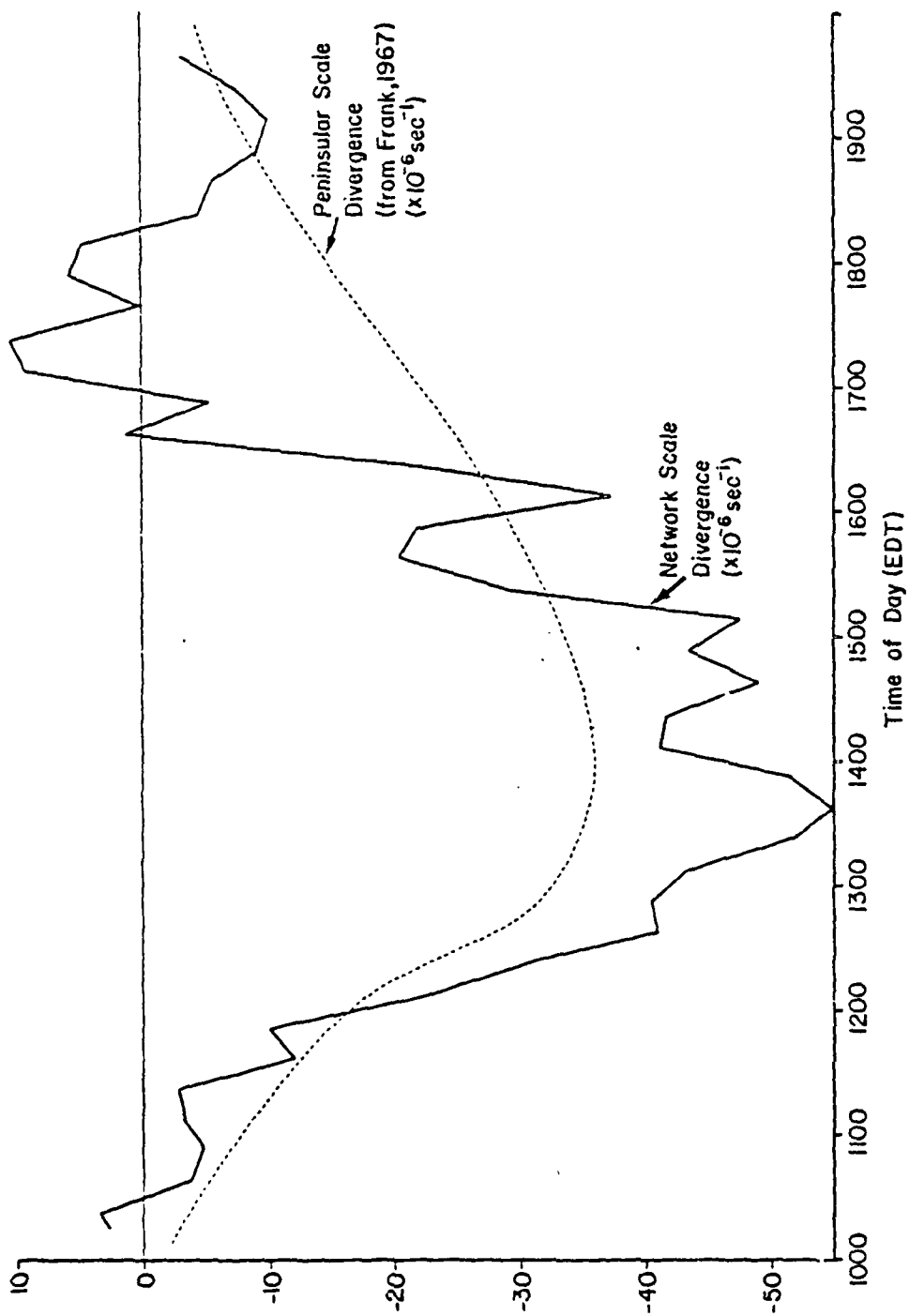
Figure 68. The Florida peninsula scale convergence as calculated by Frank (1967) compared to the network area-averaged divergence, 1975.

1) Upward transports due to accelerations produced by the peninsular scale convergence.

2) Convergence produced by the presence of thermals, which, in aggregate, produce regions of convergence large enough to be sensed by the anemometer network.

3) Upward transports caused by release of latent heat in cumuli, the resulting buoyancy being transmitted to and sensed at the surface.

4) Convergence, and the resulting upward transport, produced by intrusion of downdrafts into the surface layer, which lift surface air through the level of the anemometers.

The behavior of the convective transports in Figure 67 can be used to illustrate a possible sequence of physical processes. Such a sequence may start with the fact that, as is seen in Figure 67, an excess in upward convective transports over downward transports is initiated sometime around 1200 EDT, followed by their associated downdrafts sometime later. These downdrafts can be assumed to produce convergence at the surface which, together with the other three components listed above, produces new upward convective transports. The resulting upward mass transport is larger than the initial upward transport and is likely to produce more rainfall, and stronger downdrafts. These stronger down-drafts, acting together with the other three components, produce even stronger convergences. This process continues until around 1615 EDT, when the upward transports start to decrease in magnitude.

One explanation for the relatively sudden decay in the production of strong upward transports, downward transports and heavy rainfall, and for the breakdown in the hypothesized feedback mechanism in the later afternoon is that the land-sea temperature difference has decreased to the point where the peninsular scale convergence can no longer contribute effectively to the convective activity. Also, the effects on the surface radiation by cirrus outflow from thunderstorms

and their cooling downdrafts would tend to increase the rate of diurnal cooling which would take place over the peninsular, compared to days when little or no cloudiness was present. In addition, as thunderstorm activity increases in the later afternoon, competition between storms for high energy surface air will increase (Garstang et al., 1980), possibly to the point where the convection can no longer be triggered as easily as it was earlier in the day.

The surface heating of the peninsula is directly related to the peninsular scale convergence, and a close relationship exists between the net convective transports and the network scale divergence (Figure 67). Figure 68 shows that the network scale divergence bears a relationship to the peninsular scale convergence. This suggests that there is a relationship between the peninsular scale convergence and the convective mass transports as calculated over the 1975 network.

The peninsular scale surface convergence can be viewed as a vertical velocity, and its time derivative may be taken to obtain estimates of the contribution to vertical accelerations, on the network scale, by the peninsular scale convergence.

From the observations of Frank (1967), the hourly change in (or accelerations due to) the peninsular scale convergence is plotted in Figure 69, along with the ratio of the upward convective transports to the downward convective transports. In Figure 69, the maximum hourly rate of change in the peninsular scale convergence occurs between 1200 EDT and 1300 EDT, at which time the rapid increase in upward transports is initiated. The maximum value of the ratio of upward convective transports to downward convective transports occurs at roughly the same time, between 1230 EDT and 1345 EDT. The rate of change in the peninsu-
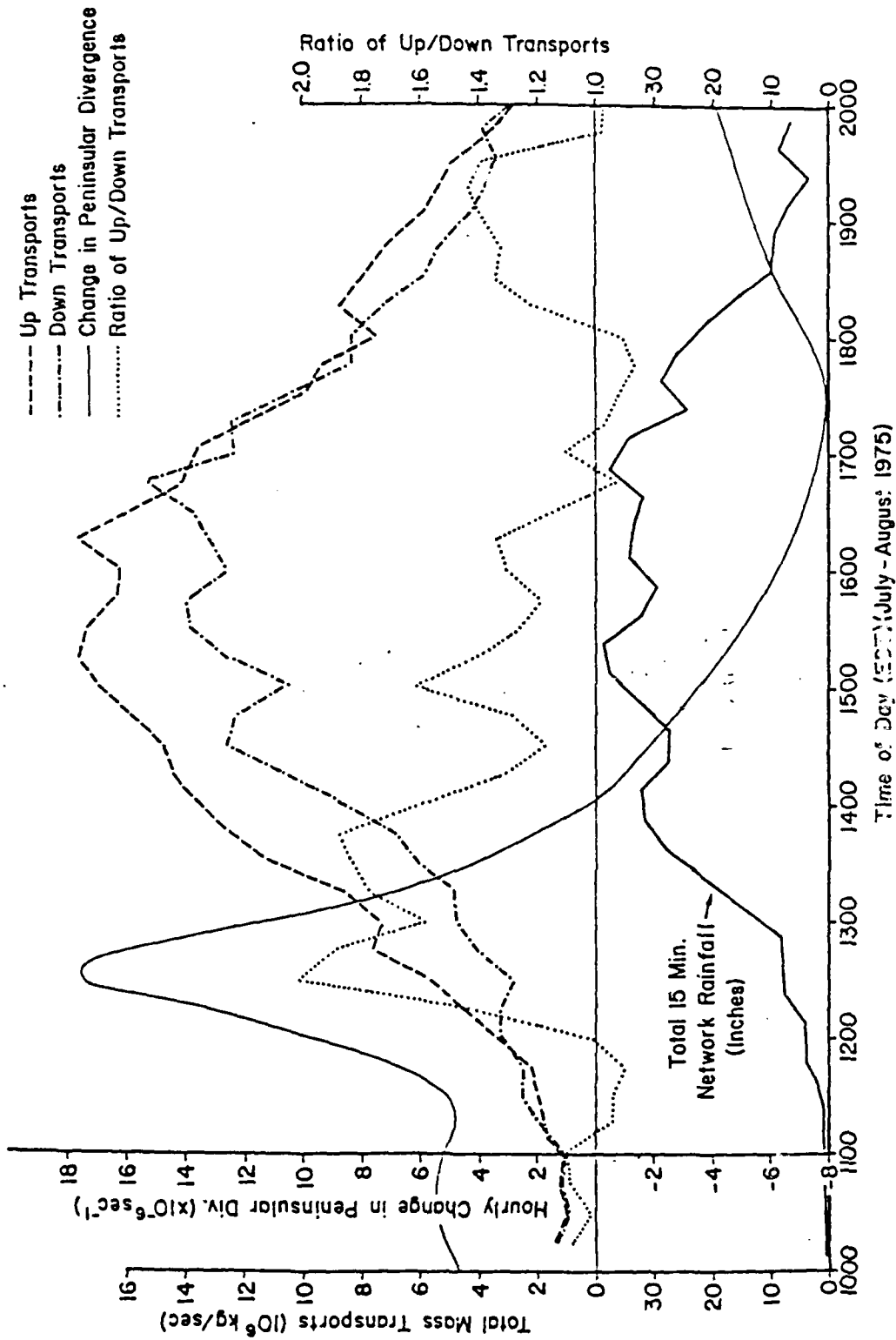
Figure 63. A comparison of upward transports, downward transports, rainfall, transport excess and the rate of change of the peninsular scale divergence.

lar scale convergence drops off rapidly after 1300 EDT, becoming zero at 1400 EDT and negative thereafter. After 1400 EDT, the accelerations due to the peninsular scale convergence are working against the convective processes, in the sense that the peninsular scale vertical velocity is decelerating, but the upward convective transports continue to increase, because of local convective release of latent heat energy, and the feedback processes discussed above. However, the excess of upward convective transports over downward convective transports decreases along with the deceleration in the peninsular scale velocity.

The following conclusions can be drawn from Figure 69.

1) The peninsular scale convergence has its largest positive rate of change at the same time that the persistent excess in upward convective mass transports over downward convective mass transports is initiated.

2) The percent excess of upward convective transports over downward convective transports is also greatest when the peninsular scale convergence has its largest positive rate of change.

3) As the rate of change of peninsular scale convergence increases, so does the percent excess of convective upward transports over downward transports.

4) As the peninsular scale convergence rate of change decreases, so does the percent difference between the upward and downward convective mass transports.

5) The peninsular scale rate of change in convergence becomes negative at 1400 EDT, but the absolute value of the upward and downward convective transports continues to increase, although their difference decreases.

6) Earlier in the day, the peninsular scale moist static energy supply must increase to supply the growing rate of convective activity which has been initiated by the larger scale forcing. By 1600 EDT, the convective activity has begun to out run the ability of the peninsular scale forcing to supply energy and starts to shut down, dying out completely by 2000 EDT.

D. THE FIELDS ON DRY DAYS

Of all the days examined during 1975, only eight were dry days. While this is an extremely small sample, it is important to compare the

diurnal distributions of upward and downward convective transports for these days with the calculations made for rainy days.

Figure 70a is a comparison between the upward and downward transport on dry and rainy days. The magnitudes of the convective transports on the dry days are much lower than on the wet days, as expected. The excess of upward transports over downward transports is also much smaller, not as persistent, is initiated later in the day, and has a maximum much later in the afternoon.

Burpee (1979) found that on days with little rainfall over the Florida peninsula, the peninsular scale convergence had a slightly stronger maximum, and the peak in the convergence occurred later in the day than it did on wet seabreeze days. However, the maximum rate of change in the average peninsular scale convergence on dry and rainy days, which occurred about an hour before 1300 EDT on both types of day, was the same.

For eight dry days for which data are available in 1975, applying Burpee's findings, we might therefore expect that the rapid accelerations in the peninsular scale convergence occurring between 1200-1300 EDT on the wet days occurs on the dry days, but does not initiate convection early enough or strong enough to start up the feedback process hypothesized here.

The application of monthly averages to a sample of eight days must be treated with caution, but nevertheless, the suggestion is made that unless the thermodynamic conditions in the late morning are appropriate to the initiation of sufficiently active convection then, and are such as to maintain the feedback process as described, then the daily procession of convective activity outlined above will not evolve.
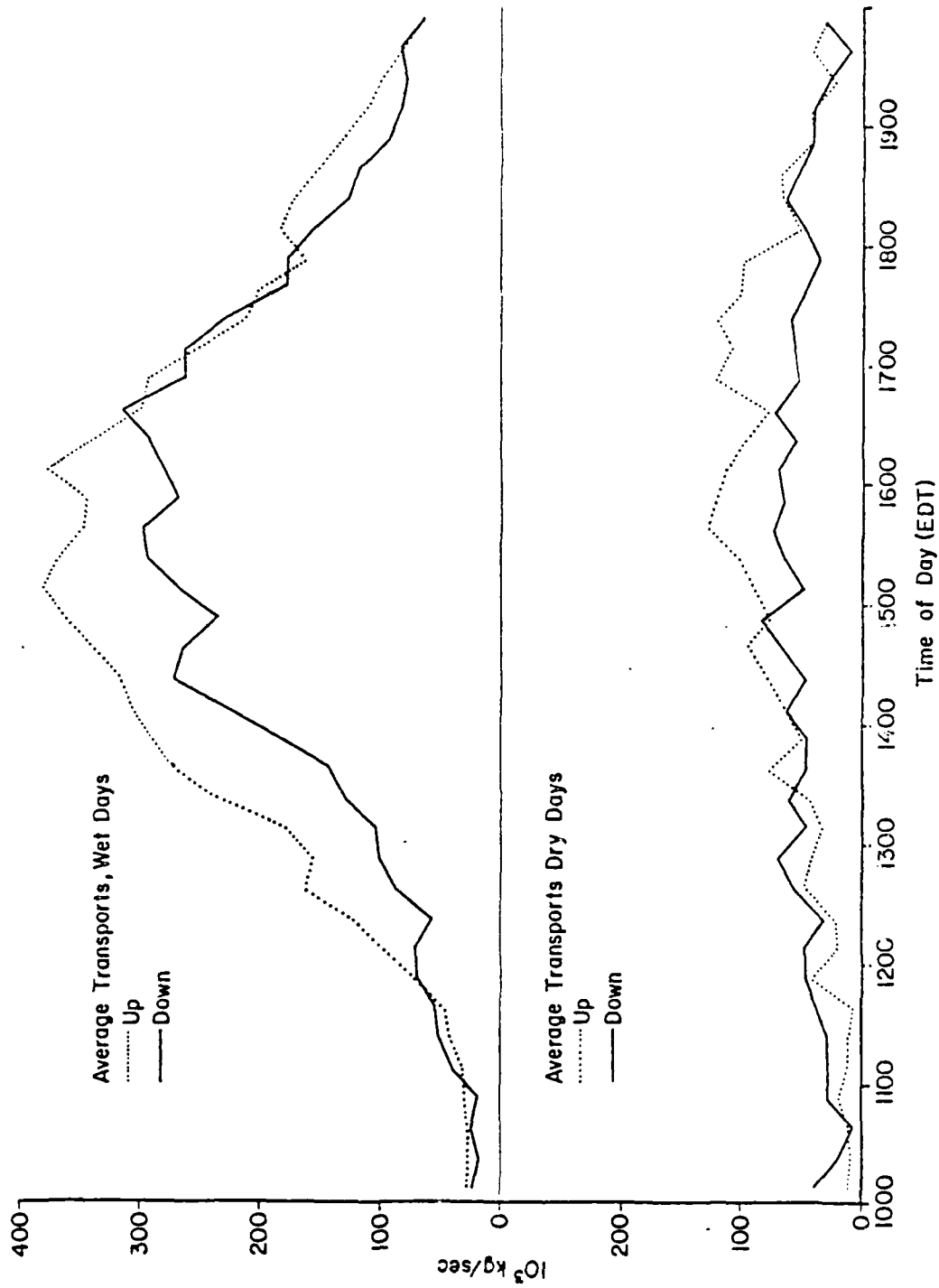
Figure 70a The convective transports on wet days and on dry days.

The thermodynamic structure of the atmosphere above the network will be considered in the following chapter.

E. THE RELATIONSHIP BETWEEN DOWNWARD CONVECTIVE TRANSPORTS AND RAINFALL

The average downward mass transport is plotted against the previous 15 minute rainfall in Figure 70b. For small amounts of rainfall, there is little downward mass flux into the surface layer. For rain rates between 0 and about 2.0 inches per hour, the relationship is essentially parabolic. For rain rates greater than about 2.0 inches per hour, the downward mass transports into the surface layer increase much more rapidly for a given increase in rain rate than is the case for the lighter rainfall rates. Heavy storms are therefore likely to modify the thermodynamics of the surface layer much more dramatically than moderately sized storms only slightly less intense in rainfall rate (Barnes and Garstang, 1981). Figure 70b also provides an empirical estimate of the amount of mass being brought into the surface layer by a given rain rate, and is of value in the attempt to parameterize cumulus convection.

F. THE RELATIONSHIP BETWEEN UP TRANSPORTS AND DOWN TRANSPORTS

As can be seen from Figure 67, for the rainy days plotted, there is a good relationship between up transports at a given time and downward transports about an hour later. We have seen that the downward transports are closely related to rainfall, so it is of interest to determine the relationship between the updrafts and the resulting downdrafts an hour later, based on the average diurnal data.

From Figure 67, it is seen that the efficiency with which convergence produces divergence one hour later varies with the time of day.
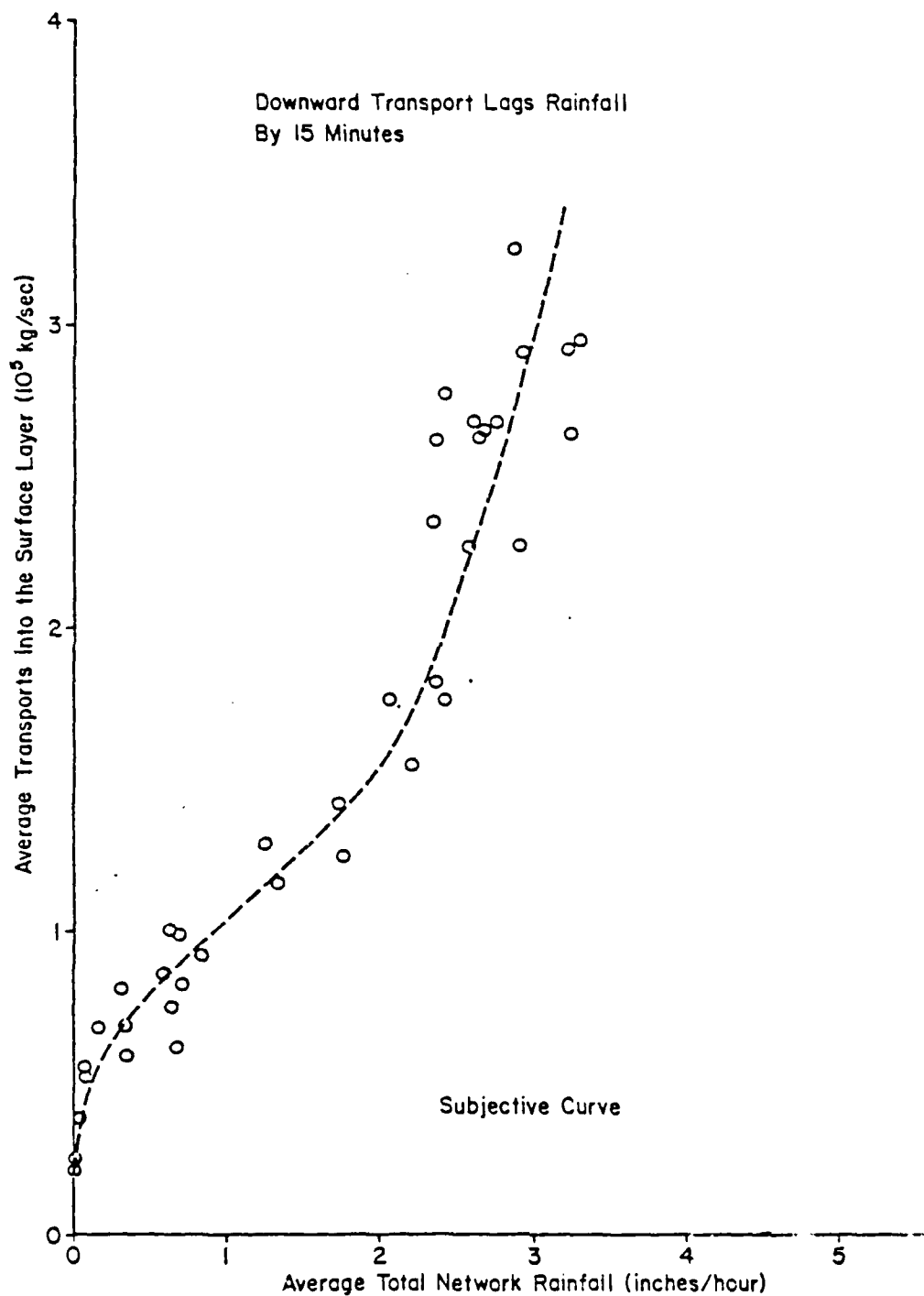
Figure 70b. Downward transports versus total network rainfall rate.

Until 1645, the magnitude of downdrafts continues to increase, possibly as part of the feedback mechanism described earlier. After 1545, the efficiency with which updrafts produce downdrafts an hour later falls off drastically, as does the rainfall rate, indicating a shutting down of convective activity.

Figures 71a and b contain the relationship between updrafts and downdrafts during the two phases, i.e., before 1645 and after 1645. In both diagrams, the downward transport one hour after a given time has been plotted against the upward transport at that time. The two diagrams show the growing and mature stages of diurnal convective activity over the network (pre-1545) and the decaying stage (post-1545).

In the early stages of convective activity, the smaller up transports produce downward transports an hour later which can equal or even slightly exceed the upward transports an hour earlier (see Figure 71a). As the convective activity increases, larger and larger downward transports are produced in response to the upward transport. By the time that the upward transports reach a magnitude of about 1.5 x 10^5 kg/sec, they are producing, one hour later, downward transports of equal magnitude. After that, the upward transports continue to produce downward transports an hour later of around 84% of their (the upward transports) value. On the average, during the growing and mature stages of the diurnal convective activity, the upward transports produce downward transports an hour later of around 90% of their value.

Considering Figure 71b, which represents the post-1545 or decaying stage of the diurnal convective activity over the network, it is seen that the upward transports produce downward transports an hour later which are only 53% of the magnitude of the upward transports an hour
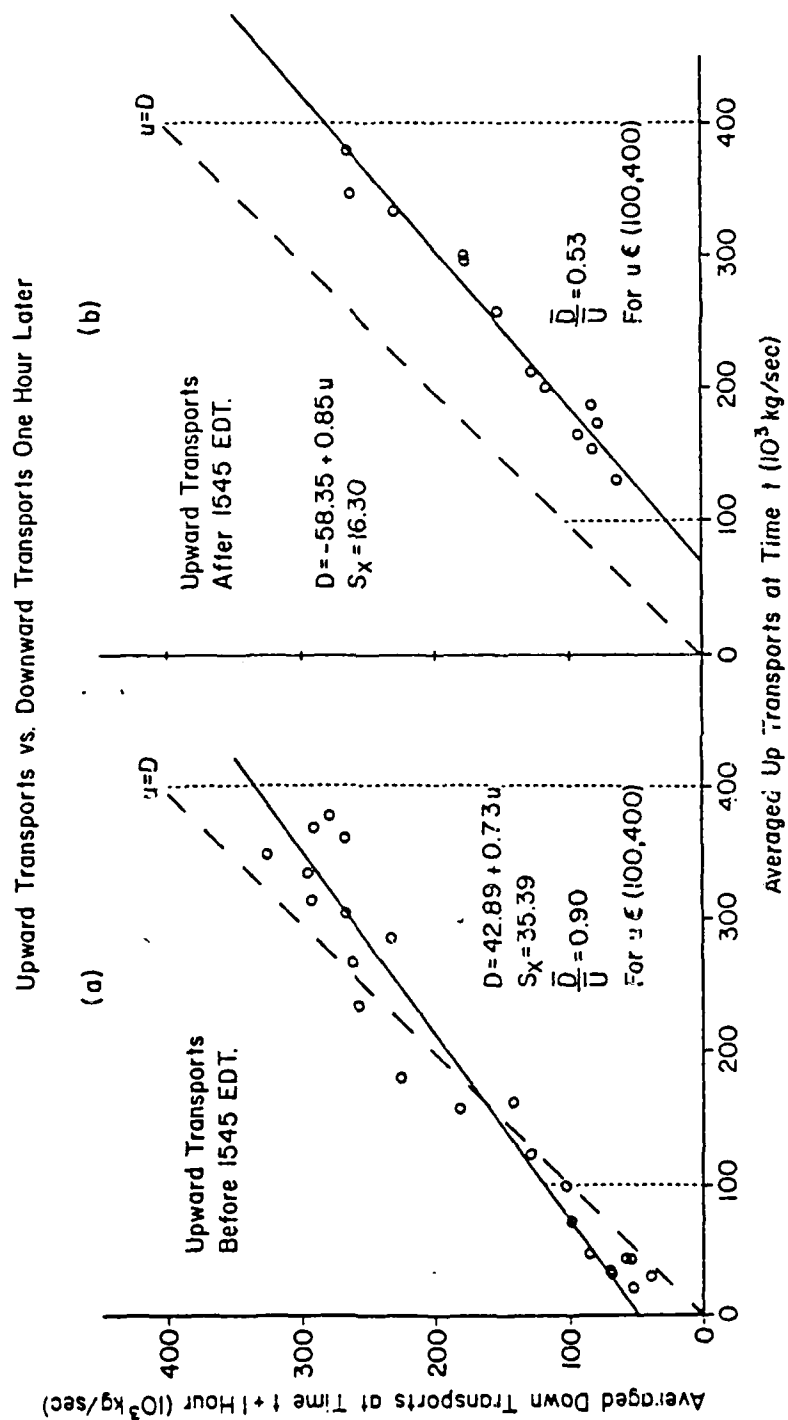
Figure 71. a) Upward transports versus downward transports one hour later (pre-1545 EDT).
b) Upward transports versus downward transports one hour later (post-1545 EDT).

earlier. This stage coincides with the rapid decay in rainfall rates.

The rapid decay in the averaged diurnal convective activity starts about an hour and three quarters after the peak peninsular scale convergence, and coincides with the minimum in the rate of change of the peninsular scale convergence.

Figures 72a and b formalize what is obvious from Figures 67 and 69, that is, that before 1645 EDT, the upward mass transports exceed the downward mass transports whereas after 1645, the upward transports and downward transports are essentially equal in magnitude.

The rainfall rate in relation to upward transports one hour earlier follows two regimes. The upward transports which occur before 1315 were compared to the amount of rainfall which fell in the network one hour later and the resulting relationship is shown in Figure 73a. Compared to that relationship, the upward transports after 1545 and their associated rainfall rates one hour later follows a different pattern, as shown in the same figure. In the pre-1315 regime, a given rainfall rate is associated with roughly half as great an amount of upward transport as is required in the post-1545 EDT regime, to produce the same amount of rainfall.

The simultaneous rainfall rates and upward transports are plotted in Figure 73b. There is a linear relationship between the two, reflecting the fact that for the most part, the strong convergence in the network is a result of outflow from rainfall-driven downdrafts.

Simoultaneous Upward and Downward Transports
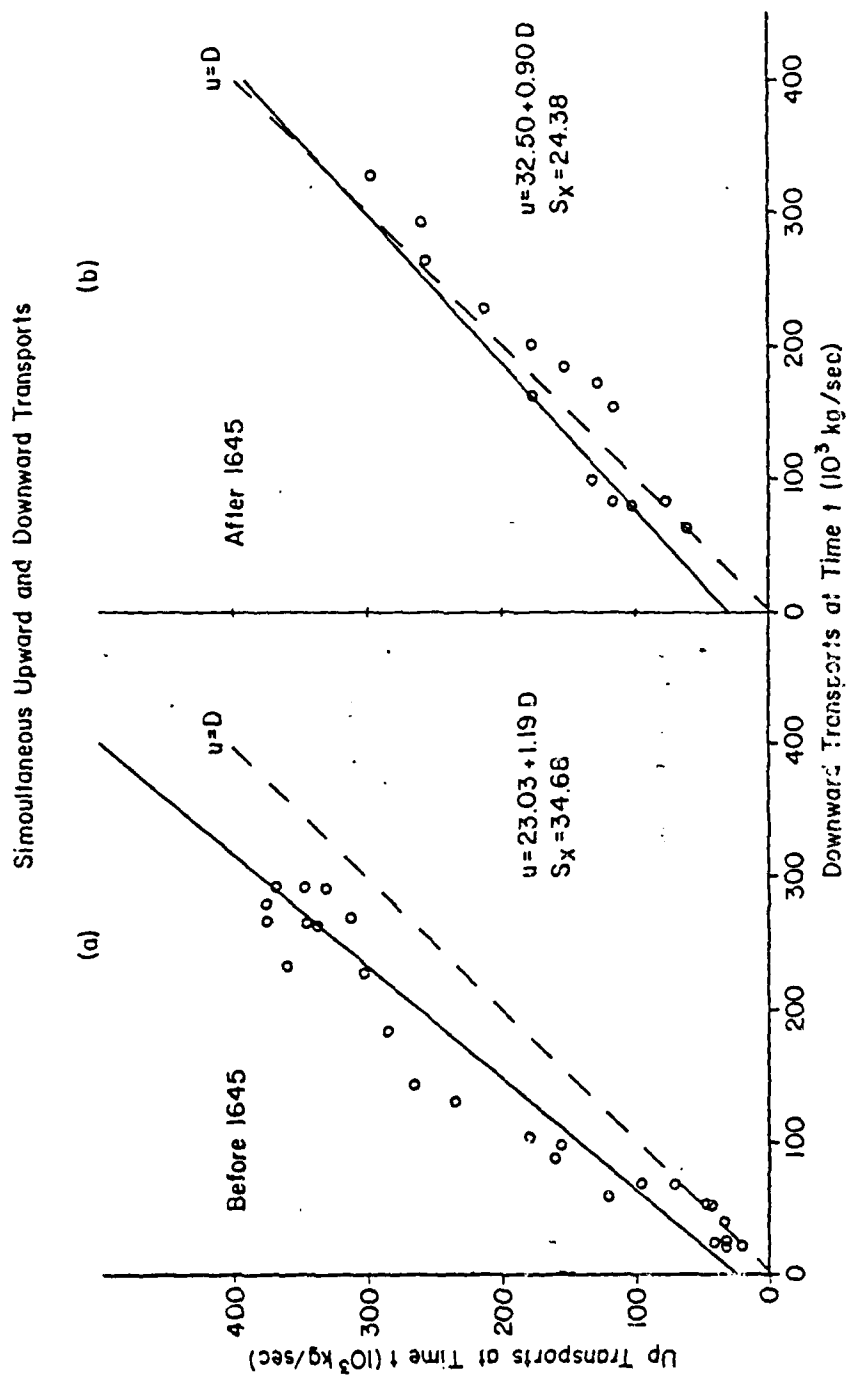
Figure 72. a) *Simultaneous upward and downward transports before 1645 EDT.*
b) *Simultaneous upward and downward transports after 1645 EDT.*
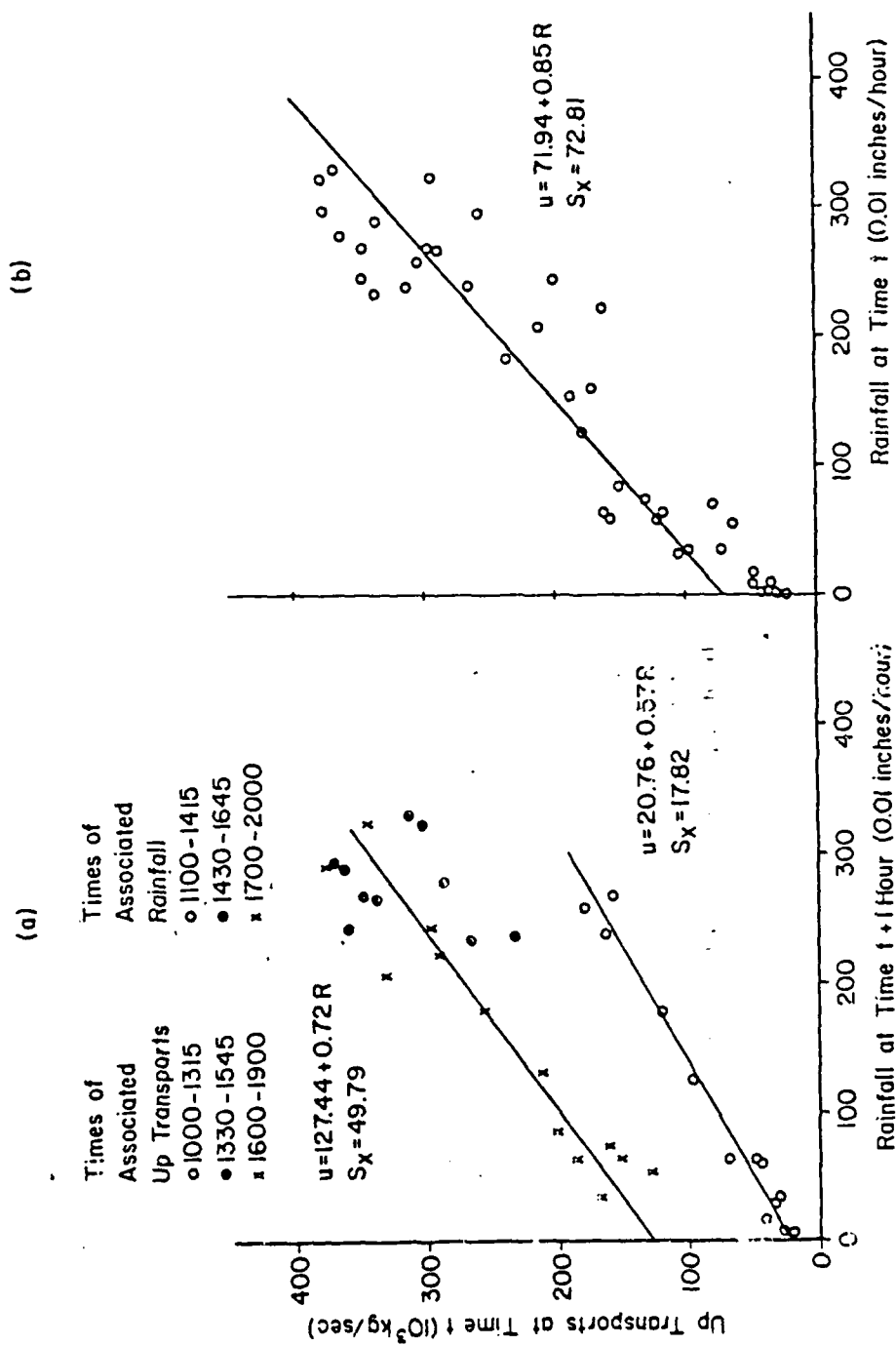
Figure 73. a) Upward transports versus rainfall one hour later.
b) Upward transports versus rainfall rate at time t.

CHAPTER 6

THE VERTICAL THERMODYNAMIC PROFILES AND
STORM EFFICIENCIES

In this chapter the effect of storms on the profiles of
thermodynamic variables and the efficiency with which the storms
process water vapor are investigated.

A. THE THERMODYNAMIC PROFILES

During FACE 1975, three soundings were taken each day, one at
1400 Z (1000 EDT), one at 1700 Z (1300 EDT) and one at 2000 Z (1600
EDT). The storms themselves do not occur over the network on such a
regular basis, so the problem exists of assessing the effects of
storms which occurred at various times of day using data samples
taken at fixed times during the diurnal cycle and the relating fixed
time soundings to storms in different stages of their life cycle.

It was therefore decided to form a composite Florida storm,
which would then represent a typical storm cycle over south Florida.
In the composition, diurnal effects are removed, and the processes
which are solely a result of the presence of convective activity are
isolated, and placed in a time frame relative to the storms life
cycle.

A total of 87 soundings were used in the composite. Soundings
which were launched earlier than four hours before the time of maxi-
mum total network rainfall were not used, nor were those soundings which
were launched later than four hours after the time of the maximum
total network rainfall rate.

As has been noted previously, there were eight days when no rain fell into the network. These days are defined as "dry" days, whereas days which did have some rainfall inside the network are defined as "wet" days.

For the dry days, all the soundings taken at 1400 Z were formed into an average 1400 Z "dry" day sounding. Similarly, all the 1700 Z and 2000 Z dry day soundings were formed into average dry day soundings for 1700 Z and 2000 Z.

The "wet" day soundings were then separated according to their time of launch, that is, into the 1400 Z group, the 1700 Z group, or the 2000 Z group. Then the average "dry" day sounding variable at each level for each time of launch was subtracted from the appropriate "wet" day variable.

In this way, three sets of soundings were made available, (i) the perturbation 1400 Z soundings (1400 Z wet day soundings minus 1400 Z dry day average sounding), (ii) the perturbation 1700 Z soundings (1700 Z wet day soundings minus 1700 Z dry day average sounding), and (iii) the perturbation 2000 Z soundings (2000 Z wet day soundings minus 2000 Z dry day average soundings). Next, on each wet day, the time of the maximum total network rainfall rate was found, and the time before or after the maximum rainfall that each rawinsonde on that day was launched was noted.

Each perturbation sounding on a given wet day was then placed into one of eight time categories. The time category into which a perturbation sounding was placed was determined by the time before or after the maximum total network rainfall rate that the launch occurred. Categories consisted of one hour intervals ranging from four hours before

the time of the maximum total network rainfall rate, to four hours after

that time. In this way, using a total of 47 storms, a 1-hourly composite

about the maximum total network rainfall rate was obtained, in mixing

ratio and temperature.

Finally, the composited perturbation soundings were averaged

together, appropriately weighted according to the number of soundings

used in each category, to form a "total" composite of 87 soundings.

Of 21 of the shower days, the 1400 Z (1000 EDT) soundings were

launched more than four hours before the time of occurrence of the

maximum network rainfall rate and were not used in the composite.

Because the maximum rainfall rate generally occurs between 1500 EDT and

1600 EDT, there were only 4 soundings available for compositing in the

3rd and 4th hours after the maximum rainfall rate, and the values obtained

there must be treated with caution. Figures 74 and 75 contain the results

of the compositing in terms of the departures in temperature and mixing

ratio of wet days from dry days.

The temperature composite (Figure 74) shows the wet days to be

slightly cooler in the lower levels (between the surface and approxi-

mately 600 mb) than the no-rain days. Four hours before the composite

maximum rainfall rate, the temperature in the subcloud layer (cloud

base is assumed to be around 1000 m) is slightly warmer than on dry

days, cooler up to around 600 mb, and then warmer aloft. As the time

of maximum rainfall rate is approached, the cooling in the layers

between the surface and 600 mb is greater, with the maximum cooling

occurring in the hour after the maximum rainfall rate, probably in

association with the greatest downdrafts (Augstein et al., 1980). The

average cooling by the storms is on the order of 4-5°C at the surface,
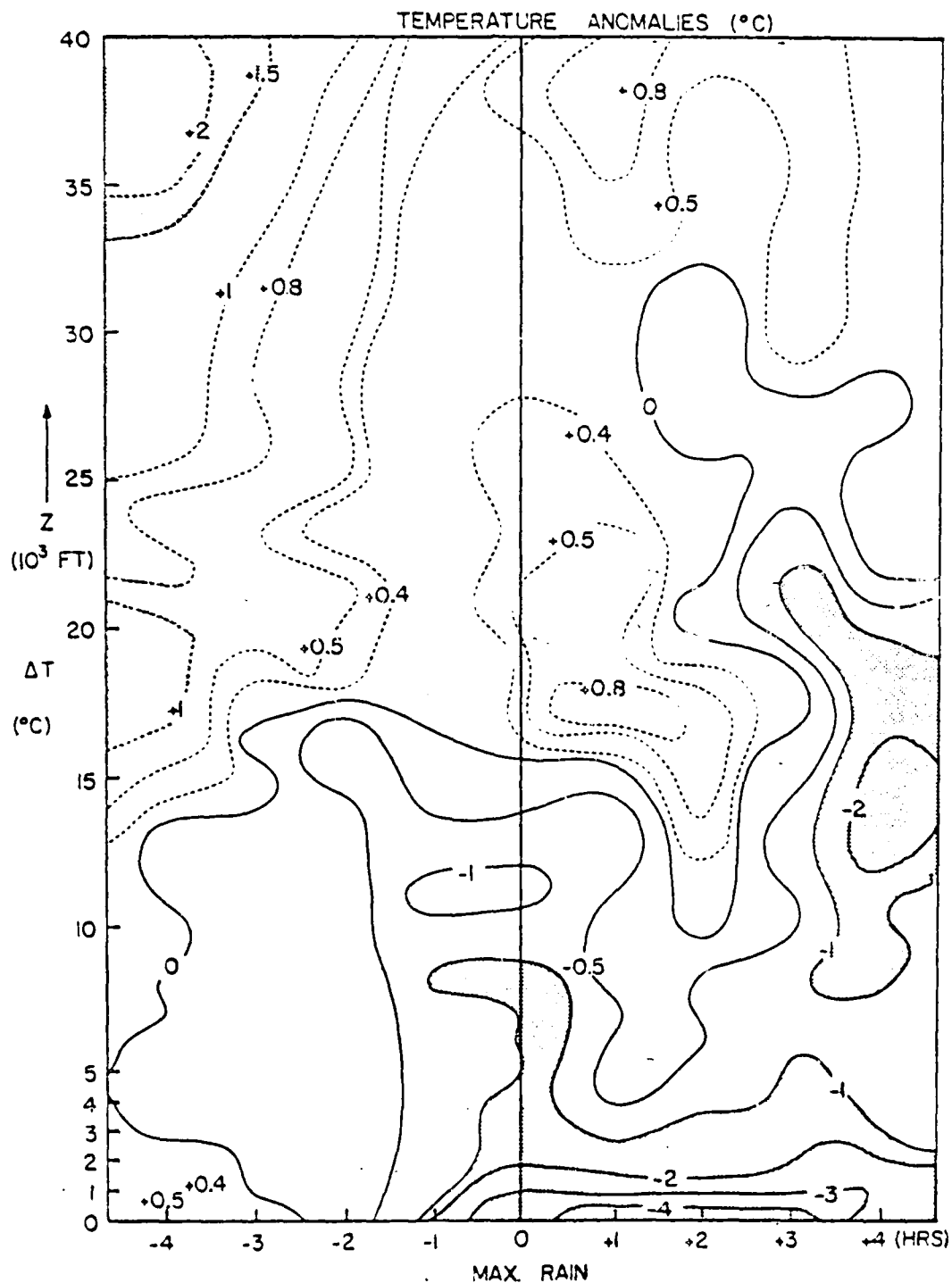
Figure 74. Composite temperature departures due to passage of a storm. Shaded areas are those regions where the departures are greater than one standard deviation about the average value of the unused 1400 Z wet day soundings.
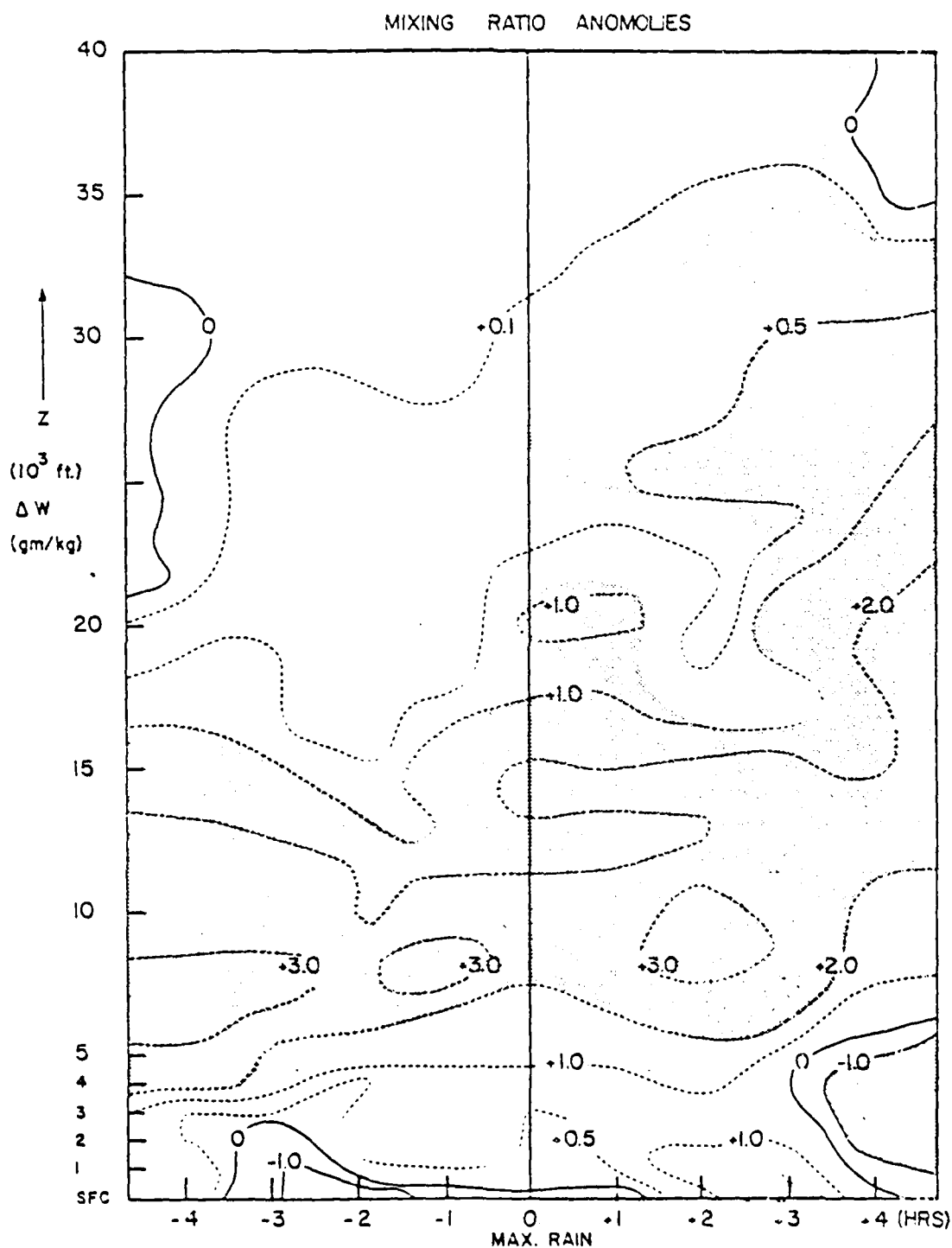
Figure 86. Composite mixing ratio departures due to passage of a storm. Shaded areas are those regions where the departures are greater than one standard deviation about the average value of the unused 1400 Z wet day soundings.

that value is maintained through the third hour after the maximum rain-
fall rate (Barnes et al., 1980; Fitzjarrald et al., 1980a; Emmitt, 1973).

The relatively warm layer between 600 mb and 500 mb (15,000 ft-
20,000 ft) during the hour of maximum rainfall and the following hour
is probably a result of release of latent heat at these levels, occurring
in conjunction with the strong cooling in the lower levels, especially
at the surface. The warming aloft and cooling in the lower levels
reflect the overall overturning effect of these storms.

The mixing ratio composite (Figure 75) shows the wet days to be
much more moist at all levels up to 500 mb (15,000 ft) than the dry
days. Drying occurs in the surface and subcloud layers during the second
and third hours before maximum rainfall. The drying in this surface
layer continues until the hour after the maximum rainfall, after which
there is an increase in moisture at the surface.

The maximum moisture excess of the wet days over dry days occurs
in the layer between 850-750 mb, the excess being about 3 gm/kg in
magnitude. The effect of the storm circulation as it goes through the
network is to raise the vertical location of this excess in moisture to
the 750-650 mb layer by the second and third hours after peak rainfall.
A secondary effect is to redistribute moisture in the vertical to the
layers above 500 mb.

Combining Figures 74 and 75 gives a composite of the moist static
energy departures of wet days from dry days (Figure 76), and outlines the
procession from pre-storm state to post-storm state. We see a loss of
energy in the subcloud layer, an increase in energy in the 750-350 mb
layer, and a relative loss in the layers above 600 mb. This again
reflects the overturning effect of these storms, the moist static energy
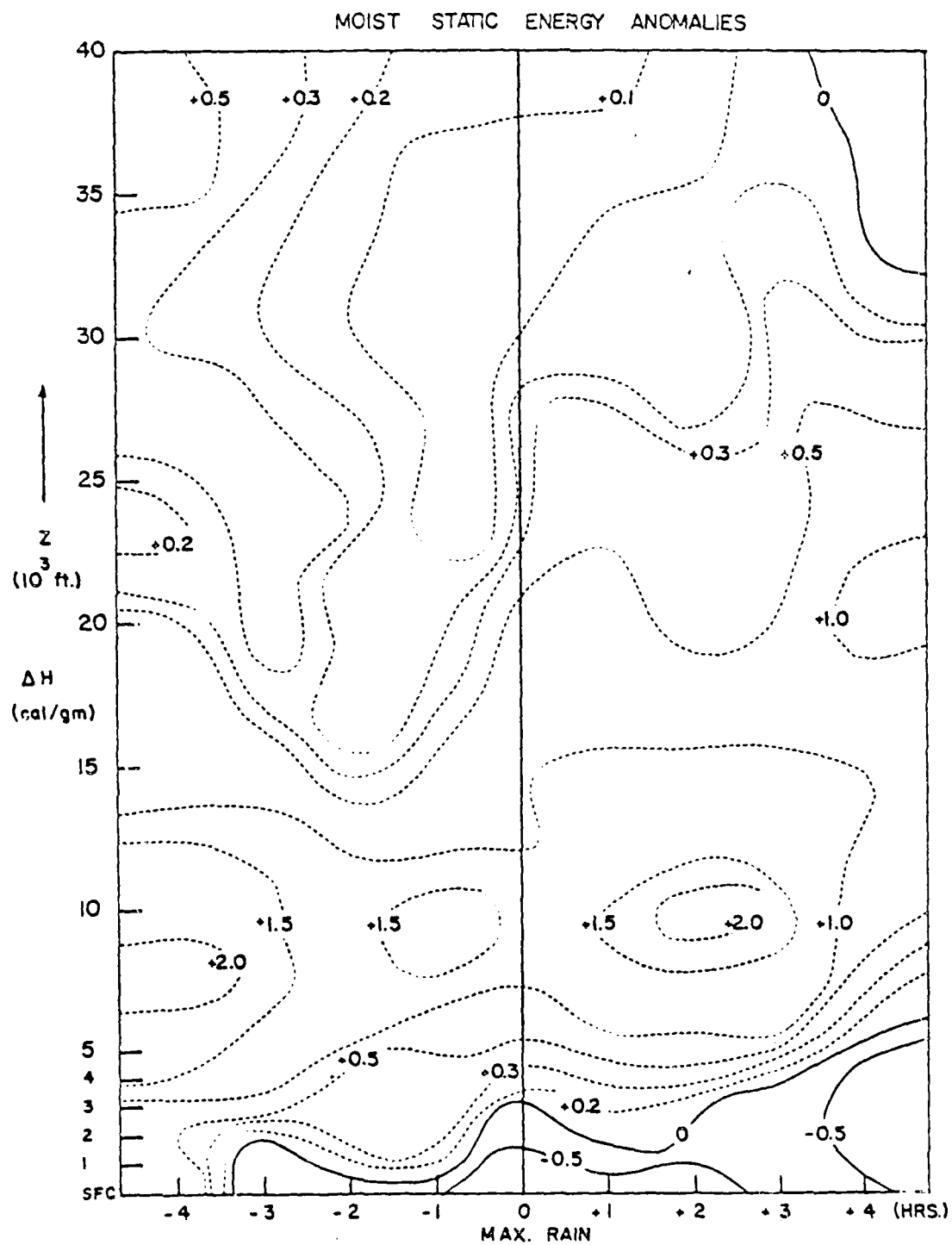
Figure 76. Composite moist static energy departures due to the passage of a storm.

profile being "straightened out" in the vertical by their passage. A
comparison of Figure 76 with Figures 74 and 75 shows that the redistri-
bution of moist static energy in the vertical is accomplished in the
subcloud layer by a loss of enthalpy and latent heat energy there,
whereas in the layer between the lower cloud region and above, it is
a result of a redistribution of latent heat energy, or, the redistribu-
tion of moisture.

The role played by the vertical moisture distribution in the
diurnal evolution of convection is reflected in the excess of moisture
(on the wet days over the dry days) between 5000 ft ($\sim$ 850 mb) and 17000
ft ($\sim$ 550 mb). The average soundings on dry days were compared to the
average soundings on wet days which were launched in the fourth hour
before maximum rainfall, that is, at the beginning of the composite
period.

It was found using a t-test, that the difference in moisture
between the dry and wet days was significant at the 99% level at all
levels between 850 mb and 550 mb, with the exceptions of the 5000 ft,
14000 ft and 17000 ft levels where the differences were significant
at the 95% level. At other levels, the differences were not signifi-
cant. We can conclude that the amount of moisture in the region between
850 mb and 550 mb plays a role in the evolution of deep convection.

A schematic of the progression from a "weak convective" state to
a "pre-rain" state can be obtained by comparison of the wet day and dry
day soundings taken at various times of day. It will be recalled that
21 soundings taken at 1400 Z (1000 EDT) were launched more than four
hours before the maximum rainfall, and were not included in the composi-
tion process. We consider the earliest sounding on the dry days to be

furthest removed in time from a "pre-rain" state, followed, in sequence,
by dry day soundings taken later in the day, after relatively little
convective activity has mixed more moisture into the 850-550 mb layer.
The average of the 1400 Z (1000 EDT) soundings which was not used in the
composite because the launch times occurred more than four hours before
the maximum rainfall rate is considered to be a step closer to a "pre-
rain" state than all of the dry day soundings. The soundings (1700 Z
and 1400 Z) used in the composite to make up the average sounding for
four hours before maximum rainfall rate are considered to represent
the "pre-rain" state. Thus we progress from a "weak-convective" state
at 1400 Z (1000 EDT) on dry days, through the soundings on dry days
launched at 1700 and 2000 Z, through the early morning soundings on
wet days when the storms occurred late in the afternoon to the "pre-
rain" state represented by the soundings used to make up the first,
pre-storm, average sounding four hours before the composite maximum
rainfall rate. As a result, the progression from the "weak-convective"
state to the "pre-rain" state can be presented in six stages, as follows;

"weak convective" state	Stage 1:	The early morning 1400 Z (1000 EDT) soundings on dry days.
	Stage 2:	The 1700 Z sounding on dry days.
	Stage 3:	The 2000 Z sounding on dry days.
	Stage 4:	The early morning sounding (1400 Z) on wet days when storms occurred later in the afternoon.
"pre-rain" state	Stage 5:	The 1400 Z sounding four hours before the occurrence of maximum total network rainfall rate.
	Stage 6:	The 1700 Z sounding four hours before the occurrence of maximum

total network rainfall
rate.

The results are shown in Figure 77, which is a plot of moist

static energy with height for this sequence of soundings, and shows

the progressive increase in moist static energy, in the levels between

5000 ft and 15000 ft, from the "weak-convective" state at 1400 Z (1000

EDT) on dry days to the "pre-rain" state represented by the 1700 Z and

1400 Z soundings on wet days which were launched four hours or less

before the maximum total network rainfall rate.

That the increase in moist static energy at these levels is due

mainly to the presence of moisture is illustrated in Figure 78 which

shows a plot of the dry and moist static energy for 1700 Z on dry days

compared with the composited pre-convective dry and moist static energies

for 1700 Z on wet days.

There is little or no difference between the dry static energies,

but a considerable difference in the moist static energy profiles.

The amount of moisture difference between the six stages is seen in

Figure 79. The soundings taken on wet days, at 1000 EDT, which were

not used in the composite because they were launched more than four

hours before the maximum rainfall are considered to represent a "midway"

point between the "weak-convective" and "pre-rain" states. The

perturbations, in mixing ratio, for the dry day soundings and pre-rain

soundings about this midway point were calculated, and are plotted in

this figure. We see again, the progression from "weak-convective" to

"pre-rain" state similar to that displayed in the moist static energy

plots of Figure 77. As previously stated, the differences in moisture

in the levels between 5000 ft and 17000 ft are statistically significant

at the 99% level.
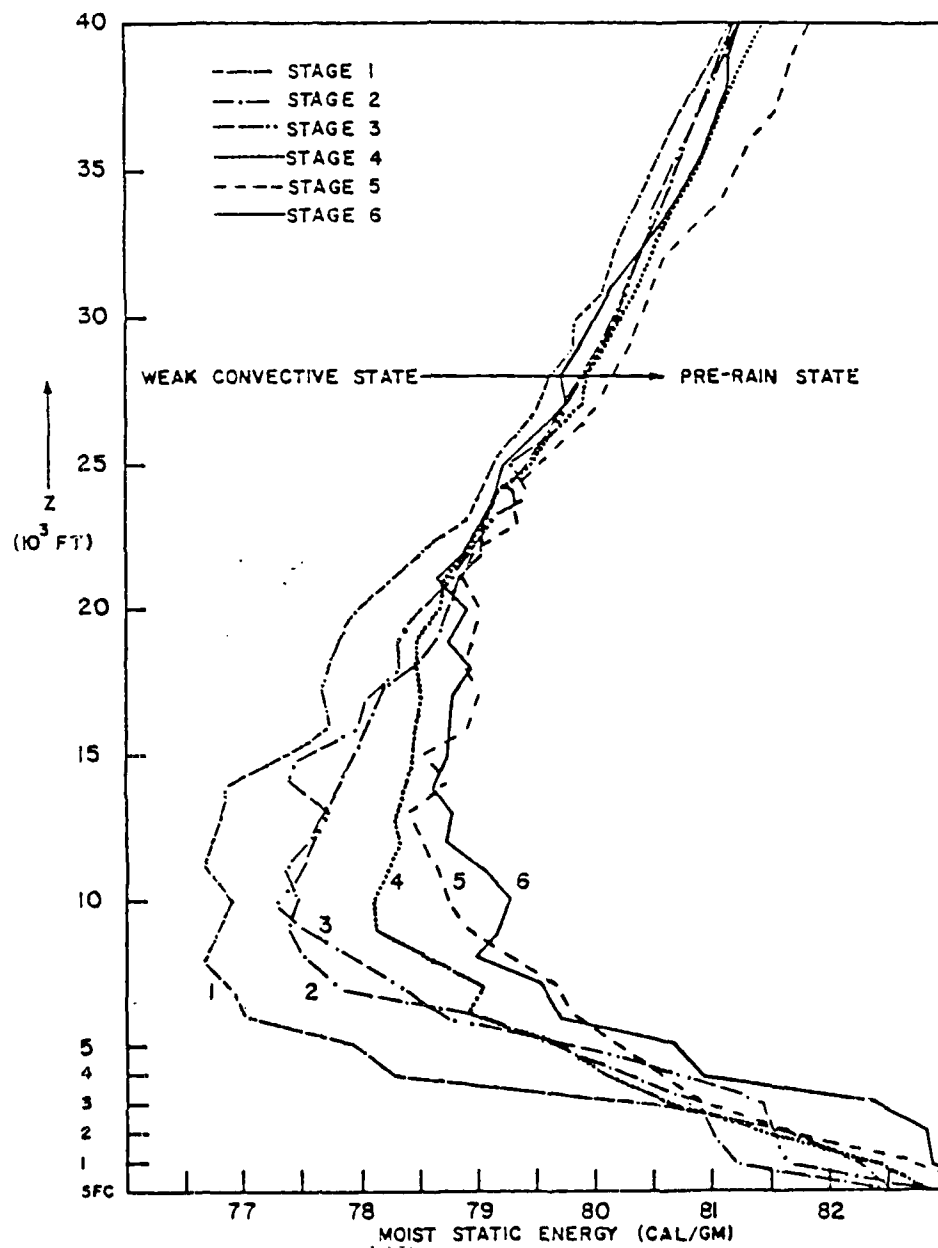
Figure 77. The progression of upper air of moist static energy profiles from a weak-convective state to a pre-rain state.
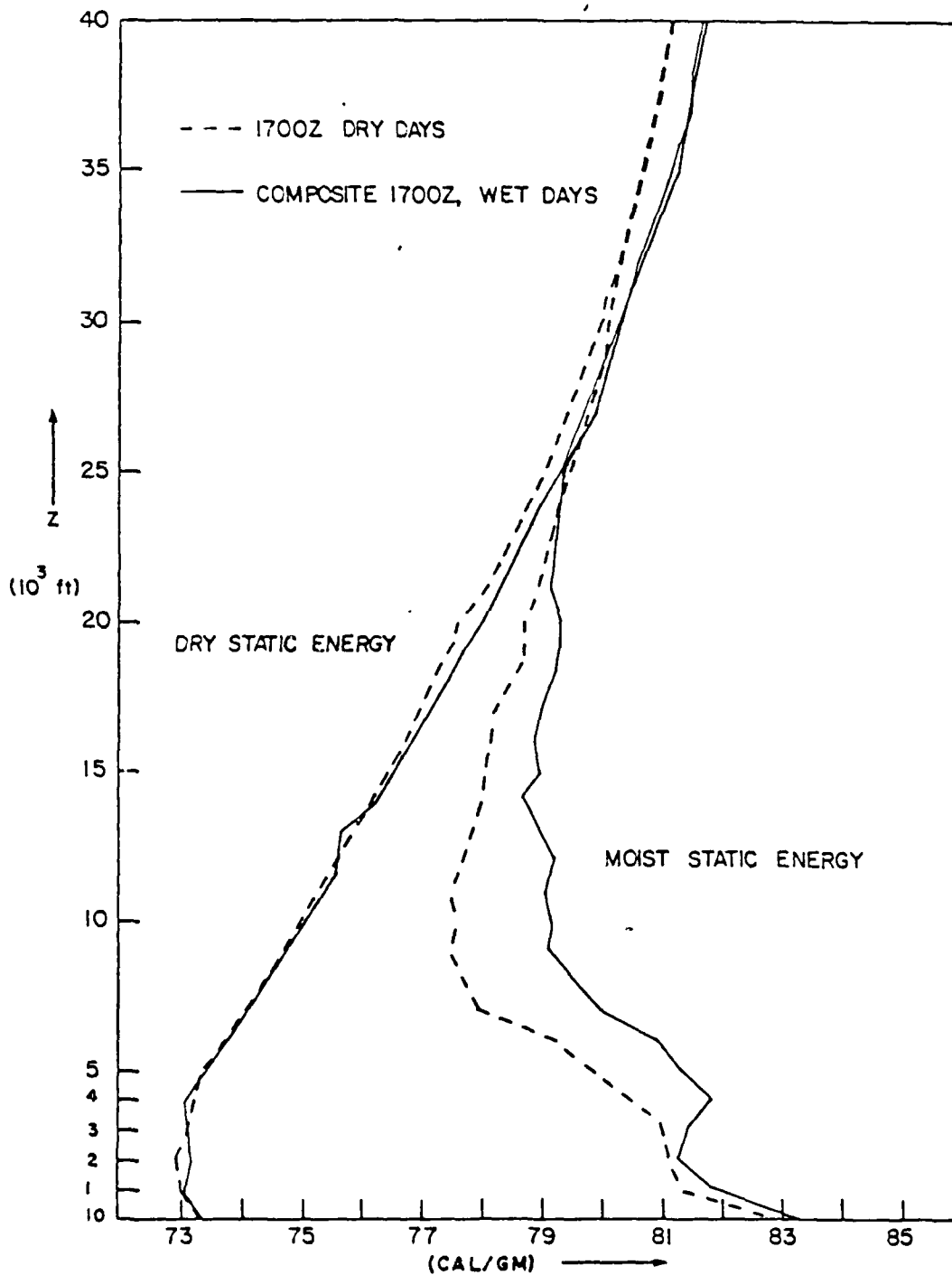
Figure 78. The profiles of moist and dry static energy for dry days and for the composite pre-rain state.
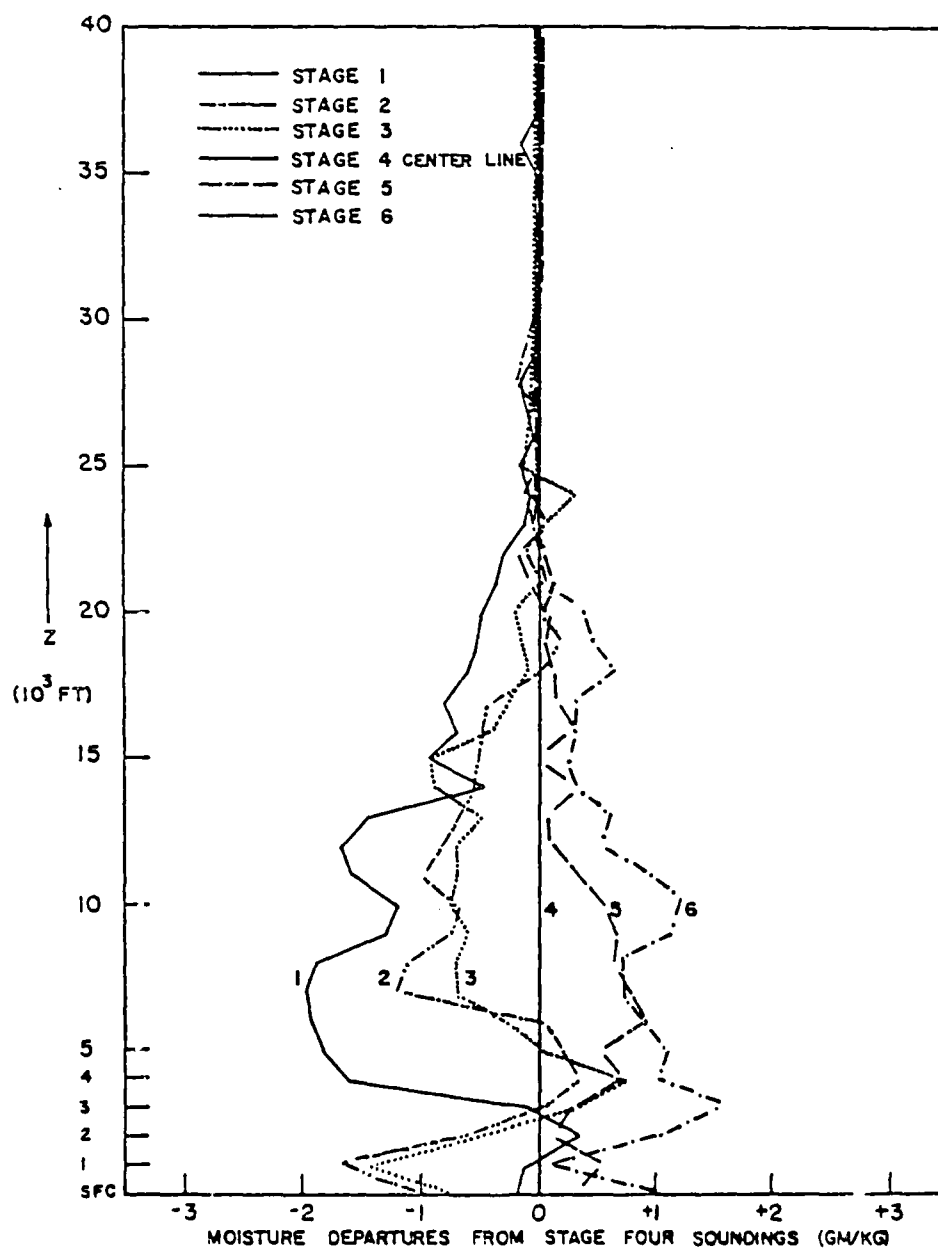
Figure 72. The departures in mixing ratio of the weak-convective states and pre-rain states from the stage 4 sounding.

B. THE COMPOSITE SURFACE DATA

In addition to a composite of the upper air thermodynamic data,
a composite of the surface kinematic and rainfall data was constructed,
again using the maximum network rainfall rate as the point about which
composition was accomplished. The composited surface data represent a
"typical" south Florida storm which was constructed using 15-minute
data from 47 showers in 1975. Figure 80 contains a graph of the behavior
of the surface wind fields during such an average storm. The surface
divergence fields were integrated to cloud base ($\approx$ 1000 m), assuming
incompressibility.

Figure 80a shows the estimates of the vertical upward and down-
ward transports through cloud base which took place during the life
cycle of the composite storm as seen in the surface data. There is a
steady increase in upward transports starting three hours before maxi-
mum rainfall rate, with a corresponding increase in downward transports,
which lag the upward transports.

The peak in upward transports occurs fifteen minutes prior to
peak composite rainfall, the peak in downward transports fifteen minutes
after the peak rainfall. The difference in the upward and downward
transports (Figure 80b) shows the characteristic shape of the area-
averaged divergence fields typical of larger storms. The peak in the
net upward transport occurs some 30-45 minutes before the maximum net-
work rainfall, the inflection point almost during the maximum rainfall,
and the peak in the net downward transports occurs between 15-30 minutes
afterwards.
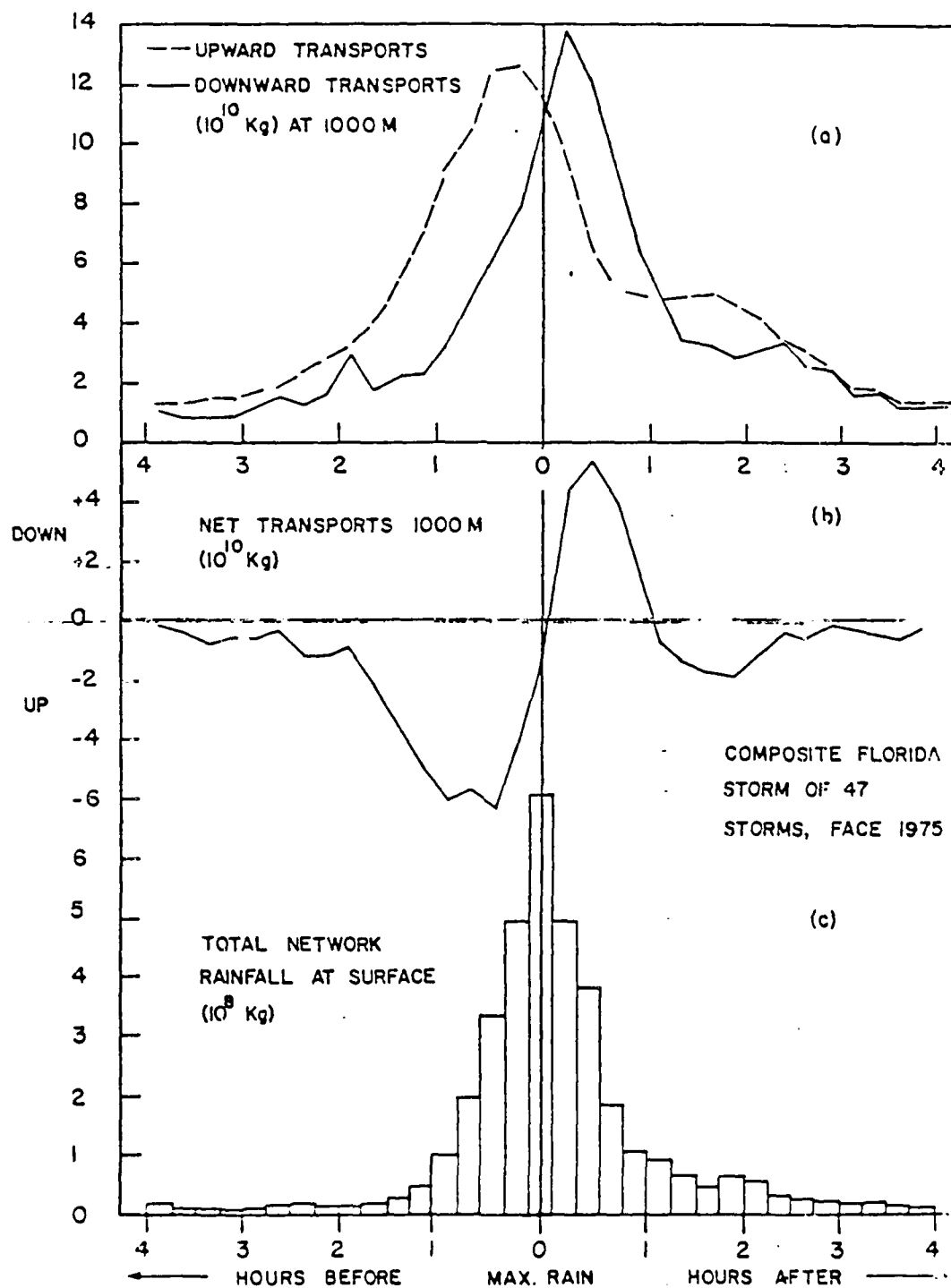
Figure 80. The composite Florida storm as seen in the surface wind fields.

C. STORM EFFICIENCIES

The composited surface data, which represent an average storm, can be used in conjunction with the upper air thermodynamic composite to construct a time series of the processing of moisture in the network as a storm passes overhead.

Using the upward and downward transports pictured in Figure 80, and the network rainfall rates represented there, Table 12 was produced. The upward moving air was assumed to have the characteristics of the pre-rain composited sounding, while the downward moving air was assumed to have the values of the composited rawinsonde data calculated for the appropriate period during the life cycle. The moisture content of the updrafts was considered to be the average moisture content of the pre-rain sounding in the layer from the surface to 1000 m, while the moisture content of the downdrafts was assumed to be that at the surface at time t.

The calculations of moisture and precipitation efficiencies for these storms is, like the formulation of forecasting criteria for local convective rainfall, a sampling problem. We can expect to sample only parts of large storms, the occasional smaller storms in their entirety, and portions of storms of all degrees of intensity at various stages in their life cycles. The Florida composite storm represented in Figure 80 and Table 12 is made up of 47 storms in various stages and covering various amounts of the surface wind network, which when taken as a whole, provides an excellent example of a typical complete storm life cycle. This composite storm may be used to provide estimates of the moisture and precipitation efficiencies of an average Florida storm during different stages in its life cycle.

If, as has been strongly suggested by the radar composites of Chapter 3 and specifically demonstrated in the case studies of Chapter

Table 12. The mass and moisture transports for the Florida composite storm.

Time Relative to Maximum Network Rainfall Rate (t Hour:Min)	Upward Moisture Transports (x 10^7 kg)	Upward Mass Transports (x 10^10 kg)	Downward Mass Transports (x 10^10 kg)	Downward Moisture Transports (x 10^7 kg)	Rainfall at Surface (x 10^7 kg)	Total Downward Moisture Transports (x 10^7 kg)
-4:00	10.535	1.234	1.037	17.048	0.17	17.218
-3:45	18.369	1.223	0.893	14.681	0.12	14.801
-3:30	21.326	1.553	0.849	13.958	0.15	14.108
-3:15	22.365	1.409	0.903	14.850	0.26	15.110
-3:00	25.699	1.711	1.147	17.457	0.01	18.267
-2:45	27.727	1.816	1.593	24.245	1.86	26.105
-2:30	36.123	2.405	1.250	19.025	1.39	20.415
-2:15	42.191	2.809	1.688	25.691	1.13	26.821
-2:00	50.137	3.338	2.479	37.631	1.69	39.321
-1:45	60.095	4.001	1.924	29.206	2.18	31.386
-1:30	84.518	5.627	2.142	32.516	2.76	35.276
-1:15	104.930	6.986	2.103	31.924	4.87	36.794
-1:00	139.476	9.286	3.228	49.873	9.97	59.843
-0:45	153.940	10.249	4.620	71.379	19.22	90.599
-0:30	186.849	12.440	6.198	95.759	33.03	128.789
-0:15	189.703	12.630	7.871	121.607	40.74	170.347
Time of Maximum Rain	179.409	11.950	10.65	166.140	70.99	237.130
+0:15	145.664	9.690	13.89	214.878	48.84	263.718
+0:30	99.710	6.638	12.12	107.496	20.09	215.506
+0:45	78.615	5.234	9.255	143.175	18.40	161.575
+1:00	77.583	5.165	6.470	100.091	10.54	111.450
+1:15	79.357	5.283	4.933	81.345	8.51	89.855
+1:30	75.599	5.031	3.504	59.100	6.13	65.230
+1:45	77.595	5.166	3.379	55.720	4.95	60.670
+2:00	71.213	4.741	2.894	47.722	5.63	53.352
+2:15	65.040	4.330	3.097	54.079	5.20	60.079
+2:30	54.007	3.595	3.261	57.785	3.00	60.705

Table 12 (cont.)

Time Relative to Maximum Network Rainfall Rate (t Hour:Min)	Upward Moisture Transports (x 10^7 kg)	Upward Mass Transports (x 10^{10} kg)	Downward Mass Transports (x 10^{10} kg)	Downward Moisture Transports (x 10^7 kg)	Rainfall at Surface (x 10^7 kg)	Total Downward Moisture Transports (x 10^7 kg)
+2:45	49.234	3.277	2.757	40.054	2.29	51.144
+3:00	39.396	2.622	2.496	44.229	2.23	46.459
+3:15	29.471	1.962	1.596	26.557	2.04	20.597
+3:30	28.266	1.081	1.617	26.907	2.30	29.207
+3:45	22.652	1.508	0.973	16.184	1.07	17.254
+4:00	21.817	1.452	1.335	22.214	0.98	23.194

4, we assume a cause and effect relationship between the upward trans-
ports, rainfall and downward transports, we must associate a given
upward transport value with an appropriate value of rainfall and down-
ward transport in order to calculate the precipitation and moisture
efficiencies during the various stages in the life-cycle. That is,
there must be a time lag between time of upward transport and the time
of production of the resulting rainfall and downdraft.

If the values of upward transports, downward transports and
rainfall in Figure 80 are shifted on the time axis such that all three
are in phase with one another, then corresponding values of upward
transports, downward transports and rainfall can be used to estimate
moisture and precipitation efficiencies throughout the life cycle of
the storm.

The result of shifting the graphs of upward and downward trans-
ports and rainfall rates into phase with one another is shown in
Figure 81 and Table 13.

The "efficiency" of the composite storm (during the different
stages of its life cycle) is represented in four ways,

    i) water vapor efficiency,
   ii) precipitation efficiency,
  iii) total water substance efficiency,

and

   iv) net precipitation efficiency, each defined as follows.

i) <u>The water vapor efficiency</u>

This gives the "efficiency" with which the storm returns water
vapor into the subcloud layer after rainfall has been processed out.
It is the amount of water vapor brought down, $q\downarrow$, divided by the
associated amount of water vapor originally taken up by the storm, $q\uparrow$.
That is,
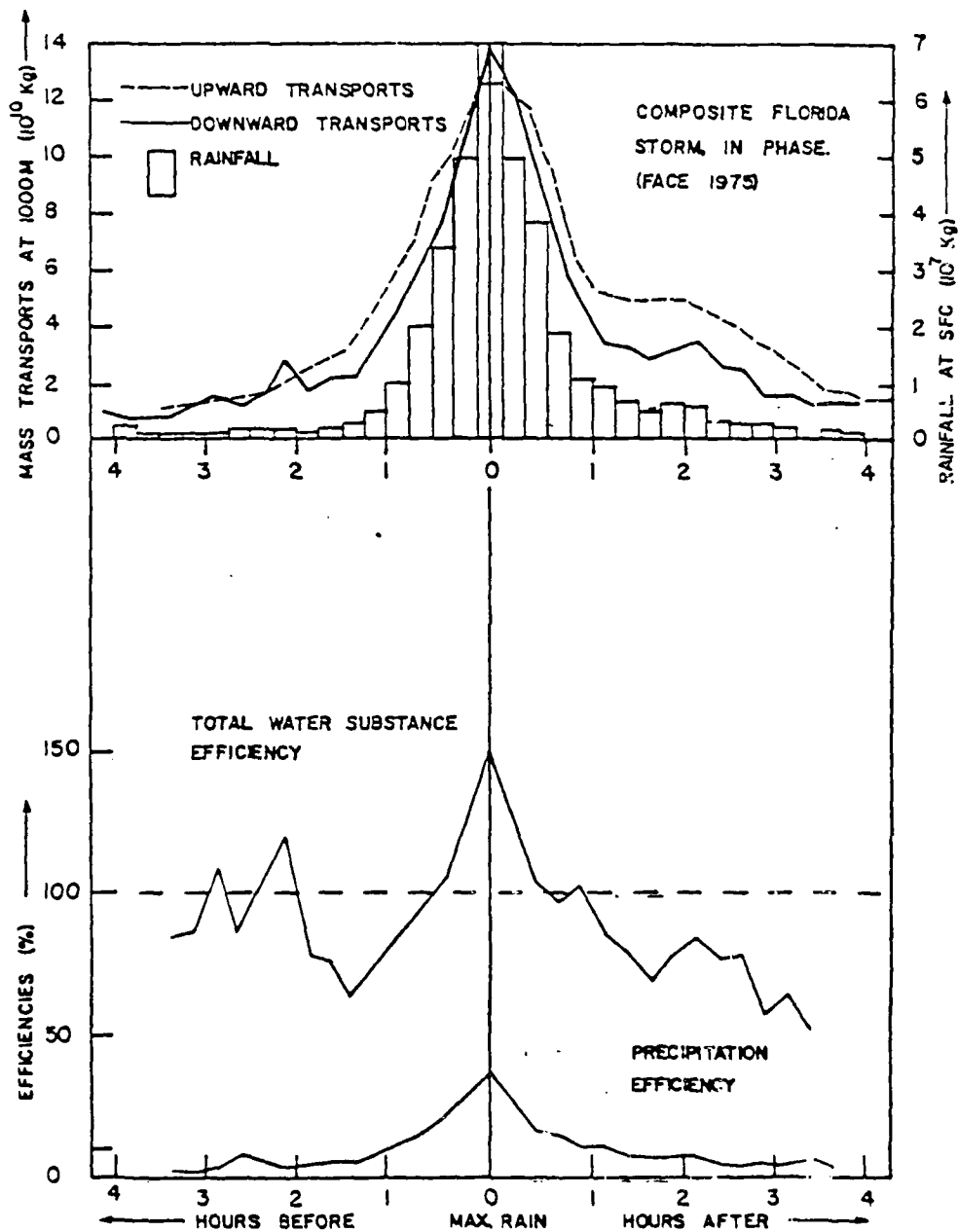
Figure 81. The composite Florida storm as seen in the surface wind fields, in phase.

Table 13. The mass and moisture transports and storm efficiencies for the Florida composite storm, in phase.

Time Relative to Maximum Rain	Rain (x 10^7 kg)	(x 10^7 kg) Upward Water Vapor	(x 10^7 kg) Downward Water Vapor	Water Vapor Efficiency %	Precipitation Efficiency %	(x 10^7 kg) Downward Total Water Substance	Total Water Substance Efficiency %
-3:30	0.15	18.452	14.850	80.5	0.0	15.650	84.8
-3:15	0.26	20.048	17.457	83.7	1.2	17.717	85.0
-3:00	0.81	22.046	24.245	106.1	3.5	25.055	109.7
-2:45	1.86	24.032	19.025	79.2	7.7	20.855	86.9
-2:30	1.39	26.713	25.691	96.2	5.2	27.001	101.4
-2:15	1.13	31.925	37.631	117.9	3.5	30.761	121.4
-2:00	1.69	39.157	29.206	74.6	4.3	30.896	78.9
-1:45	2.18	46.164	32.516	70.4	4.7	34.696	75.2
-1:30	2.76	55.116	31.924	57.9	5.0	34.684	62.9
-1:15	4.87	72.307	49.873	69.0	6.7	54.743	75.7
-1:00	9.97	94.724	71.379	75.4	10.5	81.349	85.9
-0:45	19.22	122.203	95.759	78.4	15.8	114.979	94.1
-0:30	33.03	146.708	121.607	82.9	22.5	154.637	105.4
-0:15	48.74	170.395	166.140	97.5	28.6	214.880	126.1
Max. RW	70.99	108.276	214.878	114.1	37.7	205.868	151.8
+0:15	48.04	184.596	187.496	101.6	26.5	236.336	128.0
+0:30	28.09	162.577	143.175	88.1	17.3	171.265	105.3
+0:45	18.40	122.687	100.091	81.6	15.0	110.491	96.6
+1:00	10.54	89.163	81.345	91.2	11.8	91.005	103.1
+1:15	8.51	78.099	59.100	75.7	10.9	67.610	86.6
+1:30	6.13	78.470	55.720	71.0	7.8	61.850	78.8
+1:45	4.95	77.478	47.722	61.6	6.4	52.672	68.0
+2:00	5.63	76.597	54.879	71.6	7.4	60.509	79.0
+2:15	5.20	74.404	57.705	77.7	7.0	62.905	84.7
+2:30	3.00	60.127	48.854	71.7	4.4	51.854	76.1
+2:45	2.29	59.524	44.229	74.3	3.8	46.519	78.2

Table 13 (cont.)

Time Relative to Maximum Rain	Rain (x 10⁹ kg)	(x 10⁷ kg) Upward Water Vapor	(x 10⁷ kg) Downward Water Vapor	Water Vapor Efficiency	Precipitation Efficiency	(x 10⁷ kg) Downward Total Water Substance	Total Water Substance Efficiency
+3:00	2.23	51.621	26.557	51.4	4.3	20.787	55.8
+3:15	2.04	44.315	26.907	60.7	4.6	20.947	65.3
+3:30	2.30	34.414	16.184	47.0	6.7	18.404	53.7
+3:45	1.07	28.066	22.214	77.0	3.7	23.284	80.7
Totals	348.27	2310.82	1924.44	83.3	15.1	2276.31	90.5

Net upward water vapor = $(2310.82 - 1924.44) \times 10^7$ kg = 386.3×10^7 kg

Net precipitation efficiency = $(348.27 \times 10^7)/(386.38 \times 10^7)$ = 90.1%

Total storm precipitation efficiency = 15.1%

Total storm water vapor efficiency = 83.3%

Total storm water substance efficiency = 98.5%

water vapor efficiency = $(q\downarrow/q\uparrow) \times 100$

ii) The precipitation efficiency

This is defined as the amount of precipitation (RR) produced during a stage in the storm's life cycle, divided by the amount of water vapor taken up by the storm, $q\uparrow$, to produce that amount of rain. That is,

precipitation efficiency = $(RR/q\uparrow) \times 100$

iii) The total water substance efficiency

This is defined as the amount of rainfall produced by the storm (RR), plus the amount of water vapor returned to the subcloud layer divided by the associated amount of water vapor taken up by the storm during a given stage, that is,

total water substance efficiency = $[(q\downarrow + RR)/q\uparrow] \times 100$

iv) The network precipitation efficiency

If the vertical motions beneath the storms had not been known in such detail, the association of equivalent upward and downward transports and their efficiency in production of rainfall could not have been made. The network precipitation efficiency is an estimation of the precipitation efficiencies which would have been calculated if only an area averaged divergence over a scale larger than the individual storm cell size had been available.

If knowledge of the smaller, convective scale transports had been unavailable, then the storm precipitation efficiency may have been defined as the convergence of moisture into a region surrounding the storm, divided by the amount of rainfall detected in that region.

We have seen in previous chapters that the area-averaged divergence taken about the entire network can be duplicated by subtracting

the downward convective transports from the upward convective transports, as defined. The <u>network</u> precipitation efficiency is therefore defined as,

<u>Network</u> precipitation efficiency = [RR/(q↑ - q↓)] x 100

Referring to Table 13, the figures for the total storm behavior at the bottom of the table show that, taken over the entire storm life-cycle, the network is essentially in moisture balance, with a total water substance efficiency of 98.5%. That is, in terms of total water substance (water vapor plus rainfall), there is no net loss or gain in the network over the entire life cycle of the storm. The <u>network</u> precipitation efficiency is high, at 90.1%, which at first glance would suggest a highly efficient, precipitation-producing process. However, the efficiency of the convection in producing rainfall in its different stages is actually much less than 90%. Precipitation efficiencies during the life cycle of convective activity range from a low of 0.8% at the onset to a maximum of 37.7% at its height. The total storm water vapor efficiency is 83.3%, while the total storm precipitation efficiency is only 15.1%.

Figure 81 shows a plot of the in-phase relationships between the upward and downward transports and rainfall, and plots of the total water substance efficiency and precipitation efficiencies during the entire life cycle of the convection.

At the time of greatest precipitation efficiency, there is an excess of water substance brought down by the storm over that taken up from beneath cloud base, of around 50%. Some of this excess may come from moist air entrained from aloft by the storm during this stage in its life cycle, but most of it probably is due to the delay in processing of moist air previously mixed up by convection. In fact, from the total

water substance efficiency plot of Figure 81, we see that in the second
hour before the maximum rainfall rate, the total water substance
efficiency is at its lowest so far in the life cycle, followed by the
"super-efficiency" period mentioned above. This suggests that much of
the excess water substance being brought down by the storm during its
most super efficient stage comes from water substance stored aloft
previously by the convective processes. Viewed in conjunction with
Figure 75, we see that over this period of time in the life cycle (the
second hour before maximum rainfall) the moisture content of the
atmosphere begins to spread out in the vertical, and the location, in
the vertical, of the moisture excess maximum begins to rise to the
higher levels reached in the decaying stages of the convective life
cycle.

Later in the convective life cycle, the storm becomes "sub-
efficient" (that is, its total water substance efficiency is less
than 100%), and the moisture in the atmospheric column continues to
spread out in the vertical (Figure 75).

CHAPTER 7

MIDWESTERN STORMS

Surface thermodynamic and kinematic data were available on tape from the data set collected during the 1979 VIN experiment in Illinois.

Two case studies were selected from the Illinois data to demonstrate the comparative behavior of the surface wind fields of Florida storms to midwestern storms, and to examine their surface thermodynamic fields. Thermodynamic data was available from Illinois which was not available in the FACE data set, as a result of the deployment of the NCAR PAM system during VIN.

Both the kinematic data and thermodynamic data are available to a resolution of 1-minute in time, and are well synchronized, the information being transmitted every minute to a central location by radio.

The storms analyzed here are those that occurred on 13 July and 30 July 1979. The storm of 13 July is a relatively moderate storm in comparison with that which passed over the network on 30 July. Only the PAM network data has been used in these surface analyses.

The methods used in the thermodynamic calculations can be found in Appendix B.

A. THE STORM OF 30 JULY 1979

This day was under the influence of large scale features and the storm was associated with a massive frontal line of showers which, in its final form, extended from Illinois to Texas. The storms which

passed over the VIN network marked the northern end of this massive line of squalls. The maximum point rainfall during the storm was 8.0 inches which was recorded 15 miles east of the PAM network, but was within the intense rain gauge array set up by the Illinois State Water Survey. A funnel cloud was observed outside the PAM network, and small and medium sized hail was recorded.

Figures 82 and 83 show the surface values of θ_e, mixing ratio, relative humidity, area-averaged divergence and rainfall averaged over all stations in the PAM network.

The area-averaged divergence and rainfall have the familiar relationship, with the peak in the area-averaged convergence occurring at 1855 CDT (40 minutes before the peak network rainfall) followed by the maximum in area-averaged divergence at 1925 CDT. During the rest of the day, the area-averaged divergence oscillates between $\pm$ 50 x 10^{-6} sec^{-1}, until around 1300 CDT, when it becomes convergent, remaining so until the onset of heavy rain during the passage of the squall.

The θ_e profile shows a gradual decrease from around 350°K at midnight on the 29 July, to around 340°K at 0500 CDT. At 0500 CDT θ_e slowly increases as the surface is heated to a maximum network average value of 370°K around 1720 CDT. With the onset of heavy rainfall in the network, there is a rapid drop of some 40°K to 330°K, in the average, which takes place between 1720 CDT and 2005 CDT. The values of θ_e then start to slowly recover and are approaching values of 336°K at the time of the end of the data for that day.

The profile in mixing ratio follows that of the θ_e curve, increasing from dawn to an average value of 21.8 gm/kg by 1715. It then drops rapidly to values around 13.2 gm/kg as the storm passes.
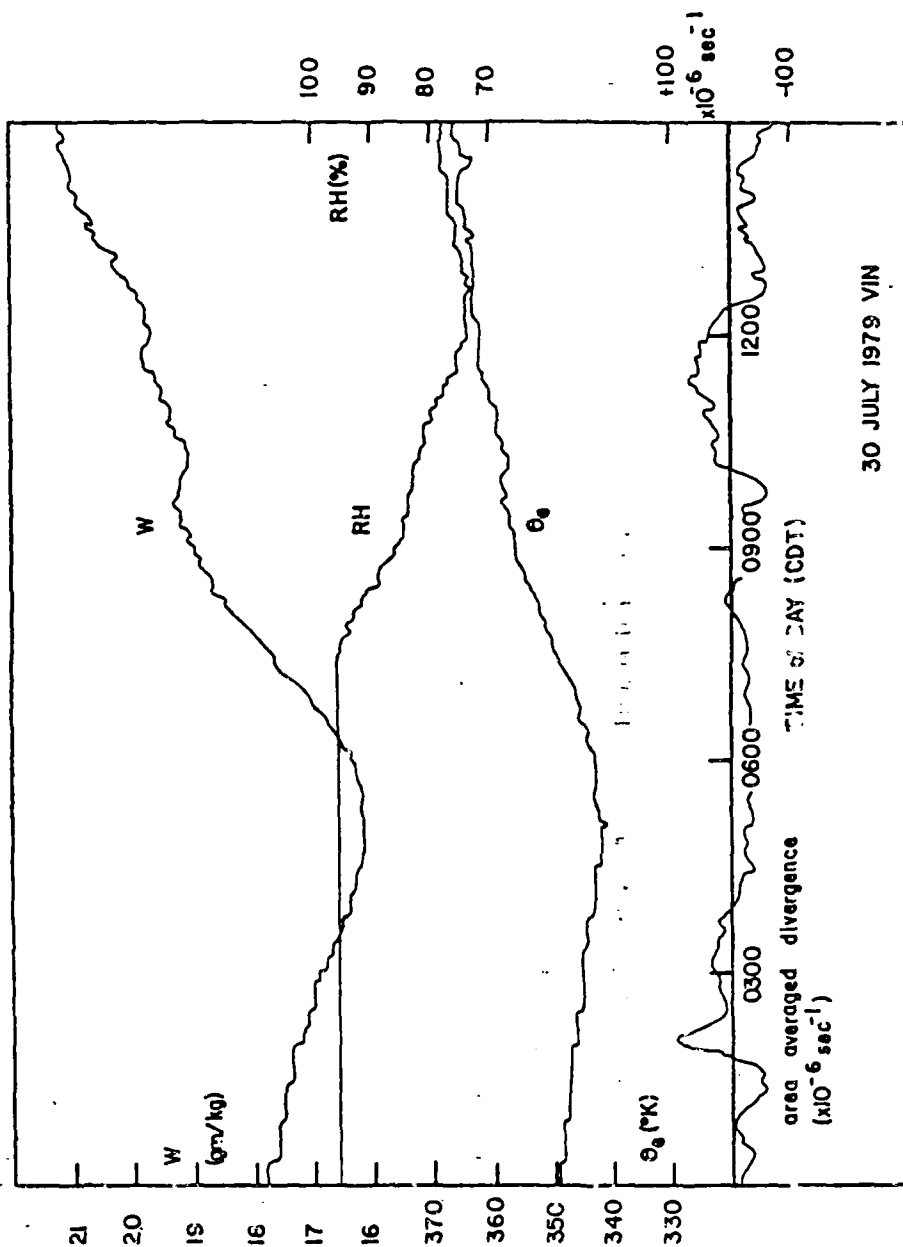
Figure 82. Daily profiles for the storm of 30 July 1979.
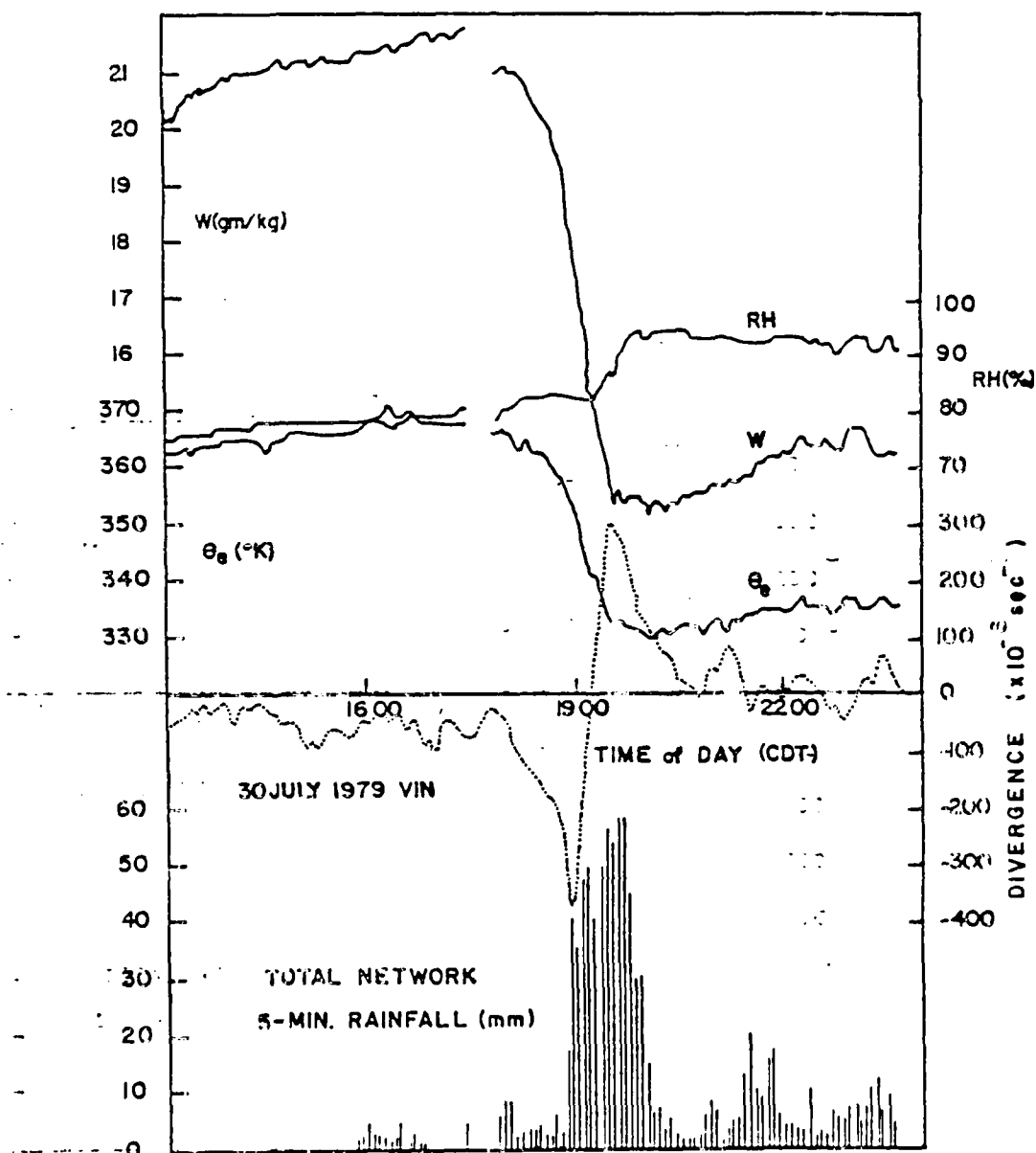
Figure 83. Daily profiles for the storm of 30 July 1979.

The relative humidity profile is such that there is a steady decrease in the network averaged relative humidity from an almost saturated value of 96% during the nighttime, to a minimum of 73% by noon. The relative humidity remains steady at 75% or so until 1600 CDT, at which time it climbs slowly to 82% during the early stages of the storm; then rises rapidly to 94% during the period of maximum rainfall rate. The relative humidity stays above 90% for the rest of the evening.

The availability of satellite observations on this day, prior to the arrival of the major storm system over the network provides an opportunity to correlate the visible cloud patterns over the network with the observed patterns in the surface divergence fields. These satellite observations (Figure 84) show a small line of convective activity present just north of the PAM network at 1500 CDT (2000 GMT) and the surface wind fields (Figure 85b) show a modest (-300×10^{-6} sec^{-1}) convergence zone in the center of the network. By 1530 CDT (2030 GMT) the small line has intensified (Figure 86), with a fairly large cell just northeast of the network and a weaker line orientated WSW-NE across the northwestern corner of the array. The surface divergence fields for this time (Figure 87) show a weak zone of convecgence orientated roughly parallel to the line of convection across the northern part of the network.

The larger storm NE of the PAM network is in its mature stage by 1600 CDT, and the smaller storm to the SSW over the NW corner of the array starts to rain in the network at 1530 CDT (Figure 88). The divergence fields calculated at 1600 (Figure 89) show divergence associated with the very light rainfall recorded from this smaller storm, and a slight intensification of the convergence zone over the

2001 30JL79 12A-1   02106 17132 DA1
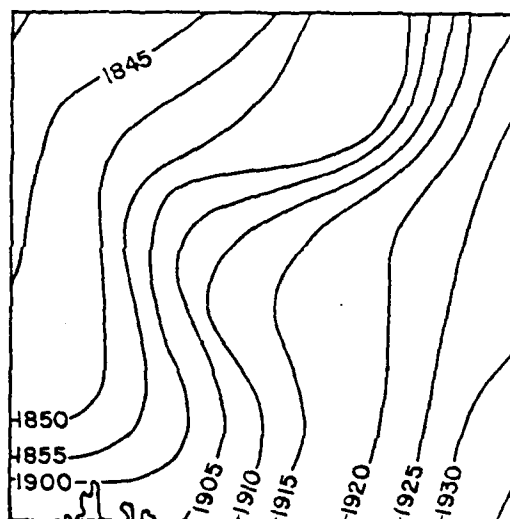
30 JULY 1979 VIN
POSITIONS OF THE
MAIN GUST FRONT (CDT)
FOR GMT (Z) TIME
ADD 5 HOURS
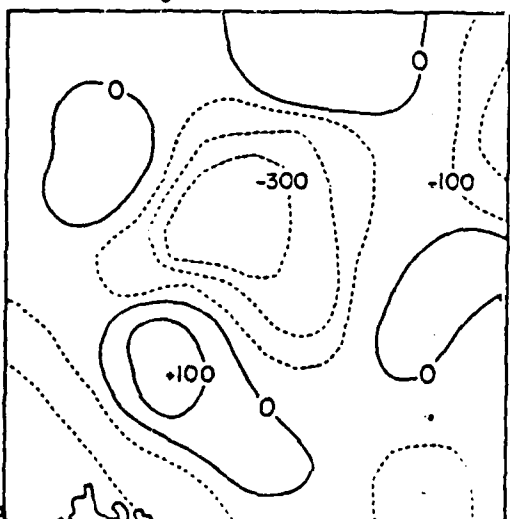
30 JULY 1979 VIN
CONTOURS EVERY
$100 \times 10^{-6} \text{ sec}^{-1}$
1500 CDT (2000Z)

km
0 2 4 6 8

o Light Rain
⊘ Heavy Rain
---- Convergence
—— Divergence

Figure 85.   a) Positions of main gust front (CDT) on 30 July 1979 during VIN.
             b) Surface divergence, 1500 CDT, 30 July 1979.

Figure 46. Satellite observations of the VIP pattern, half 1, to the left. Base.
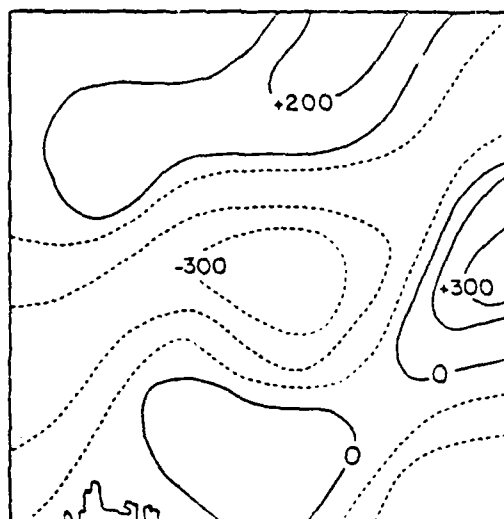
30 JULY 1979 VIN
CONTOURS EVERY
$100 \times 10^{-6} \sec^{-1}$
1530 CDT (2030Z)
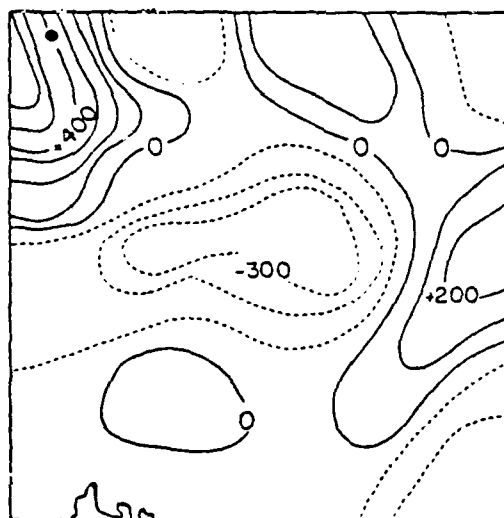
30 JULY 1979 VIN
CONTOURS EVERY
$100 \times 10 \sec$
1600 CDT (2100Z)

km
0 2 4 6 8

∘ Light Rain
• Heavy Rain

--- Convergence
— Divergence

Figure 88.   Same as Figure 86 except for 1530 CDT.

Figure 89.   Same as Figure 86 except for 1600 CDT.

2131 30JL79 12A-1 02112 17122 DA1

Figure 90. Same as Figure 84, except for 2131 G.

center of the network. Rain and divergence continue in the northern part of the network at 1630 CDT (Figure 91), and other storms are reaching maturity west of the network, in association with the large line of thunderstorm activity which stretches from Illinois to Texas (Figure 90). As the network comes increasingly under the influence of this large storm the convergence zone across the center of the network is re-orientated NW-SE.

At 1700 CDT the weak convergence and divergence zones persist (Figure 92), and towering cumuli form ahead of the large storms which lie in a line across the northwestern corner of the network (Figure 93).

The satellite observations for 2230, 2300 and 2330 GMT show the intensification of this line of storms into a solid line of activity (Figures 94, 95 and 96). The associated surface convergence fields are shown in Figures 97 and 98. No surface data was available at 2230 GMT. Figure 98 shows the extent of the entire mature line. The large line of storms shown in Figure 99 moves eastward, and the storm under consideration is at its northern edge.

The two mature storms which lie E-W across the northern edge of the network show up on radar as an arc of intense echoes about the E-N-W borders of the array by 1840 CDT (Figure 101). The associated surface fields are shown in Figure 102. The gust front and the convergence zone it creates are in the northwestern part of the interpolation grid. The θ_e field shows a strong θ_e gradient in an arc across the northern parts of the network. Light rain has fallen in the previous five minutes in the NW.

From 1840 CDT onwards the surface wind and thermodynamic fields were analyzed for each 10-minute period that digitized radar plots were
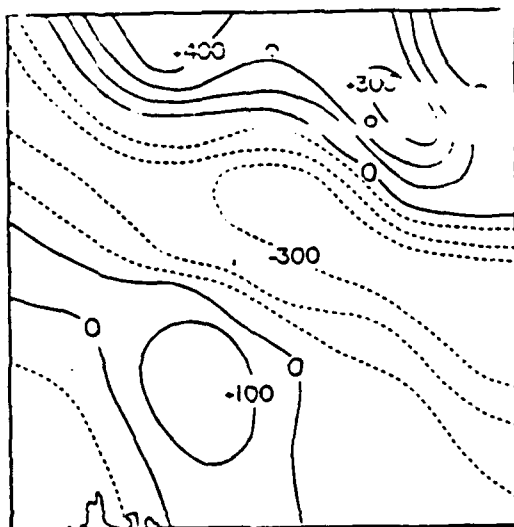
JO JULY 1979 .'N

.ONTOURS EV ·▿

$100 \times 10^{-6} \, sec^{-1}$

163C .. ₊130Z)

km
0 2 4 6 8

° Light Rain
• Heavy Rain
---- Convergence
—— Divergence
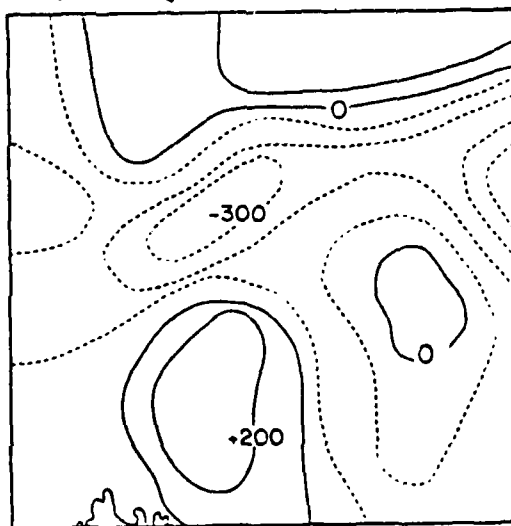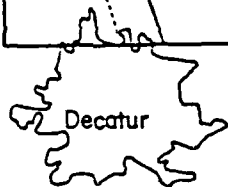
30 JULY 1979 VIN

CONTOURS EVERY

$100 \times 10^{-6} sec^{-1}$

1700 CDT (2200Z)

1730 NO S.F.C.
DATA AVAILABLE
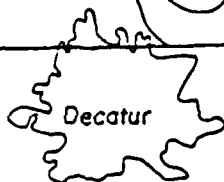
Figure 91.   Same is Figure 85 except for 1630 CDT.
Figure 92.   Same as Figure 85 except for 1700 CDT.
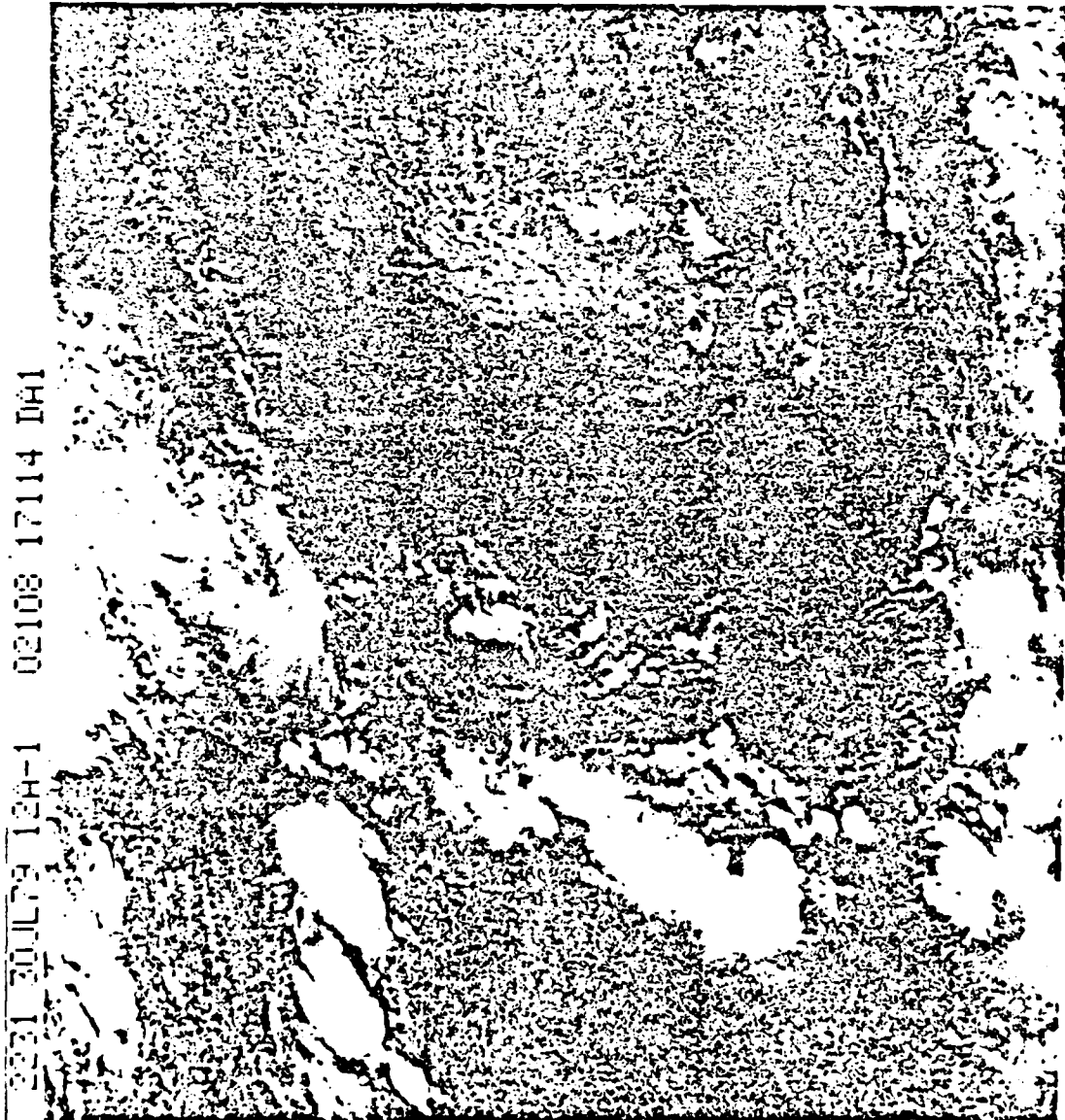
Figure 34. Same as Figure 33 except for Bell ...

Figure 36. Same as Figure 34 except for A-prime test.
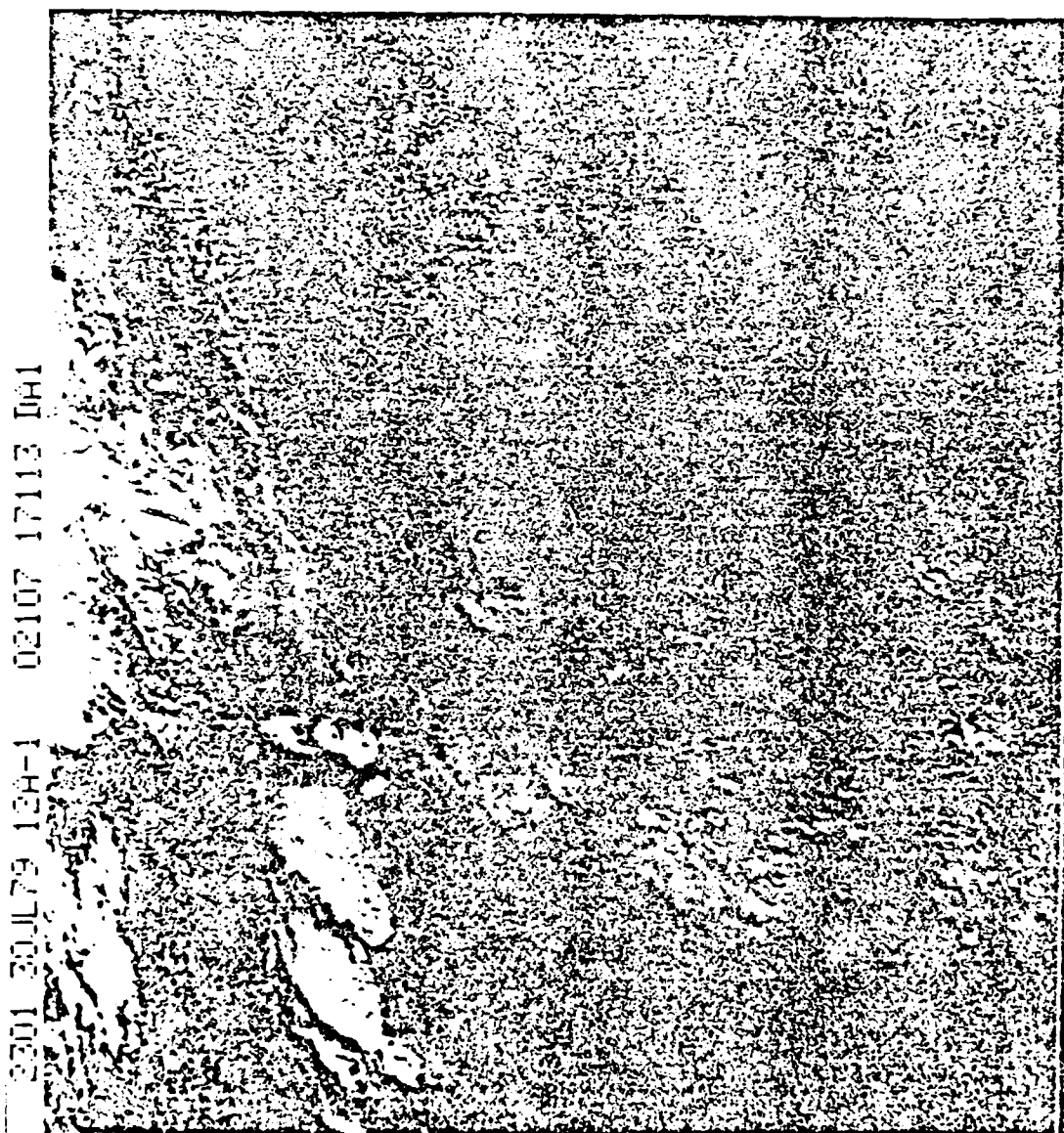
Figure 50. Same as Figure 84 except for orbit 2.
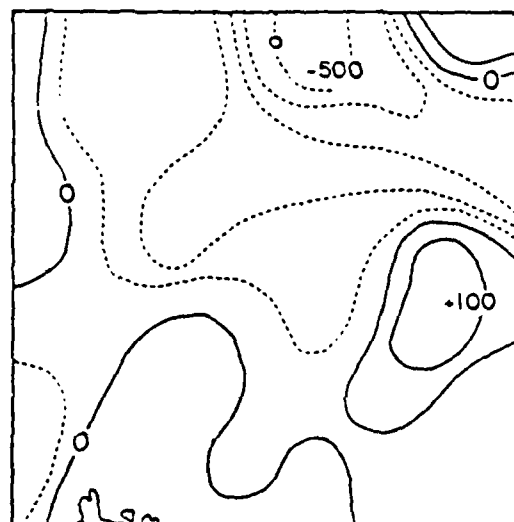
30 JULY 1979 VIN
CONTOURS EVERY
$100 \times 10^{-6} \, sec^{-1}$
1800 CDT (2300Z)

km
0 2 4 6 8
○ Light Rain
● Heavy Rain
---- Convergence
—— Divergence
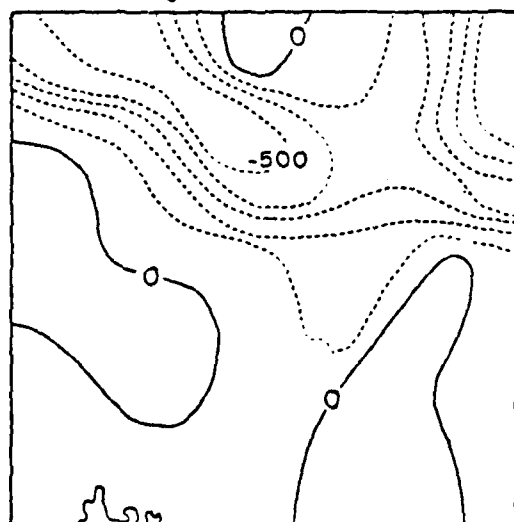
30 JULY 1979 VIN
CONTOURS EVERY
$100 \times 10^{-6} \, sec^{-1}$
1830 CDT (2330Z)

Figure 97.   Same as Figure 85 except for 1800 CDT.
Figure 98.   Same as Figure 85 except for 1830 CDT.

0100 31JL79 13E-2MB 00871 13302 KB8

Figure 39. Satellite view of the entire squall line.

available for this storm, and show the fields beneath the storm as it progresses from NW to SE across the network. By considerations of time series plots of 1-minute wind speeds for all 27 of the PAM stations, it was possible to identify the position of the gust front of this storm. An example of the wind speed time plot for station 8 is contained in Figure 100. Figure 85a shows the position of the gust front each five minute interval during the storm. For each of the following periods, plots of convergence and divergence, the gust front positions, rainfall rate and surface θ_e are presented for comparison with the positions of the active portions of the storm as depicted on digitized radar.

Figures 101 through 116 show the progression of the storm across the network. The gust front locations, the zones of intense convergence and the steep drop in θ_e across the gust front are clearly defined, and show in detail the relationship between the intense convergence and storm outflow. The gust front enters the network at 1840 CDT and crosses the interpolation grid in roughly a NW to SE direction in 55 minutes, leaving the grid between 1935 and 1940. An estimate of its average surface speed is thus 16.5 m/sec.

Initially, the radar echo contours show a sharp gradient in rainfall rate at the leading edge of the storm, which generally lies behind the position of the gust front by about 5-10 km. The intense convergence regions associated with the gust front generally are about 10 km in width and lie ahead of the gust front, towards the direction of propagation. The echo spreads out perpendicular to the gust front and behind it, leaving light rain and low θ_e at the surface as it passes over the grid.

30 JULY 1979 VIN

PAM #8 WIND SPEED (M/SEC)
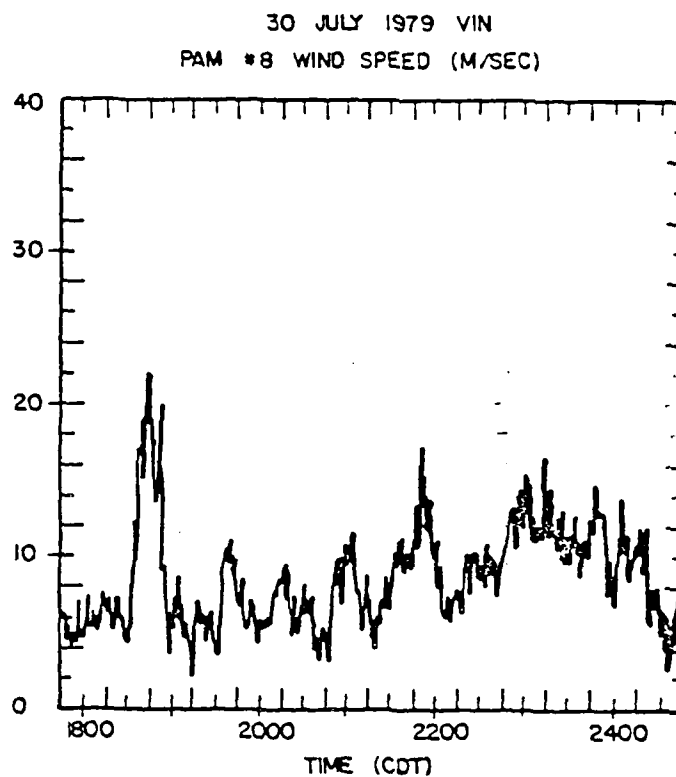
Figure 100. The measurement of time of passage of the major gust front, 30 July 1979, VIN.
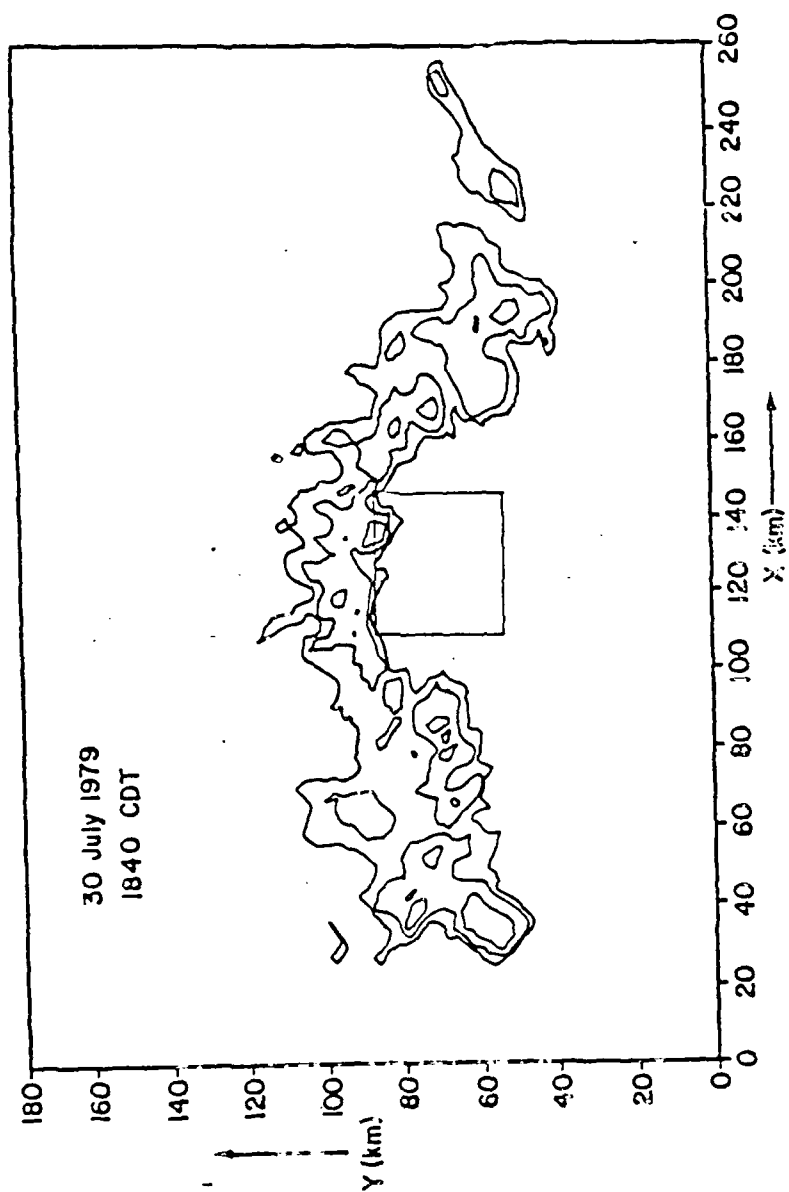
Figure 101. Position of the storm on radar 1840 CDT.
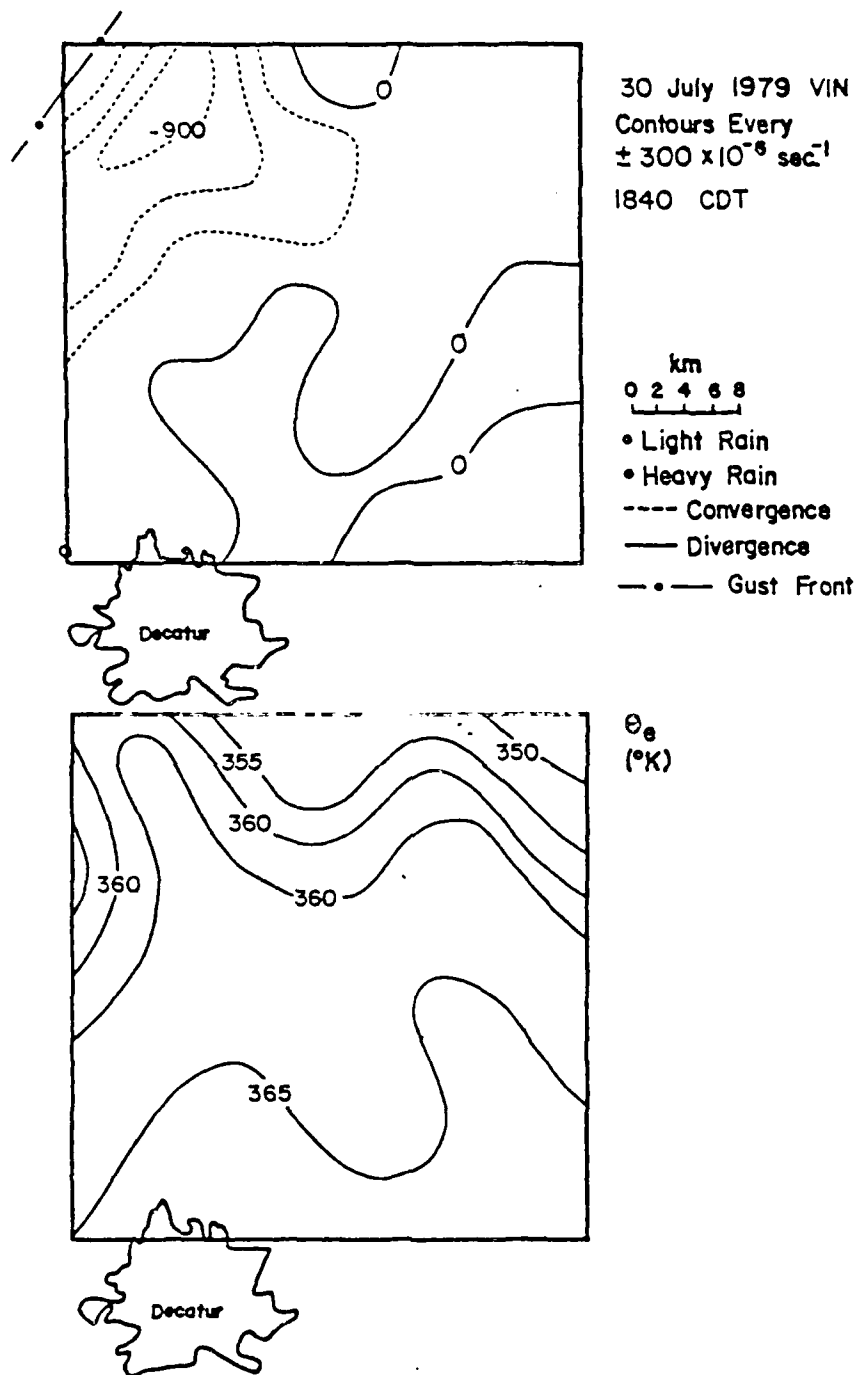
Figure 102. Surface wind and equivalent potential temperature fields 30 July 1979, VIN, 1840 CDT.
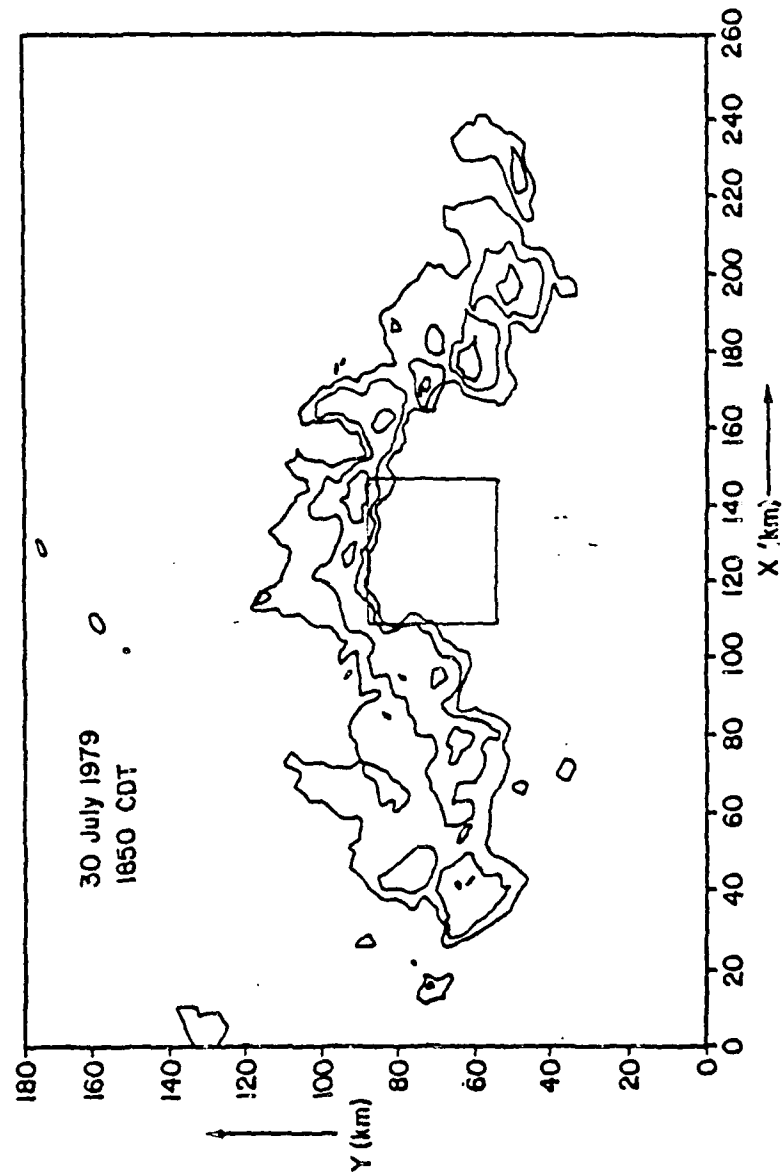
Figure 103. Same as Figure 101 except for 1850 CDT.

30 July 1979 VIN
Contours Every
$\pm 300 \times 10^{-6}$ sec.$^{-1}$
1850 CDT

km
0 2 4 6 8

o Light Rain
• Heavy Rain
---- Convergence
—— Divergence
—•— Gust Front

θ_e

(°K)
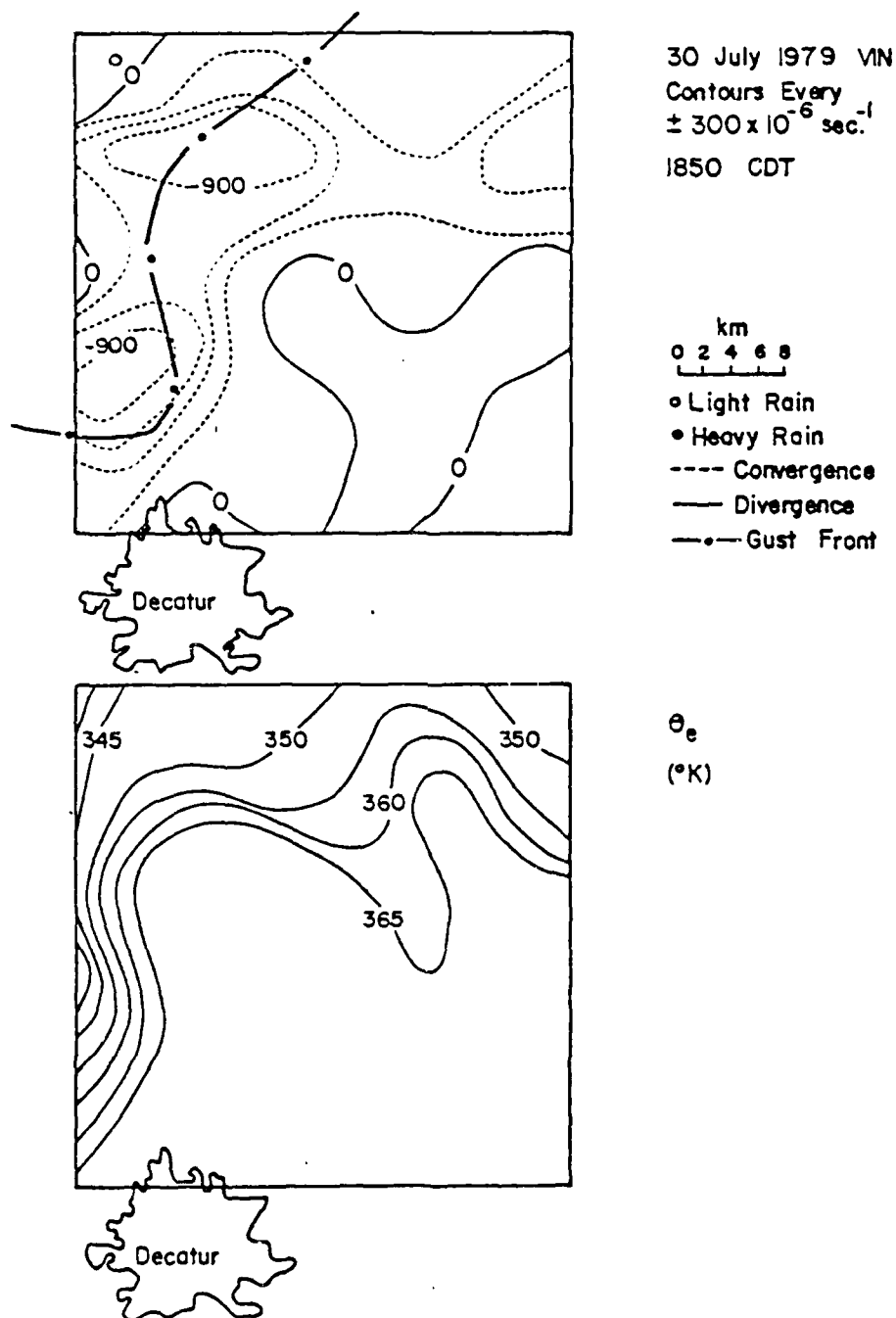
Figure 104.   Same as Figure 102 except for 1850 CDT.
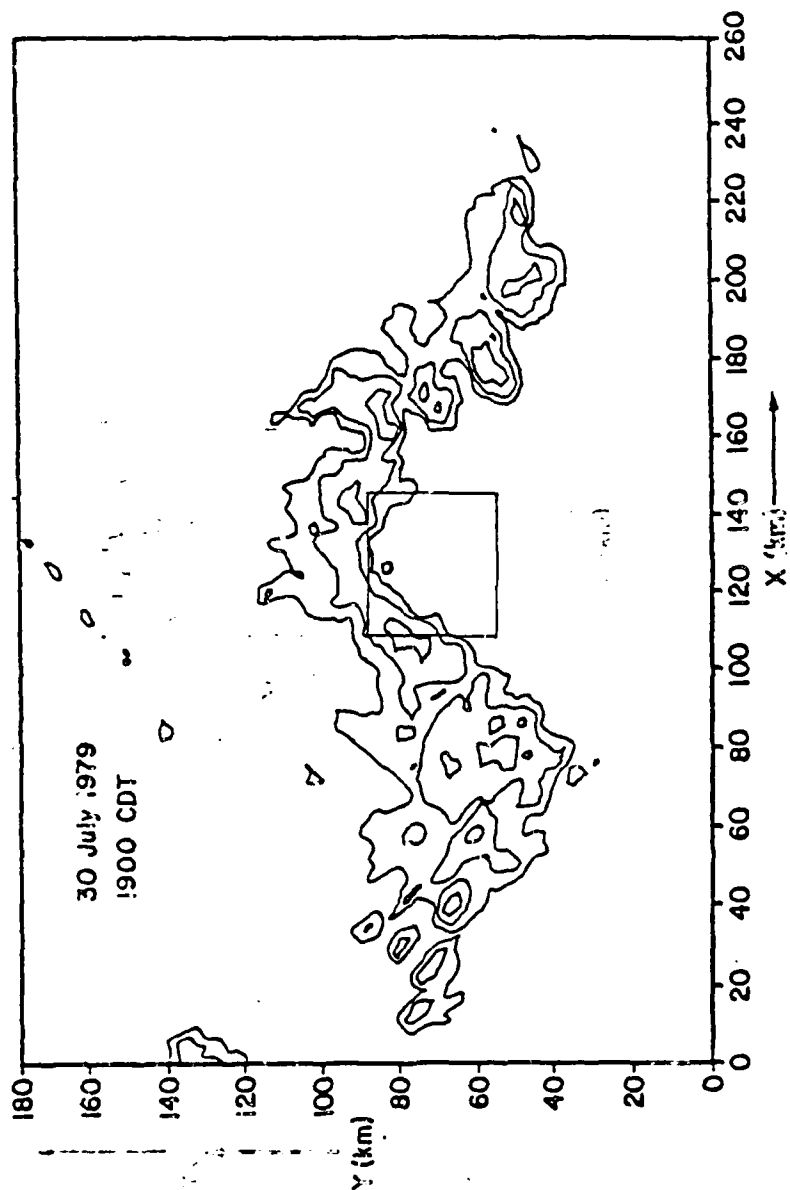
Figure 105. Same as Figure 101 except for 1900 CDT.

30 July 1979 VIN
Contours Every
$\pm 300 \times 10^{-6}$ sec^{-1}
1900 CDT

km
0 2 4 6 8

• Light Rain
• Heavy Rain
---- Convergence
—— Divergence
—•— Gust Front

θ_e
(°K)
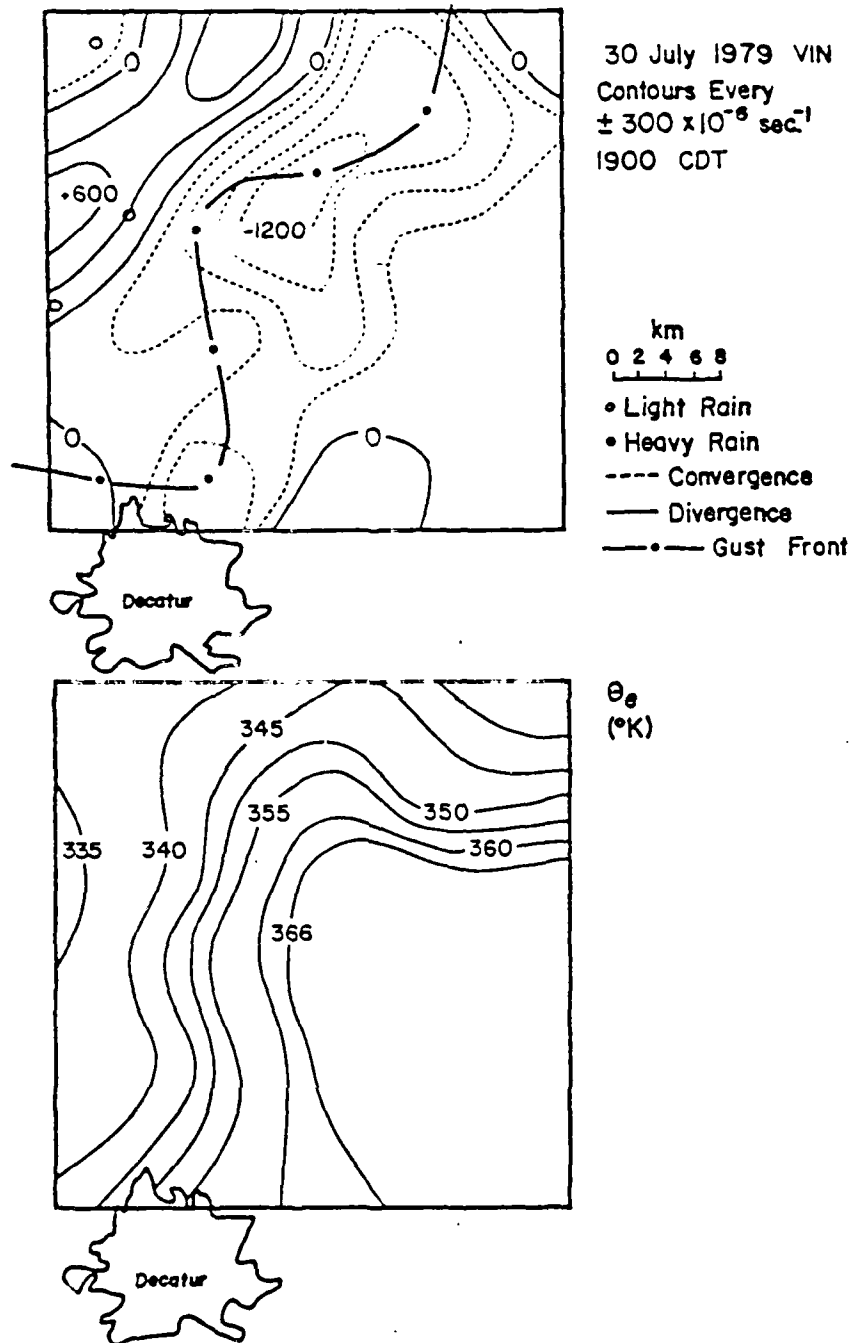
Figure 106. Same as Figure 105 except for 1900 CDT.

30 July 1979 VIN
Contours Every
$\pm 300 \times 10^{-6}$ sec^{-1}
1910 CDT

km
0 2 4 6 8
• Light Rain
• Heavy Rain
---- Convergence
—— Divergence
—•— Gust Front
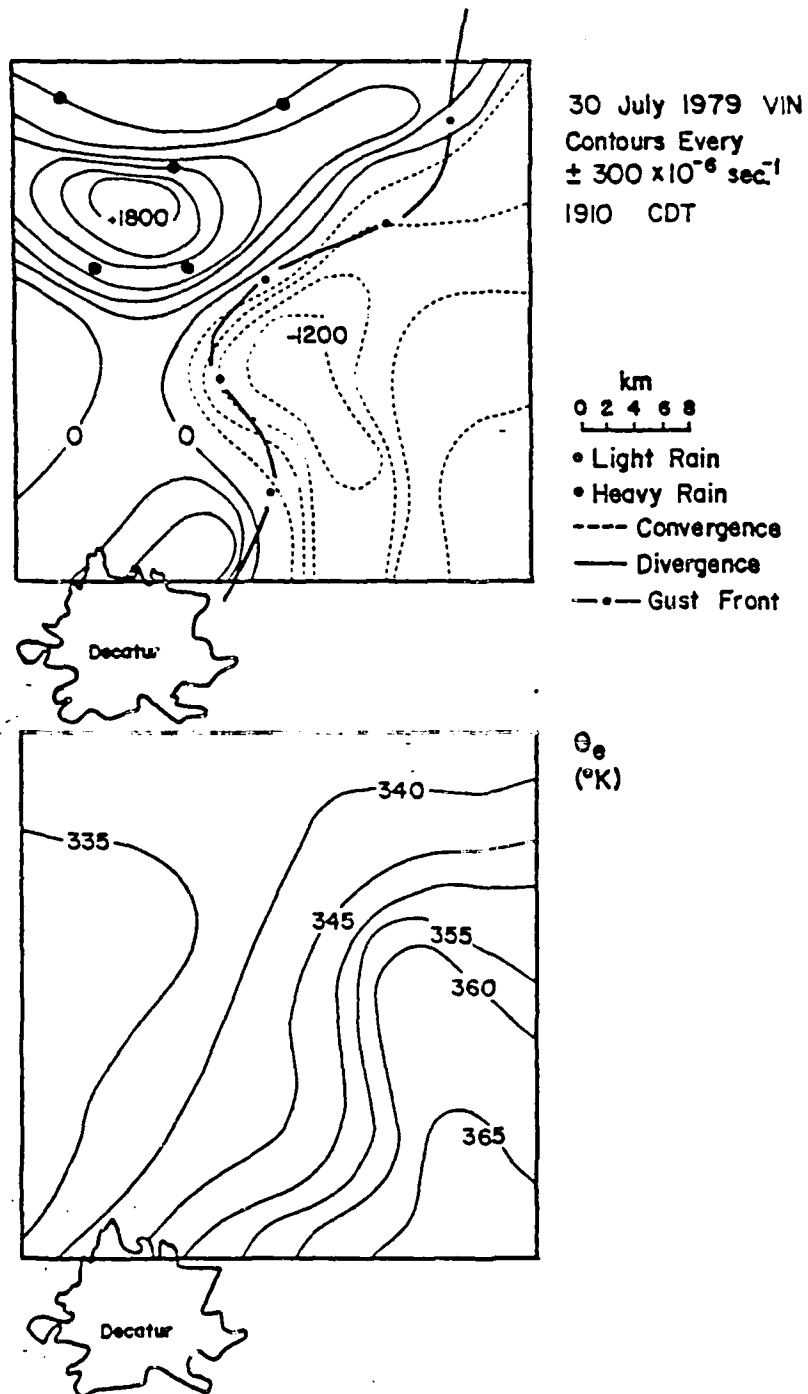
Figure 107. Same as Figure 102 except for 1910 CDT.
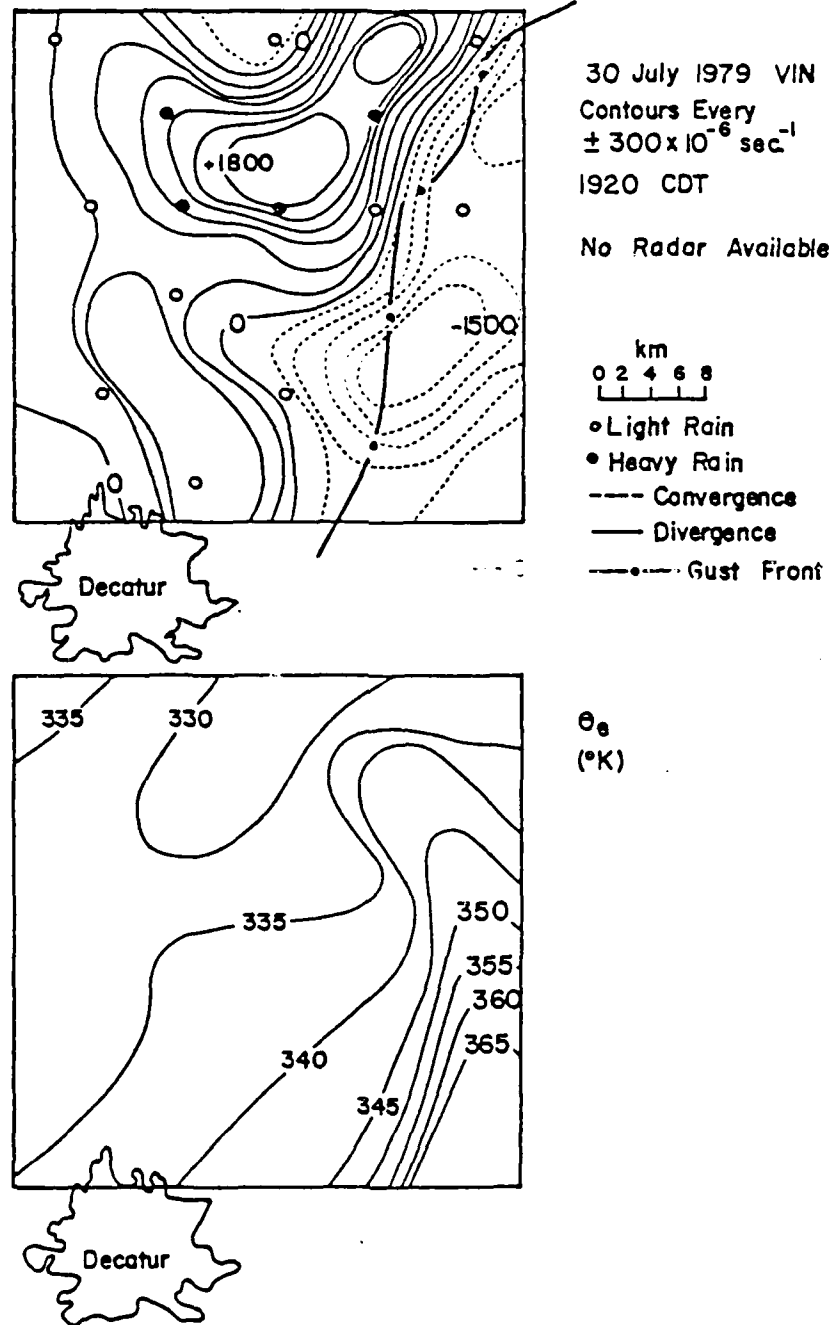
Figure 108. Same as Figure 102 except for 1920 CDT.

30 July 1979
1930 CDT

Y (km)

X (km)
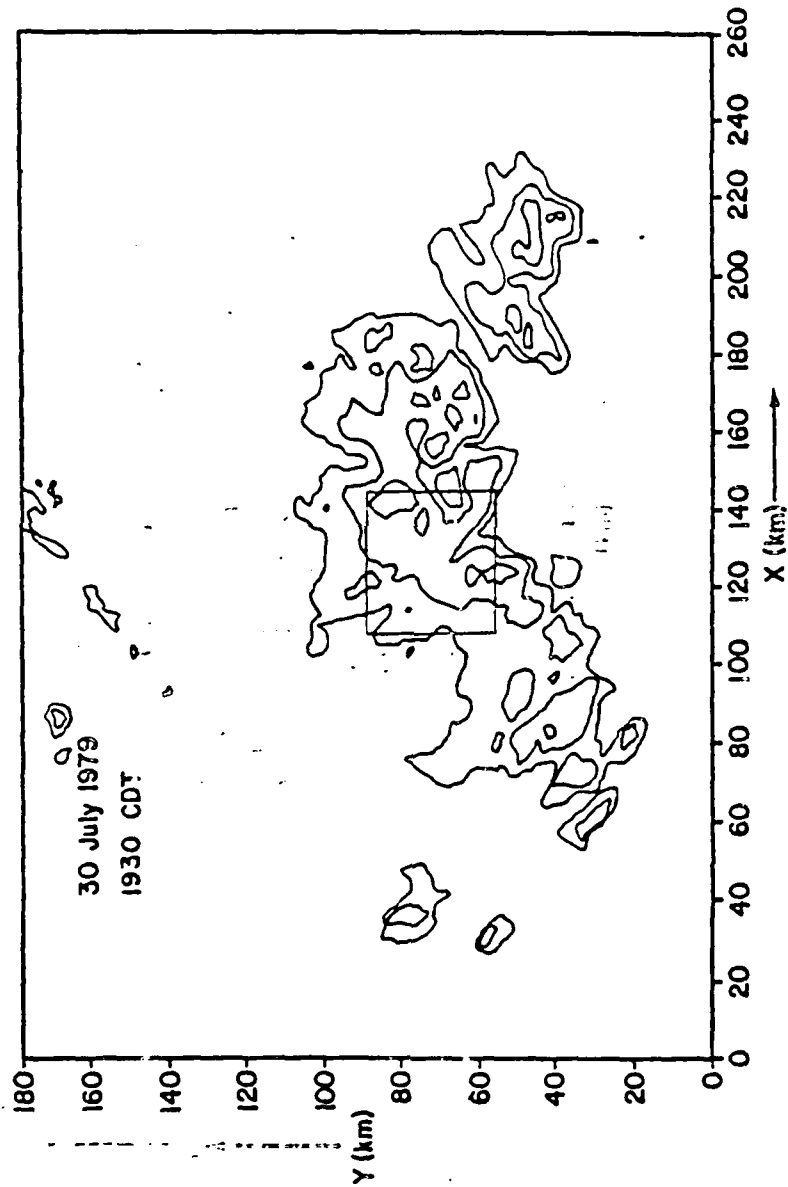
Figure 109. Same as Figure 101 except for 1930 CDT.

30 July 1979 VIN
Contours Every
±300 ×10⁻⁶ sec⁻¹
1930 CDT

km
0 2 4 6 8

• Light Rain
• Heavy Rain
---- Convergence
—— Divergence
—•— Gust Front

Θₑ
(°K)
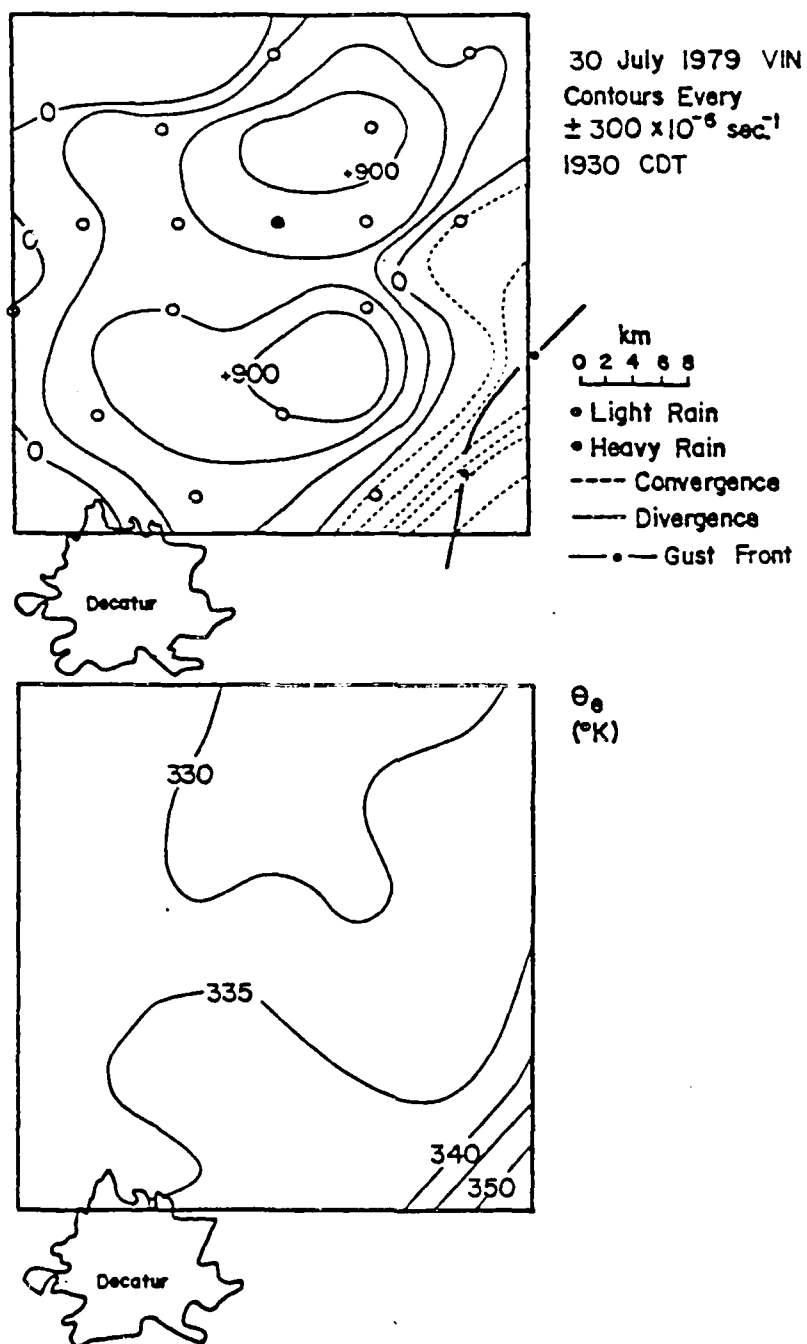
Figure 110. Same as Figure 102 except for 1930 CDT.

30 July 1979
1940 CDT
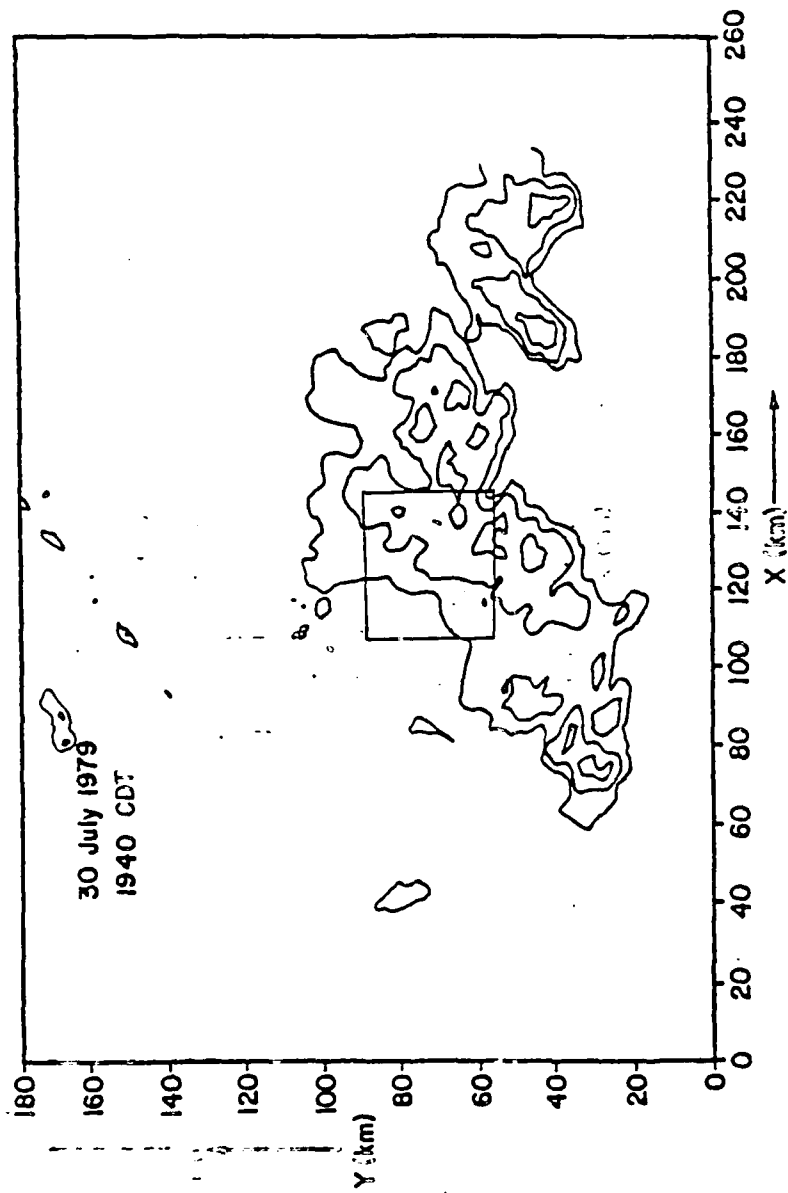
Figure 111. Same as Figure 101 except for 1940 CDT.

30 July 1979 VIN
Contours Every
$\pm 300 \times 10^{-6}$ sec^{-1}
1940 CDT

km
0 2 4 6 8

• Light Rain
• Heavy Rain
- - - - Convergence
——— Divergence
—•—— Gust Front

Θ_e
(°K)
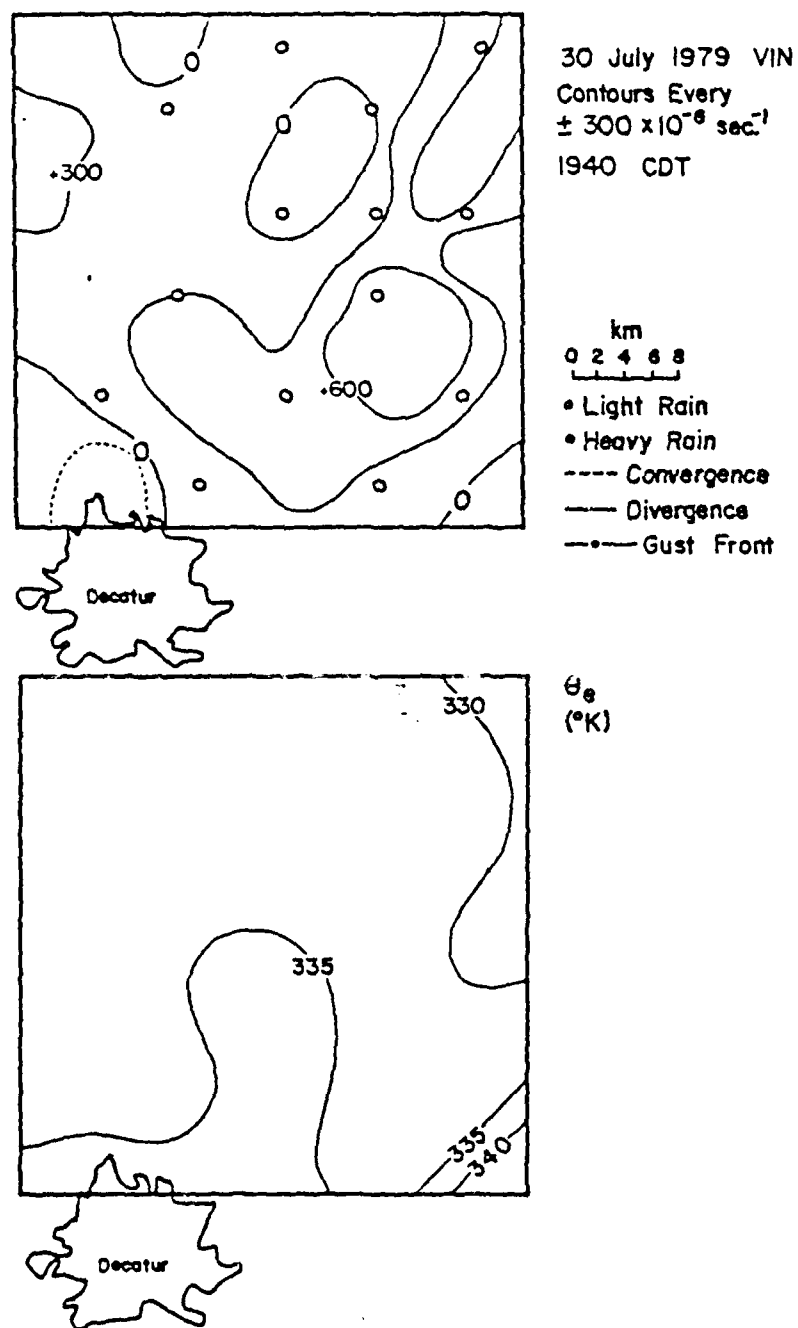
Figure 112. Same as Figure 102 except for 1940 CDT.
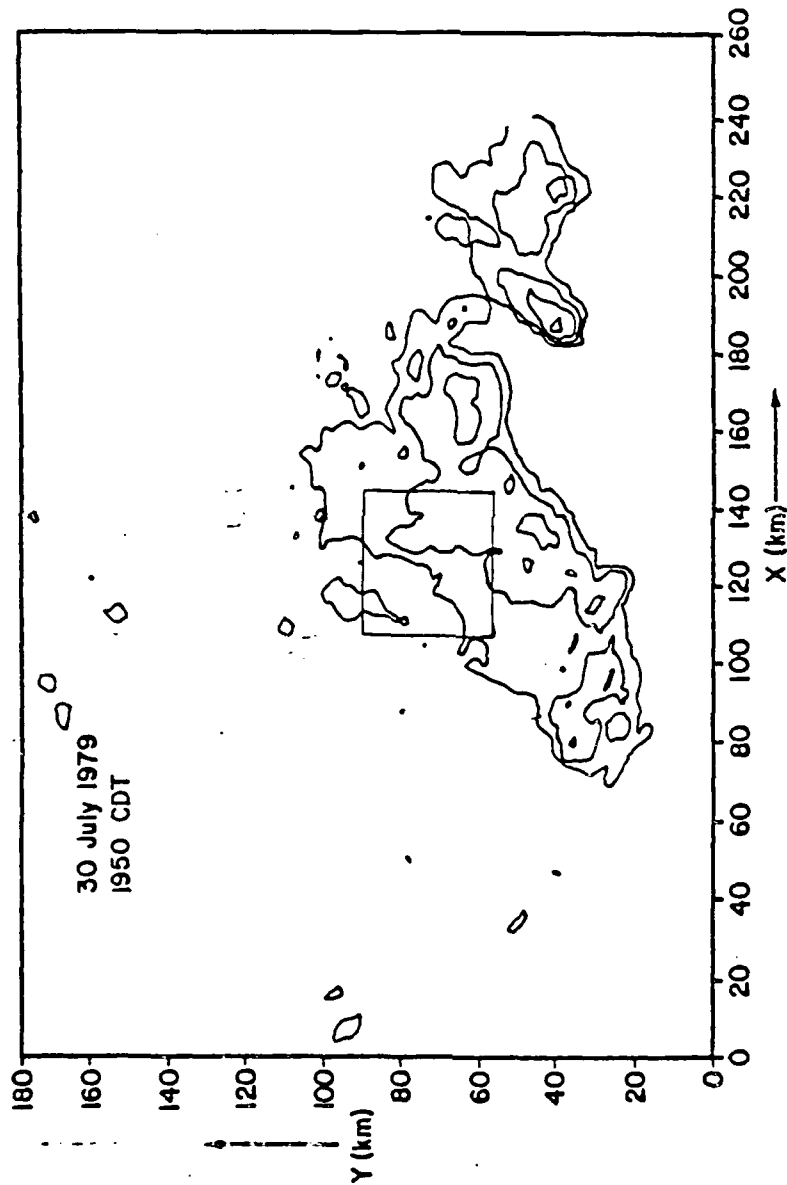
Figure 113. Same as Figure 101 except for 1950 CDT.

30 July 1979
Contours Every
$\pm 300 \times 10^{-6}$ sec.$^{-1}$
1950 CDT

km
0 2 4 6 8

° Light Rain
• Heavy Rain
---- Convergence
—— Divergence

Θ_e
(°K)
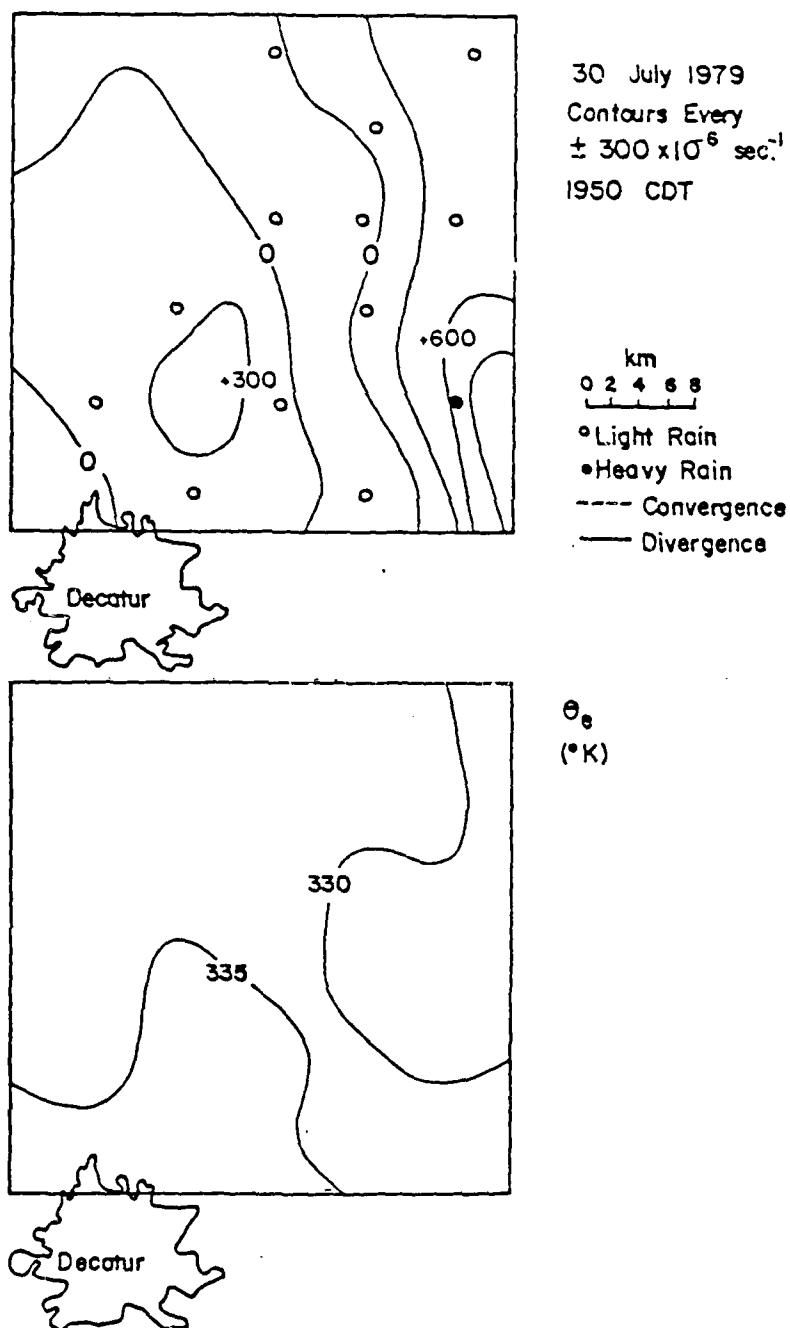
Figure 114. Same as Figure 102 except for 1950 CDT.
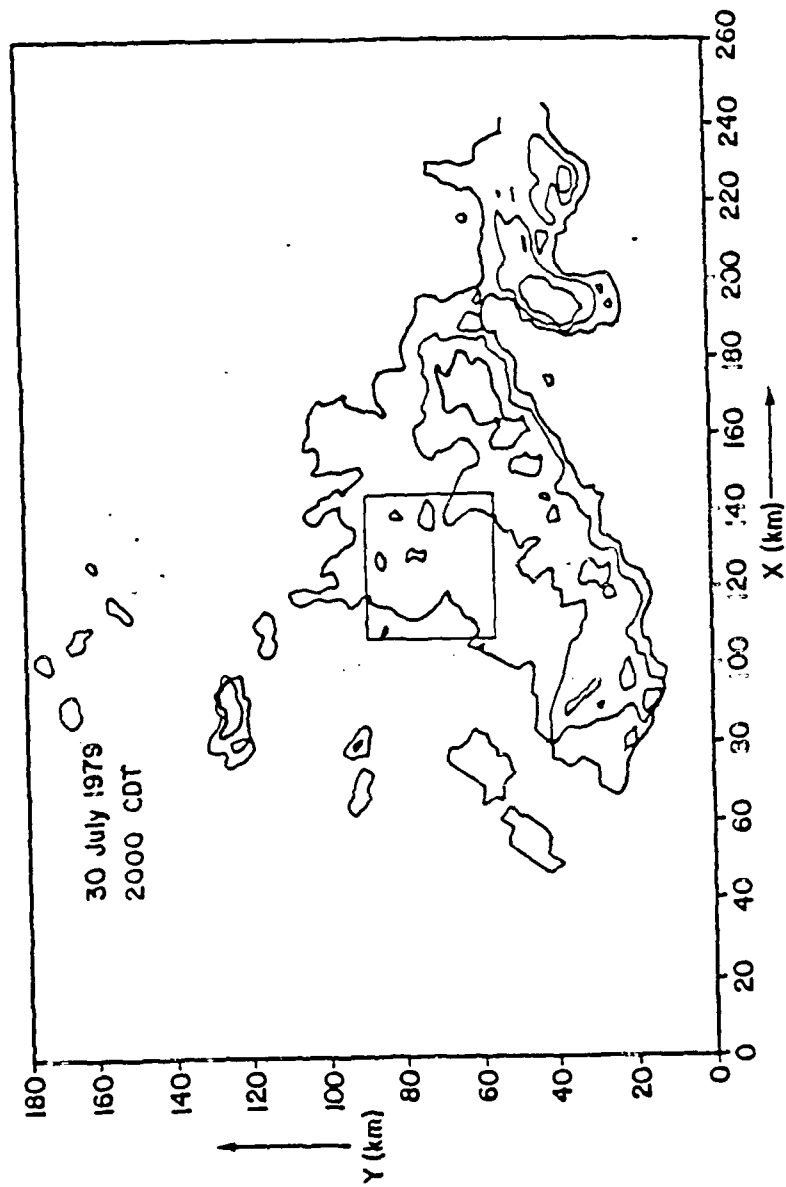
Figure 11b. Same as Figure 11l except for 2000 CDT.

30 July 1979

Contours Every
± 300 x 10⁻⁶ sec⁻¹

2000 CDT

km
0 2 4 6 8

○ Light Rain
● Heavy Rain
---- Convergence
—— Divergence

Decatur

+600

330

330

335   330

θ_e

(°K)

Decatur
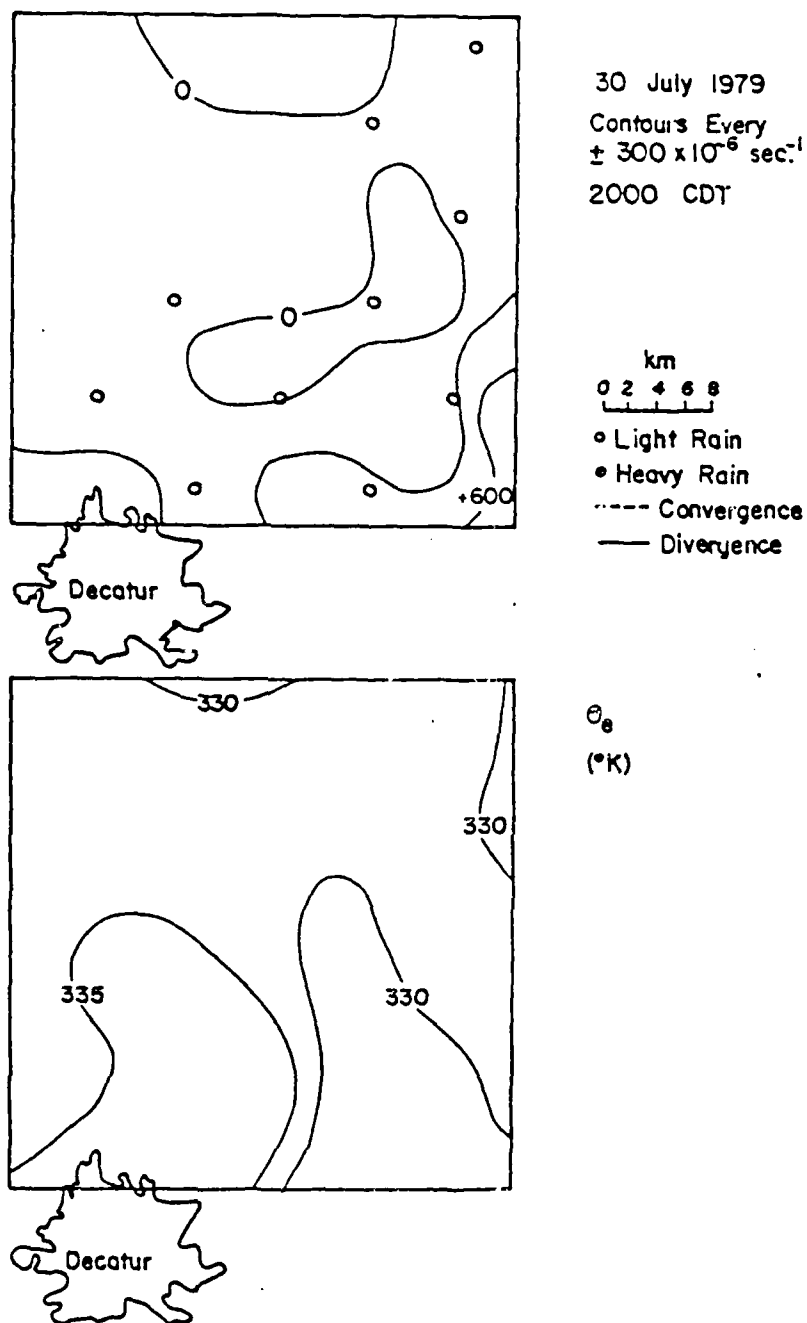
Figure 110.   Same as Figure 102 except for 2000 CDT.

8. THE STORM OF 13 JULY 1979

This storm is a more moderate one than that of 30 July, and will be treated in less detail.

Figures 117 and 118 show the diurnal surface variations in θ_e, mixing ratio, area-averaged divergence and rainfall. Comparison with Figures 82 and 83 show the surface air to be drier, much lower in moist static energy and the fluctuations in the area-averaged divergence fields to be less dramatic than on 30 July. However, the post-storm states are similar. The network average drop in θ_e and mixing ratio across the storm are only 16°K and 2.1 gm/kg in this case, in comparison with a 40° K and 8.6 gm/kg drop in the previous case.

The pre-storm profiles follow the same patterns as the 30 July case, but with lower values of all variables.

At the time of onset of the persistent area-averaged convergence (Figure 119), there is relatively weak convergence just left of the center of the grid, with values of convergence as high as -422×10^{-6} sec^{-1}. The θ_e fields show no marked gradient at this time. By 1430 CDT (Figure 120) a weak convergence-divergence dipole has evolved in the southern part of the network, and the CHILL radar shows two weak echoes over that point of the grid. Notice that although no rain was recorded at the PAM sites in this region, the presence of this small shower was detected in the surface wind fields. In fact, records of the fine-mesh rain gauge array do show light rainfall to have fallen into this part of the network (at Station 149) starting at 1430 CDT. This is the earliest recorded rainfall inside the interpolation grid for this date. It was seen in the previous case study that weak regions of surface convergence were associated with the presence of a line of towering
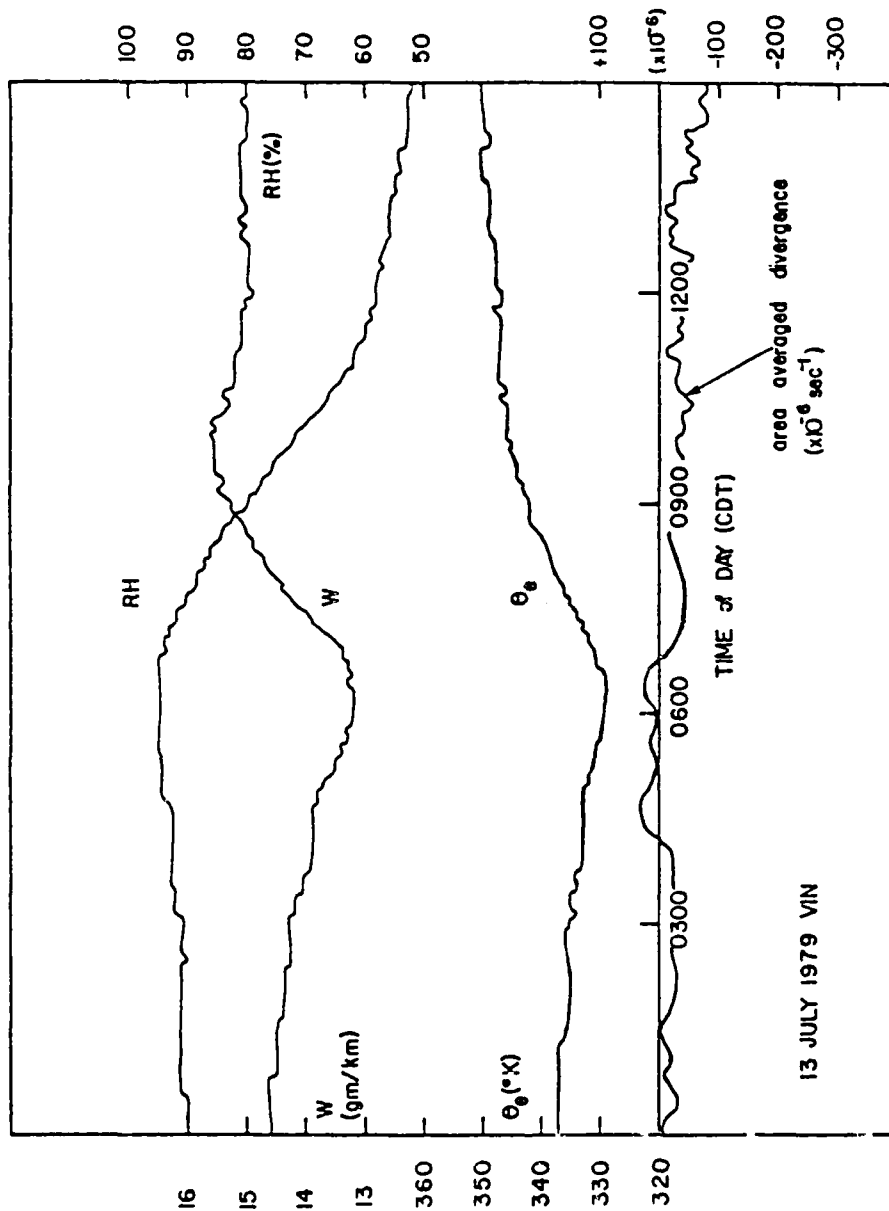
Figure 117. Daily profiles for the storm of 13 July 1979, VIN.
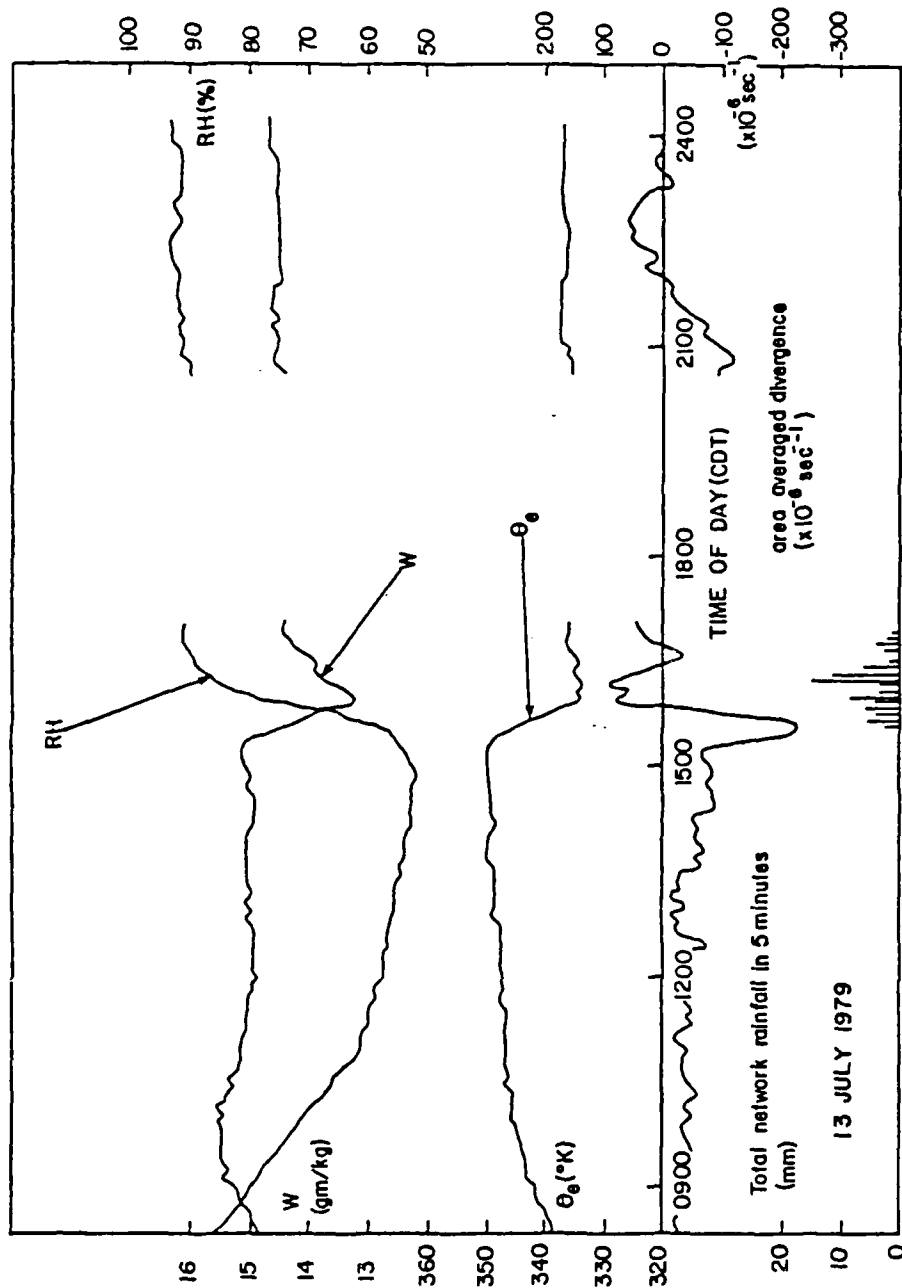
Figure 118. Daily profiles for the storm of 13 July 1979, VIN.

13 July 1979 VIN
Contours Every
$\pm$ 100 x 10^{-6} sec^{-1}
1330 CDT

km
0 2 4 6 8
• Light Rain
• Heavy Rain
---- Convergence
—— Divergence

Decatur

θ_e
(°K)

Decatur
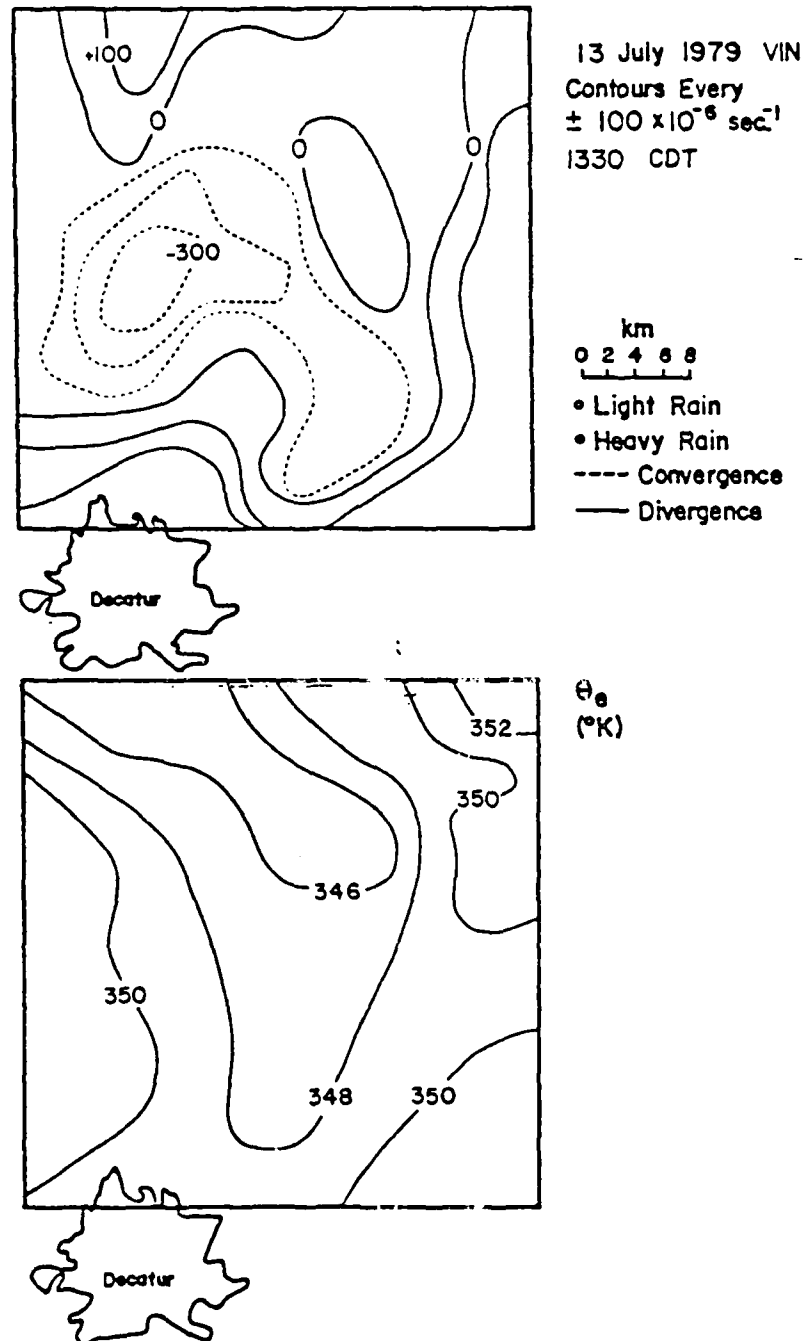
*Figure 110. Surface wind and equivalent potential temperature
fields, 13 July 1979, VIN, 1330 CDT.*

13 July 1979 VIN
Contours Every
± 300 x 10⁻⁶ sec⁻¹

1430 CDT

km
0 2 4 6 8
• Light Rain
• Heavy Rain
---- Convergence
—— Divergence

θ_e
(°K)
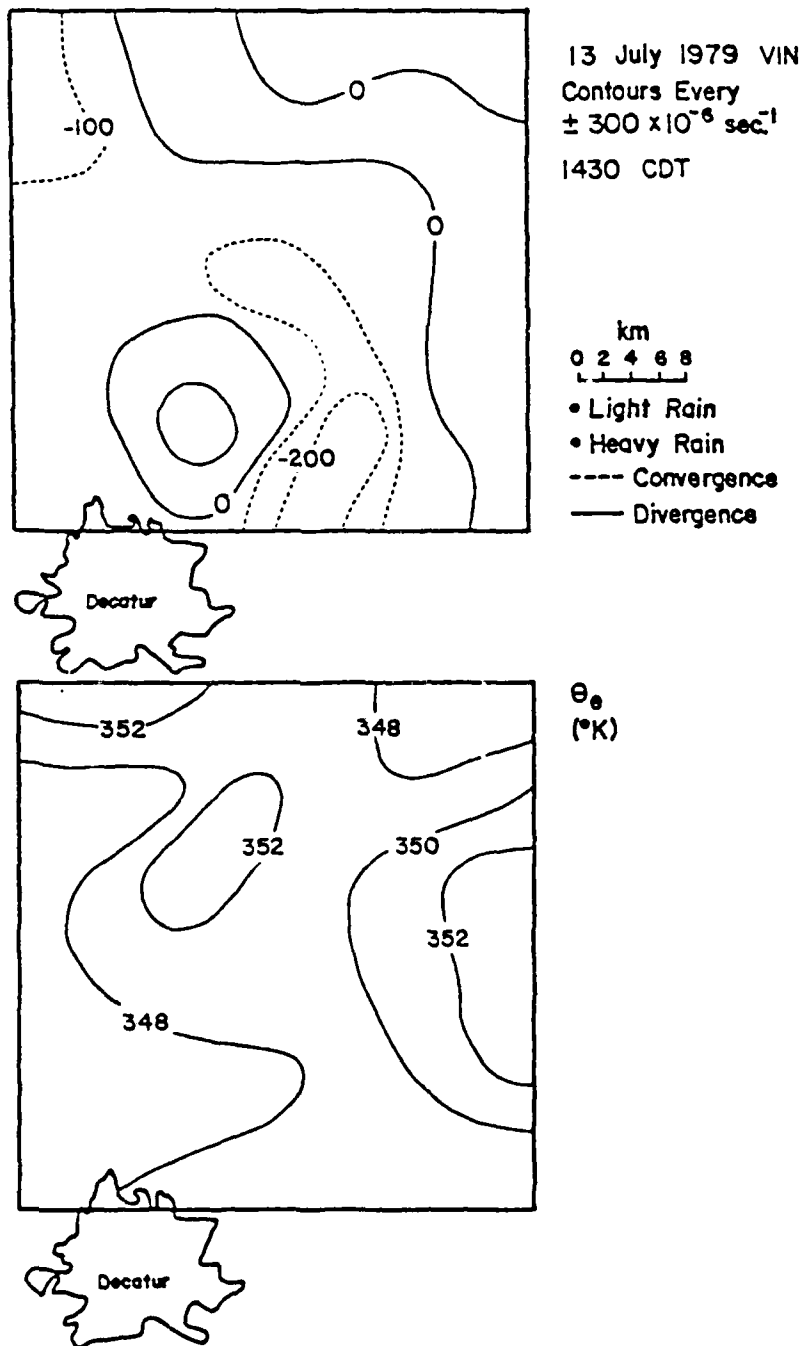
Figure 120. Same as Figure 119 except at 1430 CDT.

cumuli north of the network. It seems possible that the smaller clouds may be detectable in the surface wind fields, although many more comparisons with visible cloud data must be made before the relationship is clearly defined.

The surface θ_e fields do not seem to respond to the smaller shower.

At 1515 CDT (Figure 121) there is a rapid increase in area-averaged convergence, and the surface wind fields show a convergence zone of some strength in the NW corner, with the approach of a gust front. The radar shows that there is a fairly large system about 20 km due north of the network, and a vigorous isolated cell off the SE corner. The surface θ_e fields show little response.

The time of peak area-averaged convergence is 1535 CDT, and although no rain has been detected by the PAM system within the interpolation grid, the position of the convergence zone, the θ_e gradients, the gust front position and the divergence zone show clearly the location of the storm (Figure 122). A PAM station just north of the divergence area reported 0.10" of rainfall in the previous 5 minutes. The system which was 20 km north of the grid moved southwards over the network, while the cell off the southeastern corner remained stationary. By 1550 CDT the gust front, convergence zone and strong θ_e gradients all moved southward, and there is a region of strong divergence beneath the storm in the southeastern corner. The position of the gust front at this time is on the northern edge of the stationary echo southeast of the grid (Figure 123).

The radar at 1615 CDT shows dissipation of weak echoes over the western third of the grid, with an intense echo off the southeastern

13 July 1979 VIN
Contours Every
$\pm 300 \times 10^{-6}$ sec.$^{-1}$
1515 CDT

km
0 2 4 6 8

○ Light Rain
● Heavy Rain
---- Convergence
—— Divergence
—•— Gust Front

θ_e
(°K)
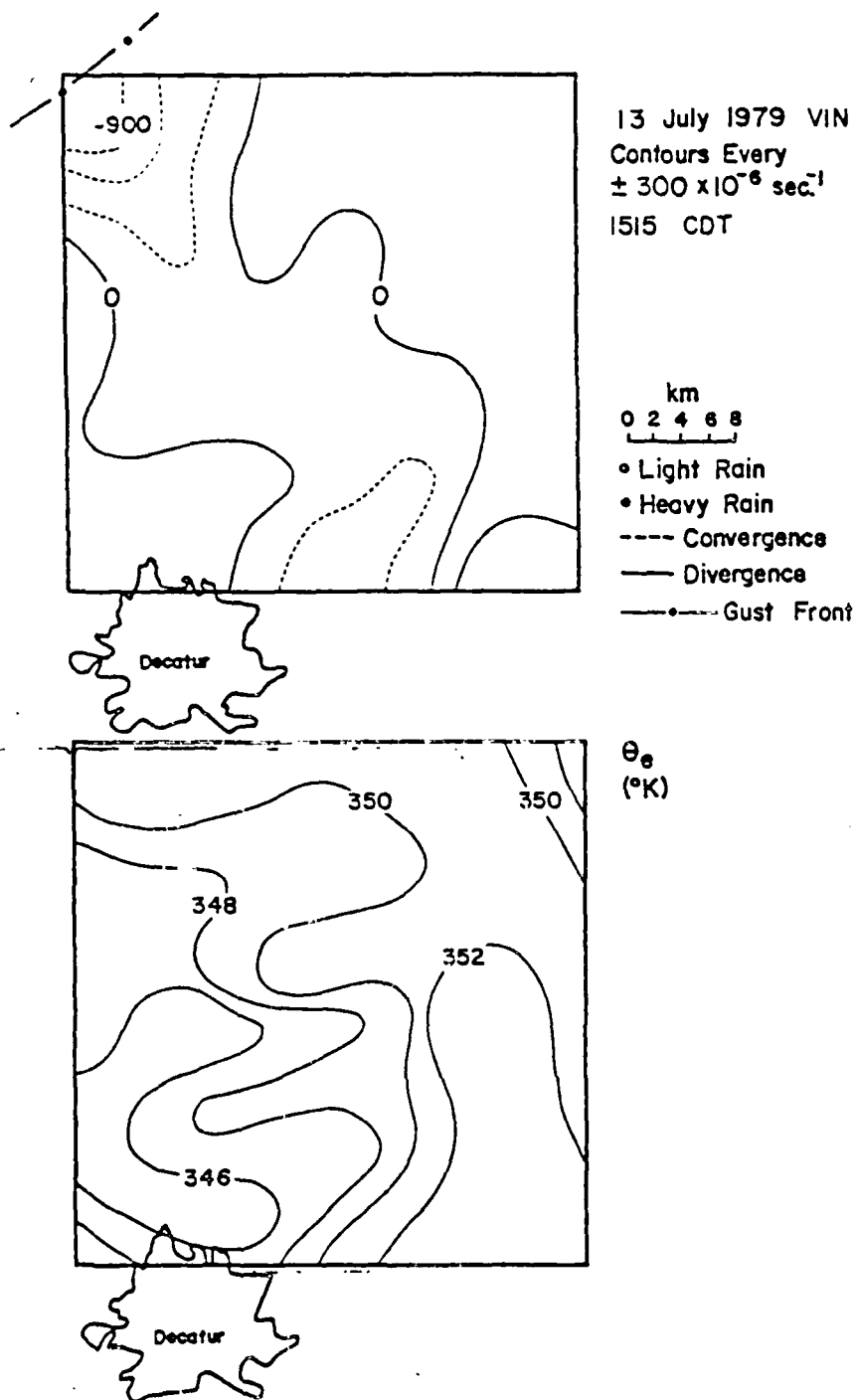
Figure 121. Same as Figure 113 except at 1515 CDT.

13 July 1979 VIN
Contours Every
$\pm 300 \times 10^{-6}$ sec^{-1}
1535 CDT Peak Convergence
Heavy Rain Just
North Of Divergence
Zone

km
0 2 4 6 8

• Light Rain
• Heavy Rain
---- Convergence
—— Divergence
—o— Gust Front

θ_e
(°K)
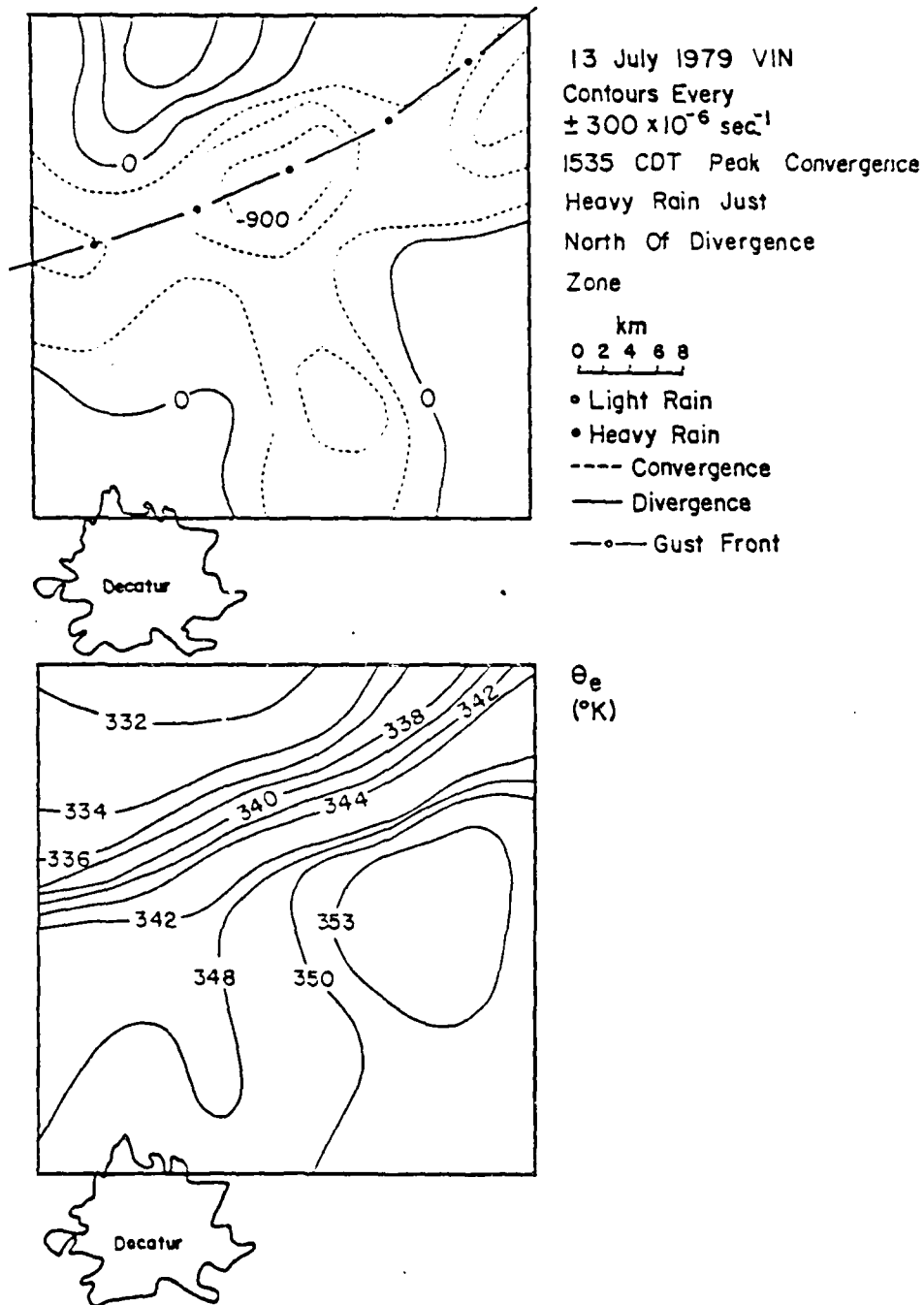
Figure 122. Same as Figure 119 except at 1535 CDT.
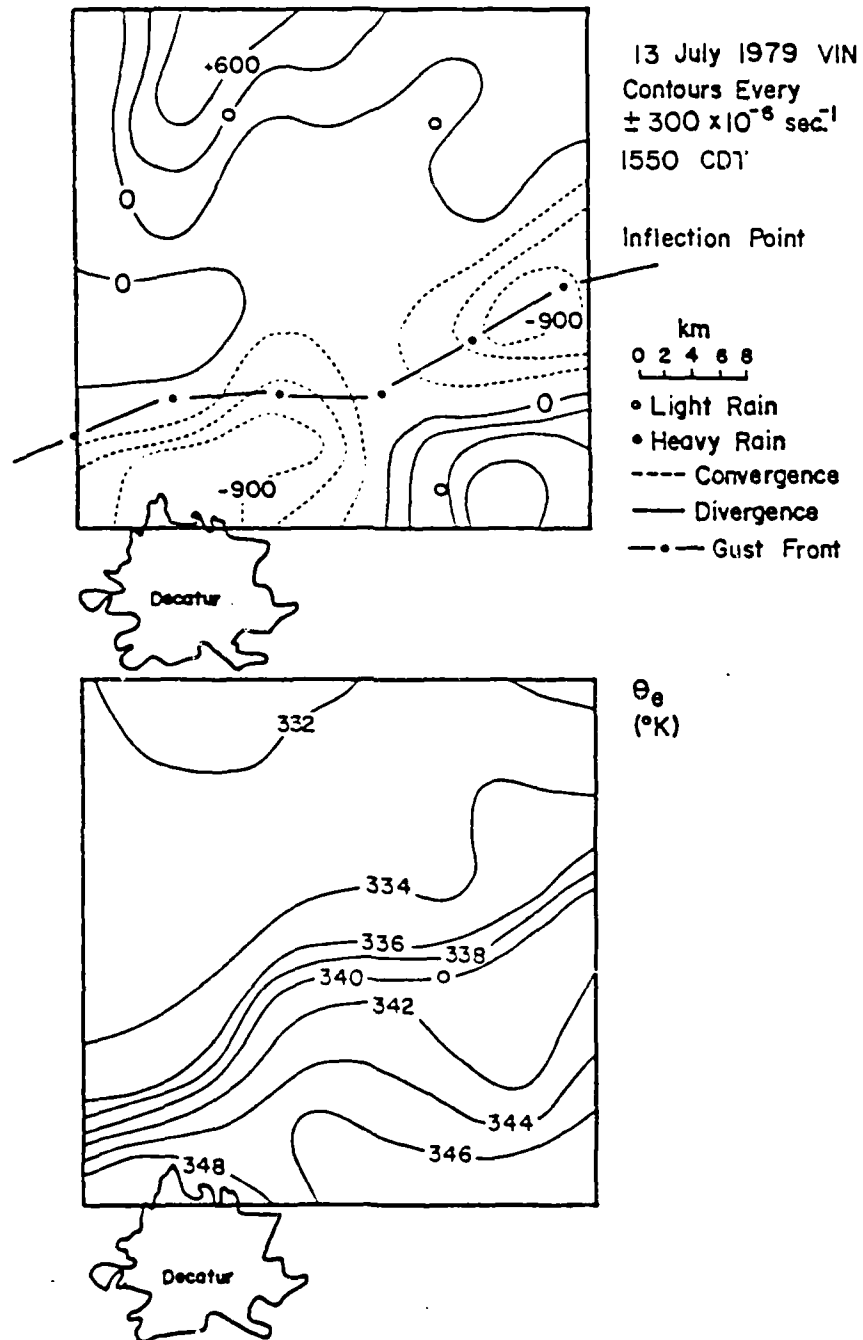
Figure 123. Same as Figure 119 except at 1550 CDT.

corner. By 1655, the system has moved eastward (Figures 124 and 125).

The two examples of Illinois storms illustrated in this chapter show that the surface divergence fields behave in a manner which is similar to that seen beneath deep Florida convection. The magnitudes and relative positions of the convergent and divergent regions are the same, and storms in both regions exhibit the same sequence of propagation and initiation of new activity in the direction of the intense regions of surface convergence.

The PAM data allowed conclusive identification of the relationship between the regions of intense convergence and the positions of the gust front, which marks the leading edge of the outflow from the parent storm. The morphology of the surface wind divergence fields is the same in Florida and Illinois, although the initiation mechanisms are of a *different nature*. It is suggested by these comparisons, that propagation and maintenance of convective activity is partly a property of the convection itself. However, the convective activity is not sufficient in itself to sustain continuous cumulus convection. In addition, moist static energy input from the mesoscale (e.g., Florida sea breeze) or synoptic scale (e.g. frontal squall lines over Illinois), is also required to sustain the convection.

13 July 1979 VIN
Contours Every
$\pm\ 300 \times 10^{-6}\ \text{sec}^{-1}$
1615 CDT

Peak Divergence

km
0 2 4 6 8

• Light Rain
• Heavy Rain
---- Convergence
—— Divergence

θ_e
(°K)
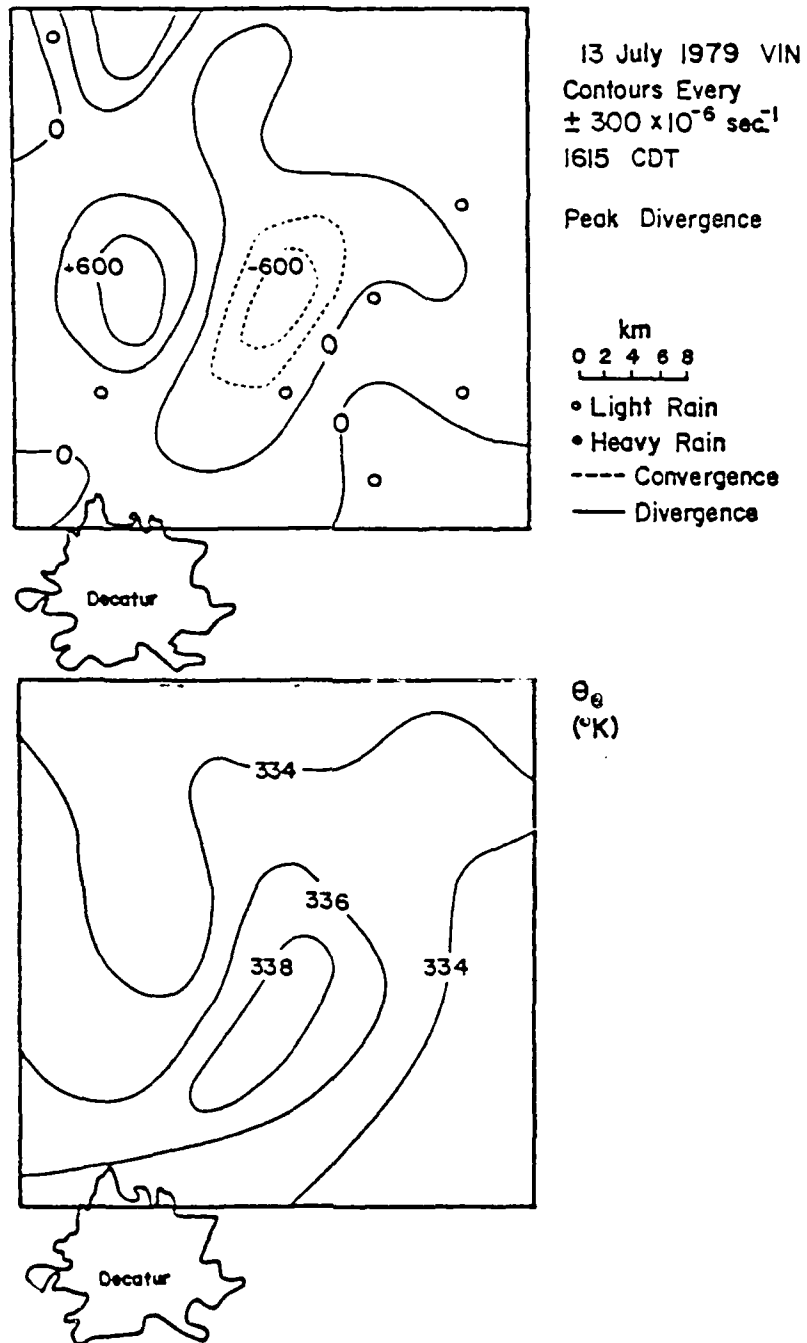
Figure 124. Same as Figure 119 except at 1615 CDT.
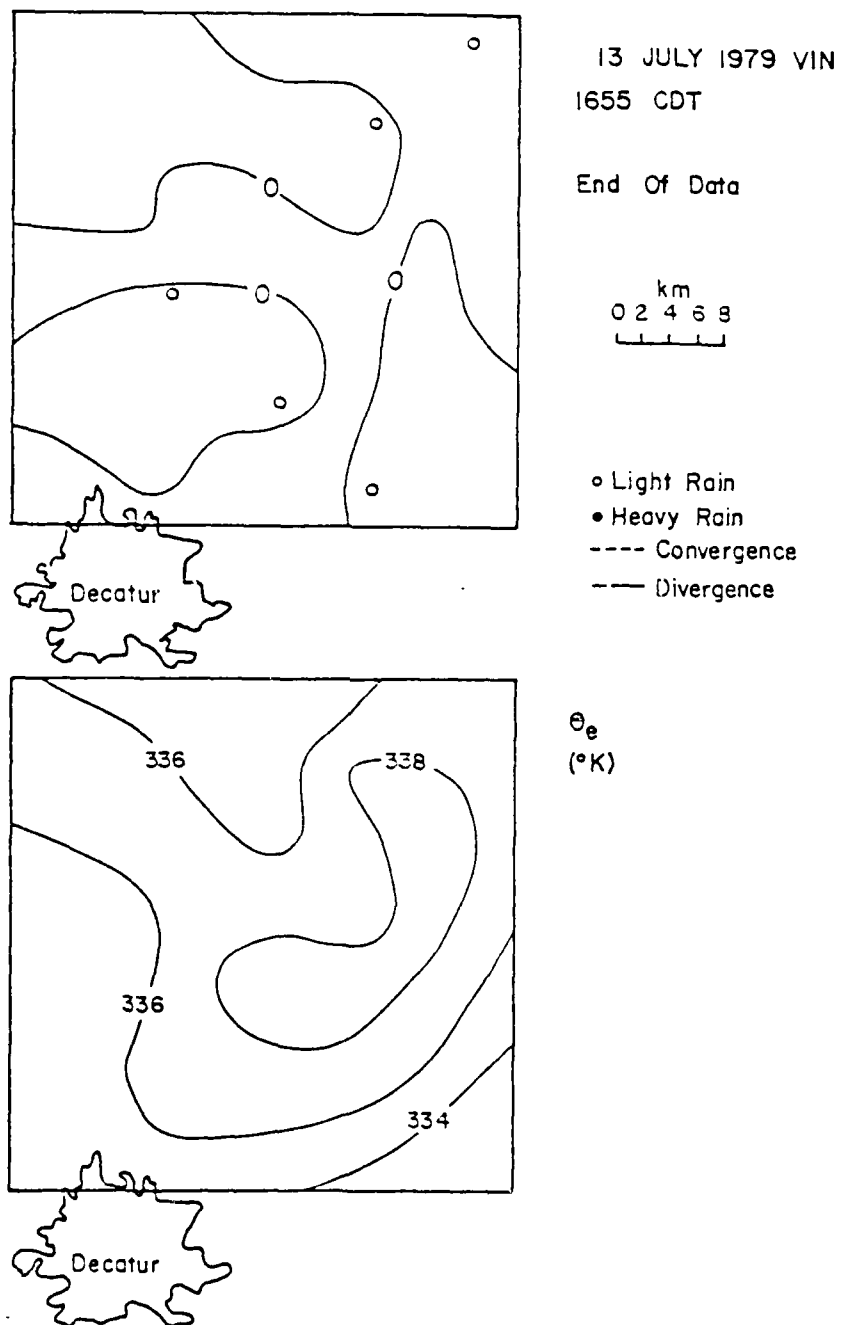
Figure 125. Same as Figure 119 except at 1655 CDT.

CHAPTER 8

SUMMARY AND CONCLUSIONS

The findings of previous workers, such as Byers and Braham
(1949), Matsumoto (1967), Newton (1968), Charba (1974), Goff (1976),
Brandli and Orndorff (1976), Ogura and Chen (1977), Fankhauser and
Mohr (1979), Chen and Orville (1980), Houze and Leary (1979) and Simpson
(1980), that outflows from intense convection play a major role in
the initiation and prolongation of convective activity are substan-
tiated in this study. The study, however, advances understanding of
the relationship between the outflow in terms of location, intensity
and subsequent dynamical effects on the maintenance of storms.

The outflow from pre-existing convection occurs in the subcloud
layer and is clearly detectable in the surface layer. The process of
outflow generation of new convection and its role in the propagation of
deep convective activity is found to be consistent, regardless of the
process which initiates the original convection. Analyses of storms in
Florida, where the convection is initiated by the peninsular scale sea
breeze forcing and storms in Illinois which were associated with synop-
tic scale frontal activity, show the same basic response of the velocity
field in the subcloud and surface layers of the atmosphere. The Illinois
cases clearly demonstrate the causal relationship between the formation
of intense regions of surface convergence in the direction of propaga-
tion of a large near steady-state squall line, and the gust front from
the squall.

The signal in the area-averaged divergence in the surface wind fields thus contains information about the storm which is propagating into the network, in terms of the time of occurrence of maximum rainfall rate, the likely direction of passage of the storm over the network, the magnitude of the intensity of the approaching storm, and the point in time when the storm will start to leave the network, or begin to dissipate over the network. All of this information is extremely useful in terms of short range (30 min to an hour) forecasting.

The early morning triggering of convection over south Florida is related to the peninsular scale forcing and the convection thus initiated goes through a smooth diurnal cycle. In Florida, forcing on a peninsular sea breeze scale occurs on a regular, definable daily basis. The peninsular scale forcing over south Florida is linked through its rate of change to the convective scale by the initiation of convective activity. Once initiated, surface outflows serve to maintain, propagate and hence prolong the subsequent convection. The time of first occurrence of an excess of upward convective transports over downward convective transports in the morning coincides with the period of maximum rate of change in the peninsular scale forcing. The continued excess in upward convective transports over downward convective transports during the rest of the day follows a curve similar in shape as that of the rate of change, with time, of the peninsular scale forcing. After the peninsular scale convergence sets the convective feedback mechanism in motion, the feedback mechanisms (surface outflows) maintain and continue to intensify, the convective activity long after the peninsular scale convergence has passed its peak value. As the rate of change of the peninsular scale forcing becomes negative, the convective feedback mechanism becomes less effective, the outflow-convergence process

diminishes in intensity and convective activity ceases for the day.
Competition for increasingly scarce energy rich air at the surface,
and the effects of the presence of cumulonimbus anvils on the decreas-
ing surface radiation may also play an important role in the gradual
shut-down of convective activity in the late afternoon.

Analysis of soundings taken over the south Florida experimental
network, coupled with the diurnal cycle of convective activity described
above, suggest strongly that deep, raining convection over south Florida
must be viewed as the culmination of a daily process of convective
activity, with a gradual evolution towards a state of widespread cumulo-
nimbus convection. The sounding analyses demonstrate that as the
convective feedback process grows in intensity, the thermodynamic
profiles in the vertical go through successive stages which show a
progressive moistening in the layer between 850 mb-600 mb, and a
consequence increase in the moist static energy in that layer. As
the daily convective feedback activity progresses, the profiles go
from a state of relatively low moisture and moist static energy in that
layer during the periods of weak convective activity, to a condition
of relatively high moisture and moist static energy during the periods
of stronger convective activity associated with the pre-rain state.
The increase in the moisture and energy at these levels lessens the
chance that entrainment of dry, low energy air will suppress incipient
convection, and hence is a positive reinforcement of the feedback
process in itself. Once the convective mixing is premitted or
initiated by large scale forcing (both peninsular and synoptic), deep
convection can develop. In the absence of the moistening of this layer,
either by advection or by shallow convection, deep convection does not
develop.

Investigation of the way in which convective activity over
south Florida processes water vapor shows convection and convective
clouds to be extremely efficient mechanisms for the vertical mixing
of water vapor. When total water substance (rainfall plus water
vapor) in the subcloud layer is considered, for the convective storm
cycle composited about the period of most intense rainfall rate, the
complete composite storm cycle is 98% efficient. If the role of con-
vective scale up-and downdrafts in the transport of water vapor is
not considered, precipitation efficiency (as is frequently used) is
overestimated. When the role of downdrafts in the downward transport
of water vapor is considered, then the level of maximum precipitation
efficiency during the period of moist intense activity in the storm
cycle is found to be around 40%. In the early and late stages of the
composite storm, the efficiencies in processing water vapor into
precipitation are quite low. The apparent paradox of having an
efficient process in total water substance which is inefficient in
rainfall production is resolved by considering both the vertical redis-
tribution of water vapor and rainfall. The compilation of data in
composite form substantiates this conclusion.

Although the convective process is near 100% efficient in total
water substance if the entire life-cycle is considered, it is less than
100% efficient in total water substance during 68% of the lifetime of
the storm. The balance in total water substance which is obtained over
the entire life cycle is a result of large amounts of rainfall being
dropped from the storm during a single period when the composite storm
is super-efficient. This super-efficient period occurs at the time
of maximum rainfall rate, or equivalently, during the presence of heavy
showers. It is tempting to characterize intense thunderstorms as pro-

cesses which are necessary to restore to balance the total water sub-
stance budget in the subcloud layer, which is constantly being depleted
by mixing from the surface by shallow convective activity.

In exchange for restoring to balance the total water substance
budget in the subcloud layer, and for processing water vapor into liquid
water, the intense stages of convective activity remove much sensible
heat, water vapor and consequently moist static energy from the subcloud
layer, to be redistributed aloft. It is this sensible and latent heat
extracted from the subcloud layer which drives the convective process,
which in turn maintains the balance in total water substance in the
lower levels.

Future field studies of convective clouds should include attempts
to analyze in detail the relationship between convective scale activity
and mesoscale forcing. The Florida peninsula represents a particularly
good laboratory for such studies. Use of arrays of a few judiciously
spaced instrumented towers, and boundary layer probes, giving measure-
ments of kinematic and thermodynamic variables on a fine time-scale,
would eliminate the need to appeal to monthly average profiles of the
peninsular scale forcing, and would produce invaluable data for use in
the study of meso-convective scale interactions.

On the convective scale, similar soundings are needed to determine
the exact dynamic and thermodynamic nature of the relationships which
exist in the outflow-convective initiation process, and the gradual
growth of moisture anomalies in the lower cloud layer. The presence of
fine time-scale resolution tethered balloon data in the FACE mesonetwork
is long overdue, and would allow calculation of cumulonimbus energy and
moisture fluxes and budgets which would be invaluable in the study of
tropical systems. Simultaneous measurements of surface velocity and

variables of state over a domain measuring several tens of miles on a side are now entirely feasible using the present and projected National Center for Atmospheric Research's PAM system.

If the difficult task of precise time and space prediction of convective storms, including severe storms, is to be solved this study underlines the necessity of observing these atmospheric scales of motion on time and space scales commensurate with the phenomenon <u>and</u> imbedded within a framework of measurement depicting the role of the larger atmospheric scales of motion.

The relationship between the thermodynamic and kinematic fields at the surface and in the subcloud layer and the visible cloud cover has yet to be satisfactorily resolved. Fine-resolution, both in time and in space, satellite data coupled with tethered balloon and surface kinematic data would provide a rapid solution to many of the outstanding problems of scale interaction and energetics of the tropical atmosphere.

REFERENCES

Anthes, R., 1977: A cumulus parameterization scheme utilizing a one-dimensional cloud model. Mon. Wea. Rev., 105, 270-286.

Arakawa, A. and W.H. Schubert, 1974: Interaction of a cumulus cloud ensemble with the large scale environment, Part I. J. Atmos. Sci., 31, 647-701.

Augstein, E., M. Garstang and G. Emmitt, 1980: Vertical mass and energy transport by cumulus clouds in the tropics. Deep-Sea Res., Spec. Vol., 9-21.

Barnes, G. and M. Garstang, 1981: Subcloud energetics of precipitating convection. To be submitted to Mon. Wea. Rev.

Betts, A.K., 1976: The thermodynamic transformation of the tropical subcloud layer by precipitation and downdrafts. J. Atmos. Sci., 33, 1008-1020.

Black, P.G., 1979: Apollo-Souyz test project. Summary Report, Vol. II, NASA.

Bolton, D., 1980: The computation of equivalent potential temperature. Mon. Wea. Rev., 108, 204-211.

Brandli, H.W. and J.W. Orndorff, 1976: Satellite-viewed cloud lines. Mon. Wea. Rev., 104, 210-213.

Brock, F. and P. Govind, 1977: Portable Automated Mesonet in Operation. J. Appl. Meteor., 16, 229-310.

Browning, K.A. and F.H. Ludlam, 1962: Airflow in convective storms. Quart. J. Roy. Meteor. Soc., 88, 117-135.

Burpee, R., 1979: Peninsular-scale convergence in the south Florida sea breeze. Mon. Wea. Rev., 107, 852-860.

Byers, H.R. and R.R. Braham, 1949: The Thunderstorm. U.S. Government
    Printing Office, Washington, D.C., 287 pp.

Charba, J., 1974: Application of gravity current model to analysis of
    a squall line gust front. Mon. Wea. Rev., 102, 140-156.

Charnock, H., J.R.D. Francis and P.A. Sheppard, 1956: An investigation
    of wind structure in the trades: Anegada 1953. Phil. Trans. Roy.
    Soc., London, Ser. A, 249, 179-233.

Chen, J.H. and H.D. Orville, 1980: Effects of mesoscale convergence on
    cloud convection. J. Appl. Meteor., 19, 256-274.

Cho, H-R., 1975: Cumulus cloud population and its parameterization.
    Pure and Appl. Geophys., 113, 837-849.

Cotton, W., 1975: Theoretical cumulus dynamics. Rev. Geophys., 13,
    419-448.

Cressman, G.P., 1959: An operational objective analysis system. Mon.
    Wea. Rev., 87, 367-374.

Emmitt, G.D., 1978: Tropical cumulus interaction with and modification
    of the subcloud region. J. Atmos. Sci., 35, 1485-1502.

Fankhauser, J.C. and C.G. Mohr, 1979: The influence of surface wind
    kinematics on a thunderstorm evolution. A.M.S. 11th Conf. on
    Severe Local Storms, preprint volume, pp. 415-420.

Fitzjarrald, D.R. and M. Garstang, 1980: The vertical structure of the
    tropical boundary layer. Submitted to Mon. Wea. Rev.

Frank, N., P.L. Moore and G.E. Fisher, 1967: Summer shower distribution
    over the Florida peninsula as deduced from digitized radar. J.
    Appl. Meteor., 6, 309-316.

Fujita, T., 1955: Results of detailed synoptic studies of squall lines.
    Tellus, 7, 405-435.

Garstang, M., 1980: The tropical atmospheric boundary layer: role

in the formation and maintenance of hurricanes. To be published

in Aust. Meteor. Mag.

Gerrish, R., 1971: A model summer convection in south Florida. J. Appl.

Meteor., 10, 949-957.

Goff, R.C., 1976: Vertical structure of thunderstorm outflows. Mon.

Wea. Rev., 104, 1429-1439.

Hess, S., 1959: An introduction to theoretical meteorology. Holt,

Rinehart and Winston, New York.

Holle, R., J. Cunning, J. Thomas, P. Gannon and L. Teijeiro, 1977:

A case study of mesoscale convection and cloud merger over south

Florida. Conference papers, 11th Tech. Conf. on Hurricane and

Tropical Meteorology, Miami Beach, Fla.

Houze, R.A., 1977: Structure and dynamics of a tropical squall line

system. Mon. Wea. Rev., 105, 1540-1567.

Johnson, R., 1976: The role of convective-scale precipitation down-

drafts in cumulus and synoptic-scale interactions. J. Atmos.

Sci., 33, 1890-1910.

Kuo, H.L., 1974: Further studies of the parameterization of the influence

of cumulus convection on large-scale flow. J. Atmos. Sci., 31,

1232-1240.

Leary, C. and R.A. Houze, 1979: The structure and evolution of convec-

tion in a tropical cloud cluster. J. Appl. Meteor., 36, 437-456.

Ludlam, F.H. and R.S. Scorer, 1956: The motions in and around isolated

thermals. Weather, 11, 151-154.

Levine, J., 1959: Spherical vortex theory of bubble-like motion in

cumulus clouds. J. Meteor., 16, 653-662.

Lilly, D.K., 1979: The dynamical structure and evolution of thunder-
storms and squall lines. Ann. Rev. Earth Planet. Sci., 7,
117-161.

Malkus, J., 1949: Effects of wind shear on some aspects of convection.
Trans. Amer. Geophys. Union, 30, 19-25.

_____, 1952: Recent advances in the study of convective clouds and
their interaction with the environment. Tellus, 4, 71-87.

_____, 1954: Some results of a trade cumulus clouds investigation.
J. Meteor., 11, 220-237.

_____, 1955: On the formation and structure of downdrafts in cumulus
clouds. J. Meteor., 12, 350-357.

_____, 1956: On the maintenance of the trade winds. Tellus, 8, 335-
350.

_____, 1960: Recent developments in the study of penetrative convec-
tion and applications to hurricane towers. Cumulus Dynamics,
Pergamon Press, 65-84, New York.

_____, 1963: Convective processes in the tropics. Proc. Symp. on
Trop. Meteor., Rotorua, N.Z., 247-277.

_____ and M. Stern, 1953: The flow of a stable atmosphere over a
heated island. Part I. J. Meteor., 10, 30-41.

_____ and G. Witt, 1959: The evolution of a convective element: a
numerical calculation. Rept. from the Rossby Memorial Volume,
Rockefeller Institute Press, N.Y., 425-438.

Manual of Surface Observations, Circular N, U.S. Dept. of Commerce,
U.S. Government Printing Office, Washington, D.C., 1962.

Marwitz, J.D., 1972: Structure and motion of severe hailstorms, Parts
I, II and III. J. Appl. Meteor., 11, 166-201.

Matsumoto, Y., 1967: Cumulus activity in relation to the mesoscale
convergence field. J. Meteor. Soc. Japan, 45, 292-304.

Moncrieff, M.W. and M.J. Miller, 1976: The dynamics and simulation
of tropical cumulonimbus and squall lines. Quart. J. Roy.
Meteor. Soc., 102, 373-394.

Miller, M.J., 1977: Traveling convective storm over Venezuela. Mon.
Wea. Rev., 105, 833-848.

Neumann, C.J., 1971: The thunderstorm forecasting system at the
Kennedy Space Center. J. Appl. Meteor., 10, 921-936.

Newton, C., 1968: Convective cloud dynamics, a synopsis. Proc. Inter.
Conf. on Cloud Physics, Toronto, 487-498.

Ogura, Y. and J.H. Chen, 1977: A life history of an intense convective
storm in Oklahoma. J. Appl. Meteor., 34, 1458-1476.

_____ and H.-R. Cho, 1973: Diagnostic determination of cumulus
cloud populations from large scale variables. J. Atmos. Sci.,
30, 1276-1286.

Pielke, R., 1974: A three-dimensional model of the sea breeze over
south Florida. Mon. Wea. Rev., 102, 115-139.

_____ and W.R. Cotton, 1977: Mesoscale Florida analysis of a storm.
Mon. Wea. Rev., 105, 343-362.

_____ and Y. Mahrer, 1978: Verification analysis of the University
of Virginia mesoscale model prediction over south Florida for 1
July 1973. Mon. Wea. Rev., 106, 1568-1589.

Purdom, J.F.W., 1979: The development and evolution of deep convection.
A.M.S. 11th Tech. Conf. on Severe Local Storms, 143-150.

Raymond, D.J., 1975: A model for predicting the movement of continuously
propgating convective storms. J. Atmos. Sci., 32, 1308-1328.

Riehl, H., 1979: Weather and climate in the tropics. Academic Press,
New York.

Riehl, H. and J. Malkus, 1958: On the heat balance in the equatorial trough zone. Geophysica, 6, 504-537.

_____ and J. Simpson, 1979: The heat balance of the equatorial trough zone, revisited. Contr. Atmos. Phys., 52, 287-305.

Schlesinger, R., 1975: A three-dimensional numerical model of an isolated deep convective cloud: preliminary results. J. Atmos. Sci., 32, 934-957.

Scorer, R.S. and F.H. Ludlam, 1953: Bubble theory of penetrative convection. Quart. J. Roy. Meteor. Soc., 79, 94-103.

Simpson, J., 1973: The global energy budget and the role of cumulus clouds. NOAA Tech. Memo ERL WMPO-8, U.S. Department of Commerce.

_____, 1980: Downdrafts as linkages in dynamic cumulus seeding effects. J. Appl. Meteor., 19, 477-487.

_____ and V. Wiggert, 1969: Models of precipitating cumulus towers. Mon. Wea. Rev., 97, 471-489.

_____, N.E. Westcott, R.J. Clerman and R.A. Pielke, 1980: On cumulus mergers. Arch. Meteor. Geoph. Biokl., Ser. A, 29, 1-40.

Stommel, H., 1947: Entrainment of air into cumulus cloud. J. Meteor., 4, 91-94.

Smithsonian Meteorological Tables, 1949: Sixth Edition, Smithsonian Institution Press, Washington, D.C.

Tepper, M., 1950: A proposed mechanism of squall lines, the hydraulic pressure jump line. J. Meteor., 8, 24-29.

Tetens, O., 1930: Uber einige meteorologische begriffe. Z. Geophys., 6, 297-309.

Ulanski, S. and M. Garstang, 1978: Role of surface divergence and vorticity in the life cycle of convective rainfall. Parts I and II. J. Atmos. Sci., 35, 1047-1062.

Woodley, W. and R. Sax, 1974: 1973 FACE operations and preliminary summary. NOAA Tech. Memo. ERL WMPO-12, U.S. Dept. of Commerce.

_____, 1976: 1975 FACE: Operational summary. NOAA Tech. Memo. ERL WMPO-28, U.S. Dept. of Commerce.

Yanai, M., 1975: Tropical meteorology. Rev. of Geophys. and Space Phys., 13, No. 3.

_____, S. Esbensen and J.H. Chu, 1973: Determination of bulk properties of tropical cloud clusters from large-scale heat and moisture budget. J. Atmos. Sci., 30, 611-627.

Zipser, E., 1969: The role of organized unsaturated convective downdrafts in the structure and rapid decay of an equatorial disturbance. J. Appl. Meteor., 8, 799-814.

_____, 1977: Mesoscale and convective scale downdrafts as distinct components of squall line structure. Mon. Wea. Rev., 105, 1568-1589.

APPENDIX A

THE INTERPOLATION SCHEME

The basis of the method used in this study to interpolate the surface wind data to a regular grid can be found in Ogura and Chen (1977).

Calculation of the divergence in the horizontal surface wind fields from an irregularly spaced surface wind station network is complicated by the fact that there are few ways in which to check the results of the calculations, except by persistent comparison with tedious hand analyses, which defeats the purpose of computerizing the process.

Ogura and Chen solve this problem by defining a velocity potential, $\psi(x,y)$, where

$$\psi(x,y) = A \sin\left(\frac{2\pi x}{\Delta x}\right) \sin\left(\frac{\pi y}{\Delta y}\right) \tag{1}$$

where A is the amplitude of the potential and is a constant, and Δx and Δy are the constant dimensions of the entire interpolation grid. The velocity at a grid point (x,y) inside the interpolation grid is then found from the gradient of the velocity potential:

$$\nabla\psi(x,y) = \frac{\partial \psi}{\partial x} \hat{i} \quad \frac{\partial \psi}{\partial y} \hat{j} \tag{2}$$

$$= \left[A \frac{2\pi}{\Delta x} \cos\left(\frac{2\pi x}{\Delta x}\right) \sin\left(\frac{\pi y}{\Delta y}\right)\right] \hat{i}$$

$$+ \left[A \frac{\pi}{\Delta y} \sin\left(\frac{2\pi x}{\Delta x}\right) \cos\left(\frac{\pi y}{\Delta y}\right)\right] \hat{j}$$

where $\hat{i}$ and $\hat{j}$ are unit vectors in the u and v component directions of the surface wind fields.

That is, we define $u = \frac{\partial \psi}{\partial x}$ and $v = \frac{\partial \psi}{\partial y}$, so that

$$u(x,y) = \frac{A2\pi}{\Delta x} \cos\left(\frac{2\pi x}{\Delta x}\right) \sin\left(\frac{\pi y}{\Delta y}\right) \tag{3}$$
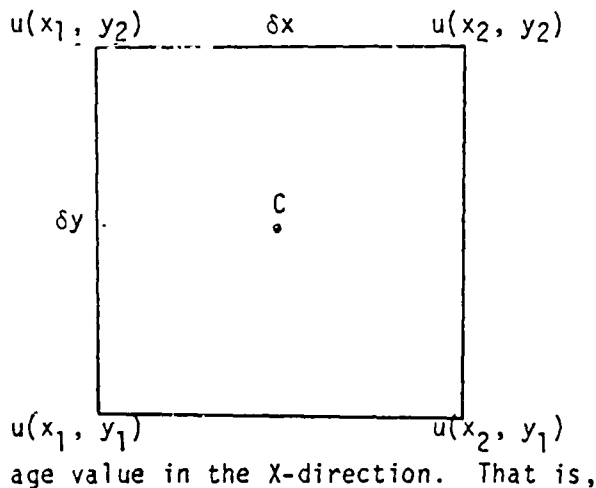
and

$$v(x,y) = A\frac{\pi}{\Delta y} \sin\left(\frac{2\pi x}{\Delta x}\right) \cos\left(\frac{\pi y}{\Delta y}\right) \tag{4}$$

then a value of u and v can be assigned analytically to each grid point in the interpolation grid.

From the analytically determined fields of $u(x,y)$ and $v(x,y)$, divergence calculations can now be made for each grid square within the interpolation grid, and an analytical divergence field produced.

The analytical divergence field from $\psi($ is calculated using a simple finite differencing method, as outlined below. At each grid point, the assigned values of $u(x,y)$ and $v(x,y)$ are used to determine the value of the divergence at the center of each grid, at point C. The gradient in X-direction of the analytically derived u-component of the horizontal wind speed is calculated by taking the average of its values in the y-direction and subtracting the averaged value obtained from the next grid point average value in the X-direction. That is,

$$\frac{\delta y}{\delta x} = \frac{1}{\delta x} \left\{ \left[\frac{u(x_1,y_2) + u(x_1,y_1)}{2} \right] - \left[\frac{u(x_2,y_1) + u(x_2,y_2)}{2} \right] \right\}$$

Similarly,

$$\frac{\delta v}{\delta y} = \frac{1}{\delta y} \left\{ \left[\frac{v(x_1 y_1) + v(x_2,y_1)}{2} \right] - \left[\frac{v(x_1,y_2) + v(x_2,y_2)}{2} \right] \right\}$$
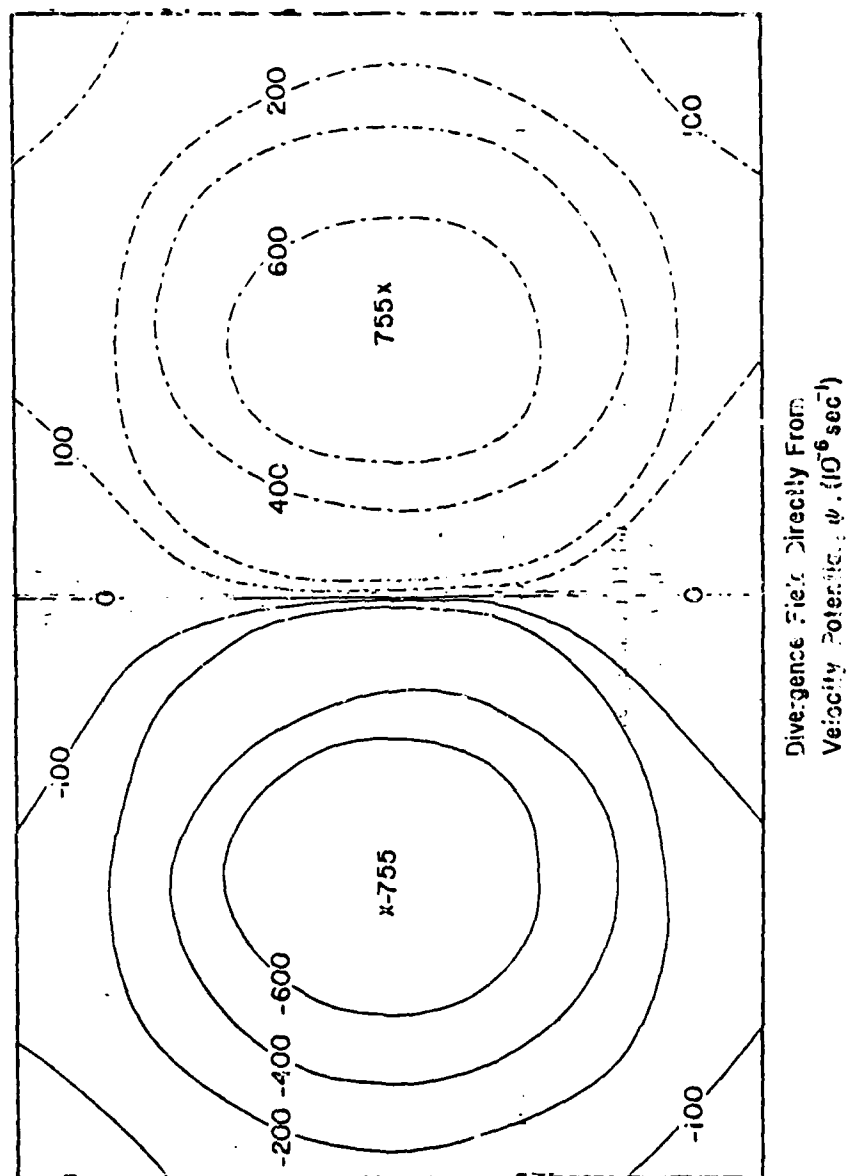
Divergence Field Directly From
Velocity Potential, ψ, (10⁻⁶ sec⁻¹)

Figure A-1. The divergence field directly from the velocity potential, ψ.

where δx, δy represent the X and Y spacing of the grid points in the interpolation grid. Then the convergence is the sum of these two terms,

$$\nabla_H \cdot v \approx \left(\frac{\delta u}{\delta x}\right) + \left(\frac{\delta v}{\delta y}\right)$$

The analytically calculated divergence field which results is shown in Figure Al. The resulting field is symmetric about the center of the network in absolute value of divergence, and consists of two large circular cells of maximum value $\pm 755 \times 10^{-6}$ sec^{-1}. This divergence field is now used in calibrating any interpolation scheme which may be used in the analysis, and allows us to compare the ability of various schemes to reproduce, from interpolated data, a known divergence field.

The interpolation schemes considered were all based on the ideas of Cressman (1959), who used a scanning method of successive approximations to obtain estimates of data at fixed grid points. About a point at which a value of the u-component or v-component of the surface wind is to be estimated, each station within a scanning radius, N, is considered. On the first (and largest radius) scan, a simple average of all the u-components of the stations within the first scanning radius is taken, and used as a first guess of the value to be given to the u-component which is to be assigned to the grid point from which the scanning takes place.

The next scan, which has a smaller scanning radius than the first, assigns values to the first guess u-component which are weighted according to how far away the station within the scanning radius is from the point in the interpolation grid.

Successive scans, each smaller than the previous scan, assign values of the u-component to the grid point which are determined by the distance of the stations within the scan from the grid point. The pro-

cess is sketched below. Stations #1-#4 would all be included in the first scan, and a simple average of their u-components taken. Then stations #3 and #4 only would be included in scan #2, with station #4 being given a greater weight than station #3, since it is closer to the grid point at A, and an average of those two stations taken, and that value added to the first guess made during scan #1. Finally, in scan #3, only station #4 would be included, and it would be assigned a weight based on its distance from the grid point at A, and the result added to give the final estimate of the value of the u-component at A. Similar calculations would provide an estimate of the value of the v-component at A.
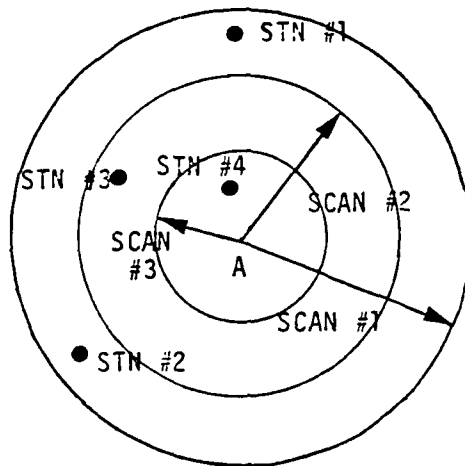
The differences between the schemes considered lay in the choice of the number of scans to be made, and the weighting functions to be used. It was decided to follow Ogura and Chen, and test the effect of fitting a bi-cubic spline to the data in order to see if in these cases, as Ogura and Chen found, the fitting of the bi-cubic spline improved the ability of these various types of interpolation schemes to reproduce the divergence fields represented in Figure A1.

Two weighting functions were considered, one similar to that used by Cressman, and an exponentially decaying function:

(a) $\quad u(x,y) \approx \sum_{j=2}^{T} \sum_{i=2}^{S_j} u_i \left(\dfrac{N_j^2 - d_i^2}{N_j^2 + d_i^2} \right)$ $\qquad$ (Cressman)

or

(b) $\quad u(x,y) \approx \sum_{j=2}^{T} \sum_{i=2}^{S_j} u_i \exp\left(\dfrac{-K\, d_i^2}{N_j^2} \right)$

In both cases, on the first scan

$$u(x,y) \approx \frac{1}{S_1} \sum_{i=1}^{S_1} u_i$$

here $u(x,y)$ is the estimate of the u-component at a grid point for a given scan, S_j is the total number of stations within scanning radius N_j and u_i is the value of the u-component at station i, within the scan. N_j is the radius of scan j, and d_i is the distance of station i from the grid point. T is the total number of scans made, and K is a parameter which is varied to achieve best results.

The interpolation grids used in 1973 and 1975 are shown in Figures A2 and A3.

A station at (x,y) in the interpolation grid was assigned values of $u(x,y)$ and $v(x,y)$ taken from $\psi(x,y)$ as defined. These values of $u(x,y)$ and $v(x,y)$ assigned to each station were then used to estimate values of u and v at grid points within the interpolation grid, using the Cressman scanning and weighting. Then divergence was calculated at the center of each grid square, and the best results obtained, using 4 scans of 15, 10, 8 and 5 km are sketched in Figure A4.

Comparing Figure A4 with Figure A1 reveals considerable distortions in the divergence field, although its general features have survived. The peak values of convergence and divergence are lower than those in Figure A1, and large spurious values of divergence appear in
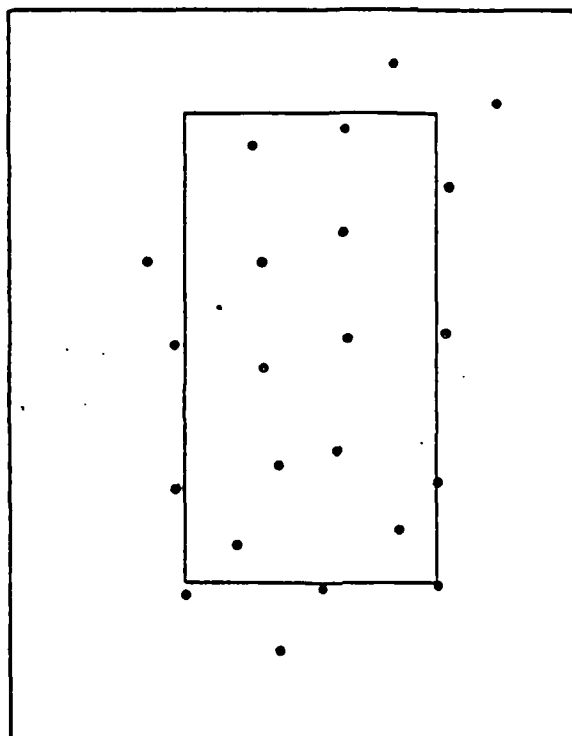
Positions of Face 73 Stations Relative to Grid

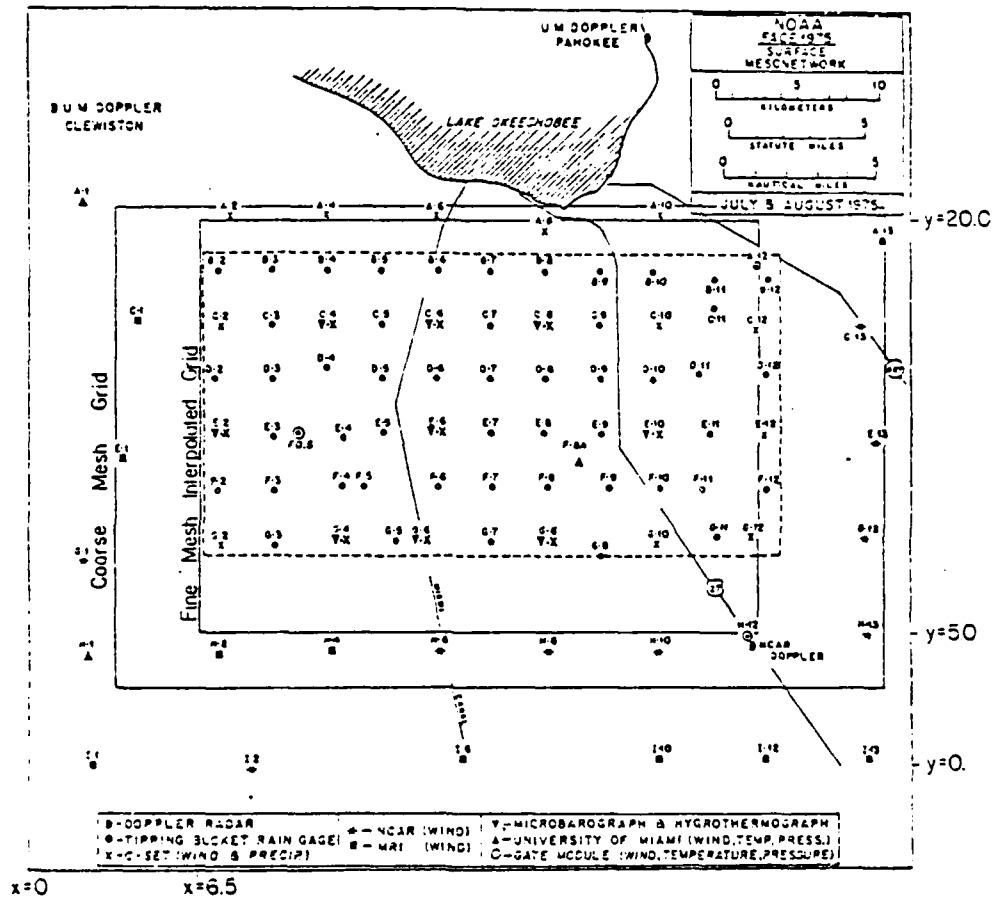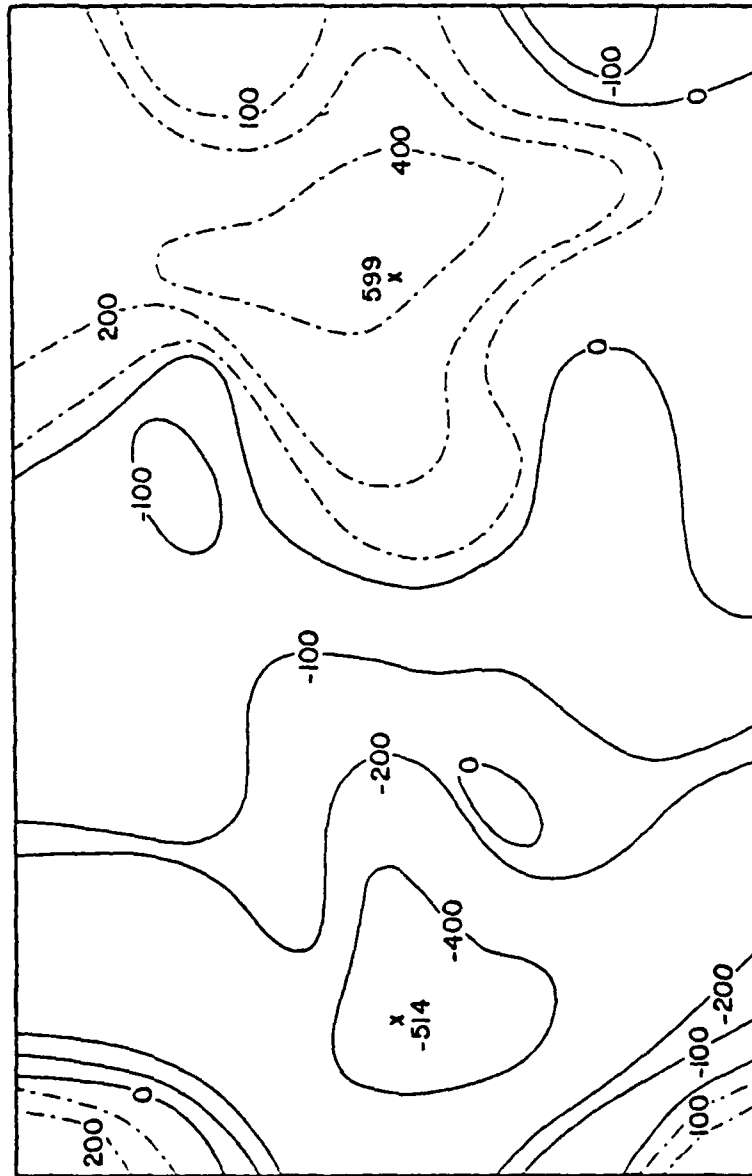*Figure A-2. The positions of the 1973 wind sets relative to interpolation grid.*

Figure A-3. The positions of the 1975 wind sets relative to interpolation grid.

Figure A-4. Interpolated divergence field, Cressman weight, no spline ($x\ 10^{-6}\ sec^{-1}$).

the northwestern corner of the network.

Figure A5 shows the result of using the exponential weighting function with optimum scans (again 4) and values of K. The field produced in this case gives slightly higher peak values of convergence and divergence, but, again, the field of divergence is seriously distorted.

The next two tests were run using a bi-cubic spline smoothing function. Values of $u(x,y)$ and $v(x,y)$ were interpolated to a coarse grid, which was larger than the interpolation grid used in the other two tests, and contained that grid. After values had been interpolated from the stations in the network to the coarse-meshed grid, a bi-cubic spline was fitted to the coarse grid points, and from the values of the resulting surface, grid points on the fine-meshed grid were assigned values of $u(x,y)$ and $v(x,y)$. The smoothed values of $u(x,y)$ and $v(x,y)$ were then used to calculate divergence at the center of each grid in the fine-meshed grid. The fine-meshed grid in this case is the same grid which was used in the first two attempts at interpolation which used only the Cressman weighting and scanning or the exponential weighting and scanning, without the spline.

The results of smoothing the Cressman weighted interpolation scheme are contained in Figure A6. The resulting field is smooth and reproduces the field in Figure A1 quite well, except that the peak values of the convergence and divergence are too low.

The spline was then applied to the exponentially weighted interpolation scheme, and the best results were achieved, using four scans of 10, 8, 5 and 3 km and a K-value of 0.25. The fields in Figure A1 are reproduced remarkably well in all aspects, with only slight distortions, in Figure A7.
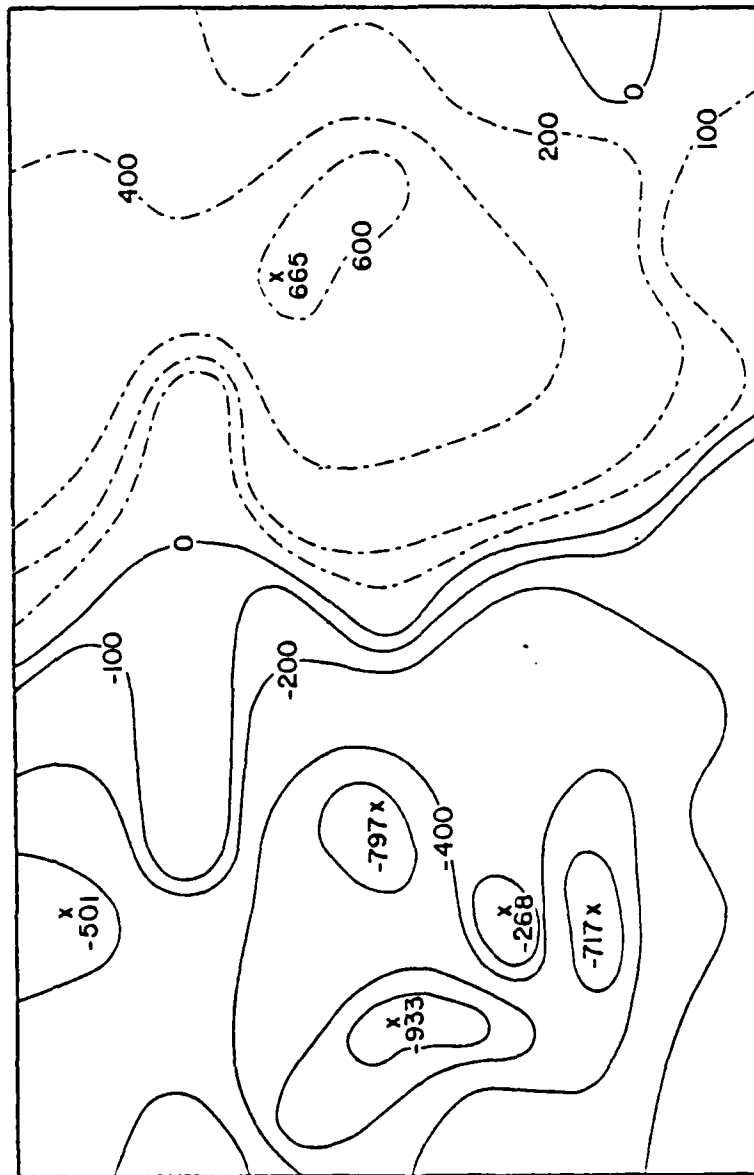
Figure A-5. Interpolated divergence field, exponential weight, no spline (x 10^{-6} sec^{-1}).
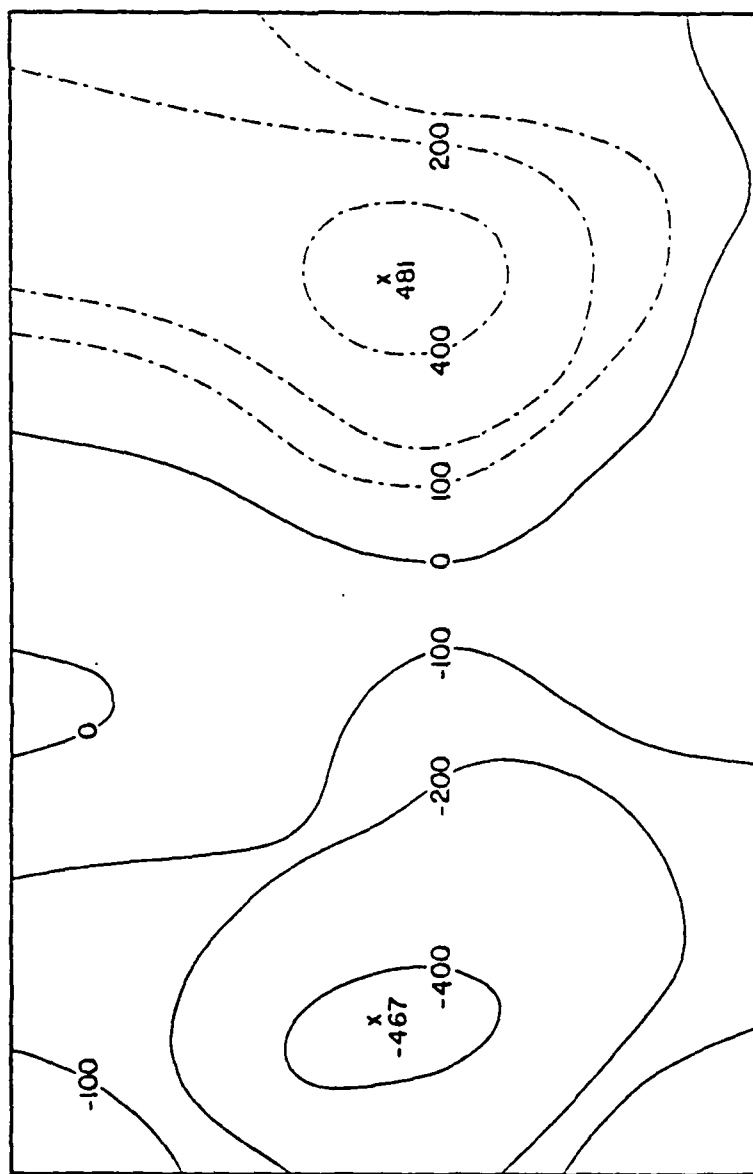
Interpolated Divergence Field
Cressman Weight, With Spline ($10^{-6} sec^{-1}$)

Figure A-6. Interpolated divergence field, Cressman weight, with spline ($x \ 10^{-6} \ sec^{-1}$).

APPENDIX B

CALCULATION OF THERMODYNAMIC VARIABLES

1. Vapor Pressure

$$e = e' - [0.00066(1 + 0.00115\ T_{wet})]P(T - T_{wet})$$

$$= e' - \Delta e \qquad \text{(Smithsonian Tables, 5th edition, 1971)}$$

where e = vapor pressure (mb),

P = pressure (mb),

T = temperature (°C),

and T_{wet} = wet bulb temperature (°C),

where $e' = e\ (T_{wet}) = 6.11 \times 10^{(7.5\ T_{wet}/(T_{wet} + 237.3))}$

(from Tetens, 1930)

2. Mixing Ratio

$$w = 0.622\ \left(\frac{e}{p-e}\right)$$

$$= 0.622\ \left(\frac{e'-\Delta e}{p-(e'-\Delta e)}\right)$$

(from Hess, 1959)
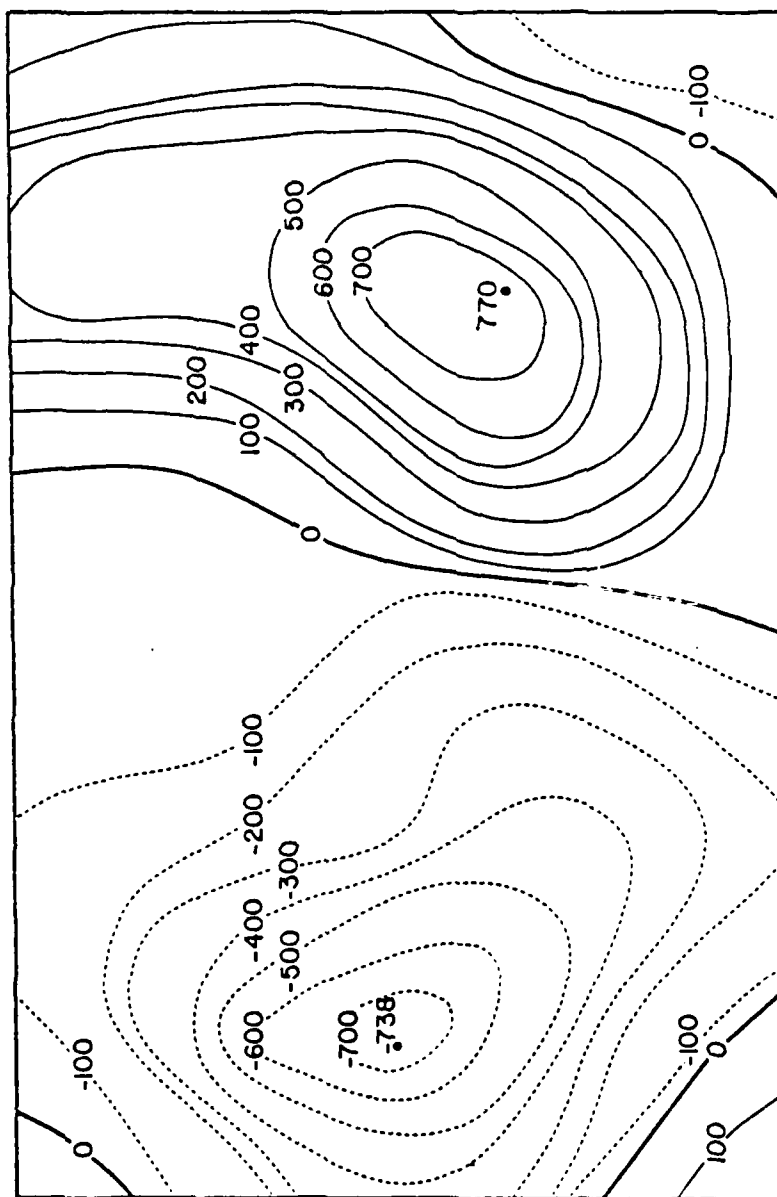
3. Equivalent Potential Temperature (Bolton, 1980)

Let $A = (0.2854\ (1 - 0.256 \times 10^{-3}))$,

and T_L = temperature at LCL, then

$$\theta_e = T(°K)\left(\frac{1000}{P}\right)^A \times \exp\left\{\left(\frac{3.376}{T_L} - 0.00254\right) \times w(1 + 0.81 \times 10^{-3}\ w)\right\}$$

where $T_L = \left\{(2840 \times (3.5\ \ln T(°K) - \ln e - 4.805)^{-1} + 55\right\}$

(w in gm/kg)

Interpolated Divergence Field
Exponential Weight with Spline (IO⁻⁶sec⁻¹)

Figure A-7. Interpolated divergence field, exponential weight, with spline (x 10⁻⁶ sec⁻¹).

DATE
ILME